

A MULTI-WAVELENGTH STUDY  
ON THE X-RAY EMISSIONS  
FROM YOUNG STELLAR OBJECTS  
IN ORION MOLECULAR CLOUD 2 AND 3

Masahiro Tsujimoto

Department of Physics, Graduate School of Science, Kyoto University  
*Kitashirakawa Oiwake-cho, Sakyo-ku, Kyoto, 606-8502, Japan*  
tsujimot@cr.scphys.kyoto-u.ac.jp

Thesis submitted to the Department of Physics,  
Graduate School of Science, Kyoto University  
on January 6, 2003  
in partial fulfillment of the requirements  
for the degree of Doctor of Philosophy in physics

## Abstract

We made a multi-wavelength study to reveal the variety and to understand the mechanisms of X-ray emissions from young stellar objects (YSOs), selecting Orion molecular cloud (OMC) 2 and 3 as our study field. OMC-2 and OMC-3 are intermediate mass star-forming regions, which contain YSOs at all evolutionary classes from class 0 protostars to T Tauri stars in a wide range of mass from early-type stars to brown dwarfs.

We conducted deep observations on OMC-2 and OMC-3 in the X-ray and near-infrared (NIR) band respectively using the *Chandra X-ray Observatory* and the University of Hawaii 88 inch (2.2 m) telescope. In the X-ray band, we detected 385 sources in the Advanced CCD Imaging Spectrometer (ACIS)-I image of  $17 \times 17$  arcmin<sup>2</sup>, which is complete down to  $F_X \sim 10^{-14.5}$  ergs s<sup>-1</sup> cm<sup>-2</sup> with the faintest detected source of  $F_X \sim 10^{-15.5}$  ergs s<sup>-1</sup> cm<sup>-2</sup> in the 0.5–8.0 keV energy range. In the NIR band, we obtained the *J*- (1.2  $\mu$ m), *H*- (1.6  $\mu$ m), and *K*-band (2.2  $\mu$ m) Quick Infrared Camera (QUIRC) images to extract 1448 NIR sources in a 512 arcmin<sup>2</sup> region. The survey is complete down to *J*  $\sim$  17.5, *H*  $\sim$  16.5, and *K*  $\sim$  16.0 mag, matching well with the *Chandra* limit.

Combining the 2MASS (Two Micron All Sky Survey) and our QUIRC data, we identified the NIR counterpart for 278 ( $\sim$ 72%) X-ray sources (NIR-identified [NIR-IDed] X-ray sources). Most of these sources are YSOs that belong to OMC-2 and OMC-3 considering their magnitude and luminosity function in the *K* band. The rests of the X-ray sources are unidentified with NIR sources (NIR-unidentified [NIR-unIDed] X-ray sources).

For NIR-IDed X-ray sources, we estimated their mass and evolutionary class using their *J*-, *H*-, *K*-band flux. We also derived their X-ray flux variability through the X-ray temporal analysis, and their plasma temperature and X-ray luminosity by the X-ray spectral analysis. By comparing the averaged X-ray properties among different mass ranges, we found that YSOs in the intermediate ( $2.0 M_\odot \leq M < 10.0 M_\odot$ ), low ( $0.2 M_\odot \leq M < 2.0 M_\odot$ ), and very low ( $M < 0.2 M_\odot$ ) mass ranges have the same X-ray emission properties in contrast to the high mass ( $M \geq 10.0 M_\odot$ ) sources. We further revealed that the X-ray emissions from intermediate to very low mass YSOs consist of two thin-thermal plasma components of different temperatures ( $k_B T \sim 1$  keV and 2–3 keV). Based on the time-sliced X-ray spectroscopy of some bright variable sources and on comparison with the sun and other main and pre-main-sequence sources, we proposed that the soft X-ray component is from coronae while the hard component is due to flares.

Most of the NIR-unIDed X-ray sources are background extragalactic sources from their hard X-ray spectra. However, the spatial distribution of these sources has an excess along the ridge of star-forming cloud cores, which indicates that some of the NIR-unIDed X-ray sources are related to star formations. We made follow-up imaging observations using the University of Hawaii 88 inch (2.2 m) telescope, the Subaru telescope, and the Infrared Telescope Facility in the  $J$ ,  $H$ ,  $K$ ,  $L'$  ( $3.8 \mu\text{m}$ ), and  $\text{H}_2 v = 1 - 0 \text{ S}(1)$  ( $2.12 \mu\text{m}$ ) bands in addition to the centimeter interferometer imaging observation with Very Large Array (VLA). Four NIR-unIDed X-ray sources are associated with jet and outflow systems and share many multi-wavelength characteristics in common. We proposed that these X-ray emissions can be explained by the high temperature plasma induced by protostellar jets. Other NIR-unIDed X-ray sources along the cloud core do not have such association. However, their heavily absorbed X-ray spectra and the association of some with sub-millimeter cores infer that they are heavily embedded X-ray-emitting YSOs, such as class 0 objects.





# Contents

<b>1</b>	<b>Introduction</b>	<b>19</b>
<b>2</b>	<b>X-ray Observations on YSOs</b>	<b>25</b>
2.1	Basic Features of YSOs . . . . .	26
2.1.1	Evolution and Classification . . . . .	26
2.1.2	Jets and Outflows . . . . .	29
2.1.3	Magnetic Activities . . . . .	31
2.2	X-ray Observations on YSOs . . . . .	33
2.2.1	Low-mass YSOs: (1) Recent Results with <i>Chandra</i> . . . . .	33
2.2.2	Low-mass YSOs: (2) X-ray Emission Mechanisms . . . . .	37
2.2.3	Very Low Mass YSOs (=Young Brown Dwarfs) . . . . .	41
2.2.4	Intermediate-mass YSOs . . . . .	42
2.2.5	High-mass YSOs . . . . .	42
2.2.6	Diffuse X-ray Emissions . . . . .	43
2.2.7	Problems to be Addressed . . . . .	45
<b>3</b>	<b>Orion Molecular Cloud 2 and 3</b>	<b>47</b>
3.1	Global Properties . . . . .	48

3.2	Radio Observations . . . . .	49
3.2.1	Identifying Protostellar Cores with Dust Emissions . . . . .	49
3.2.2	Centimeter Observations of Free-free Emissions . . . . .	51
3.2.3	Millimeter Observations of Molecular Cores and Outflows . . . . .	56
3.2.4	Polarization Measurements . . . . .	56
3.3	NIR Observations . . . . .	56
3.3.1	Bright Discrete Sources in OMC-2 . . . . .	56
3.3.2	Surveys with Broad-band Imaging Observations . . . . .	57
3.3.3	Narrow-band Studies of Molecular Outflows . . . . .	58
3.4	Optical Observations . . . . .	59
3.4.1	Membership Studies with Proper Motion Measurements . . . . .	59
3.4.2	Detection of Circumstellar Disks . . . . .	59
3.5	X-ray Observations . . . . .	62
3.5.1	Surveys in the Soft X-ray Band . . . . .	62
3.5.2	Surveys in the Hard X-ray Band . . . . .	62
<b>4</b>	<b>Observing Facilities and Instruments</b>	<b>67</b>
4.1	<i>Chandra X-ray Observatory</i> . . . . .	68
4.1.1	Spacecraft . . . . .	68
4.1.2	Optics . . . . .	69
4.1.3	Instrument (ACIS) . . . . .	73
4.2	University of Hawaii 88 inch (2.2 m) Telescope . . . . .	79
4.2.1	Telescope . . . . .	79
4.2.2	Instrument (QUIRC) . . . . .	82
4.3	Subaru Telescope . . . . .	83

<i>CONTENTS</i>	7
4.3.1 Telescope . . . . .	83
4.3.2 Instrument (IRCS) . . . . .	83
4.4 Infrared Telescope Facility . . . . .	85
4.4.1 Telescope . . . . .	85
4.4.2 Instrument (NSFCam) . . . . .	85
4.5 Very Large Array . . . . .	87
4.5.1 Telescope . . . . .	87
4.5.2 Radio Interferometry . . . . .	89
<b>5 <i>Chandra</i> and QUIRC Observations</b>	<b>93</b>
5.1 X-ray Observation with <i>Chandra</i> /ACIS . . . . .	94
5.1.1 Observation . . . . .	94
5.1.2 Data Reduction . . . . .	94
5.1.3 Source Extraction . . . . .	96
5.1.4 2MASS Counterpart of <i>Chandra</i> Sources . . . . .	96
5.1.5 Results . . . . .	101
5.2 NIR Observation with UH88/QUIRC . . . . .	104
5.2.1 Observation . . . . .	104
5.2.2 Data Reduction . . . . .	106
5.2.3 Source Extraction and Photometry . . . . .	107
5.2.4 2MASS Counterpart of QUIRC Sources . . . . .	109
5.2.5 Results . . . . .	109
5.2.6 QUIRC Counterpart of <i>Chandra</i> Sources . . . . .	114
<b>6 NIR-IDed X-ray Sources: (1) NIR Properties</b>	<b>117</b>

6.1	NIR Sources . . . . .	118
6.1.1	<i>K</i> -band Luminosity Function . . . . .	118
6.1.2	Color-color Diagram of QUIRC Sources . . . . .	119
6.1.3	Color-magnitude Diagram of QUIRC Sources . . . . .	120
6.2	The NIR-IDed X-ray Sources . . . . .	124
6.2.1	Cloud Membership . . . . .	124
6.2.2	Evolutional Class Estimates . . . . .	124
6.2.3	Mass and Bolometric Luminosity Estimates . . . . .	127
<b>7</b>	<b>NIR-IDed X-ray Sources: (2) X-ray Properties</b>	<b>131</b>
7.1	Temporal Analysis . . . . .	132
7.2	Spectral Analysis . . . . .	139
7.2.1	Spectrum Models and Fittings . . . . .	139
7.2.2	One-temperature Plasma Fittings . . . . .	140
7.2.3	Two-temperature Plasma Fittings . . . . .	151
7.2.4	Time-sliced Spectroscopy . . . . .	159
7.3	Relations between Parameters . . . . .	162
7.3.1	X-ray absorption versus NIR extinction . . . . .	162
7.3.2	X-ray counts versus X-ray flux . . . . .	162
7.3.3	X-ray counts versus X-ray luminosity . . . . .	162
<b>8</b>	<b>NIR-unIDed X-ray Sources</b>	<b>167</b>
8.1	The Nature of NIR-unIDed X-ray Sources . . . . .	168
8.1.1	Background AGNs . . . . .	168
8.1.2	Sources with YSO-like Features . . . . .	175

8.2	H <sub>2</sub> Imaging Observations on OMC-3 . . . . .	177
8.2.1	Observation . . . . .	177
8.2.2	Analysis & Results . . . . .	178
8.3	NIR Observations on MMS 2 and MMS 3 . . . . .	178
8.3.1	Observation . . . . .	178
8.3.2	Analysis & Results . . . . .	181
8.3.3	Discussion . . . . .	187
8.4	Centimeter Observations on MMS 2 and MMS 3 . . . . .	188
8.4.1	Observation . . . . .	188
8.4.2	Analysis & Results . . . . .	189
8.4.3	Discussion . . . . .	190
<b>9</b>	<b>Discussion</b>	<b>193</b>
9.1	X-ray Emissions from NIR-IDed Sources: (1) Mass . . . . .	194
9.1.1	X-ray Properties among Mass Ranges . . . . .	194
9.1.2	High Mass Sources . . . . .	194
9.1.3	Intermediate Mass to Very Low Mass Sources . . . . .	196
9.2	X-ray Emissions from NIR-IDed Sources: (2) Plasma Temperature . . . . .	201
9.2.1	Two-temperature Plasma Emissions . . . . .	201
9.2.2	Origins of Two-temperature Plasma . . . . .	203
9.2.3	X-ray Properties among Evolutional Classes . . . . .	206
9.3	X-ray Emissions from NIR-unIDed Sources . . . . .	208
9.3.1	Jet-induced Plasma Emissions . . . . .	208
9.3.2	Magnetic Activities of Deeply Embedded YSOs . . . . .	213

10 Conclusions	217
A <i>Chandra</i> Sources and NIR Counterpart	235
B QUIRC Sources and 2MASS Counterpart	247

# List of Figures

1.1	Orion Nebula . . . . .	19
1.2	Absorption or scattering cross section by ISM . . . . .	20
2.1	Classification of YSOs and their SEDs . . . . .	28
2.2	<i>Chandra</i> image of ONC . . . . .	34
2.3	X-ray detections from class I protostars in R Coronae Australis . . . . .	35
2.4	X-ray detections from class I protostars in $\rho$ Oph . . . . .	35
2.5	Magnetic field geometries of YSOs . . . . .	38
2.6	Quasi-periodic flares from a protostar . . . . .	38
2.7	DEM distribution of SU Aur . . . . .	40
2.8	X-ray CCD and grating spectra of TW Hya . . . . .	40
2.9	X-ray detection from a HH object . . . . .	44
3.1	Location of OMC-2 and OMC-3 (1) . . . . .	48
3.2	Location of OMC-2 and OMC-3 (2) . . . . .	50
3.3	1.3 mm map of OMC-2 and OMC-3 . . . . .	52
3.4	350 $\mu$ m map of OMC-2 and OMC-3 . . . . .	53
3.5	Past NIR observations of OMC-2 and OMC-3 . . . . .	60
3.6	Past optical observations of OMC-2 and OMC-3 . . . . .	61

3.7	Past X-ray observations of OMC-2 and OMC-3 . . . . .	64
4.1	<i>Chandra</i> spacecraft . . . . .	68
4.2	Configuration of HRMA . . . . .	69
4.3	Energy dependence of HRMA effective area . . . . .	70
4.4	Spatial dependence of HRMA effective area . . . . .	71
4.5	PSF of HRMA at on-axis . . . . .	71
4.6	PSF of HRMA at off-axis . . . . .	72
4.7	Configuration of ACIS array . . . . .	73
4.8	Energy resolution of ACIS . . . . .	74
4.9	Effective energy range of ACIS . . . . .	76
4.10	Energy dependence of the ACIS background . . . . .	77
4.11	Long-term variation of the ACIS background . . . . .	78
4.12	Spatial dependence of the ACIS background . . . . .	80
4.13	Schematic view of the University of Hawaii 88 inch (2.2 m) telescope . . . . .	81
4.14	QUIRC filter transmissions . . . . .	83
4.15	Schematic view of Subaru telescope . . . . .	84
4.16	Broad-band filter transmissions of Mauna Kea system . . . . .	86
4.17	Configuration of VLA . . . . .	88
4.18	Schematic view of radio interferometry . . . . .	91
5.1	FOV of <i>Chandra</i> observation . . . . .	95
5.2	Pseudo-color image of <i>Chandra</i> observation . . . . .	97
5.3	2MASS Second Incremental Data Release coverage . . . . .	98
5.4	Astrometric accuracy of 2MASS sources . . . . .	99



5.5	Photometric accuracy of 2MASS sources . . . . .	100
5.6	Astrometric accuracy of <i>Chandra</i> sources . . . . .	102
5.7	Histogram of <i>Chandra</i> source counts . . . . .	103
5.8	FOV of QUIRC mosaic mapping observations . . . . .	105
5.9	Pseudo-color image of QUIRC observation . . . . .	108
5.10	Astrometric accuracy of QUIRC sources . . . . .	110
5.11	Photometric accuracy of QUIRC sources . . . . .	111
5.12	Completeness limit of QUIRC observations . . . . .	112
5.13	QUIRC <i>K</i> -band source counts . . . . .	113
5.14	X-ray off-axis angle versus separation of the closest QUIRC– <i>Chandra</i> pairs . . . . .	114
5.15	NIR identification of ACIS-I sources . . . . .	115
6.1	Differential KLF of QUIRC sources . . . . .	119
6.2	Color-color diagram of QUIRC sources . . . . .	121
6.3	Color-magnitude diagram of QUIRC sources . . . . .	122
6.4	Histogram of <i>K</i> -band extinction . . . . .	123
6.5	Color-color diagram of X-ray sources . . . . .	126
6.6	Spatial distribution of <i>Chandra</i> sources (1) . . . . .	128
6.7	Color-magnitude diagram of <i>Chandra</i> sources . . . . .	129
6.8	Spatial distribution of <i>Chandra</i> sources (2) . . . . .	130
7.1	NIR-IDed <i>Chandra</i> sources for temporal analysis . . . . .	133
7.2	Light curves of bright variable NIR-IDed <i>Chandra</i> sources (1) . . . . .	134
7.3	Light curves of bright variable NIR-IDed <i>Chandra</i> sources (2) . . . . .	135
7.4	Light curves of bright variable NIR-IDed <i>Chandra</i> sources (3) . . . . .	136

7.5	Light curves of bright variable NIR-IDed <i>Chandra</i> sources (4)	137
7.6	Light curves of bright variable NIR-IDed <i>Chandra</i> sources (5)	138
7.7	NIR-IDed <i>Chandra</i> sources for spectral analysis	141
7.8	One-temperature plasma fittings of bright NIR-IDed <i>Chandra</i> sources (1)	145
7.9	One-temperature plasma fittings of bright NIR-IDed <i>Chandra</i> sources (2)	146
7.10	One-temperature plasma fittings of bright NIR-IDed <i>Chandra</i> sources (3)	147
7.11	One-temperature plasma fittings of bright NIR-IDed <i>Chandra</i> sources (4)	148
7.12	One-temperature plasma fittings of bright NIR-IDed <i>Chandra</i> sources (5)	149
7.13	One-temperature plasma fittings of bright NIR-IDed <i>Chandra</i> sources (6)	150
7.14	Best-fit models of bright NIR-IDed ACIS-I sources	151
7.15	Two-temperature plasma fittings of bright NIR-IDed <i>Chandra</i> sources (1)	154
7.16	Two-temperature plasma fittings of bright NIR-IDed <i>Chandra</i> sources (2)	155
7.17	Two-temperature plasma fittings of bright NIR-IDed <i>Chandra</i> sources (3)	156
7.18	Two-temperature plasma fittings of bright NIR-IDed <i>Chandra</i> sources (4)	158
7.19	Time-sliced spectroscopy of bright NIR-IDed <i>Chandra</i> sources (1)	159
7.20	Time-sliced spectroscopy of bright NIR-IDed <i>Chandra</i> sources (2)	160
7.21	X-ray absorption versus NIR extinction	163
7.22	X-ray counts versus flux	164
7.23	X-ray counts versus luminosity	165
8.1	<i>Chandra</i> sources for spectral analysis	169
8.2	Power-law fittings of bright NIR-unIDed <i>Chandra</i> sources (1)	171
8.3	Power-law fittings of bright NIR-unIDed <i>Chandra</i> sources (2)	172
8.4	Histogram of <i>Chandra</i> hardness ratio	173
8.5	Power-law fittings of combined spectra of NIR-unIDed <i>Chandra</i> sources	174

8.6	Spatial distribution of NIR-unIDed <i>Chandra</i> sources . . . . .	176
8.7	FOV of QUIRC H <sub>2</sub> observations . . . . .	177
8.8	QUIRC H <sub>2</sub> -band images of OMC-3 . . . . .	179
8.9	<i>Chandra</i> image of MMS 2 . . . . .	180
8.10	Schematic view of NIR dithering observations . . . . .	181
8.11	IRCS <i>K</i> -band image of MMS 2 . . . . .	182
8.12	NSFCam <i>L'</i> -band image of MMS 2 . . . . .	183
8.13	IRCS H <sub>2</sub> -band image of MMS 2 . . . . .	186
8.14	Color-color diagram of IRCS sources . . . . .	187
8.15	VLA image of MMS 2 . . . . .	189
8.16	Centimeter flux density versus outflow momentum rate . . . . .	191
9.1	Light curve and spectrum of high mass sources . . . . .	197
9.2	Mass versus the ratio of X-ray and bolometric luminosity of NIR-IDed X-ray sources	199
9.3	Mass versus X-ray luminosity of NIR-IDed X-ray sources . . . . .	200
9.4	Histogram of plasma temperature . . . . .	202
9.5	DEM distributions of coronally active main sequence stars . . . . .	204
9.6	Evolution of two-temperature plasma emissions . . . . .	205
9.7	X-ray and NIR images of NIR-unIDed X-ray sources . . . . .	209
9.8	Multi-wavelength view on MMS 2 . . . . .	211
9.9	Schematic view of the X-ray and centimeter emissions of protostellar jet origin.	211
9.10	One-temperature plasma fittings of NIR-unIDed X-ray sources . . . . .	213
10.1	Summary . . . . .	219



# List of Tables

2.1	Multi-wavelength properties of low-mass YSOs . . . . .	29
2.2	<i>Chandra</i> and <i>XMM-Newton</i> studies of star-forming regions . . . . .	36
2.3	Detected numbers of X-ray sources in <i>Chandra</i> survey studies . . . . .	36
3.1	Properties of protostellar cores in OMC-2 and OMC-3 (1) . . . . .	54
3.2	Properties of protostellar cores in OMC-2 and OMC-3 (2) . . . . .	55
3.3	Past observations of OMC-2 and OMC-3 . . . . .	65
3.4	Past NIR survey studies of OMC-2 and OMC-3 . . . . .	66
3.5	Past X-ray survey studies of OMC-2 and OMC-3 . . . . .	66
4.1	Background count rate of <i>Chandra</i> ACIS . . . . .	79
4.2	Comparison of NIR imagers used in this thesis . . . . .	82
4.3	VLA configurations . . . . .	88
4.4	VLA frequency bands . . . . .	89
5.1	QUIRC observation log . . . . .	106
7.1	One-temperature plasma fittings of bright NIR-IDed <i>Chandra</i> sources . . . .	142
7.2	Two-temperature plasma fittings of bright NIR-IDed <i>Chandra</i> sources (1) . .	152
7.3	Two-temperature plasma fittings of bright NIR-IDed <i>Chandra</i> sources (2) . .	157

7.4	Two-temperature plasma fittings of bright NIR-IDed <i>Chandra</i> sources (3) . . .	157
7.5	Time-sliced spectroscopy of bright NIR-IDed <i>Chandra</i> sources (1) . . . . .	161
8.1	Power-law fittings of NIR-unIDed <i>Chandra</i> sources . . . . .	170
8.2	Power-law fittings of combined spectra of NIR-unIDed <i>Chandra</i> sources . . .	173
8.3	IRCS & NSFCam sources . . . . .	185
8.4	VLA sources . . . . .	190
9.1	Number of sources among mass ranges . . . . .	195
9.2	Comparison of X-ray properties among mass ranges . . . . .	195
9.3	One-temperature plasma fittings of the high mass source . . . . .	196
9.4	Number of sources among classes . . . . .	206
9.5	Comparison of X-ray properties among classes . . . . .	207
9.6	NIR-unIDed X-ray sources associated with jet and outflow systems . . . . .	210
9.7	One-temperature plasma fittings of NIR-unIDed <i>Chandra</i> sources . . . . .	214
A.1	<i>Chandra</i> source list . . . . .	236
B.1	QUIRC source list . . . . .	248

# Chapter 1

## Introduction

The night sky, without stars, should be boring. The stars we see are the mixture of young and old, which indicates that our universe keeps forming stars and not all stars were born at the beginning. The sites of star formation, however, had been long inaccessible to human beings. They are born deep in dense molecular clouds, so the visual light from these baby stars is almost extinct before reaching our eyes. These star-forming clouds appear dark in visual images, hence are called dark clouds.

One of the representatives is the Orion molecular cloud (Fig. 1.1). Between two spectacular nebulae, there exists a dark lane. It appears to contain nothing at a glance, but this is where stars are born. Babies are surrounded by dense blankets of molecular clouds.

The veil was lifted at the advent of new astronomy in the 20th century, when we became able to see the universe at any electromagnetic wavelengths. Figure 1.2 shows the absorption or scattering cross section of electromagnetic waves by the

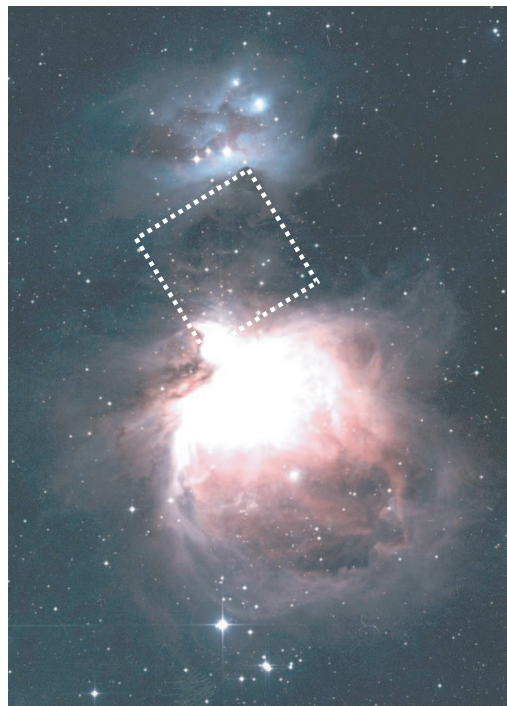


**Figure 1.1:** Visual image ( $60' \times 94'$ ) of the Orion nebula (M42), the brightest nebula seen from the Earth (Guinness World Records 2003<sup>[58]</sup>). Our study field (*the dashed square*) is located  $\sim 20'$  north of the nebula. Courtesy; the Kiso Observatory, the University of Tokyo.

interstellar medium (ISM). Typically, cloud cores have the visual extinction of  $A_V > 10$  mag. In other words, the visual light ( $\lambda \approx 550$  nm) from forming stars is attenuated to less than  $10^{-4}$  times. However, when we observe at the wavelengths of lower cross sections like X-ray, infrared, and radio lights, we can delve into the dense clouds.

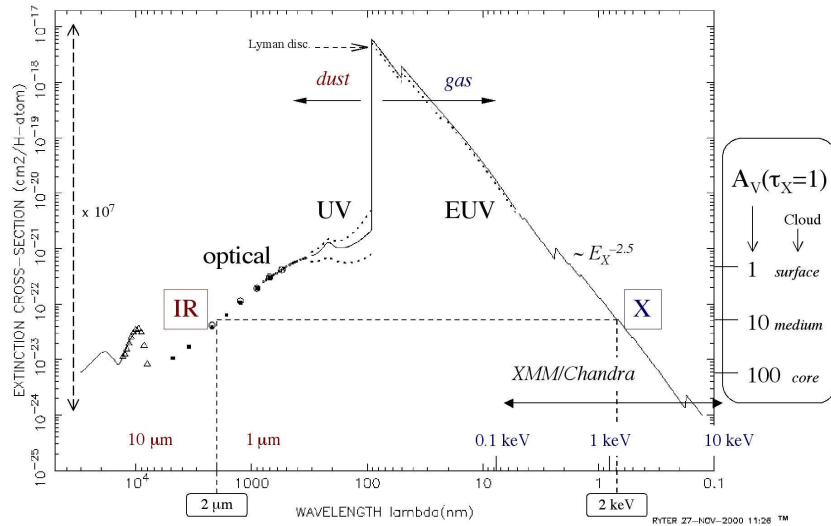


**Figure 1.2:** Absorption or scattering cross section by ISM of the electromagnetic wave at a given wavelength in the infrared (IR), optical, ultraviolet (UV), extreme ultraviolet (EUV), and X-ray band (Ryter 1996<sup>[168]</sup>). The *Chandra* and *XMM-Newton* satellites cover the range of 0.1–10.0 keV. The wavelengths of lower cross section have larger penetrating power into dense matter.

In 1967, Becklin & Neugebauer<sup>[19]</sup> discovered an infrared star in the Orion nebula. This object, unlike seven other objects found in their study field, had no optical counterpart. Successive near-infrared (NIR) observations found a dozen of sources with similar characteristics in dark clouds, and revealed that they are the stars at their birth. This was the first observational evidence of forming stars.

These stars are yet to begin the nuclear fusion at their center, hence are called pre-main-sequence sources or young stellar objects (YSOs). They are cool ( $T = 100$ – $1000$  K at the surface) and embedded sources that are just generated from gravitationally contracting cold ( $T \sim 10$  K) gas. It was astonishing, therefore, that strong X-ray emissions corresponding to the temperature of  $T \sim 10$  MK were found from these sources. Babies were found to be crying loud! In 1980's, the *Einstein Observatory* detected soft ( $E < 2$  keV) X-ray emissions from T



Tauri stars (TTSs), which comprise a class of YSOs with the mass of  $0.5\text{--}2.0 M_{\odot}$ <sup>1</sup> and the age of  $\sim 1$  Myr (Feigelson, & DeCampli 1981<sup>[50]</sup>; Montmerle et al. 1983<sup>[133]</sup>). Using the *Advanced Satellite for Cosmology and Astrophysics* (*ASCA*) satellite, Koyama et al. (1996)<sup>[107]</sup> further discovered hard ( $E > 2$  keV) X-ray emissions from a cluster of class I protostars, which are low-mass YSOs younger than TTSs ( $\sim 0.1$  Myr). Protostars are severely extinct by dense cores and are hard to access even with NIR observations.

The X-ray studies on YSOs are important in a wide area of astronomy and astrophysics. First, the X-ray emissions from these stars are so intense that they can affect heavily on the circumstellar environment. Glassgold, Feigelson, & Montmerle (1999)<sup>[70]</sup> discussed that the photoionization of circumstellar matter by X-rays can surpass the collision ionization by cosmic rays inside the distance from the core of

$$r \approx 0.02 \times \left( \frac{L_X}{10^{29} \text{ ergs s}^{-1}} \right) \text{ [pc]}, \quad (1.1)$$

where  $L_X$  is the X-ray luminosity of YSOs. At active phases of YSOs,  $L_X$  can exceed  $10^{30}\text{--}10^{31}$  ergs  $\text{s}^{-1}$ , which indicates that the X-ray ionization is the dominant mechanism inside the whole cloud core of typically  $\sim 0.1$  pc. As circumstellar matter should be ionized before being coupled with the magnetic field, the ionization rate and efficiency are key parameters in star formations. Without establishing the average features and revealing the mechanism of X-ray emissions from YSOs, therefore, we would not be able to understand the star formation process, a long-standing subject in astronomy and astrophysics.

Once the ubiquity of the X-ray emission is established for protostars as well as for TTSs, X-ray observations will be one of the most efficient tools to conduct a census on star-forming clouds. With a larger penetrating power than NIR observations (particularly of hard X-rays; Fig. 1.2), with a better spatial resolution than FIR–millimeter observations, and with a very wide field of view, we will soon encounter a large number of “X-ray-selected” YSOs. The investigation on these sources, we believe, will proceed our understanding on star births.

X-ray observations on protostars and TTSs with the mass of  $\sim 1 M_{\odot}$  also give us a picture on the past activities of our sun. Its enhanced activity by 3–5 orders of magnitude in the past should have given a large impact on the evolution of the solar system.

Finally, YSOs are one of the enigmatic sources in the universe that emit radiation by releasing their gravitational energy, such as neutron stars, galactic black holes, and active

---

<sup>1</sup>Masses in the unit of solar mass ( $2.0 \times 10^{33}$  g) are given with  $M_{\odot}$ .

galactic nuclei (AGNs). These sources have many processes in common; formation of jets, gravitational energy release through accretion disks, and acceleration of charged particles. YSOs are much closer to us than the other types of sources, which enables us to investigate fine structures of these high energy phenomena.

Previous studies with the *Einstein*, *ROSAT*, and *ASCA* satellites on the X-ray emissions from YSOs are mainly focused on low-mass sources. Higher mass YSOs have lower population densities and evolve more quickly, making these samples fewer and more distant. Lower mass YSOs are also difficult to observe because of their intrinsic faintness. The X-ray spectra of low-mass YSOs revealed that the X-ray emissions are of thin-thermal plasma origin. In addition, their X-ray light curves often show flares with a rapid rise and a slow decay, which are similar in profile but higher in flux and temperature compared to solar flares. These lead to the general consensus that the X-ray emissions from low-mass YSOs are solar-like; YSOs have thin-thermal plasma to emit X-rays with occasional flares triggered by magnetic reconnections. However, not all observational results are accountable by a simple extension of the solar flares. Moreover, YSOs of different mass ranges ( $M < 0.2 M_{\odot}$  or  $M > 2.0 M_{\odot}$ ) are not well studied. What are different between YSOs and our sun? Do higher-mass or lower-mass YSOs possess high temperature plasma like low-mass YSOs? If so, how is the plasma generated? Are there any other X-ray emission mechanisms besides flares? The aim of this thesis is to give an answer to these questions through a multi-wavelength study on Orion molecular cloud 2 and 3 (OMC-2 and OMC-3).

Our study field is located at the center of the dark lane in Figure 1.1 and contains YSOs at all evolutionary phases from class 0 protostars to TTSs in a wide range of mass from early-type stars to brown dwarfs. OMC-2 and OMC-3 are full of phenomena related to star formation; radio jets, molecular outflows, Herbig-Haro (HH) objects, sources with accretion disks, dust emissions, etc. In particular, the condensation of protostars in OMC-2 and OMC-3 is the highest among all near-by star forming regions (Reipurth, Rodríguez, & Chini 1999<sup>[162]</sup>). They are proximate to us at a distance of  $\sim 450$  pc (Genzel & Stutzki 1989<sup>[66]</sup>) and have an appropriate size of  $10' \times 20'$  that can be covered with one field of view of the current X-ray cameras. All these features make these clouds ideal sites for our study.

In order to study the X-ray emissions from YSOs, we employ a multi-wavelength approach. OMC-2 and OMC-3, although hard to see in the optical light, can be accessed with X-ray, NIR, and radio observations (see our X-ray and NIR images of the field in Figs. 5.2

and 5.9). Information obtained at different wavelengths complements with each other. In addition to the X-ray observations that trace high temperature ( $T = 1\text{--}100$  MK) plasma of YSOs, NIR–millimeter observations detect blackbody emissions from stars, accretion disks and dusts, which indicate the mass and evolutionary phase. Outflows and jets from YSOs can be seen through the optical, NIR, millimeter, and centimeter observations. In this thesis, we conduct a deep X-ray and NIR observations on OMC-2 and OMC-3 respectively using the *Chandra X-ray Observatory* and the University of Hawaii 88 inch (2.2 m) telescope. Follow-up observations are also performed on interesting sources using the Subaru telescope, the Infrared Telescope Facility (IRTF), and the University of Hawaii 88 inch (2.2 m) telescope at the NIR band and the Very Large Array (VLA) at the centimeter band.

The plan of this thesis is as follows. We review on the recent progress of X-ray observations on YSOs in Chap. 2 and previous multi-wavelength observations of our study field in Chap. 3. The basic features of the telescopes and instruments used in this work are summarized in Chap. 4. In Chap. 5, we explain our X-ray and NIR observations on OMC-2 and OMC-3. In total, 385 X-ray sources are found in our observation. By correlating them with our 1448 NIR sources as well as NIR all-sky survey catalog sources, we discriminate the NIR-identified (NIR-IDed) and NIR-unidentified (NIR-unIDed) X-ray sources. The following two chapters (Chap. 6 and Chap. 7) are devoted for the NIR and X-ray properties of the NIR-IDed X-ray sources, where we estimate the mass and the evolutionary phase of our samples and discuss the X-ray spectral and temporal features of these sources. In Chap. 8, we deal with the NIR-unIDed X-ray sources, where we focus on sources related to star formation. In Chap. 9, we discuss the X-ray emission mechanisms of both the NIR-IDed and NIR-unIDed sources. Finally, we conclude in Chap. 10. Figure 10.1 will help readers to follow the flow of this thesis.



# Chapter 2

## X-ray Observations on YSOs

### Contents

---

<b>2.1</b>	<b>Basic Features of YSOs . . . . .</b>	<b>26</b>
2.1.1	Evolution and Classification . . . . .	26
2.1.2	Jets and Outflows . . . . .	29
2.1.3	Magnetic Activities . . . . .	31
<b>2.2</b>	<b>X-ray Observations on YSOs . . . . .</b>	<b>33</b>
2.2.1	Low-mass YSOs: (1) Recent Results with <i>Chandra</i> . . . . .	33
2.2.2	Low-mass YSOs: (2) X-ray Emission Mechanisms . . . . .	37
2.2.3	Very Low Mass YSOs (=Young Brown Dwarfs) . . . . .	41
2.2.4	Intermediate-mass YSOs . . . . .	42
2.2.5	High-mass YSOs . . . . .	42
2.2.6	Diffuse X-ray Emissions . . . . .	43
2.2.7	Problems to be Addressed . . . . .	45

---

In the first section (Sect. 2.1) of this chapter, we briefly review the basic feature of YSOs. In the following section (Sect. 2.2), we review the X-ray observations on YSOs. As the progress made on low-mass YSOs with the *Einstein*, *ROSAT*, and *ASCA* satellites are concisely summarized in a review paper by Feigelson & Montmerle (1999)<sup>[53]</sup>, we focus mainly on recent advances made with the following *Chandra* and *XMM-Newton* observations. The problems to be solved on the X-ray emissions from YSOs are summarized in the last subsection, for which this thesis tries to give an answer.

## 2.1 Basic Features of YSOs

### 2.1.1 Evolution and Classification

A star formation begins with the onset of gravitational collapse of molecular cloud cores with the density of  $10^{-17}$ – $10^{-16}$  g cm<sup>-3</sup>. Gas and dust keep contracting freely on the central core until the density reaches  $\sim 10^{-13}$  g cm<sup>-3</sup>. At this density, the core becomes optically thick. The thermal pressure adiabatically increases and finally balances with the gravitational force to stop dynamical accretion. YSOs at this stage are called protostars. Protostars commonly accompany jets and outflows, which function to release angular momentum. Without the mechanism of angular momentum release, they can not keep accumulating mass because matters inside the Keplerian radius can not accrete onto their surface.

After most of the circumstellar matter accretes onto the star or is blown away by jets and outflows, YSOs quasi-statically contract with increasing temperature and density. YSOs at this stage are called T Tauri stars (TTSs). The contraction continues with a constant surface temperature, which makes TTSs move down along the Hayashi track on the Hertzsprung-Russell (H-R) diagram (Hayashi 1966<sup>[81]</sup>). The circumstellar disk gradually disappears as TTSs evolve. TTSs are divided into two classes; classical TTSs (cTTSs) that are in the earlier phase of TTSs with an optically thick accretion disk and weak-lined TTSs (wTTSs) that are in the later phase with an optically thin or no accretion disk. Finally, when nuclear burning starts at the center, YSOs turn into the main sequence stars. In general, “pre-main-sequence source” indicates TTSs, while “YSO” indicates the collection of protostars and TTSs.

The evolution of low-mass YSOs, which have been the main targets of previous obser-

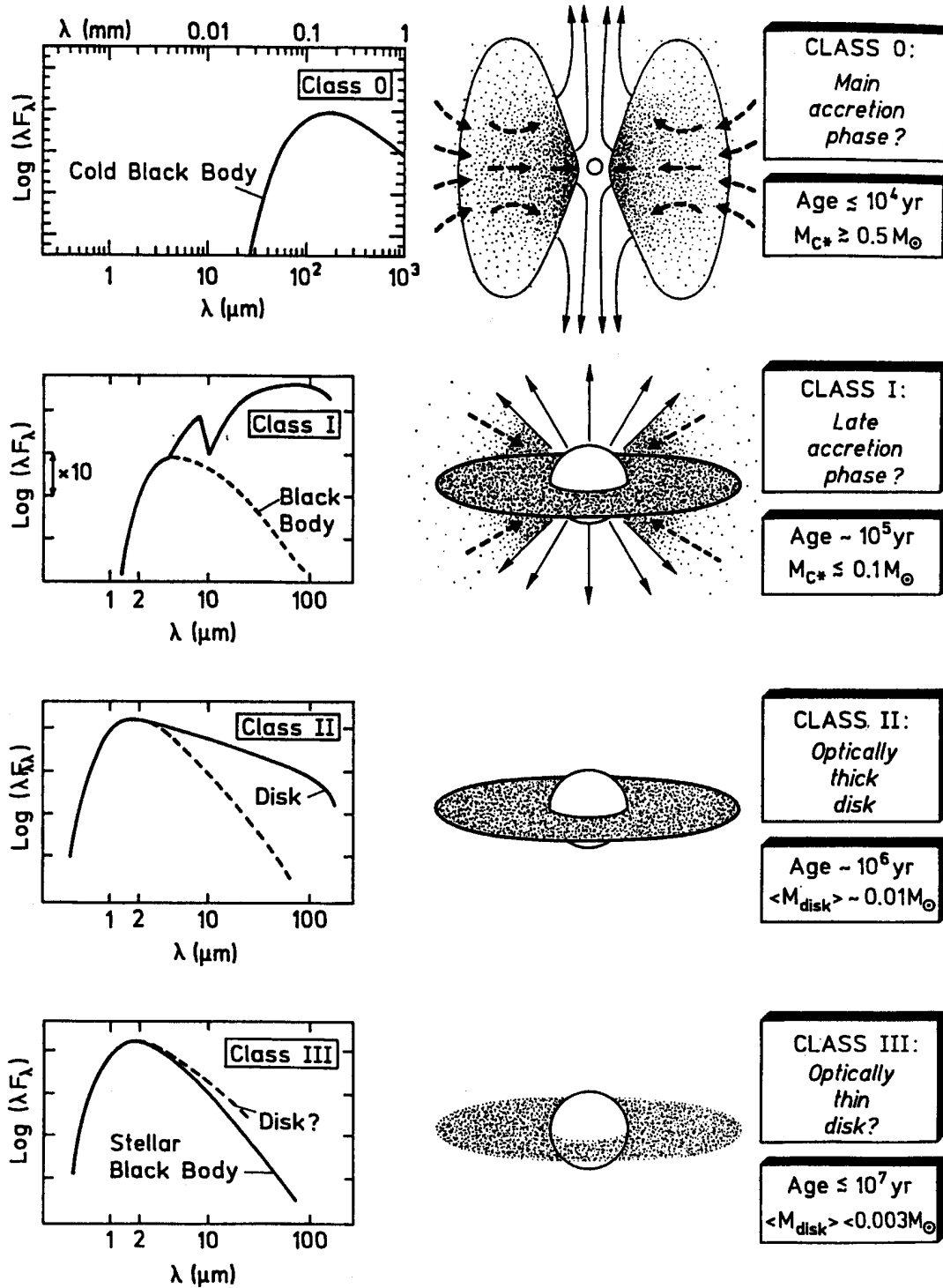
vations due to their proximity and ample samples, is traced by several measurements. One is to use the equivalent width ( $EW$ ) of the  $H_\alpha$  emission in the optical band, which is a direct indicator of mass accretion. CTTSs are defined as YSOs with  $EW > 10 \text{ \AA}$  while wTTSs are with  $EW < 10 \text{ \AA}$ . As cTTSs are younger ( $\sim 10^6$  yr in case of low-mass YSOs) than wTTSs ( $\sim 10^7$  yr) and have mass accretion from their circumstellar disk, they show larger  $EW$  values than wTTSs.

YSOs in much younger phases than TTSs are invisible with the optical light. Lada & Wilking (1984)<sup>[112]</sup>, Adams et al. (1987)<sup>[1]</sup>, and Lada (1991)<sup>[113]</sup> established a classification scheme using the NIR to mid-infrared (MIR) excess, in which younger YSOs show stronger NIR excess emission in addition to their photospheric blackbody emission. This excess emission comes from circumstellar disks and envelopes that have lower temperature ( $T = 100\text{--}1000$  K) than the photosphere ( $T \sim 3000$  K). The spectral index between  $2.2 \mu\text{m}$  (the  $K$  band) and  $10 \mu\text{m}$  (the  $M$  band) in the spectral energy distributions (SEDs) of YSOs;

$$\alpha = - \left. \frac{d \log \nu F_\nu}{d \log \nu} \right|_{2.2-10 \mu\text{m}} \quad (2.1)$$

is used to classify sources into class I, class II, and class III (Fig. 2.1). As class I sources are younger ( $\sim 10^5$  yr), they show larger NIR excess hence larger  $\alpha$  values than class II and class III sources. When the  $M$ -band flux is not available, which is often the case because of the difficulty of sensitive observations in this band, the  $J$  ( $1.2 \mu\text{m}$ )-,  $H$  ( $1.6 \mu\text{m}$ )-, and  $K$ -band fluxes are alternatively used to discriminate among classes using the color-color diagram (Sect. 6.1). CTTSs usually have the class II SED, while wTTSs have the class III SED. In this thesis, we use cTTSs and wTTSs for the same meaning as class II and class III sources.

In addition to the class I, II, and III objects, André, Ward-Thompson, & Barsony (1993)<sup>[5]</sup> introduced class 0 objects, which are younger than class I. The lower temperature and higher obscuration make this class sources invisible even with NIR and MIR lights. Barsony (1994)<sup>[17]</sup> defined the class 0 sources with the following features: (1) undetectable at the wavelengths of  $\lambda < 10 \mu\text{m}$ , (2) a high ratio of  $L_{\text{smm}}/L_{\text{bol}}$ , where  $L_{\text{smm}}$  and  $L_{\text{bol}}$  are the sub-millimeter and bolometric luminosity, (3) a relatively narrow SED resembling that of a single blackbody at  $T \leq 30$  K, (4) presence of a molecular outflow, (5) existence of centimeter continuum emission, and (6) presence of HH objects. Class 0 objects are considered to be at the age of  $10^4\text{--}10^5$  yr, which are the youngest stellar objects that are accessible with the current observational technology.

Figure 2.1: Classification of YSOs and their SEDs (Bachiller 1996<sup>[13]</sup>)



**Table 2.1:** Multi-wavelength properties of low-mass YSOs

	YSOs				main sequence
	class 0	class I	class II	class III	
properties	infalling protostar	evolved protostar	classical T Tauri	weak-lined T Tauri	
age (yr)	$10^4$	$10^5$	$10^6$	$10^7$	$>10^7$
accretion disk	thick	thick	thick	thin or nonexistent	planetary system (?)
X-ray emission	?	strong	strong	strong	weak
jet and outflow	yes	yes	yes	no	no
non-thermal radio	?	yes	no (?)	yes	yes

### 2.1.2 Jets and Outflows

Jets and outflows from YSOs are traced using several observational tools. From the origin, radio jets at the distance of  $\sim 100$  AU, optical jets and fast neutral winds at the distance of  $\sim 0.01$  pc, and molecular outflows at the distance of 0.1–1 pc are ubiquitously observed from protostars. More evolved YSOs accompany weak or no jet and outflow phenomena.

#### Radio Jets

Radio jets from YSOs were first studied by Cohen, Bieging, & Schwartz (1982)<sup>[37]</sup>. They appear to be thermal emissions at the centimeter band and are detected from almost all the class 0 and some of the class I protostars. The observational characteristics of these emissions in near-by star-forming regions are summarized as (1) the elongated morphology at sub-arcsecond scale, (2) association with both high and low luminosity objects, (3) alignment within a few degrees with the large scale outflow, (4) weak flux with the flux density typically in the range of 0.5–10 mJy, (5) positive or flat spectral indices, and (6) dynamical time scales of only a few years (Anglada 1996<sup>[8]</sup>).

Because these emissions are associated with low as well as high luminosity YSOs, the free-free emission from the H<sub>II</sub> region produced by stellar photo-ionization is unlikely. The alignment with and the elongation in the direction of global outflows strongly infer that these emissions are related to jet and outflow phenomena. Curiel, Cantó, & Rodríguez (1987)<sup>[42]</sup>

and Curiel et al. (1989)<sup>[43]</sup> proposed an idea of shock-induced ionization, where protostellar jets collide into high density ambient matter at the speed of a few times of  $100 \text{ km s}^{-1}$ , and the UV photons are irradiated from the shock front to produce  $\text{H}_{\text{II}}$  regions. An empirical relation is seen between the outflow momentum rate and the centimeter flux, which supports this scenario (Anglada 1992<sup>[7]</sup>). Martí, Rodríguez, & Reipurth (1998)<sup>[122]</sup> monitored one of the radio jets from YSOs and found that a pair of centimeter condensations are traveling away from the central core at the speed of  $\sim 500 \text{ km s}^{-1}$ .

### Optical Jets

Because Herbig (1951)<sup>[82]</sup> and Haro (1952)<sup>[78]</sup> were the first to identify knotty structures in the Orion region, they are called HH objects. Together with optical jets that were detected later by Mundt & Fried (1983)<sup>[138]</sup> and Mundt et al. (1984)<sup>[139]</sup>, these are the typical phenomena that characterize star-forming regions. These emissions are considered to originate from cooling regions of high velocity shocks that are produced as a result of highly collimated jets from YSOs colliding into dense ambient matter.

HH objects and optical jets altogether have the following characteristics: (1) knotty structures sometimes spaced periodically, (2) bow-shock-shaped HH objects located at the end of a series of knots, (3) half of the HH objects and optical jets with a bipolar structure, (4) collimated structure of the opening angles in the range of  $5^\circ$ – $20^\circ$ , and (5) the typical length, velocity and number density of optical jets in the range of 0.01–1 pc,  $200$ – $600 \text{ km s}^{-1}$ , and  $10$ – $200 \text{ cm}^{-3}$  (Edwards, Ray, & Mundt 1993<sup>[46]</sup>).

### Fast Neutral Winds

CTTSs are known to possess high velocity ( $100$ – $300 \text{ km s}^{-1}$ ) wind based on the P Cygni-type profile in various lines in the optical wavelengths (Kuhi 1964<sup>[110]</sup>; Hartmann 1982<sup>[80]</sup>). Similar high velocity winds were also detected from much younger phase of YSOs (protostars) using the neutral  $\text{H}_I$  line (Giovanardi et al. 1992<sup>[69]</sup>). Although cTTSs and protostars are in different phases of the YSO evolution, the stellar wind from these sources is considered to have the same origin because they have similar velocities, mechanical energies, and momentum flux. The origin of the phenomena is not well known, but it is somewhat related to accretion disks. A detailed discussion on this topic can be found in Edwards et al. (1993)<sup>[46]</sup>.

## Molecular Outflows

Circumstellar matter is dragged by high velocity and high density jet from protostars, which forms molecular outflows moving at the velocity of 10–200 km s<sup>-1</sup>. They are well traced by rotational transition lines of molecules in the millimeter band and vibrational-rotational transition lines in the NIR band. Snell, Loren, & Plambeck (1980)<sup>[174]</sup> was the first to detect a bipolar CO outflow from L1551 region. More than 200 outflows are cataloged to date.

The vibrational-rotational transition lines of H<sub>2</sub> and the rotational transition lines of CO are commonly used. The H<sub>2</sub> and CO outflows together with the optical jets are powerful tracers of jet and outflow activities from protostars that work complementarily, where the lowest velocity ( $\sim 10$  km s<sup>-1</sup>) component is traced by CO, the moderate velocity ( $\sim 100$  km s<sup>-1</sup>) component by H<sub>2</sub>, and the highest velocity ( $\sim 500$  km s<sup>-1</sup>) component in the optical wavelengths.

About a half of molecular outflows are observed to have a bipolar structure with a pair of red-shifted and blue-shifted lobes and the powering source is always at the center of the symmetry. They are moderately collimated with the opening angle of 10°–50°. Recent progress of observations on molecular outflows can be found in Fukui et al. (1993)<sup>[59]</sup>, Eislöffel et al. (2000)<sup>[47]</sup>, and Richer et al. (2000)<sup>[163]</sup>.

### 2.1.3 Magnetic Activities

As YSOs are fully convective in their interior and rotate much faster ( $\sim 1$  day) than main sequence stars ( $\sim 30$  days in case of the sun), they are expected to possess enhanced magnetic activities. This is supported by three major observational indications: (1) X-ray flares that trace the magnetic reconnections, (2) centimeter gyro-synchrotron emissions that indicate accelerated charged particles to the energy of  $\sim 1$  MeV, and (3) various optical photometric and spectroscopic studies. X-ray emissions are separately reviewed in Sect. 2.2.

### Gyro-synchrotron Emissions

In addition to the thermal free-free emissions, YSOs emit non-thermal emissions in the centimeter band. These emissions are considered to originate from the gyro-synchrotron emissions for the following reasons (André 1996<sup>[6]</sup>). First, they show flux variability of the

time scale of hours to days, including intense “radio flares” (Feigelson & Montmerle 1985<sup>[51]</sup>; Becker & White 1985<sup>[18]</sup>; Bieging & Cohen 1989<sup>[23]</sup>). Second, they have a moderate degree of circular polarization of  $|V/I| < 5\%$  at outbursts and  $|V/I| < 20\%$  at quiescence. Third, a brightness temperature of  $>10^7$  K is measured by Very Long Baseline Interferometer (VLBI) observations, directly confirming the size of the emitting regions. Electrons with the energy of  $\sim 1$  MeV are gyrating around large-scale magnetic fields with the size of  $\sim 5$  stellar radii and the strength of 1–10 G, which emit non-thermal emissions detectable at the centimeter band.

These emissions are only seen in evolved YSOs except for a class I protostar (Feigelson, Carkner, & Wilking 1998<sup>[52]</sup>). The centimeter flux of this emission is somewhat related to the X-ray luminosity, which can be extended to magnetically-active main sequence stars such as RS CVns and dMe stars. A recent simultaneous observation on an RS CVn-type binary in the X-ray and the centimeter band using *XMM-Newton* and VLA reported the detection of the Neupert effect, in which the time derivative of the X-ray light curve is proportional to the centimeter light curve (Güdel et al. 2002<sup>[75]</sup>). This confirms to understand the phenomena in solar analog; i.e., accelerated electrons via magnetic reconnections reach the chromosphere to heat the plasma that emits X-rays.

## Optical Studies

The most successful approach to measure the magnetic field strength of TTSs is the Zeeman splitting measurements, although this is applicable only to ideal cases. Some TTS samples were studied and revealed to have a strong magnetic field with the strength of 0.5–4 kG (Johnstone & Penston 1986<sup>[97]</sup>; Johnstone & Penston 1987<sup>[98]</sup>; Johns-Krull, Valenti & Koresko 1999<sup>[95]</sup>).

There are many indirect methods to investigate magnetic activities. Doppler imaging technique showed that large cool spots are moving on the surface of some TTSs.  $H_\alpha$  and  $Mg_{II}$  emission lines, which are the tracers of chromospheric activities, are other indicators of strong magnetic activities of these sources.

## 2.2 X-ray Observations on YSOs

### 2.2.1 Low-mass YSOs: (1) Recent Results with *Chandra*

In X-ray observations as well as observations in other wavelengths, low mass ( $0.2\text{--}2.0 M_{\odot}$ ) YSOs have been the main targets. Previous studies using *Einstein*, *ROSAT*, and *ASCA* are concisely summarized in a review paper by Feigelson & Montmerle (1999)<sup>[53]</sup>. Here, we briefly review recent results made with *Chandra* (Table 2.2).

Two capabilities are required for the X-ray studies on YSOs: (1) the spatial resolution of  $\sim 1''$  to resolve each YSO member in a usually crowded star-forming region and (2) the sensitivity in the hard X-ray band ( $E > 2$  keV) to penetrate through dark clouds. The preceding X-ray observatories did not meet either of these two requirements; *ASCA* the former and *Einstein* and *ROSAT* the latter. *Chandra* has both capabilities, which makes this satellite the best tool for YSO studies. The charge coupled device (CCD) detector onboard *Chandra* further enables us to obtain temporal ( $\Delta t \sim 3$  s) and spectral ( $\Delta E \sim 100$  eV) information on a photon basis. With a wide field of view (FOV) of  $17' \times 17'$ , we can simultaneously derive the light curve and spectrum of  $\sim 100$  X-ray sources in a star-forming region (Fig. 2.3). Table 2.3 summarizes the survey studies made with *Chandra*.

The X-ray properties of TTSs were found to have the following characteristics: (1) thin-thermal plasma spectrum with the X-ray luminosity of  $L_X < 10^{30}\text{--}10^{31}$  ergs  $\text{s}^{-1}$  and the plasma temperature of  $k_B T = 0.5\text{--}5$  keV, (2) flare-like flux variability with some hints of spectral hardening, (3) an empirical relation of  $L_X/L_{\text{bol}} = 10^{-3}\text{--}10^{-5}$ , and (4) no clear difference in X-ray properties between cTTSs and wTTSs. All these results are already obtained with previous *Einstein*, *ROSAT*, and *ASCA* observations (Feigelson & Montmerle 1999<sup>[53]</sup>). *Chandra* studies on TTSs confirmed these results with larger number of samples.

Major advances are seen in the studies of class I protostars. In the era of *ASCA* and *ROSAT*, only a limited number of class I samples were identified (Fig. 2.3, Koyama et al. 1996<sup>[107]</sup>; Kamata et al. 1997<sup>[103]</sup>; Ozawa et al. 1999<sup>[145]</sup>; Tsuboi et al. 2000<sup>[187]</sup> using *ASCA* and Grosso et al. 1997<sup>[72]</sup>; Neuhäuser & Preibisch 1997<sup>[141]</sup>; Grosso 2001<sup>[73]</sup> using *ROSAT*). With poor photon statistics, it was difficult to address their X-ray properties. A textbook case of the X-ray studies on class I protostars was presented by Imanishi, Koyama, & Tsuboi (2001a)<sup>[91]</sup> using the *Chandra* deep exposure observation on the  $\rho$  Ophiuchi dark cloud (Fig. 2.4). They detected X-rays from  $\sim 70\%$  of class I protostars and their candidates.

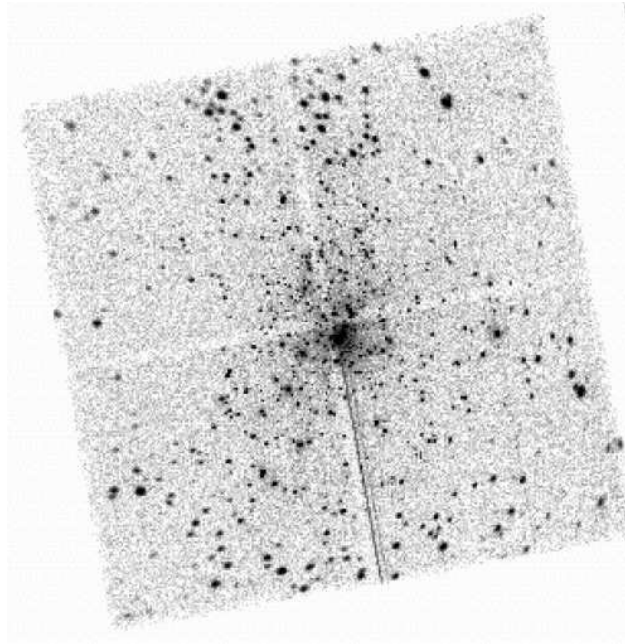


**Figure 2.2:** *Chandra*/ACIS image of ONC (Feigelson et al. 2002b<sup>[55]</sup>). Inside a  $17' \times 17'$  region of ACIS-I,  $\sim 1000$  X-ray sources were detected.

Moreover, they investigated their X-ray spectra and light curves and found that class I protostars have similar X-ray features with TTSs, with higher plasma temperature, larger column density and X-ray luminosity, and more occasional flare-like events.

The X-ray sources in star-forming regions that are not identified with NIR and optical sources can be an interesting topic. The number of these sources is 30–100 in some (Table 2.3). Although this number depends on the significance level of the source detection algorithm and the completeness limit of the NIR and optical catalog, it generally exceeds the expected number of background sources, particularly in cases of Orion Nebula Cluster (ONC; Feigelson et al. 2002b<sup>[55]</sup>) and OMC-2/3 (Tsujiimoto et al. 2002a<sup>[189]</sup>; 2003<sup>[192]</sup> [this thesis]) observations. The nature of these X-ray sources is not studied at all yet. However, considering the high sensitivity of *Chandra* observations that are comparable or deeper than optical and NIR observations, some of these optically and NIR unidentified sources can be a new class of YSOs.

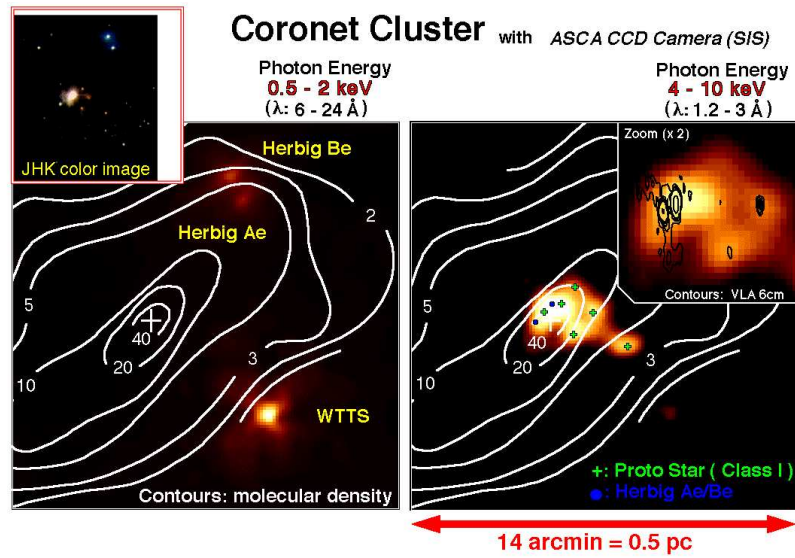


**Figure 2.3:** Hard X-ray detections from class I protostars in R Coronae Australis with *ASCA* (<http://www-cr.sphys.kyoto-u.ac.jp/IAU/gallery/gallery.html>). Unlike soft X-rays (*left*), hard X-rays (*right*) can penetrate into the densest part of the cloud core, detecting hard X-ray emissions for the first time from class I protostars (Koyama et al. 1996<sup>[107]</sup>).

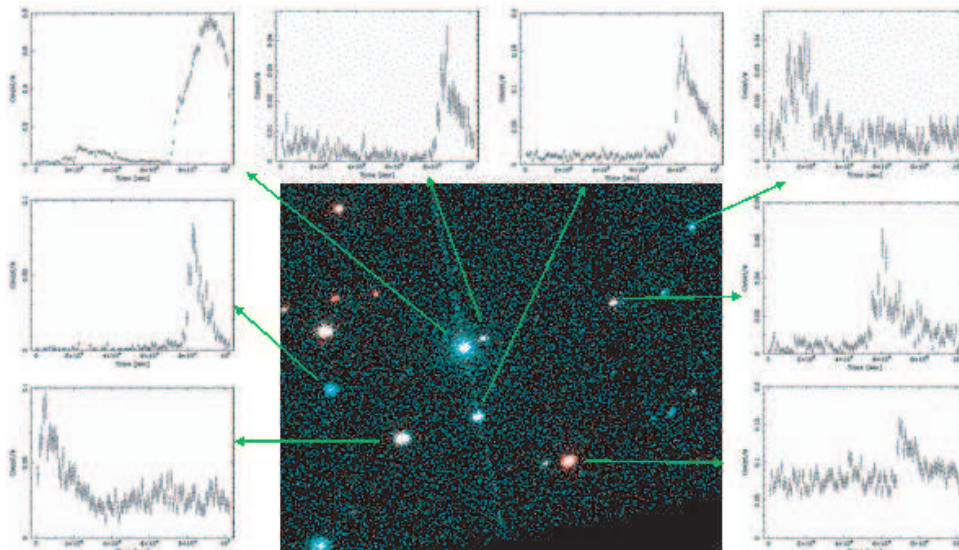


**Figure 2.4:** X-ray detections and their light curves from class I protostars in the  $\rho$  Ophiuchi cloud with *Chandra*. Courtesy; Kensuke Imanishi (Kyoto University).

**Table 2.2:** *Chandra* and *XMM-Newton* studies of star-forming regions

categories	regions (references)
survey studies . . .	$\rho$ Oph (Imanishi et al. 2001a <sup>[91]</sup> ; 2001b <sup>[92]</sup> ; 2002 <sup>[93]</sup> ) IC 348 (Preibisch & Zinnecker 2001 <sup>[155]</sup> ; 2002a <sup>[156]</sup> ) NGC 1333 (Getman et al. 2002 <sup>[67]</sup> ) ONC (Garmire et al. 2000 <sup>[62]</sup> ; Schulz et al. 2001 <sup>[169]</sup> , Feigelson et al. 2002a <sup>[54]</sup> ; 2002b <sup>[55]</sup> ; 2003 <sup>[56]</sup> ) OMC-2/3 (Tsuboi et al. 2001 <sup>[188]</sup> ; Tsujimoto et al. 2002a <sup>[189]</sup> )
intermediate- & high-mass YSOs	Mon R2 (Kohn et al. 2002 <sup>[106]</sup> ; Preibisch et al. 2002b <sup>[157]</sup> ), Sgr B2 (Takagi et al. 2002 <sup>[178]</sup> ) W 3 (Hofner et al. 2002 <sup>[90]</sup> ), IRAS 19410+2336 (Beuther et al. 2002 <sup>[22]</sup> ), M 8 (Rauw et al. 2002 <sup>[159]</sup> ) <sup>a</sup>
TTsS (grating).	TW Hya (Kastner et al. 2002 <sup>[104]</sup> )
HH objects . . . . .	HH-2 (Pravdo et al. 2001 <sup>[153]</sup> ), L1551 IRS5 (Favata et al. 2002 <sup>[49]</sup> ) <sup>a</sup>
diffuse emissions	NGC 3603 (Moffat et al. 2002 <sup>[132]</sup> ), RCW 38 (Wolk et al. 2002 <sup>[195]</sup> ) Arches Cluster (Yusef-Zadeh et al. 2002 <sup>[198]</sup> ), M 8 (Rauw et al. 2002 <sup>[159]</sup> ) <sup>a</sup>

<sup>a</sup> Studies by *XMM-Newton*. Other studies were made with *Chandra*.

**Table 2.3:** Detected numbers of X-ray sources in *Chandra* survey studies

region	distance (pc)	exposure (ks)	number of sources				references	
			all sources (SL <sup>a</sup> )	class I <sup>b</sup>	BD <sup>c</sup>	no ID <sup>d</sup> (CL <sup>e</sup> )		
$\rho$ Oph	165	101	87 ( $1 \times 10^{-7}$ )	18	7	28 ( $K < 15$ )	Imanishi et al. (2001a) <sup>[91]</sup> ; 2001b <sup>[92]</sup>	
IC 348	310	53	215 ( $3 \times 10^{-6}$ )	13	2	39 ( $K < 19$ )	Preibisch & Zinnecker (2001) <sup>[155]</sup>	
NGC 1333	318	38	127 ( $1 \times 10^{-6}$ )	8	N/A	32 ( $I < 23$ )	Getman et al. (2002) <sup>[67]</sup>	
ONC	450	83	1075 ( $1 \times 10^{-5}$ )	N/A	30	101 ( $V < 20$ )	Feigelson et al. (2002a) <sup>[54]</sup>	
OMC-2/3	450	89	385 ( $1 \times 10^{-5}$ )	13	12	107 ( $K < 16$ )	Tsujimoto et al. (2002a <sup>[189]</sup> ; 2003 <sup>[192]</sup> ) [this thesis]	

<sup>a</sup> The significance level in the X-ray source detection algorithm. The wavdetect program was used in all studies.

<sup>b</sup> The number of X-ray-emitting class I protostars.

<sup>c</sup> The number of X-ray-emitting brown dwarfs, which includes brown dwarf candidates identified with NIR photometry observations alone.

<sup>d</sup> The number of X-ray sources not identified with optical and NIR sources.

<sup>e</sup> The band and the limiting magnitude of the optical and NIR catalogs that were used to correlate with X-ray sources.



### 2.2.2 Low-mass YSOs: (2) X-ray Emission Mechanisms

The X-ray emission mechanism of YSOs should account for many observational results obtained so far: (1) the soft X-ray emissions ( $E < 2$  keV) as well as hard X-ray emissions ( $E > 2$  keV), (2) flare-like variability as well as quiescent emissions, and (3) some empirical relations, such as  $L_X/L_{\text{bol}} \sim 10^{-3}$ – $10^{-5}$ . The proposed scenarios do not successfully account for all of these pieces of evidence.

The most favored idea is the magnetic reconnection model, in which rapid energy release by reconnections of magnetic field lines (flares) generates and maintains the high temperature plasma. This model well explains the flare-like flux variability with rapid rise and slow decay and hard X-ray spectra exceeding 2 keV.

Four geometries of magnetic field lines are considered (Feigelson & Montmerle 1999<sup>[53]</sup>; Fig. 2.5): (1) both feet on the stellar surface, (2) connecting the star and the circumstellar disk, (3) above the corotation radius, and (4) both feet on the circumstellar disk. The geometry (1), which is the same with the sun, is most plausible. The reconnections are caused as a result of differential rotation and convection of the star. In contrast, Montmerle et al. (2000)<sup>[134]</sup> proposed a magnetic field geometry bridging between the star and the disk (geometry 2). This is based on the *ASCA* result by Tsuboi et al. (2000)<sup>[187]</sup>, who detected quasi-periodic flares from a class I protostar in the  $\rho$  Ophiuchi cloud (YLW 15; Fig. 2.6). They assumed the radiative cooling for the flux decay in these flares, and derived that the magnetic loop length is  $\sim 14$  times of the stellar radius. Favata, Micela, Reale (2001)<sup>[48]</sup> noted that the loop length is overestimated unless we take the recurrent heating during flares into account. At present, no clear difference is seen between cTTSs and wTTSs in X-ray luminosity functions, which casts some doubt on the geometry where the disk plays a key role (geometry 2 and 4).

Whatever the geometry is, the magnetic reconnection model does not account for the steady X-ray emissions at the quiescent phase. In the case of our sun, attempts have not been successful to explain the steady emissions (the solar coronae) by the integration of small flares (Shimizu 1995<sup>[170]</sup>; Aschwanden et al. 2000<sup>[9]</sup>; Aschwanden & Charbonneau 2002<sup>[10]</sup>). Shimizu (1995)<sup>[170]</sup> discussed, using the *Yohkoh* Soft X-ray Telescope data, that the occurrence rate of flares is expressed with a single power-law function of the flare energy ( $E$ ) as

$$\frac{dN}{dE} \propto E^{-\alpha}. \quad (2.2)$$

He derived  $\alpha = 1.5$ – $1.6$  in the energy range down to  $\sim 10^{27}$  ergs. The  $\alpha$  value of less than

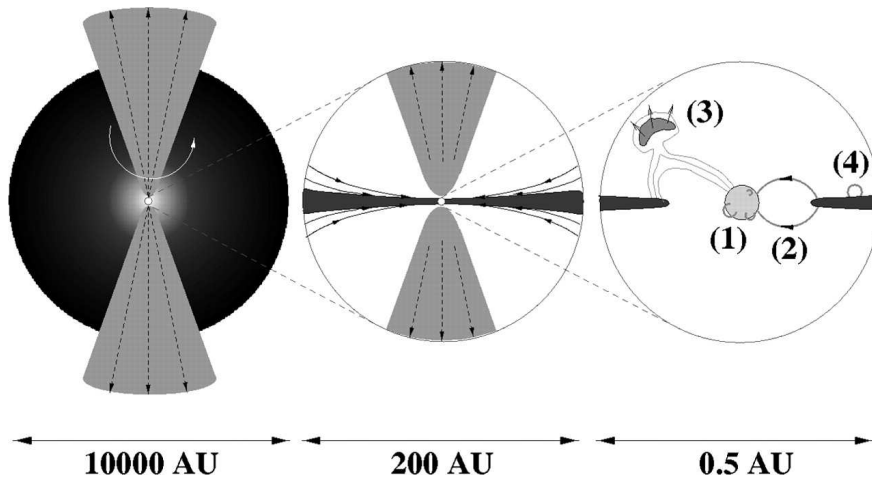


**Figure 2.5:** Magnetic field geometries of YSOs (Feigelson & Montmerle 1999<sup>[53]</sup>).

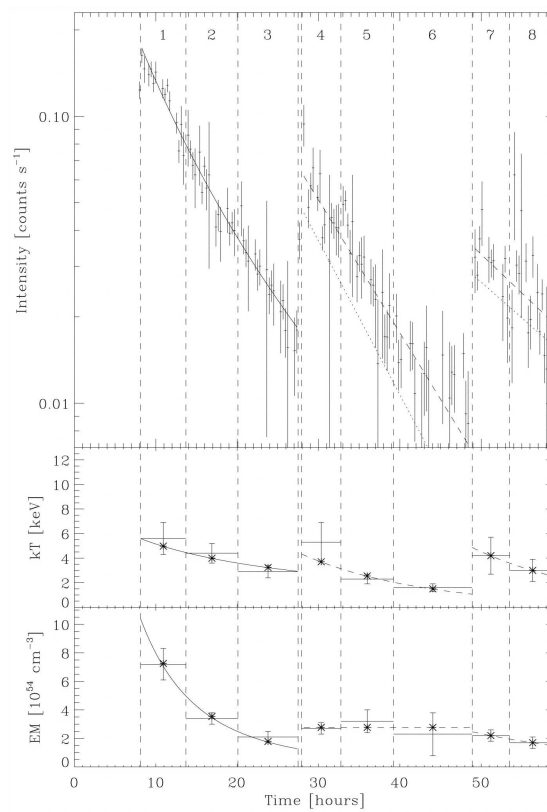


**Figure 2.6:** Quasi-periodic flare from a protostar in the  $\rho$  Ophiuchi cloud detected with *ASCA* (Tsuboi et al. 2000<sup>[187]</sup>). The time evolution of the X-ray luminosity, plasma temperature, and emission measure are given in the upper, middle, and lower panels, respectively.

2 indicates that smaller flares are not the dominant source of the total energy released by flares of all scales, if we assume that the power-law can be extrapolated to lower energies. In fact, the integration of all observed flares account for at most only one fifth of the heating rate required for the active-region coronae. With this in mind, we have to deal with flares and coronae as different phenomena, although the heating mechanism of coronae is still quite puzzling.

Another difficulty that the magnetic activity scenario is confronted with is that we see no clear relation between the X-ray luminosity and the rotation period (e.g.; Feigelson et al. 2003<sup>[56]</sup>). This is in sharp contrast with magnetically active main sequence stars, where we see a strong anti-correlation between the soft X-ray luminosity and rotation period (Pallavicini et al. 1981<sup>[147]</sup>). This should be a natural deduction when the magnetic activity is the origin of the X-ray emissions.

Skinner & Walter (1998)<sup>[173]</sup> presented an interesting result using the *ASCA* observation on the brightest cTTSs in the Taurus-Auriga complex (SU Aur). They argued that there exist two different X-ray emissions by constructing the differential emission measure (DEM) distribution of this source. The bimodal plasma temperature distribution is quite similar to those seen in active late-type main sequence stars with X-ray emissions of coronal origin. If the X-ray emissions from YSOs are commonly the combination of some different mechanisms, all previous discussions correlating  $L_X$  or  $k_B T$  with stellar parameters should be re-examined.

Kastner et al. (2002)<sup>[104]</sup> proposed yet another scenario based on their high-resolution grating spectroscopy observation on a cTTS (TW Hya) using *Chandra* (Fig. 2.8). They argued that the X-ray emission arises from the hot spot or spots on the stellar surface located at the root of accretion funnels. Three lines of evidence support this idea: (1) The DEM distribution is sharply peaked at  $T \sim 3$  MK, which is in sharp contrast with broad DEMs seen in coronally active late-type stars. (2) The temperature of  $T \sim 3$  MK is consistent with the value expected from the adiabatic shock caused by gas accretion at the speed of 150–300 km s<sup>-1</sup>, which is measured from the broadening of H $_{\alpha}$  line emissions. (3) The high-resolution spectroscopy enabled them to measure the plasma density using the density-sensitive triplet lines of O<sub>VII</sub> and Ne<sub>IX</sub>. In combination with the emission measure, the emitting volume was derived to be only 10<sup>-6</sup> of the stellar volume, which is smaller than typical coronal X-ray sources. We have no other grating spectroscopy results on YSOs besides this source. Further studies with a larger number of samples are quite prospective.

Zhekov, Palla, & Myasnikov (1994)<sup>[201]</sup> presented a model calculation to account for the

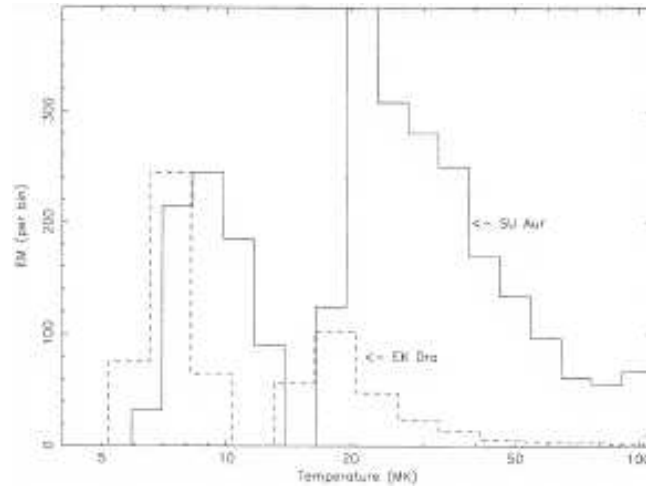


**Figure 2.7:** Differential emission measure distributions of SU Aur (a pre-main-sequence source; *solid*) and EK Dra (a main sequence star; *dashed*) derived from *ASCA* observations (Skinner & Walter 1998<sup>[173]</sup>)

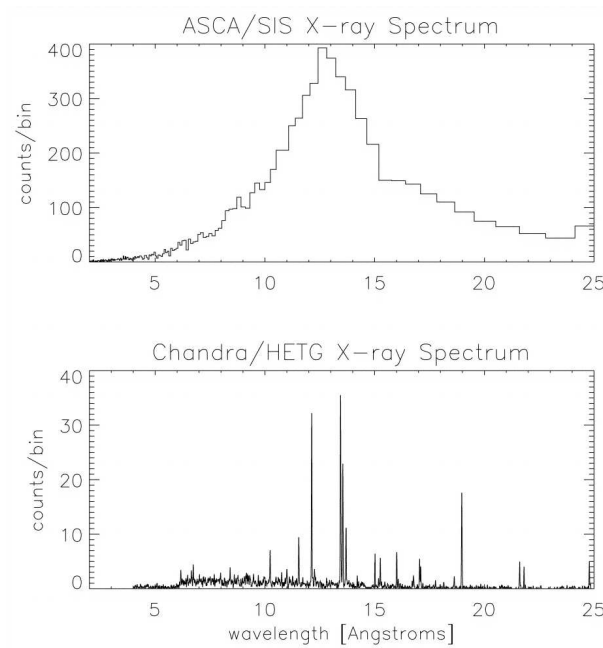


**Figure 2.8:** X-ray spectra of TW Hya taken with *ASCA*/SIS (a CCD spectrometer; *upper panel*) and *Chandra*/HETG (a grating spectrometer; *lower panel*). The density sensitive triplet lines of  $O_{VII}$  and  $Ne_{IX}$  are clearly resolved at  $\sim 22 \text{ \AA}$  and  $\sim 11 \text{ \AA}$  in the grating spectrum, which serve as a powerful tool to determine the electron density of the plasma (Kastner et al. 2002<sup>[104]</sup>).

soft X-ray emission with colliding winds from YSO binaries at the speed of 300–500 km s<sup>-1</sup> and the mass loss rate of 10<sup>-8</sup>–10<sup>-6</sup> M<sub>⊙</sub> yr<sup>-1</sup>. This model, although it well explains the soft X-ray temperature and the X-ray luminosity, has difficulties in understanding the hard X-ray emissions and flaring temporal behaviors of YSO X-rays.

### 2.2.3 Very Low Mass YSOs (=Young Brown Dwarfs)

Recent X-ray observations are also capable to study brown dwarfs in star-forming regions. Brown dwarfs are tiny objects with mass less than 0.08 M<sub>⊙</sub> that never possess nuclear burning during their life. A series of studies using *ROSAT* were the first to report the detection of X-ray emissions from young brown dwarfs (Neuhäuser & Comerón 1998<sup>[142]</sup>; Neuhäuser et al. 1999<sup>[143]</sup>) in the Chamaeleon, Taurus, and ρ Ophiuchi regions. The number of X-ray-emitting brown dwarfs drastically increased with the following *Chandra* studies on the Orion Nebula Cluster (Garmire et al. 2000<sup>[62]</sup>; Feigelson et al. 2002a<sup>[54]</sup>), ρ Ophiuchi (Imanishi et al. 2001b<sup>[92]</sup>), and IC 348 (Preibisch & Zinnecker 2001<sup>[155]</sup>; 2002a<sup>[156]</sup>). At present, X-ray observations in near-by star forming regions have reached the brown dwarf limit.

When observed with a deep exposure, X-ray observations on brown dwarfs are no longer a mere detection experiment. Imanishi et al. (2001b)<sup>[92]</sup> studied the X-ray properties of four X-ray-brightest brown dwarfs and their candidates in the ρ Ophiuchi cloud with a ∼100 ks exposure with *Chandra*. They found that brown dwarfs have similar X-ray properties with low-mass YSOs with: (1) the temperature of ∼1–2.5 keV, (2) flux variability from some sources, and (3)  $L_X/L_{\text{bol}} = 10^{-3}$ – $10^{-5}$ . Based on this similarity in X-ray properties, they discussed that young brown dwarfs have the same X-ray emission mechanism with low mass YSOs.

Interestingly enough, X-ray emissions are detected from only a few field brown dwarfs (Fleming, Giampapa, & Schmitt 2000<sup>[57]</sup>; Rutledge et al. 2000<sup>[167]</sup>) in spite of their much closer distance to us. It appears that brown dwarfs decrease their X-ray activity as they evolve. This behavior is commonly seen in low mass stars, which are X-ray active in the pre-main-sequence stage and become inactive as they evolve into the main sequence stage. However, as brown dwarfs have no clear definitions of pre-main-sequence and main sequence with no nuclear fusion in their life, it is not quite clear why their X-ray activity changes in the same manner as low mass stars.

### 2.2.4 Intermediate-mass YSOs

Intermediate-mass YSOs in the mass range of 2.0–10.0  $M_{\odot}$  are still not clear to have any X-ray emissions. Zinnecker & Preibisch (1994)<sup>[202]</sup> studied 21 Herbig Ae/Be sources (intermediate-mass counterpart of TTSs) with *ROSAT* and found that 11 of them emit X-rays. Hamaguchi (2000)<sup>[77]</sup> obtained a similar X-ray detection rate with the *ASCA* data. He also discussed, based on the hard X-ray spectra and flare-like variability of some Herbig Ae/Be stars, that these sources also have magnetic activity similar to low-mass YSOs. Zinnecker & Preibisch (1994)<sup>[202]</sup>, on the contrary, raised a possibility that the X-ray emissions from these sources can be from their low-mass companion and not intrinsically from the intermediate-mass YSOs. Feigelson et al. (2002a)<sup>[54]</sup> studied the ONC sources with A or B spectral types and discussed that the X-ray emissions can be fully attributable to their low-mass companions. Their samples, however, are not confined to pre-main-sequence sources and may include main sequence intermediate-mass sources. This can mislead the conclusion because intermediate-mass main sequence sources do not emit X-rays at all due to their lack of convection zones.

### 2.2.5 High-mass YSOs

Some *Chandra* observations detected X-ray emissions from ultra-compact H<sub>II</sub> regions in massive star-forming regions at a few kpc away. The ultra-compact H<sub>II</sub> regions are due to the UV photoionization from the central young massive objects of  $>10 M_{\odot}$  and are traced using the free-free emissions in the centimeter wavelengths. The X-ray emissions were reported from the infrared source “n” in the BN/KL region in OMC-1 at 450 pc (Garmire et al. 2000<sup>[62]</sup>), IRS 1, IRS 2, IRS 3, and a<sub>s</sub> in the Monoceros R2 cloud at 830 pc (Kohno et al. 2002<sup>[106]</sup>; Preibisch et al. 2002b<sup>[157]</sup>), and IRS 2, IRS 2a, and IRS 3a in the W 3 complex at 2.3 kpc (Hofner et al. 2002<sup>[90]</sup>).

The most notable characteristics of these X-ray emissions are their hard spectra of  $k_{\text{B}}T > 2$  keV and X-ray variability. These features are similar to those of low-mass YSOs, indicating that these X-ray emissions are also of magnetic origin. On the contrary, the  $L_{\text{X}}/L_{\text{bol}}$  values of some high mass YSOs are in the range of  $10^{-6}$ – $10^{-8}$  (e.g., Kohno et al. 2002<sup>[106]</sup>), which are too small for an empirical value of  $10^{-3}$ – $10^{-5}$  for low-mass YSOs and are comparable to high-mass main sequence sources that emit X-rays of stellar wind origin. The X-ray emission mechanism of these sources is not still clear.

Whatever the X-ray emission mechanism of high-mass YSOs, their hard X-ray emissions provide us with a unique tool to search for young massive stars in dense molecular clouds. The penetrating power of hard X-rays is comparable to radio bands. Moreover, unlike millimeter and centimeter emissions, we can trace the central star with their X-ray emissions. Takagi et al. (2002)<sup>[178]</sup> illustrated this unique capability by detecting highly absorbed ( $N_{\text{H}} = 1\text{--}4 \times 10^{23} \text{ cm}^{-2}$ ) hard ( $k_{\text{B}}T = 5\text{--}10 \text{ keV}$ ) X-ray emissions from ultra-compact H<sub>II</sub> regions in the Sagittarius B2 cloud at the distance of 8.5 kpc away.

### 2.2.6 Diffuse X-ray Emissions

High sensitivity observations using *Chandra* and *XMM-Newton* extended the X-ray studies to weaker but new X-ray emissions. One example is HH objects. In strong adiabatic shocks, the plasma temperature of  $T$  is expected at the shock velocity of  $v_s$  (Raga, Noriega-Crespo, Velázquez 2002<sup>[158]</sup>), where

$$T = 1.5 \times 10^5 \left( \frac{v_s}{100 \text{ km s}^{-1}} \right)^2 \text{ [K]}. \quad (2.3)$$

With the typical velocity of optical jets (200–300 km s<sup>-1</sup>), we can expect soft X-ray emissions from HH objects.

Pravdo et al. (2001)<sup>[153]</sup> reported the detection of X-ray emission from HH-2 using *Chandra*. The emission has a very soft spectrum with an extended spatial distribution. They proposed that this emission originates from the plasma with the temperature of  $\sim 10^6 \text{ K}$  and the plasma is generated by collision of the protostellar jet with ISM at the speed of  $\sim 250 \text{ km s}^{-1}$ . A similar soft X-ray emission was later reported by Favata et al. (2002)<sup>[49]</sup> from L1551 IRS5 using *XMM-Newton*.

Another example of new findings is the diffuse X-ray emissions from massive star-forming regions. Moffat et al. (2002)<sup>[132]</sup> reported the detection of the diffuse emission with the extent of  $\sim 2'$  (4 pc) from the center of NGC 3603. The emission is of thermal origin with  $k_{\text{B}}T \sim 3.1 \text{ keV}$  and the total luminosity of  $L_{\text{X}} \sim 2 \times 10^{34} \text{ ergs s}^{-1}$ . They probably arise from merging or colliding hot stellar winds of massive stars. Similar diffuse thermal emissions were also found by Yusef-Zadeh et al. (2002)<sup>[198]</sup> in the Arches Cluster and by Rauw et al. (2002)<sup>[159]</sup> in the Lagoon Nebula (M8). Wolk et al. (2002)<sup>[195]</sup> reported, on the other hand, that the diffuse X-ray emission found from RCW 38 is of non-thermal origin. They insisted that this emission might be attributable to synchrotron emissions from hidden supernova

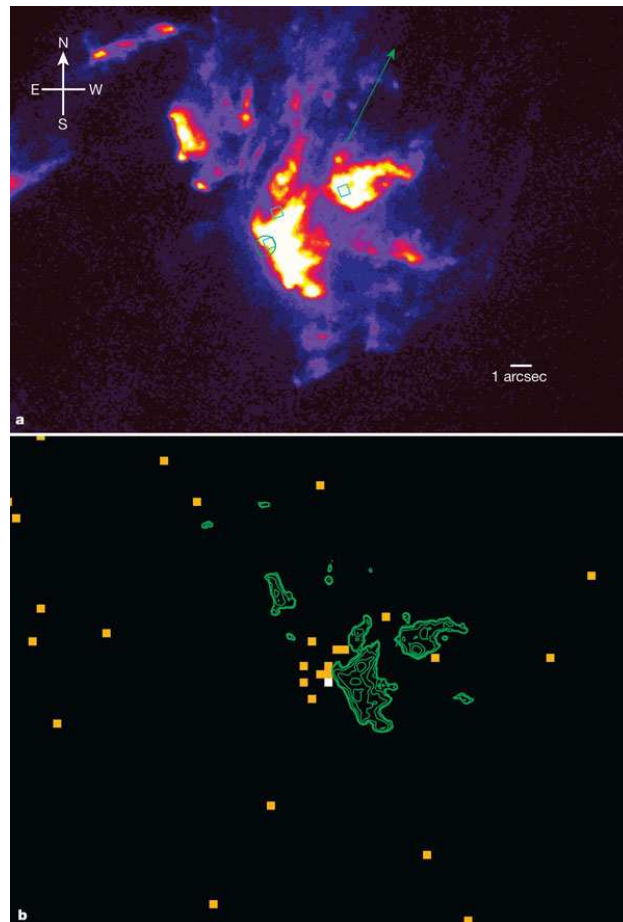


**Figure 2.9:** Soft X-ray detection from a HH object (HH-2) with *Chandra* (Pravdo et al. 2001<sup>[153]</sup>). The upper panel gives the *Hubble Space Telescope* image with the position of the *Chandra* and VLA sources with a circle and squares, respectively. The lower panel gives the X-ray event map of *Chandra* with the contours giving the  $H_{\alpha}$  intensity.



remnants. These diffuse X-ray emissions from star-forming regions are restricted to massive star-forming regions at the distance of a few kpc, which makes it difficult to assess the contamination by a complex of point sources. Further studies are necessary to establish the diffuse X-ray emissions from star-forming regions.

### 2.2.7 Problems to be Addressed

Among a number of problems raised on X-ray emissions from YSOs, we try to give an answer for the following issues in this thesis.

(1) Are there any class I protostars or brown dwarfs in our field? The X-ray emitting samples of these sources are still limited, so it is important to enrich them for further investigations. The combination of our sensitive X-ray and NIR observations is quite useful for this purpose.

(2) Do intermediate-mass YSOs intrinsically emit X-rays? The possible contamination by low-mass binary companions or main sequence intermediate-mass sources prevented previous studies from drawing a definite conclusion. We confine the sample to ostensibly single, pre-main-sequence intermediate-mass sources, and compare the binary rate and the X-ray detection rate of these well-defined intermediate-mass YSO samples to address whether they are intrinsic X-ray emitters.

(3) Are there any differences in averaged X-ray features among sources in different mass ranges? Using large number of samples, we can first compare the averaged features of YSOs spanning from intermediate-mass to brown dwarfs in a single star-forming region.

(4) What are the X-ray emission mechanisms of all these samples? Skinner & Walter (1998)<sup>[173]</sup> raised a possibility that the X-ray emission mechanism of YSOs can be the combination of different mechanisms that is represented by a bimodal structure in plasma temperatures. Their result alone is not conclusive, because their source (SU Aur) is a spectroscopic binary (Bouvier et al. 1986<sup>[25]</sup>) that can mimic two-temperature plasma. Two things are required. First, we need to try multi-temperature plasma models for the X-ray spectral fittings. All previous *Chandra* papers present only the result of one-temperature fittings. Second, we need to deal with a large number of samples collectively to statistically discuss whether the bimodal temperature structure is attributable to the binarity or not.

(5) What is the nature of X-ray sources that have no NIR counterpart? We conduct

multi-wavelength follow-up observations to reveal their nature.

# Chapter 3

## Orion Molecular Cloud 2 and 3

### Contents

---

<b>3.1</b>	<b>Global Properties</b>	<b>48</b>
<b>3.2</b>	<b>Radio Observations</b>	<b>49</b>
3.2.1	Identifying Protostellar Cores with Dust Emissions	49
3.2.2	Centimeter Observations of Free-free Emissions	51
3.2.3	Millimeter Observations of Molecular Cores and Outflows	56
3.2.4	Polarization Measurements	56
<b>3.3</b>	<b>NIR Observations</b>	<b>56</b>
3.3.1	Bright Discrete Sources in OMC-2	56
3.3.2	Surveys with Broad-band Imaging Observations	57
3.3.3	Narrow-band Studies of Molecular Outflows	58
<b>3.4</b>	<b>Optical Observations</b>	<b>59</b>
3.4.1	Membership Studies with Proper Motion Measurements	59
3.4.2	Detection of Circumstellar Disks	59
<b>3.5</b>	<b>X-ray Observations</b>	<b>62</b>
3.5.1	Surveys in the Soft X-ray Band	62
3.5.2	Surveys in the Hard X-ray Band	62

---

In this chapter, we review the past observations of OMC-2 and OMC-3. In Sect. 3.1, we summarize the global properties of OMC-2 and OMC-3 and illustrate that these regions are one of the best targets for our study. In the following sections, past observations (Table 3.3) in the radio (Sect. 3.2), NIR (Sect. 3.3), optical (Sect. 3.4), and X-ray (Sect. 3.5) band are reviewed. In particular, we stress how to utilize these results in this thesis and how to complement them with our new observations.

### 3.1 Global Properties

The Orion molecular cloud (OMC) is the cradle of star formation studies. Its proximity to us and the brightness have been attracting many astronomers and astrophysicist who intend to understand the formation of stars in a wide mass range. OMC is located  $15\text{--}20^\circ$  south to the Galactic plane (Fig. 3.1) and is comprised of a large complex of molecular clouds (Fig. 3.2). Among them, the Orion A, Orion B, Northern Filament, and  $\lambda$  Ori clouds are physically associated with each other, judging from the fact that they are located at similar distances and have similar velocities. The association of these clouds with Monoceros R2 and Southern Filament is not certain yet (Maddalena et al. 1986<sup>[120]</sup>).

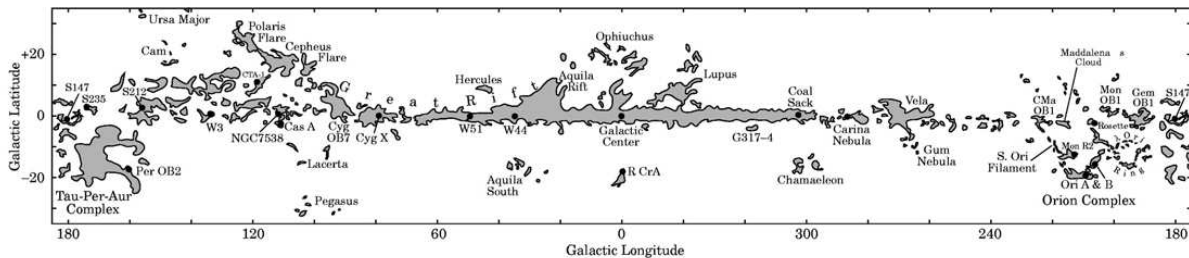


**Figure 3.1:** CO intensity map along the Galactic plane (Dame, Hartmann, & Thaddeus 2001<sup>[44]</sup>). The Orion A (Ori. A) molecular cloud, at the right side of the panel, is located at the Galactic longitude and latitude of  $l \sim 210^\circ$  and  $b \sim -20^\circ$ .

OMC-1 is the most prominent and densest cloud core in the Orion A. It contains a young stellar cluster called the Orion Nebula Cluster (ONC) that embraces an OB association known as the Trapezium. The Trapezium is the powering source of the spectacular  $H_{II}$  region of the Orion (M42; Fig. 1.1). OMC-2 and OMC-3 are located  $\sim 12'$  and  $\sim 23'$  north to ONC. OMC-2 was first discovered by chance as a complex of NIR and molecular emissions

(Gatley et al. 1974<sup>[63]</sup>). OMC-3 is another intensity peak of radio emissions at the north of OMC-2.

Successive studies in OMC-2 revealed that it is a high density as well as high column density core with the kinematic temperature (24 K) much lower than that of OMC-1 (70 K). OMC-3 has even lower kinematic temperature of 19 K (Castets & Langer 1995<sup>[30]</sup>). These indicate that both OMC-2 and OMC-3 are the sites of on-going star formation. The star formation activity first occurred in OMC-1 and propagated into the north to OMC-2 and OMC-3, which are currently active star-forming clouds. To illustrate this, these clouds are full of phenomena related to star formations; jets, molecular outflows, HH objects, accretion disks, dust emissions, etc.

Throughout this thesis, we adopt the age of OMC-2 and OMC-3 to be  $\sim 1$  Myr, which is estimated based either on the H-R diagram of some bright NIR sources in OMC-2 (Johnson et al. 1990<sup>[96]</sup>), the  $K$ -band luminosity function of cluster members (Ali & DePoy 1995<sup>[2]</sup>), direct spectroscopic evidence (Hodapp & Deane 1993<sup>[87]</sup>; Hillenbrand 1997<sup>[85]</sup>), the presence of rich outflows and NIR excesses commonly seen in YSOs (Strom, Strom, & Merrill 1993<sup>[175]</sup>; Chen & Tokunaga 1994<sup>[34]</sup>; Jones et al. 1994<sup>[101]</sup>), and the  $I$ - and  $V$ -band magnitudes of member sources (Rebull et al. 2000<sup>[160]</sup>). The distance to OMC-2 and OMC-3 is assumed to be  $\sim 450$  pc (Genzel & Stutzki 1989<sup>[66]</sup>).

## 3.2 Radio Observations

### 3.2.1 Identifying Protostellar Cores with Dust Emissions

Radio continuum observations in OMC-2 and OMC-3 have been conducted at 1.3 mm (Mezger et al. 1990<sup>[129]</sup>; Chini et al. 1997<sup>[35]</sup>), 850  $\mu\text{m}$ , 450  $\mu\text{m}$  (Johnstone & Bally 1999<sup>[99]</sup>), and 350  $\mu\text{m}$  (Lis et al. 1998<sup>[117]</sup>). All these observations aim to detect dust continuum emissions of protostellar cores and to determine the position and distribution of contracting cores, which pilots the star formation studies in these regions.

Mezger, Zylka, & Wink (1990)<sup>[129]</sup> obtained a 1.3 mm map of OMC-1 and OMC-2 with the angular resolution of  $\sim 90''$  and  $\sim 11''$ , respectively. In OMC-2, they identified six millimeter clumps (FIR 1–FIR 6). Chini et al. (1997)<sup>[35]</sup> took a higher-resolution image of OMC-2 and OMC-3 at 1.3 mm and detected a chain of 21 cores (MMS 1–MMS 10 in OMC-3,

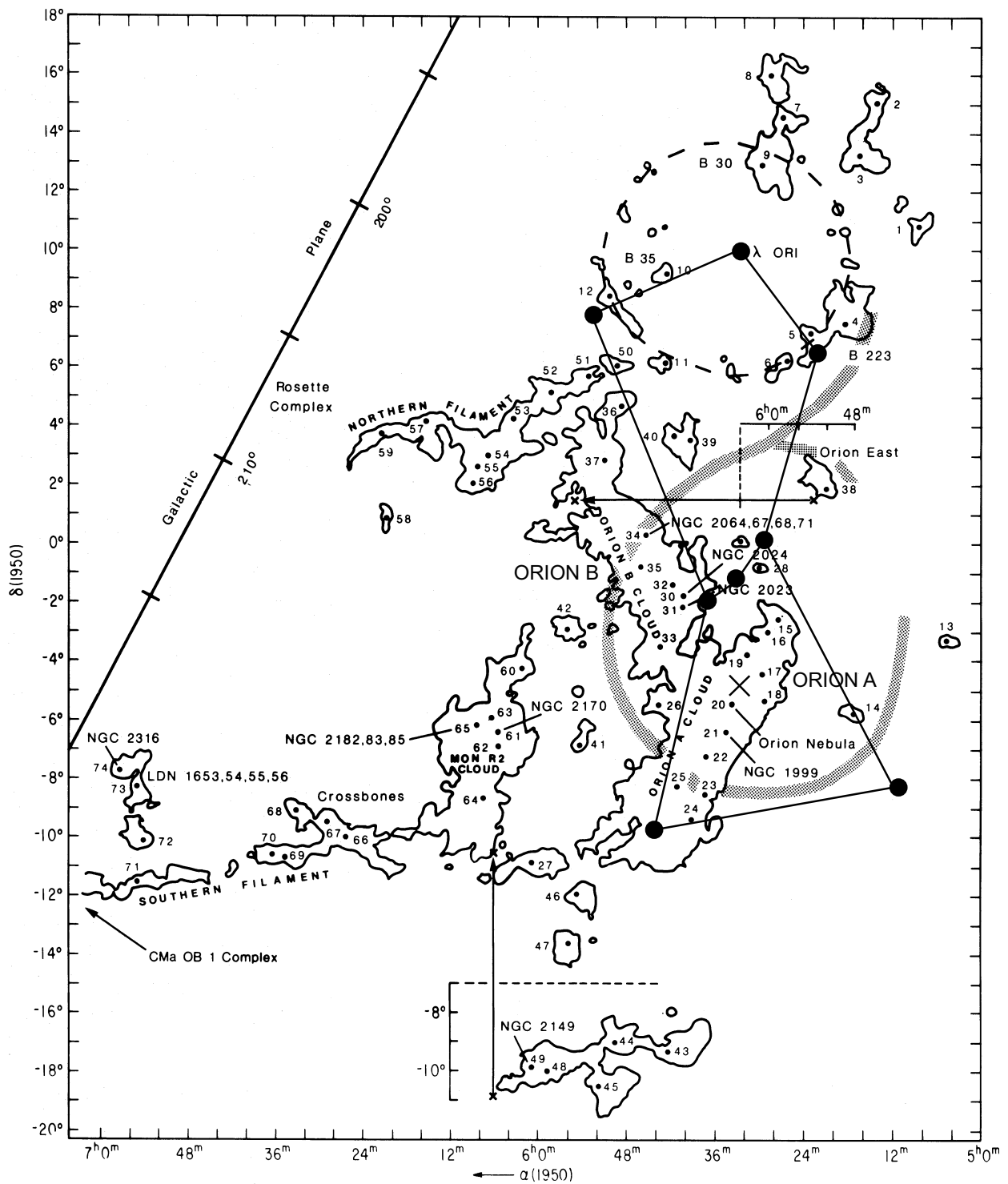


**Figure 3.2:** Schematic view of the Orion A, Orion B, and Monoceros R2 cloud complex (Maddalena et al. 1986<sup>[120]</sup>), and major stars of the Orion. OMC-2 and OMC-3 belong to the Orion A, and are located at the position marked with the cross.

FIR 1a–FIR 6d in OMC-2; Table 3.1) using the Institut de Radio Astronomie Millimétrique (IRAM) telescope. Combining the James Clerk Maxwell Telescope (JCMT) photometry from 350  $\mu\text{m}$  to 2 mm and the *Infrared Astronomical Satellite (IRAS)* photometry from 12  $\mu\text{m}$  to 100  $\mu\text{m}$ , they showed that most cores have a high ratio of sub-millimeter to bolometric luminosity ( $L_{\text{smm}}/L_{\text{bol}}$ ), insisting that these cores are class 0 protostar candidates. They also derived the temperature and mass of each condensation (Tables 3.1 and 3.2). Figure 3.3 shows the 1.3 mm intensity map of OMC-2 and OMC-3. Throughout this thesis, we use this map as the landmark of these regions.

Lis et al. (1998)<sup>[117]</sup> followed with a 350  $\mu\text{m}$  imaging observation with a larger FOV including OMC-2 and OMC-3. They detected 350  $\mu\text{m}$  emissions from almost all the 1.3 mm cores and 10 additional ones (Fig. 3.4).

Johnstone & Bally (1999)<sup>[99]</sup> observed this region in 450  $\mu\text{m}$  and 850  $\mu\text{m}$  and found similar “integral-shaped” structure identified in 1.3 mm. They constructed the spectral index map, which constrains the dust emissivity and temperature at each position.

### 3.2.2 Centimeter Observations of Free-free Emissions

Reipurth et al. (1999)<sup>[162]</sup> observed a 6'×15' region in OMC-2 and OMC-3 with VLA. The D configuration in 3.6 cm was used, which yields an angular resolution of  $\sim 8''$  (Sect. 4.5). In total, 14 sources were detected above  $\sim 0.1$  mJy, ten of which are associated with the protostellar cores seen in the 1.3 mm continuum. Some 3.6 cm sources are also associated with H<sub>2</sub> (Yu, Bally, & Devine 1997<sup>[199]</sup>) and CO and HCO<sup>+</sup> (Aso et al. 2000<sup>[111]</sup>) outflows, HH objects (Reipurth, Bally, & Devine 1997<sup>[161]</sup>), H<sub>2</sub>O masers (Morris & Knapp 1976<sup>[135]</sup>; Genzel & Downes 1979<sup>[65]</sup>), and sub-millimeter emissions (Lis et al. 1998<sup>[117]</sup>). Due to these associations, these 3.6 cm emissions are considered to be free-free emissions from the H<sub>II</sub> regions generated by shocks from protostar jets.

The detection of thermal free-free centimeter emissions gives strong evidence that there is a class 0 or class I protostar at its origin, with active mass accretion. Seven and four 3.6 cm emissions were respectively found in OMC-2 and OMC-3. In one of the protostellar cores in OMC-3, we found that D configuration observations are not fine enough to correlate with our X-ray and NIR data, so we obtained the A configuration image in this region. The details of analysis and result of this observation are discussed in Sect. 8.4.

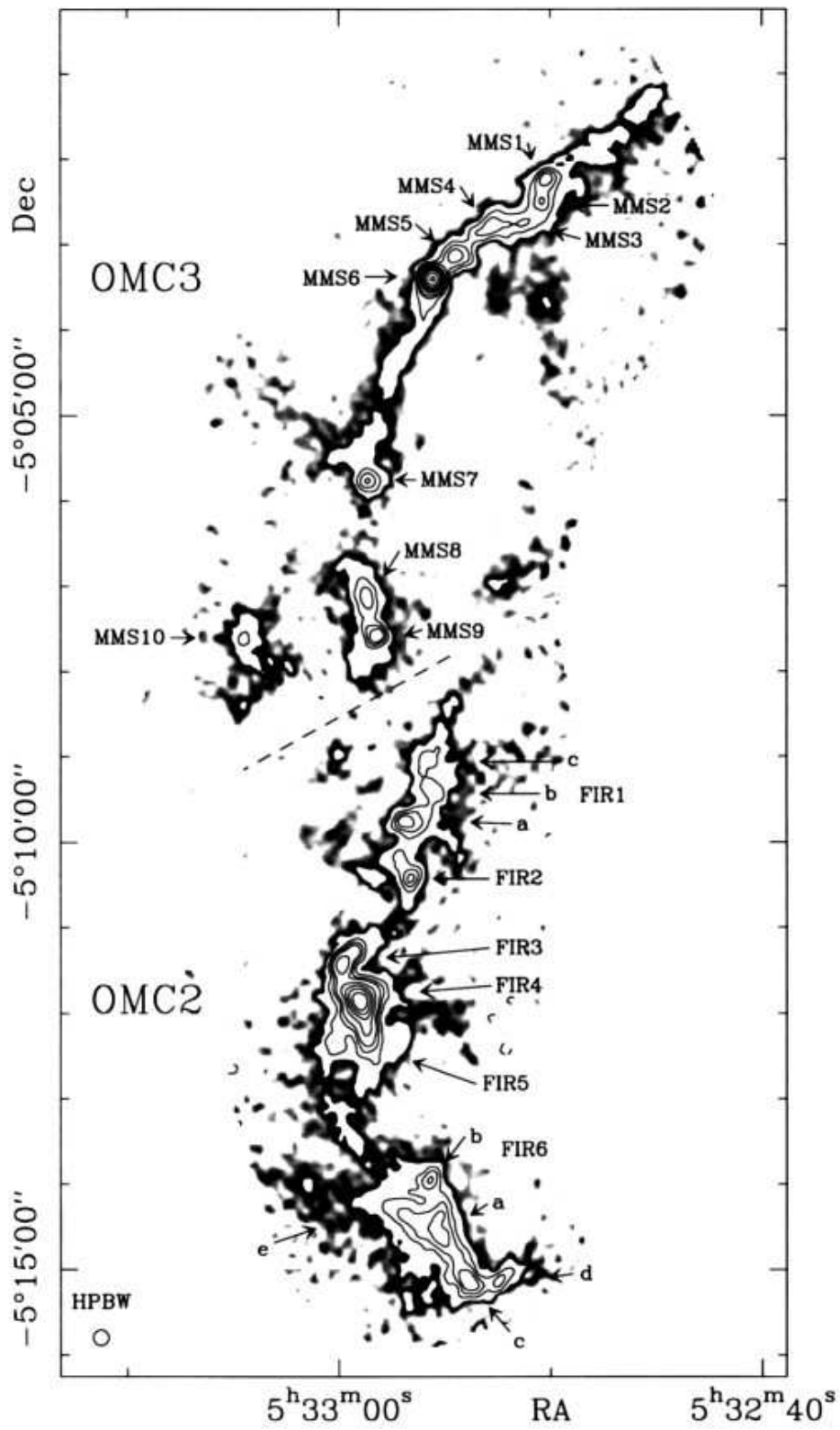


**Figure 3.3:** Distribution of protostellar cores seen in 1.3 mm (Chini et al. 1997<sup>[35]</sup>). OMC-2 and OMC-3 are separated by the dashed line into south and north. The equinox is in B1950.0.



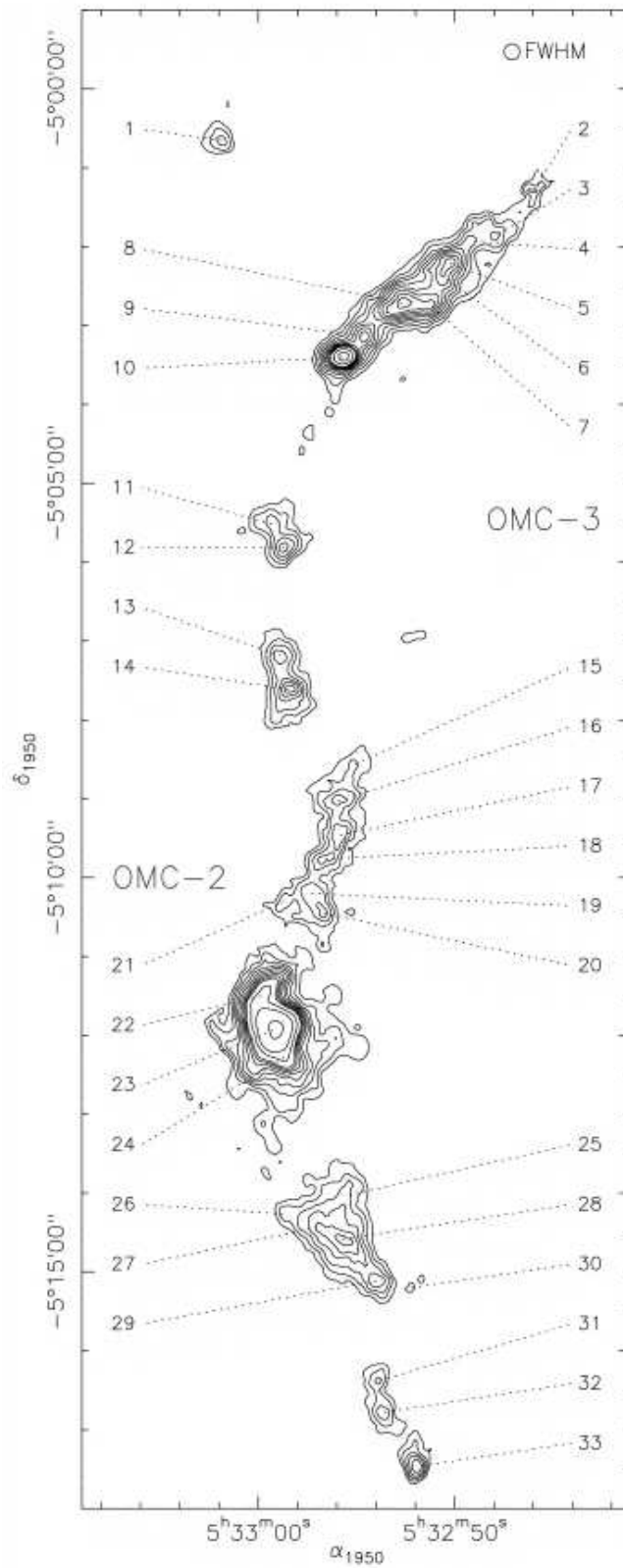


**Figure 3.4:** Distribution of protostellar cores seen in  $350 \mu\text{m}$  (Lis et al. 1998<sup>[117]</sup>). The equinox is in B1950.0.

**Table 3.1:** Properties of protostellar cores in OMC-2 and OMC-3 (1)

object <sup>a</sup>	R.A. (J2000.0)	decl. (J2000.0)	counterpart			
			350 $\mu\text{m}$ <sup>b</sup>	H <sup>13</sup> CO <sup>+</sup> <sup>c</sup>	H <sub>2</sub> <sup>d</sup>	3.6 cm <sup>e</sup>
OMC-3						
MMS 1	05:35:18	-05:00:20	CSO 5	.....	.....	.....
MMS 2	05:35:18	-05:00:35	CSO 6	AC 3	flow B	VLA 1
MMS 3 <sup>f</sup>	05:35:19	-05:00:51	CSO 7	.....	.....	.....
MMS 4	05:35:20	-05:00:53	CSO 8	.....	.....	.....
MMS 5	05:35:22	-05:01:14	CSO 9	.....	flow C	.....
MMS 6	05:35:23	-05:01:32	CSO 10	AC 4	flow A	VLA 3
MMS 7	05:35:26	-05:03:53	CSO 12	AC 8	flow F	VLA 4
MMS 8	05:35:27	-05:05:17	CSO 13	.....	.....	.....
MMS 9	05:35:26	-05:05:42	CSO 14	AC 10	flow H	VLA 5
MMS 10	05:35:32	-05:05:42	.....	AC 12	.....	.....
OMC-2						
FIR 1c	05:35:24	-05:07:10	CSO 16	.....	.....	VLA 7
FIR 1b	05:35:23	-05:07:32	CSO 17	AC 14	.....	.....
FIR 1a	05:35:25	-05:07:53	CSO 18	.....	.....	VLA 8
FIR 2	05:35:24	-05:08:33	CSO 20	AC 15	flow O	.....
FIR 3	05:35:28	-05:09:33	CSO 22	.....	flow J	VLA 11
FIR 4	05:35:27	-05:10:00	CSO 23	AC 17	.....	VLA 12
FIR 5	05:35:26	-05:10:23	CSO 24	.....	.....	.....
FIR 6a	05:35:23	-05:12:36	CSO 28	.....	.....	VLA 14
FIR 6b	05:35:23	-05:12:03	CSO 25	.....	flow L	.....
FIR 6c	05:35:21	-05:13:15	CSO 29	.....	.....	.....
FIR 6d	05:35:20	-05:13:15	CSO 30	.....	.....	.....

<sup>a</sup> Nomenclatures follow Chini et al. (1997)<sup>[35]</sup> for OMC-3 sources and Mezger, Zylka, & Wink (1990)<sup>[129]</sup> for OMC-2 sources.

<sup>b</sup> Lis et al. (1998)<sup>[117]</sup>.

<sup>c</sup> Aso et al. (2000)<sup>[11]</sup>.

<sup>d</sup> Yu, Bally, & Devine (1997)<sup>[199]</sup>.

<sup>e</sup> Reipurth, Rodrigues, & Chini (1999)<sup>[162]</sup>.

<sup>f</sup> The position of MMS 3 in Chini et al. (1997)<sup>[35]</sup> is incorrect. The corrected coordinate is given in Tsuboi et al. (2001)<sup>[188]</sup>.

**Table 3.2:** Properties of protostellar cores in OMC-2 and OMC-3 (2)

object <sup>a</sup>	$L_{\text{bol}}^{\text{a}}$ ( $L_{\odot}$ )	$L_{\text{bol}}/L_{\text{smm}}^{\text{a}}$	$T_d^{\text{a}}$ (K)	$M_{\text{gas}}^{\text{a}}$ ( $M_{\odot}$ )	$\dot{M}^{\text{b}}$ ( $M_{\odot} \text{ yr}^{-1}$ )	$\dot{P}^{\text{b}}$ ( $M_{\odot} \text{ km s}^{-1} \text{ yr}^{-1}$ )
OMC-3						
MMS 1	<55	<61	20-25	18	.....	.....
MMS 2	.....	.....	.....	.....	$7.4 \times 10^{-6}$	$3.0 \times 10^{-5}$
MMS 3	.....	.....	.....	.....	ditto <sup>e</sup>	ditto <sup>e</sup>
MMS 4	<56	<72	20-25	11	ditto <sup>e</sup>	ditto <sup>e</sup>
MMS 5	.....	.....	.....	.....	$6.7 \times 10^{-6}$	$1.9 \times 10^{-5}$
MMS 6	<60	<50	15-25	36	.....	.....
MMS 7	76	129	26	8	$1.4 \times 10^{-5}$	$8.8 \times 10^{-5}$
MMS 8	<89	<178	20	9	.....	.....
MMS 9	<94	<145	20	10	$3.6 \times 10^{-5}$	$15.1 \times 10^{-5}$
MMS 10	.....	.....	.....	.....	$3.3 \times 10^{-5}$	$11.3 \times 10^{-5}$
OMC-2						
FIR 1c	128	356	33	5	$3.1 \times 10^{-5}$	$9.8 \times 10^{-5}$
FIR 1b	.....	.....	.....	.....	ditto <sup>f</sup>	ditto <sup>f</sup>
FIR 1a	<138	.....	.....	.....	ditto <sup>f</sup>	ditto <sup>f</sup>
FIR 2	<157	<320	20	8	.....	.....

<sup>a</sup> Chini et al. (1997)<sup>[35]</sup>.<sup>b</sup> Aso et al. (2000)<sup>[11]</sup>.<sup>c</sup> Mass loss rate of the outflows.<sup>d</sup> Momentum loss rate of the outflows.<sup>e</sup> MMS 2, MMS 3, and MMS 4 were not resolved in the observations by Aso et al. (2000)<sup>[11]</sup>.<sup>f</sup> FIR 1a, FIR 1b, and FIR 1c were not resolved in the observations by Aso et al. (2000)<sup>[11]</sup>.

### 3.2.3 Millimeter Observations of Molecular Cores and Outflows

Mapping observations with various density tracers have been conducted on OMC-2 and OMC-3; with  $^{13}\text{CO}$  by Bally et al. (1987)<sup>[14]</sup>,  $\text{C}^{18}\text{O}$  by Dutrey et al. (1993)<sup>[45]</sup>,  $^{13}\text{CO}$ ,  $\text{C}^{18}\text{O}$ ,  $\text{C}^{32}\text{S}$ , and  $\text{C}^{34}\text{S}$  by Castes & Langer (1995)<sup>[30]</sup>, and  $\text{C}_1(^3P_1-^3P_0)$  and  $\text{CO}$  ( $J = 3 - 2$ ) by Ikeda et al. (1999)<sup>[94]</sup>. These observations identified a filamentary structure extending from OMC-1 to OMC-2 and OMC-3. Hundreds of dust condensations along this filament were extracted by two high resolution mapping observations in  $\text{CS}$  ( $J = 1 - 0$ ) by Tatematsu et al. (1993)<sup>[179]</sup> and in  $\text{NH}_3$  by Cesaroni & Wilson (1994)<sup>[31]</sup>.

With the Nobeyama 45 m telescope, Aso et al. (2000)<sup>[11]</sup> observed OMC-2 and OMC-3 in  $\text{H}^{13}\text{CO}^+$  ( $J = 1 - 0$ ),  $\text{HCO}^+$  ( $J = 1 - 0$ ), and  $\text{CO}$  ( $J = 1 - 0$ ) lines, detecting eight molecular outflows in addition to 18 molecular cores. Blue and red lobes of these outflows are well aligned with the outflows seen in the  $\text{H}_2$  observation (Yu et al. 1997<sup>[199]</sup>). The spatial resolution of their map (the beam width of  $\sim 15''$ ) is comparable to those taken in the continuum observations by Chini et al. (1997)<sup>[35]</sup> and Lis et al. (1998)<sup>[117]</sup>, which enabled them to determine the origin, velocity, mass loss rate, and outflow momentum rate of these outflows. No interferometer millimeter observation has been conducted on these regions.

### 3.2.4 Polarization Measurements

Matthews & Wilson (2000)<sup>[124]</sup> and Matthews, Wilson, & Fiege (2001)<sup>[125]</sup> measured the polarization of dust emissions in OMC-3 at  $850 \mu\text{m}$ . They found that the polarization vectors are highly aligned. The field direction in the plane of the sky ( $B_\perp$ ) was found to be perpendicular to the filamentary structure of OMC-3.

## 3.3 NIR Observations

### 3.3.1 Bright Discrete Sources in OMC-2

A series of NIR studies in OMC-2 and OMC-3 has been made concentrating on bright discrete sources. Gatley et al. (1974)<sup>[63]</sup> was the first to observe OMC-2 with 10 broad-bands from  $1.6 \mu\text{m}$  to  $20 \mu\text{m}$  and found five separate components (IRS 1–IRS 5). Based on their lack of the optical counterparts, their SEDs, and the association with  $\text{CO}$  emissions, they suggested

that these NIR sources are protostars. The nature of these emissions was the main issue in the following three papers published once in four years (Thronson & Thompson 1982<sup>[182]</sup>; Pendleton et al. 1986<sup>[149]</sup>; Johnson et al. 1990<sup>[96]</sup>).

Thronson & Thompson (1982)<sup>[182]</sup> measured the  $K$ -band spectra of IRS 3 and IRS 4, and revealed that IRS 4 shows many emission lines of molecular hydrogen. They pointed out that the series of  $\text{H}_2$   $v = 2 - 1$  lines are relatively strong compared to  $v = 1 - 0$  lines instead of their low absolute flux, hence they are more likely produced by UV pumping. This was the first candidate of UV-pumped  $\text{H}_2$  sources, although the shock pumping origin of these  $\text{H}_2$  emission lines could not be ruled out.

Pendleton et al. (1986)<sup>[149]</sup> conducted NIR–FIR imaging and NIR polarimetry observations of OMC-2. They showed that IRS 1 and IRS 4 are reflection nebulae based on their high degree of polarization. Their FIR map revealed compact sources at IRS 1 and IRS 4, which are considered to be responsible for the reflection.

The final conclusion on the nature of these NIR sources was derived by Johnson et al. (1990)<sup>[96]</sup>, who compiled the SEDs of 11 discrete sources including IRS 1–IRS 5. Most of these SEDs are accountable with the combination of NIR emissions from reddened stellar photosphere and thermal emissions from circumstellar matter, indicating the pre-main-sequence nature of these sources. By de-reddening these SEDs, they also estimated the temperature, extinction, mass and age of these sources. The picture of OMC-2 was thus established to be a cluster of low-luminosity, low- to intermediate-mass YSOs with ages of  $\sim 1$  Myr embedded in an extended dust cloud.

### 3.3.2 Surveys with Broad-band Imaging Observations

In 1990's, the advent of large format NIR arrays prompted survey studies of star-forming clouds. Jones et al. (1994)<sup>[101]</sup> measured the  $J$ -,  $H$ -, and  $K$ -band magnitude of 219 sources in a  $15' \times 5'$  region containing OMC-2. The 90% completeness limit of their survey was  $K \sim 14$  mag. They found that almost all the sources brighter than 13 mag are cloud members and some sources show flux variability.

Ali & DePoy (1995)<sup>[2]</sup> conducted a similar survey study in a larger field ( $1472 \text{ arcmin}^2$ ) with a deeper exposure ( $K \sim 14.5$  mag at the 90% completeness) but in the  $K$  band alone. They detected 3548 sources and constructed the surface density map of these sources, iden-

tifying two density peaks; i.e., the Trapezium and OMC-2. They also studied the  $K$ -band luminosity function (KLF) of these peaks and found that KLF of the Trapezium is consistent with a Miller & Scalo (1979)<sup>[131]</sup> initial mass function (IMF) with the age of  $\sim 10^6$  yr. No age estimate of OMC-2 was available due to the paucity of sources ( $\sim 33$ ).

Carpenter (2000)<sup>[26]</sup> and Carpenter, Hillenbrand, & Skrutskie (2001b)<sup>[28]</sup> extended the survey study of the Orion A cloud with 2MASS data, which provides the  $J$ -,  $H$ -, and  $K_s$ -band magnitude down to 16.0, 15.4, and 14.8 mag at the 93.8% completeness, respectively. They showed that there is an enhanced stellar surface density over a  $0.4^\circ \times 2.4^\circ$  region containing the Trapezium, OMC-2 and OMC-3.

One of the unique outcomes of 2MASS project was presented by Carpenter, Hillenbrand, & Skrutskie (2001b)<sup>[28]</sup>, who systematically studied the NIR variability properties of pre-main-sequence sources in a  $0.84^\circ \times 6^\circ$  region across OMC. A total of 1235 variables are classified into several patterns; periodic stars, eclipsing systems, stars steadily increase their brightness, stars that change colors redder or bluer, long-term variables, and so on. Models such as hot or cool spots on the surface, changes in the mass accretion rate, inner disk radius, or extinction are employed to account for their variability. This is the most comprehensive study of NIR variability seen in pre-main-sequence sources.

We found that all above NIR surveys are not deep enough to match our X-ray observation of OMC-2 and OMC-3. Therefore, we conducted the deeper ( $K \sim 16$  mag) and more comprehensive NIR observations in these regions (this thesis; Tsujimoto et al. 2003<sup>[192]</sup>). The details of analysis and result of this observations are discussed in Sect. 5.2.

### 3.3.3 Narrow-band Studies of Molecular Outflows

The vibrational-rotational transition of  $v = 1 - 0$  S(1) works as an effective coolant of the excited hydrogen molecules, so this emission line is commonly used as a tracer of outflows from protostars (Bally et al. 1993<sup>[15]</sup>; Hodapp & Ladd 1995<sup>[88]</sup>). Yu et al. (1997)<sup>[199]</sup> conducted a narrow-band imaging observation in  $\text{H}_2$   $v = 1 - 0$  S(1) ( $2.12 \mu\text{m}$ ) and found  $\sim 80$  sources in OMC-2 and OMC-3. These sources consist a dozen of collimated outflow aligned from east to west and with millimeter cores at their center. Based on the high condensation and level of outflow activity seen in  $\text{H}_2$ , they described that OMC-2 and OMC-3 are undergoing a “microburst” of star formation.

We further obtained the H<sub>2</sub> image of OMC-3 with a better spatial resolution using the University of Hawaii 88 inch (2.2 m) telescope and with a much higher sensitivity using the Subaru telescope in order to make it easier to identify the powering source of the outflows in crowded regions. The details of analysis and result of these observations are discussed in Sects. 8.2 and 8.3.

## 3.4 Optical Observations

### 3.4.1 Membership Studies with Proper Motion Measurements

Membership studies of OMC have been conducted mainly in the optical wavelength through the measurement of proper motions (Parenago 1954<sup>[148]</sup>; Jones & Walker 1988<sup>[100]</sup>; van Altena et al. 1988<sup>[193]</sup>; McNamara et al. 1989<sup>[126]</sup>). Tian et al. (1996)<sup>[183]</sup> examined the relative proper motions and the membership probabilities for 333 sources with the plates taken over a period of 83 years in the Shanghai Observatory. 184 sources have higher membership probability than 70%, which they consider are the Orion members.

### 3.4.2 Detection of Circumstellar Disks

Two optical techniques were employed to identify sources with circumstellar disks in these regions; one is by H<sub>α</sub> emission and the other by  $UV$  excess (Fig. 3.6).

Herbig & Bell (1988)<sup>[83]</sup> compiled a catalog of 735 pre-main-sequence sources in OMC, which were observed with the slit spectrograph or at equivalent resolution. The equivalent width of H<sub>α</sub> emission ( $EW[H_\alpha]$ ) was measured for these sources, with which they were classified into cTTSs ( $EW[H_\alpha] > 10 \text{ \AA}$ ) and wTTSs ( $EW[H_\alpha] < 10 \text{ \AA}$ ).

Rebull et al. (2000)<sup>[160]</sup> surveyed the ONC flanking fields covering OMC-2 and OMC-3 with the  $U$ ,  $V$ , and  $I$  bands. The purpose of this work is to determine the  $(U-V)$  and  $(V-I)$  colors of the Orion sources and to pick up sources with circumstellar disks based on their  $UV$  excess emissions. About 5000 sources were examined for their colors and  $\sim 230$  of them were found to have a  $UV$  excess of more magnitudes than 0.5 mag, a signature of circumstellar disk. They also illustrated the consistency of this method to search for disks with other better-established methods such as NIR excess or H<sub>α</sub> emission.

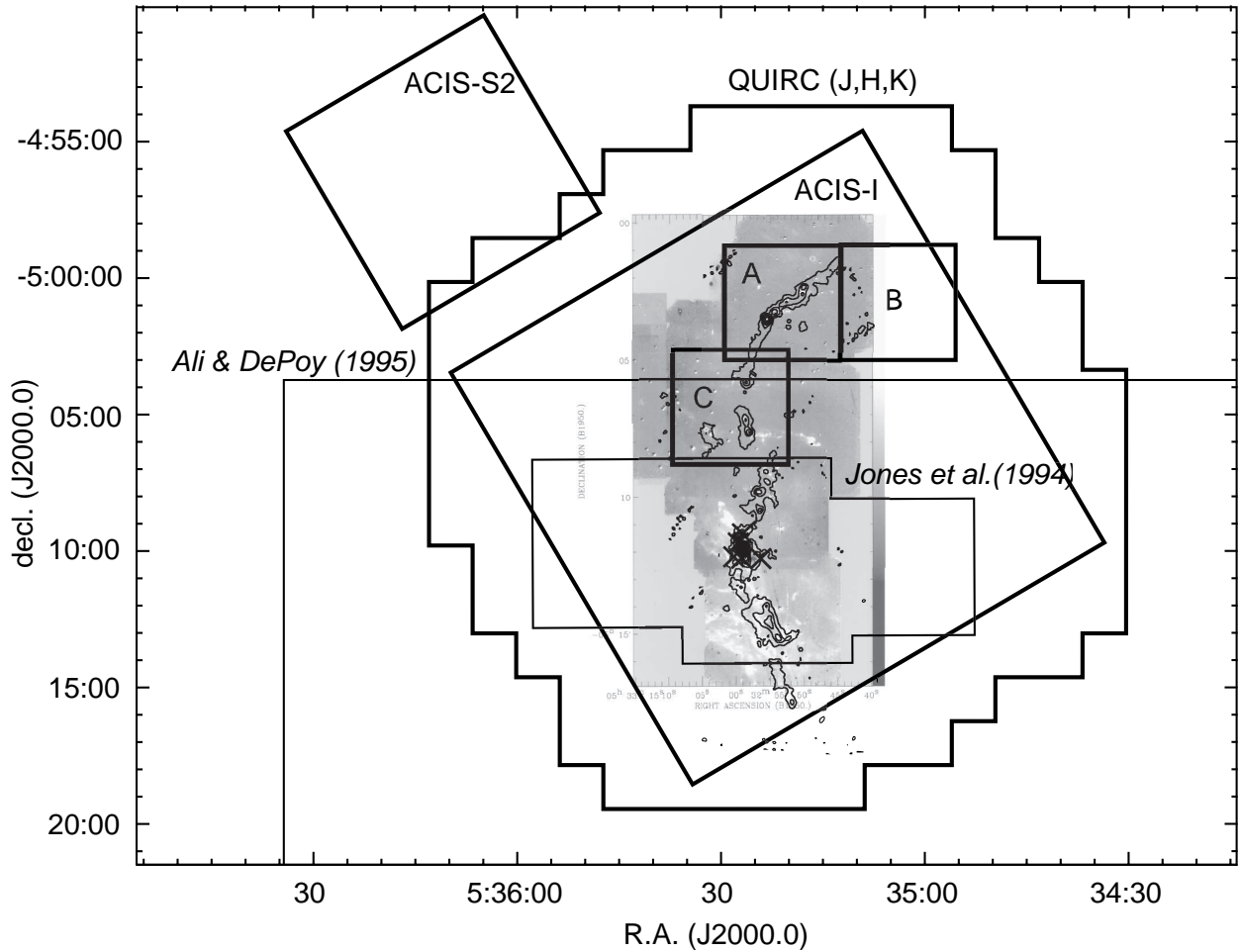


**Figure 3.5:** Past NIR observations of OMC-2 and OMC-3. The gray scale represents the continuum-subtracted  $H_2$  emission (Yu et al. 1997<sup>[199]</sup>), while the contours give the 1.3 mm intensity (Chini et al. 1997<sup>[35]</sup>). The pluses are the position of IRS 1–IRS 5 (Johnson et al. 1990<sup>[96]</sup>). The survey fields of Jones et al. (1994)<sup>[101]</sup> and Ali & DePoy (1995)<sup>[2]</sup> are shown with thin lines. The FOVs of observations conducted in this thesis; *Chandra*, QUIRC *J*, *H*, and *K* band, and QUIRC  $H_2$  band (A, B, and C) are shown with thick lines (see Sect. 8.2).



In this thesis, we combine the NIR excess (this thesis; Tsujimoto et al. 2003<sup>[192]</sup>),  $UV$  excess (Rebull et al. 2000<sup>[160]</sup>), and  $H_\alpha$  emission line (Herbig & Bell 1988<sup>[83]</sup>) data to discriminate sources with and without circumstellar disks. We recognize sources to have circumstellar disks if they have at least one positive detection among these three methods.

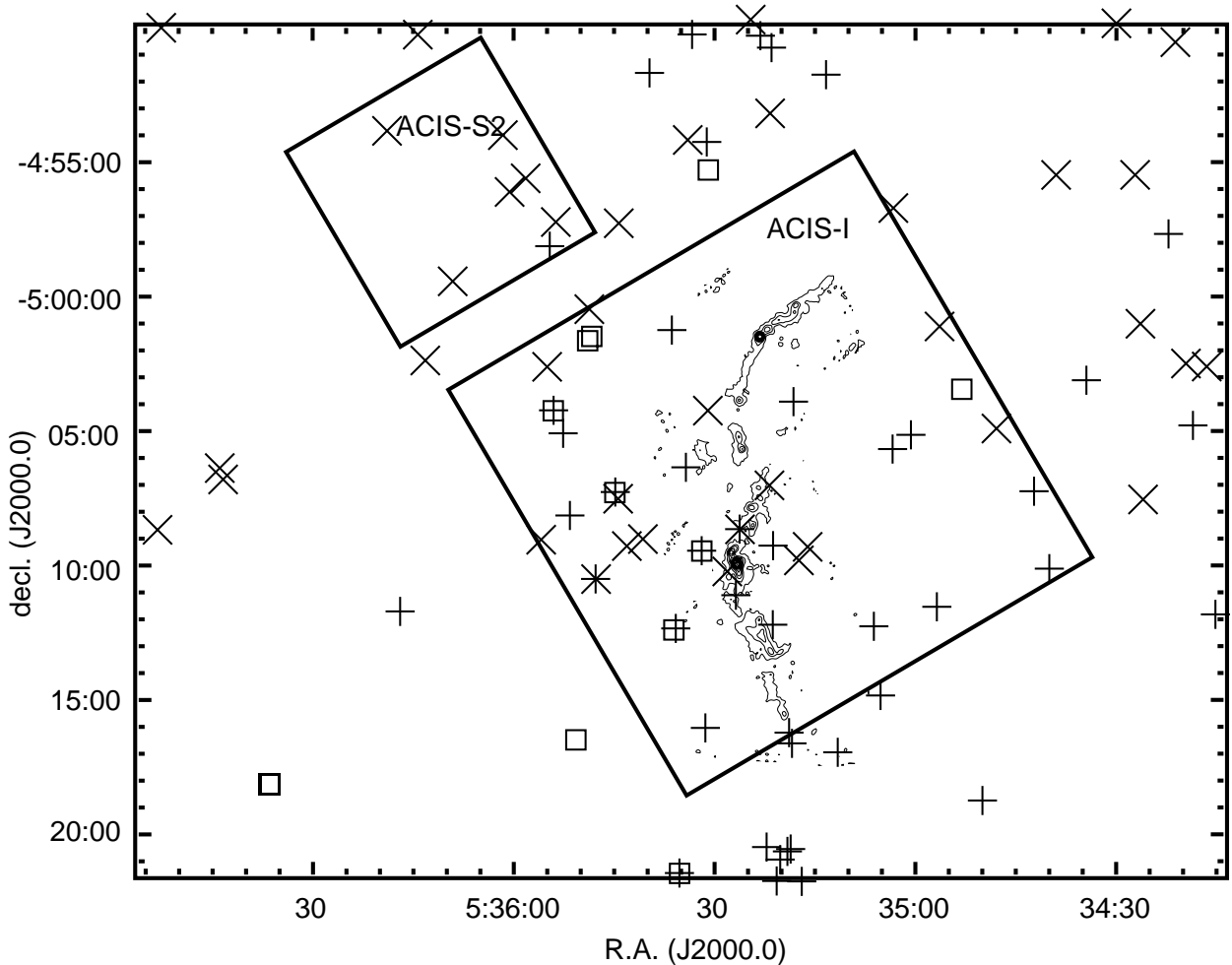


**Figure 3.6:** Past optical observations of OMC-2 and OMC-3. *squares*: sources with the equivalent width of  $H_\alpha$  larger than  $10 \text{ \AA}$  (Herbig & Bell 1988<sup>[83]</sup>). *Crosses*: sources with  $UV$  excess (Rebull et al. 2000<sup>[160]</sup>). *Pluses*: sources with the membership probability of more than 70% (Tian et al. 1996<sup>[183]</sup>). The contours represent the 1.3 mm intensity (Chini et al. 1997<sup>[35]</sup>). The *Chandra* FOVs are given in two oblique squares.

## 3.5 X-ray Observations

### 3.5.1 Surveys in the Soft X-ray Band

Two systematic X-ray studies of the Orion A were conducted by Gagné & Caillault (1994)<sup>[60]</sup> and Gagné, Caillault, & Stauffer (1995)<sup>[61]</sup> with Imaging Proportional Counter (IPC) onboard the *Einstein* satellite and with High-Resolution Imager (HRI) onboard *ROSAT* (Fig. 3.7). These observations provide the position and the count rate of 245 and 389 X-ray sources in a 4.5 square degree and a 0.8 square degree region, respectively. No spectroscopy has been made in these observations. In Gagné, Caillault, & Stauffer (1995)<sup>[61]</sup>, X-ray emission was found from sources of all spectral types, ranging from massive O- and B-type stars to late-type pre-main-sequence sources. About 75 X-ray sources with a measured spectral type were investigated for any relations between the X-ray luminosity ( $L_X$  with an assumed X-ray spectrum) and the bolometric luminosity ( $L_{bol}$ ),  $v \sin i$ , rotation period, and the effective temperature. They found that (1)  $L_X$  is related to  $L_{bol}$  with  $L_X/L_{bol} < 10^{-3}$  and (2)  $L_X$  and  $L_X/L_{bol}$  do not appear to be related with the stellar rotation.

Geier, Wendker, & Wisotzki (1995)<sup>[64]</sup> observed the Orion region with Position-Sensitive Proportional Counter (PSPC) onboard *ROSAT* and detected 171 X-ray sources. The purpose of this observation was to confirm the diffuse X-ray emission reported by Ku & Chanan (1979)<sup>[109]</sup>, but the trial was in vain because X-ray sources were too crowded. Unlike previous two detectors, PSPC has low-resolution spectral capability in the soft X-ray band (0.1–2.4 keV), so they also conducted spectral analyses for bright 95 sources to determine the plasma temperature and the interstellar absorption. Sources were separated into two groups based on these parameters: (1) those with the absorption of  $N_H < 2 \times 10^{21} \text{ cm}^{-2}$  and the temperature of  $T \sim 4 \times 10^6 \text{ K}$  (0.35 keV) and (2) those with the absorption of  $N_H \sim 10^{22} \text{ cm}^{-2}$  and the temperature of  $T \sim 10^7 \text{ K}$  (0.86 keV). The sources in the former group are randomly distributed, while the latter are concentrated on the Trapezium cluster. These results lead them to suspect that the former group consists of main sequence sources, while the latter consists of YSOs.

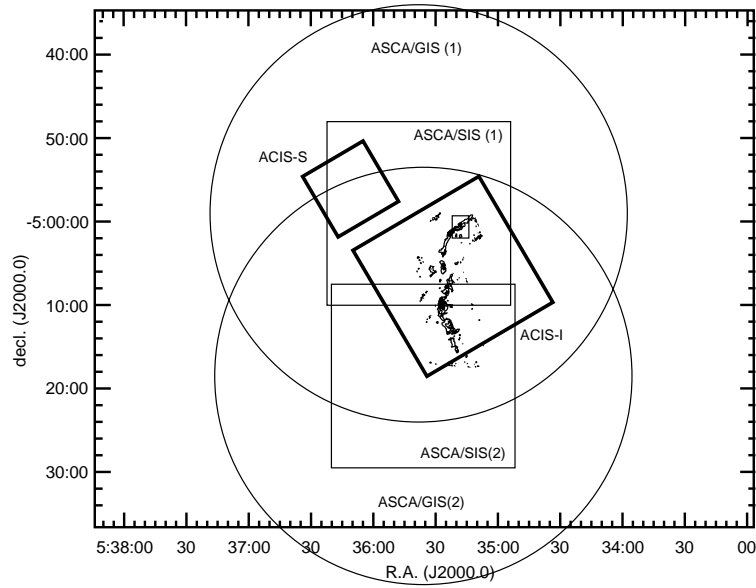
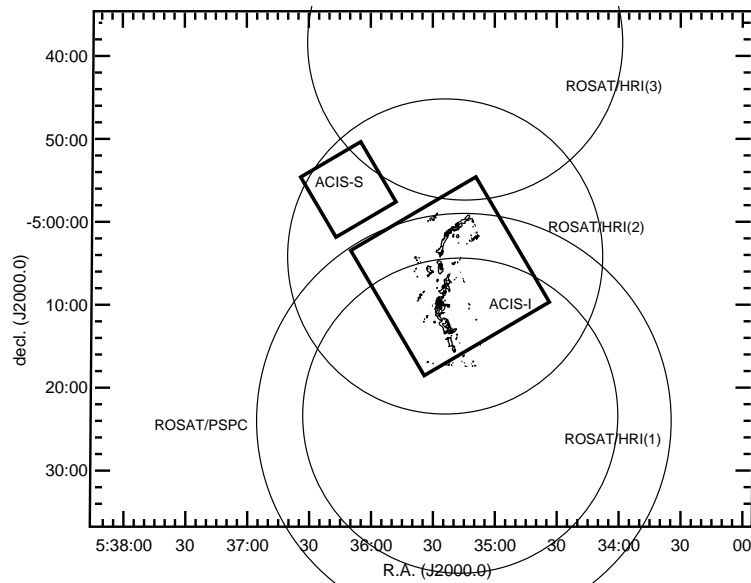
### 3.5.2 Surveys in the Hard X-ray Band

Yamauchi et al. (1996)<sup>[196]</sup> studied the whole Orion A cloud with two pointing observations with the *ASCA* satellite (Fig. 3.7). They detected 52 X-ray sources using Gas Imaging

Spectrometer (GIS) and Solid-state Imaging Spectrometer (SIS). They also derived spectral parameters of five bright X-ray sources. An interesting result was obtained that these X-ray sources have a thin-thermal plasma of two temperatures; one is 0.7–1 keV and the other is 3–5 keV. This was also confirmed in a composite spectra of many discrete sources accumulated in large areas. This was the first hard X-ray imaging observation of the Orion region. In addition to lower temperature plasma of 0.7–1 keV found by *Einstein* and *ROSAT*, higher temperature plasma of 3–5 keV was first confirmed from discrete sources in the Orion.

Two important lessons can be drawn from these previous observations. First, we need to have the spatial resolution of  $\sim 1''$  to resolve each X-ray source in star-forming regions like OMC. Second, the hard X-ray capability is inevitable to overcome high extinction and to detect high temperature plasma. Preceding X-ray observatories such as *Einstein*, *ROSAT*, and *ASCA* did not meet either of these requirements. We therefore made the X-ray observation on this region using the *Chandra X-ray Observatory*, which has  $\sim 1''$ – $5''$  spatial resolution and hard X-ray imaging and spectroscopy capability (Tsujiimoto et al. 2002a<sup>[189]</sup>; this thesis).

The initial result of our *Chandra* observation was published by Tsuboi et al. (2001)<sup>[188]</sup>, who concentrated on the hard X-ray detections from 1.3 mm cores in the northern part of OMC-3. Two hard X-ray sources were detected at the protostellar cores with a thin-thermal spectrum of  $N_{\text{H}} = 1\text{--}3 \times 10^{23} \text{ cm}^{-2}$  and  $L_{\text{X}} \sim 10^{30} \text{ ergs s}^{-1}$ . These protostellar cores are at the class 0 stage based on their SEDs. They proposed that these X-ray emissions are the first candidates of X-ray-emitting class 0 sources.

(a) *ASCA*(b) *ROSAT*

**Figure 3.7:** FOVs of the X-ray observations on OMC-2 and OMC-3. The past observations are shown in thin circles and squares, while the *Chandra* observation conducted in this thesis is in the thick squares. The contours are the 1.3 mm intensity (Chini et al. 1997<sup>[35]</sup>). (a) The FOVs of two *ASCA* observations (Yamauchi et al. 1996<sup>[196]</sup>). (b) The FOVs of three *ROSAT/HRI* observations (Geier, Wendker, & Wisotzki 1995<sup>[64]</sup>) and one *ROSAT/PSPC* observations (Gagné et al. 1995<sup>[61]</sup>).

Table 3.3: Past observations of OMC-2 and OMC-3

bands/lines	mode	observatory	reference
centimeter ...	3.6 cm	VLA	Reipurth et al. (1999) <sup>[162]</sup>
millimeter ...	3.6 cm	VLA	Tsujimoto et al. (2002c) <sup>[191]</sup> (this thesis)
	<sup>13</sup> CO	AT&T Bell Lab.	Bally et al. (1987) <sup>[14]</sup>
	1.3 mm	IRTF, IRAM	Metzger et al. (1990) <sup>[129]</sup>
	CS	NRO	Tatematsu et al. (1993) <sup>[179]</sup>
	C <sup>18</sup> O	AT&T Bell Lab.	Dutrey et al. (1993) <sup>[45]</sup>
	NH <sub>3</sub>	Effelsberg	Cesaroni & Wilson (1994) <sup>[31]</sup>
	<sup>13</sup> CO, C <sup>18</sup> O, C <sup>32</sup> S, C <sup>34</sup> S	SEST	Castets & Langer (1995) <sup>[30]</sup>
	1.3mm	IRAM	Chini et al. (1997) <sup>[35]</sup>
	H <sup>13</sup> CO <sup>+</sup> , HCO <sup>+</sup> , CO	NMA	Aso et al. (2000) <sup>[11]</sup>
	<sup>12</sup> CO	NRAO	Yu et al. (2000) <sup>[200]</sup>
	CO	BIMA	Williams et al. (2003) <sup>[194]</sup>
sub-millimeter	40–400 $\mu$ m	LJO, KAO, MLO	Thronson et al. (1978) <sup>[181]</sup>
	C I, C II	KAO	Herrmann et al. (1997) <sup>[84]</sup>
	350 $\mu$ m	CSO	Lis et al. (1998) <sup>[117]</sup>
	450 $\mu$ m, 850 $\mu$ m	JCMT	Johnstone & Bally (1999) <sup>[99]</sup>
	C I, CO	Mt. Fuji	Ikeda et al. (1999) <sup>[94]</sup>
	850 $\mu$ m	JCMT	Matthews & Wilson (2000) <sup>[124]</sup>
NIR–MIR ...	1.6–20 $\mu$ m	Wilson, Hale	Gatley et al. (1974) <sup>[63]</sup>
	K	Steward	Thronson & Thompson (1982) <sup>[182]</sup>
	1.25–100 $\mu$ m	IRTF, KAO	Pendleton et al. (1986) <sup>[149]</sup>
	J, H, K, L	WIRO	Johnson et al. (1990) <sup>[96]</sup>
	J, H, K	KPNO	Jones et al. (1994) <sup>[101]</sup>
	K	Perkins	Ali & DePoy (1995) <sup>[2]</sup>
	H <sub>2</sub>	KPNO, CTIO	Yu et al. (1997) <sup>[199]</sup>
	J, H, K <sub>s</sub>	2MASS	Carpenter (2000) <sup>[26]</sup>
	J, H, K <sub>s</sub>	2MASS	Carpenter et al. (2001b) <sup>[28]</sup>
	J, H, K, L', H <sub>2</sub>	Subaru, IRTF	Tsujimoto et al. (2002b) <sup>[190]</sup> (this thesis)
	J, H, K, H <sub>2</sub>	UH88	Tsujimoto et al. (2003) <sup>[192]</sup> (this thesis)
optical .....	V	Shanghai	Tian et al. (1996) <sup>[183]</sup>
	U, V, I	KPNO, WIYN	Rebull et al. (2000) <sup>[160]</sup>
X-ray .....	0.1–4.0 keV	<i>Einstein</i>	Gagné, & Caillault (1994) <sup>[60]</sup>
	0.1–2.4 keV	ROSAT	Geier et al. (1995) <sup>[64]</sup>
	0.2–2.0 keV	ROSAT	Gagné et al. (1995) <sup>[61]</sup>

(cont.)

bands/lines	mode	observatory	reference
0.5–8.0 keV	imaging, spectroscopy	<i>ASCA</i>	Yamauchi et al. (1996) <sup>[196]</sup>
0.5–8.0 keV	imaging, spectroscopy	<i>Chandra</i>	Tsuboi et al. (2001) <sup>[188]</sup>
			Tsujimoto et al. (2002a) <sup>[189]</sup> (this thesis)

**Table 3.4:** Past NIR survey studies of OMC-2 and OMC-3

reference	area (arcmin <sup>2</sup> )	region	band	completeness limit <sup>a</sup> (mag)	num. of sources
Jones et al. (1994) <sup>[101]</sup> .....	90	OMC-2	<i>J, H, K</i>	~14	219
Ali & DePoy (1995) <sup>[2]</sup> .....	1472	Trapezium, OMC-2	<i>K</i>	~14.5	3548
Carpenter (2000) <sup>[26]</sup> .....	.....	Orion A, B, etc.	<i>J, H, K<sub>s</sub></i>	~14.8	.....
Tsujimoto et al. (2003) <sup>[192]</sup> (this thesis)	512	OMC-2, OMC-3	<i>J, H, K</i>	~16.0	1448

<sup>a</sup> The 90% completeness limit in the *K* band, except for Carpenter (2000)<sup>[26]</sup> with the 94% limit.

**Table 3.5:** Past X-ray survey studies of OMC-2 and OMC-3

reference	area (arcmin <sup>2</sup> )	instrument	band (keV)	num. of sources
Gagné & Caillault (1994) <sup>[60]</sup> .....	16000	<i>Einstein/IPC</i>	0.1–4.0	245
Gagné et al. (1995) <sup>[61]</sup> .....	2900	<i>ROSAT/HRI</i>	0.2–2.0	389
Geier et al. (1995) <sup>[64]</sup> .....	1900	<i>ROSAT/HRI</i>	0.1–2.4	171
Yamauchi et al. (1996) <sup>[196]</sup> .....	3900	<i>ASCA/GIS, SIS</i>	0.5–8.0	52
Tsujimoto et al. (2002) <sup>[189]</sup> (this thesis)	360	<i>Chandra/ACIS</i>	0.5–8.0	398

# Chapter 4

## Observing Facilities and Instruments

### Contents

---

<b>4.1</b>	<b><i>Chandra X-ray Observatory</i></b> . . . . .	<b>68</b>
4.1.1	Spacecraft . . . . .	68
4.1.2	Optics . . . . .	69
4.1.3	Instrument (ACIS) . . . . .	73
<b>4.2</b>	<b>University of Hawaii 88 inch (2.2 m) Telescope</b> . . . . .	<b>79</b>
4.2.1	Telescope . . . . .	79
4.2.2	Instrument (QUIRC) . . . . .	82
<b>4.3</b>	<b>Subaru Telescope</b> . . . . .	<b>83</b>
4.3.1	Telescope . . . . .	83
4.3.2	Instrument (IRCS) . . . . .	83
<b>4.4</b>	<b>Infrared Telescope Facility</b> . . . . .	<b>85</b>
4.4.1	Telescope . . . . .	85
4.4.2	Instrument (NSFCam) . . . . .	85
<b>4.5</b>	<b>Very Large Array</b> . . . . .	<b>87</b>
4.5.1	Telescope . . . . .	87
4.5.2	Radio Interferometry . . . . .	89

---

In this chapter, we review on all telescopes and instruments that we used for this thesis. The first section is devoted for the *Chandra X-ray observatory* (Sect. 4.1), where we mention the basic features of the spacecraft, optics, and detectors. For detectors, ACIS onboard *Chandra*, which we actually used, is particularly focused. The following three sections are for NIR telescopes and instruments; QUIRC on the University of Hawaii 88 inch (2.2 m) telescope (Sect. 4.2), IRCS on the Subaru telescope (Sect. 4.3), and NSFCam on IRTF (Sect. 4.4). The last section deals with VLA (Sect. 4.5). Along with the properties of the array, the basic idea of radio interferometry is briefly reviewed.

## 4.1 *Chandra X-ray Observatory*

### 4.1.1 Spacecraft

The *Chandra X-ray Observatory* was successfully launched in July 1999 by National Aeronautics and Space Administration (NASA). The spacecraft circulates around the earth once in 64 hours on an elliptical orbit with the perigee and the apogee distance of 10000 km and 140000 km, respectively. It is comprised of several modules, including the solar panels, the mirror assembly, the telescope, and the integrated science instrument module (Fig. 4.1). Details of *Chandra* can be found in the *Chandra Proposers' Observatory Guide* (2001)<sup>[32]</sup>.

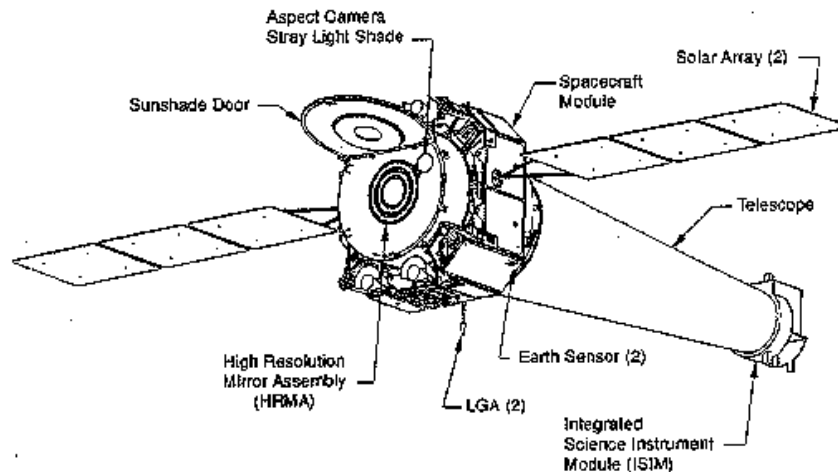


**Figure 4.1:** Schematic view of the *Chandra* spacecraft (*Chandra Proposers' Observatory Guide* 2001<sup>[32]</sup>).

The pointing accuracy of the spacecraft, which is measured and stabilized by the Point-



ing Control and Aspect Determination (PCAD) system, is  $\sim 0.1'' \text{ s}^{-1}$ . The *Chandra* line-of-sight is kept dithered during observations drawing a Lissajous pattern. The dithering distributes photons over many detector pixels for several purposes; to prevent a bad pixel to ruin the entire observation, to reduce uncertainty due to pixel-to-pixel variations in the quantum efficiency, to pick up sources in the gaps between CCD chips, and to allow sub-sampling of the image.

## 4.1.2 Optics

### Mirror Assembly

High Resolution Mirror Assembly (HRMA) is the mirror assembly carried on *Chandra*. It consists of a nested set of four paraboloid-hyperboloid (Wolter-1) grazing-incidence X-ray mirror pairs, with the focal length of  $\sim 10 \text{ m}$  and the largest mirror having a diameter of  $\sim 1.2 \text{ m}$  (Fig. 4.2). The most precisely shaped and aligned, and the smoothest X-ray mirrors ever constructed allow *Chandra* to obtain unprecedentedly sharp X-ray images.

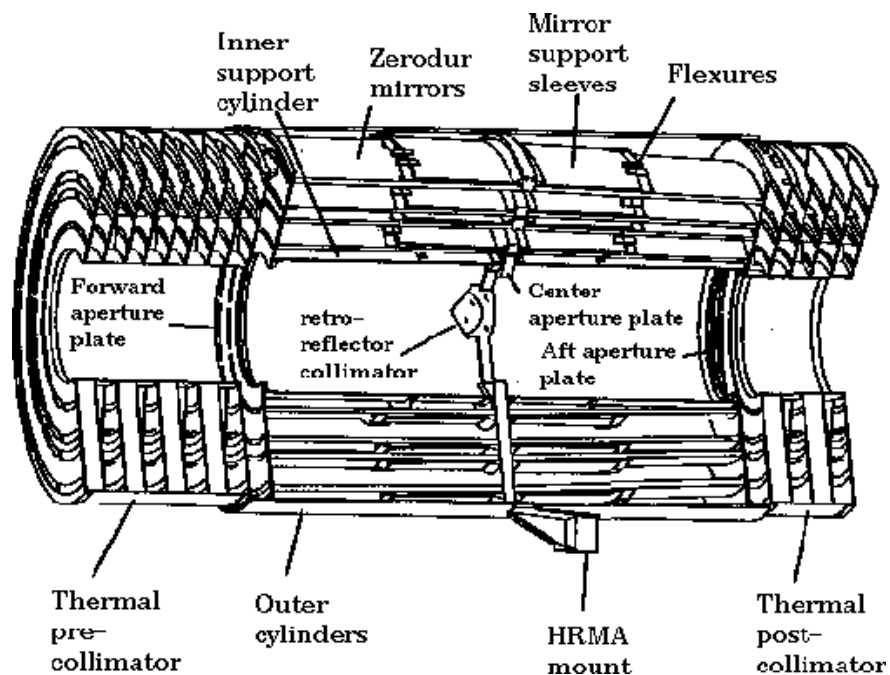


**Figure 4.2:** Configuration of four nested mirror pairs (*Chandra* Proposers' Observatory Guide 2001<sup>[32]</sup>).

## Effective Area

The on-axis effective area of HRMA is shown in Figure 4.3, together with the expected effective areas when the detector quantum efficiency is convolved. The effective area decreases as the increasing off-axis angle (the vignetting effect; Fig. 4.4) depending on the energy.

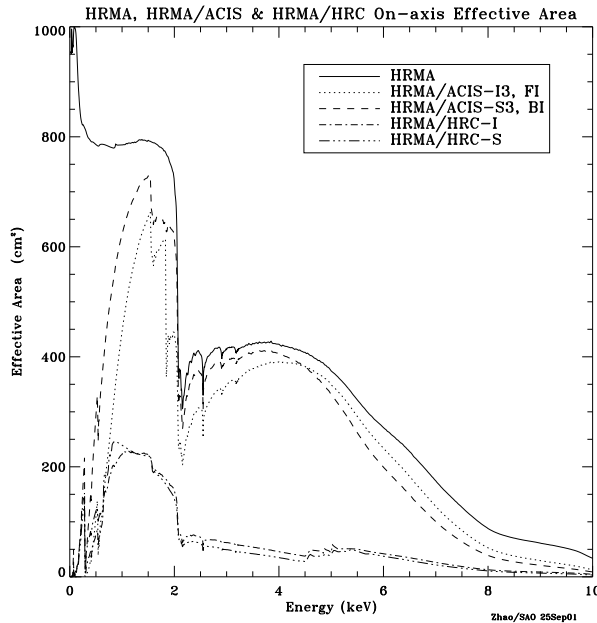


**Figure 4.3:** Energy dependence of the on-axis effective area of HRMA (*solid curve*). The expected effective areas convolved with the detector quantum efficiency are separately shown with dotted (front-illuminated ACIS), dashed (back-illuminated ACIS), dashed-and-dotted (HRC-I), and dashed-and-triplicated-dotted (HRC-S) curves (*Chandra Proposers' Observatory Guide 2001*<sup>[32]</sup>).

## Point Spread Function

The point spread function (PSF) is a spatial distribution function over the detector surface of incident X-ray photons at a given energy. The PSF is approximately shaped Gaussian. The sharpness of images is evaluated either by the full width half maximum (FWHM) or the encircled energy radius of PSFs. A circle of 50% encircled energy radius, which equals to the half of FWHM if the PSF is exactly Gaussian, accumulates the 50% of incident photons. Figure 4.5 gives the on-axis PSF, while Figure 4.6 shows the dependence of PSFs on the off-axis angle.

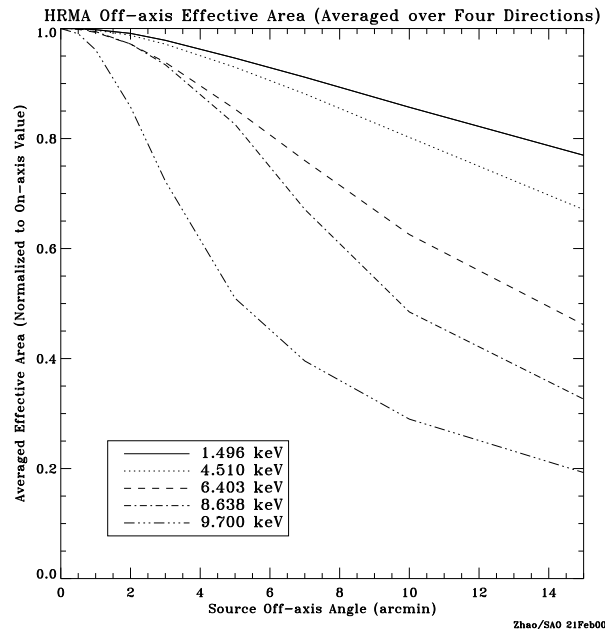


**Figure 4.4:** Spatial dependence of the effective area as a function of off-axis angle for several representative incident X-ray energies (*Chandra* Proposers' Observatory Guide 2001<sup>[32]</sup>).

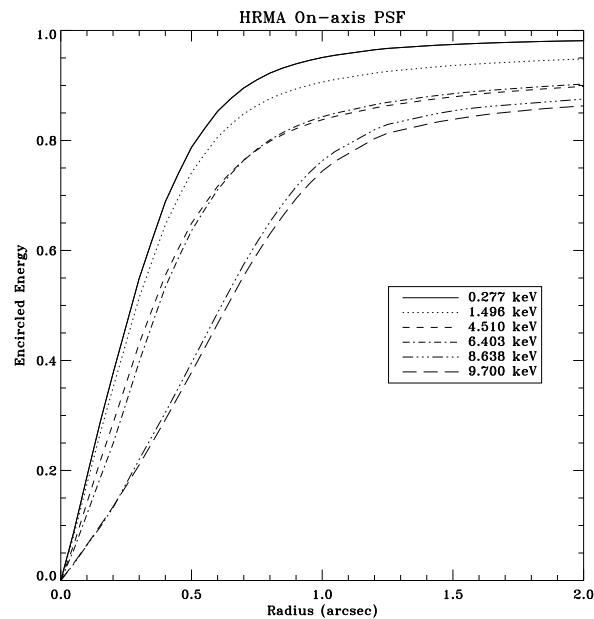


**Figure 4.5:** On-axis PSFs of several representative incident X-ray energies as a fraction of the encircled photons (energy) inside the circle with a given radius (*Chandra* Proposers' Observatory Guide 2001<sup>[32]</sup>).

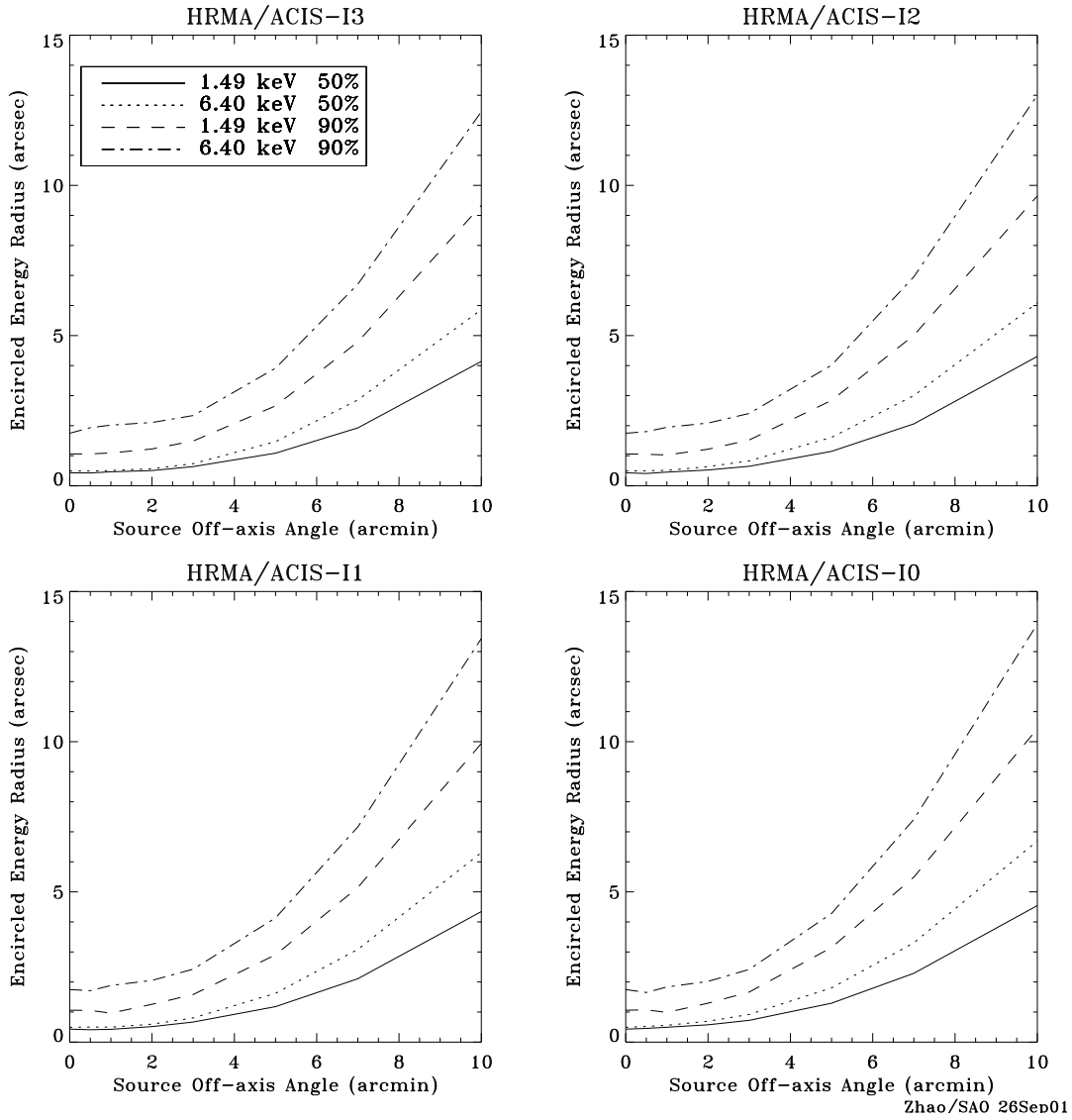


**Figure 4.6:** The 50% and 90% encircled energy radii at a given off-axis angle. The four panels give the radii of representative incident X-ray energies separately for ACIS-I0, -I1, -I2, and -I3 (*Chandra* Proposers' Observatory Guide 2001<sup>[32]</sup>).

### 4.1.3 Instrument (ACIS)

#### Configuration

Ten X-ray CCDs comprise the Advanced CCD Imaging Spectrometer (ACIS) array (Fig. 4.7). The array consists of two parts; ACIS-I with 2×2 CCDs (ACIS-I0, -I1, -I2, and -I3) and ACIS-S with 1×6 CCDs (ACIS-S0, -S1, -S2, -S3, -S4, and -S5), which are mainly used for the imaging-spectroscopic and the grating-spectroscopic purposes, respectively. The format of CCD chips is 1024×1024 pixels with the pixel scale of 0.492'' pixel<sup>-1</sup>. All CCDs utilize front-illuminated CCDs except for ACIS-S1 and ACIS-S3 that are back-illuminated CCDs.

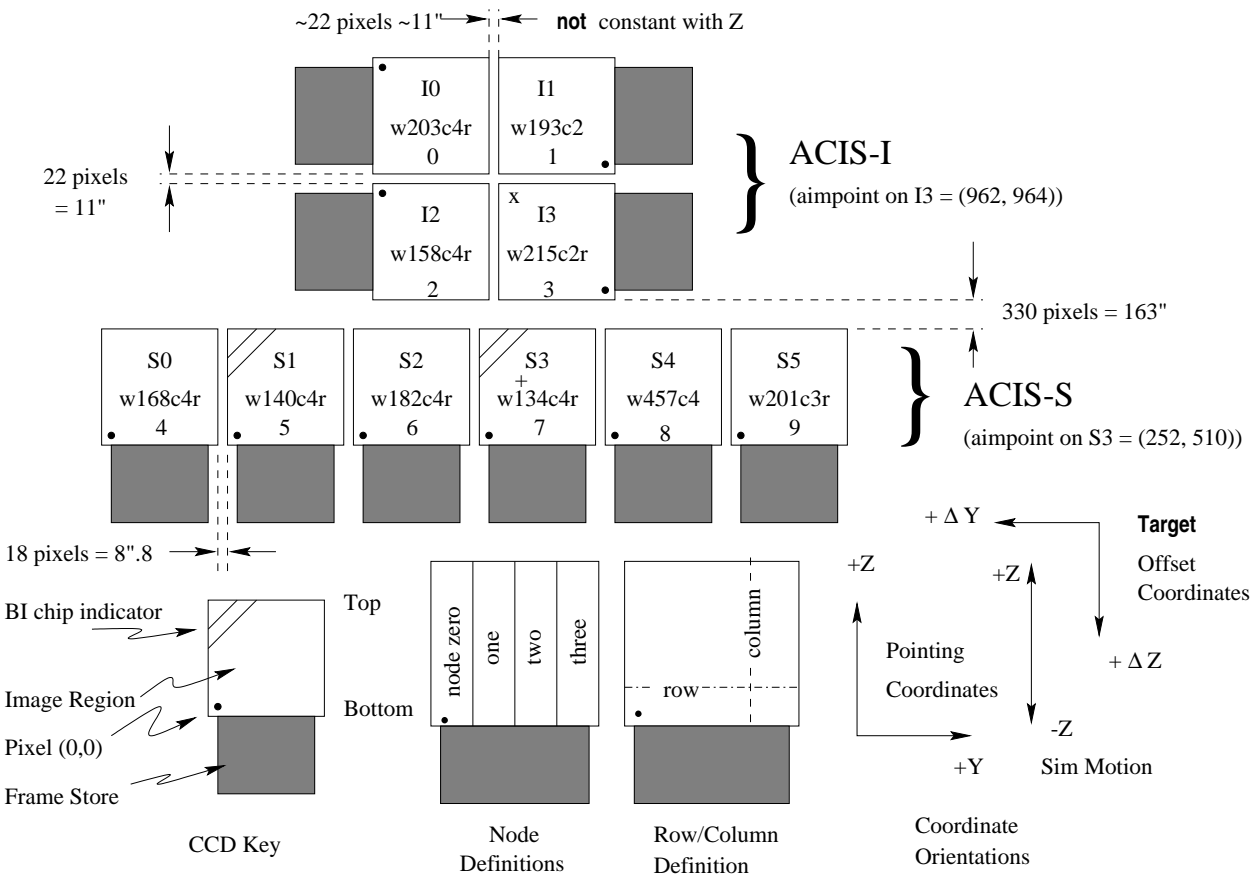


**Figure 4.7:** Configuration of the ACIS array. The top two panels show the ACIS-I and ACIS-S arrays, while the schematic view of each CCD chip is given at the bottom panel. In our observation, ACIS-I0, I1, I2, I3 and S2 were used with the aim point on the cross at the top left corner of ACIS-I3 (*Chandra* Proposers' Observatory Guide 2001<sup>[32]</sup>).

## Energy Resolution

An X-ray CCD can work as a medium-resolution ( $E/\Delta E = 10\text{--}50$ ) spectrometer as well as an imager. When an incident X-ray photon with the energy of  $E$  keV is photoelectrically absorbed by silicon atoms in the depletion layer of the device, it emits a photoelectron with the corresponding kinematic energy. The photoelectron keeps ionizing other atoms until all energy is consumed, which finally produces  $n = E/W$  electrons where  $W$  keV is the average energy required to ionize an atom. By measuring  $n$  with the device, the incident X-ray energy is determined on a photon basis. The energy resolution is determined by the convolution of the Poisson fluctuation of  $n$  and the readout noise (Fig. 4.8). In case of silicon ( $W = 3.65$  keV), the lower limit of the energy resolution is  $\sim 120$  eV at 6 keV.

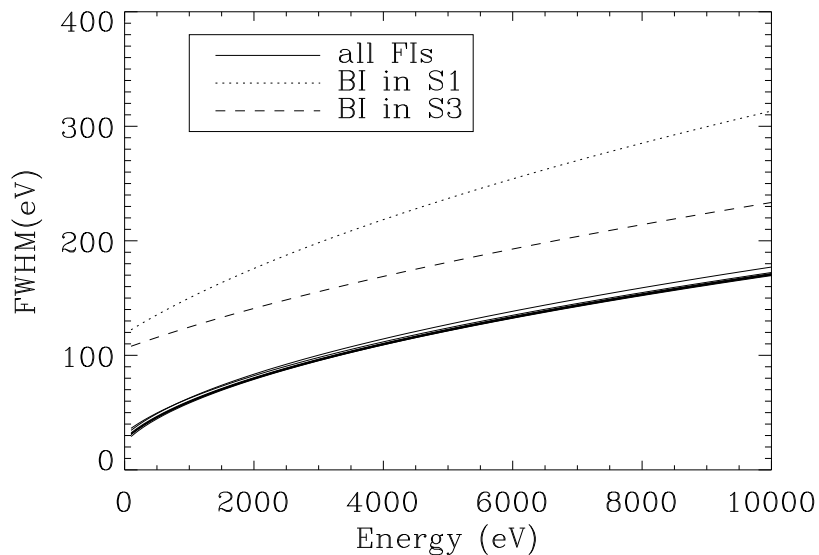


**Figure 4.8:** Pre-launch energy resolution of front-illuminated (*solid*), back-illuminated S1 (*dotted*), and S3 (*dashed*) chips (*Chandra* Proposers' Observatory Guide 2001<sup>[32]</sup>).

Unfortunately, the CCD chips onboard *Chandra* were damaged by charged particles on the orbit, degrading the energy resolution of ACIS. This is currently handled by lowering the temperature of the device to  $-110^{\circ}\text{C}$  (as of our observation date) and by introducing a new set of detector response functions.

### Effective Energy Range

Three factors are convolved to determine the energy range that an ACIS observation is sensitive to. The first factor is the quantum efficiency of the CCD chip itself. At higher energies, the efficiency is constrained by the thickness of the depletion layer, where X-ray photons with higher energy are more difficult to be photoelectrically absorbed. At lower energies, on the other hand, the efficiency is reduced by the absorption of X-ray photons by electrodes and insulators on the surface of the device. This makes back-illuminated chips to have higher quantum efficiency at lower energies than front-illuminated ones. The second factor is the transmission of the optical blocking filters (OBFs). ACIS has three OBFs with the thickness of 2000 Å (thick), 1200 Å (medium), and 400 Å (thin) to block photons in the optical wavelengths. Filters are composed of polyimide (a poly-carbonate plastic) sandwiched between two thin layers of aluminum. The third is the effective area of HRMA, which depends on the incident X-ray energy. Figure 4.9 shows the effective area of all these factors combined. In our observation, we used front-illuminated CCDs with the medium thickness filter, making our observation sensitive to X-ray photons in the 0.5–8.0 keV energy range.

### Background Events

The background events of ACIS are dominated by two components; cosmic ray (CR) events and the cosmic X-ray backgrounds (CXB). The CR events are reduced by various filtering procedures, including the grade filtering and the elimination of flaring events caused by CRs. A typical background spectrum after these procedures is given in Figure 4.10. The CR events are dominant in the lower energy band than 5 keV, while CXB in the higher energy band. The average count rate of this background spectrum is shown for some representative energy ranges (Table 4.1). The background count rate is roughly constant within a period of the same CCD temperature (Fig. 4.11). Unlike CXB, the rate of CR events also depend on the position on the chip (Fig. 4.12) by a factor of  $\sim 20\%$ .

### Other Detectors

High-Resolution Imager (HRI) is another focal plane instrument. HRI is comprised of two imaging detectors using micro-channel plates; High Resolution Camera (HRC)-I designed

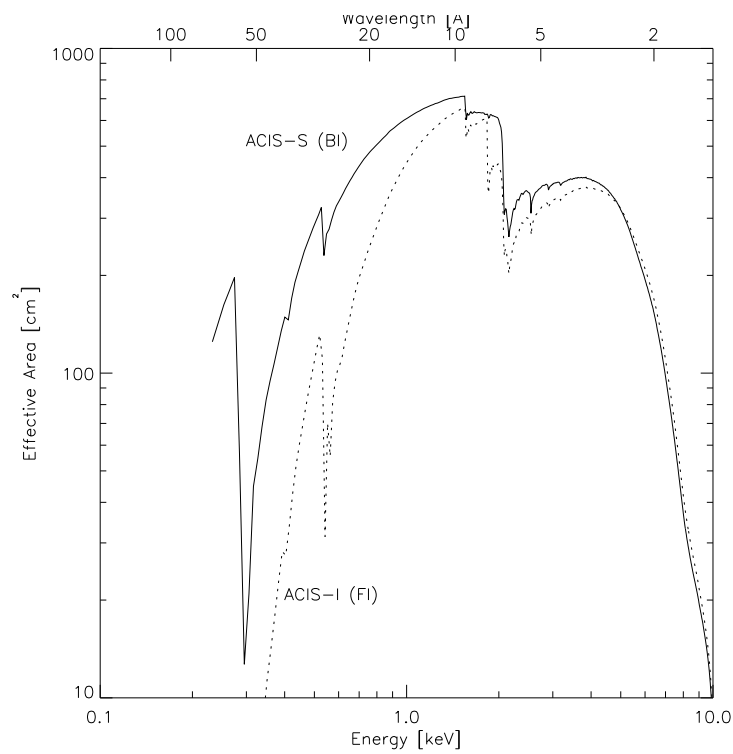


**Figure 4.9:** Expected effective area of ACIS with the dotted (front-illuminated chips) and the solid (back-illuminated chips) curves. The quantum efficiency, the filter transmission, and the effective area of the optical system are all combined (*Chandra* Proposers' Observatory Guide 2001<sup>[32]</sup>).



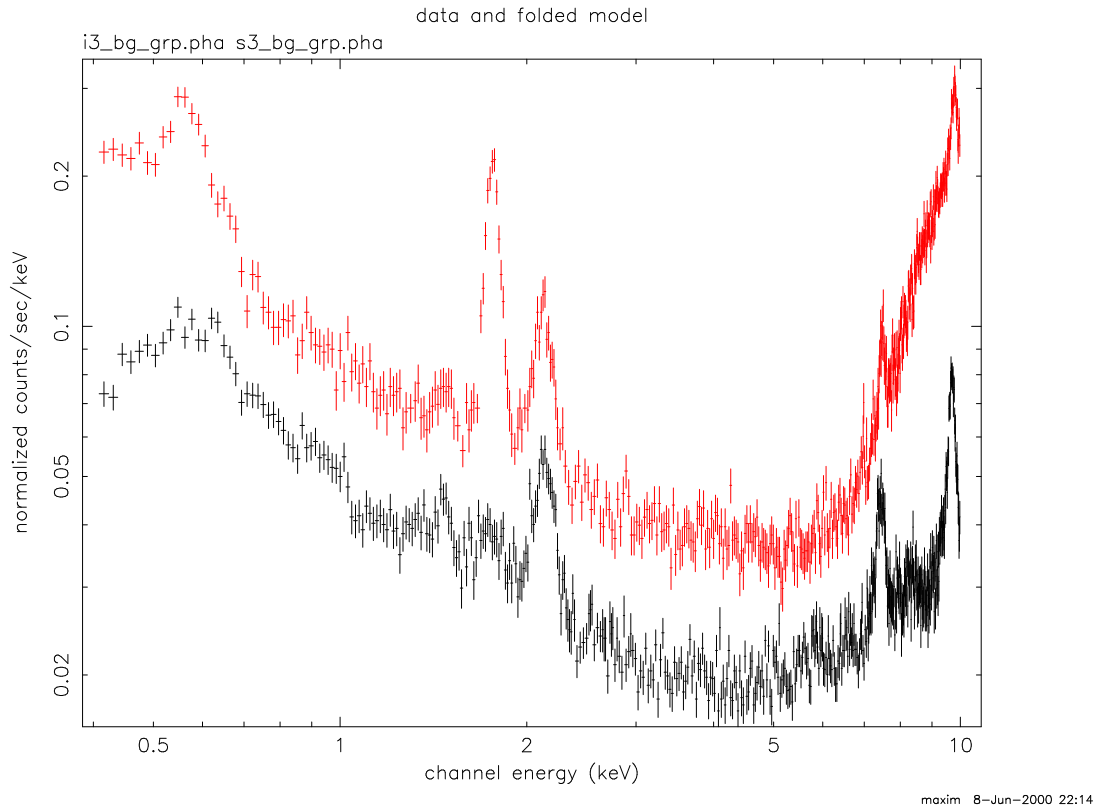


**Figure 4.10:** Background spectra of the back-illuminated ACIS-S3 chip (the upper spectrum) and the front-illuminated ACIS-I3 (the lower spectrum) chip. The spectra, containing both the CR and CXB components, are extracted from the whole relevant chips from the September 1999 – January 2000 data. The events with bad grades, bad pixels and bright celestial sources are eliminated (Markevitch 2001<sup>[121]</sup>).

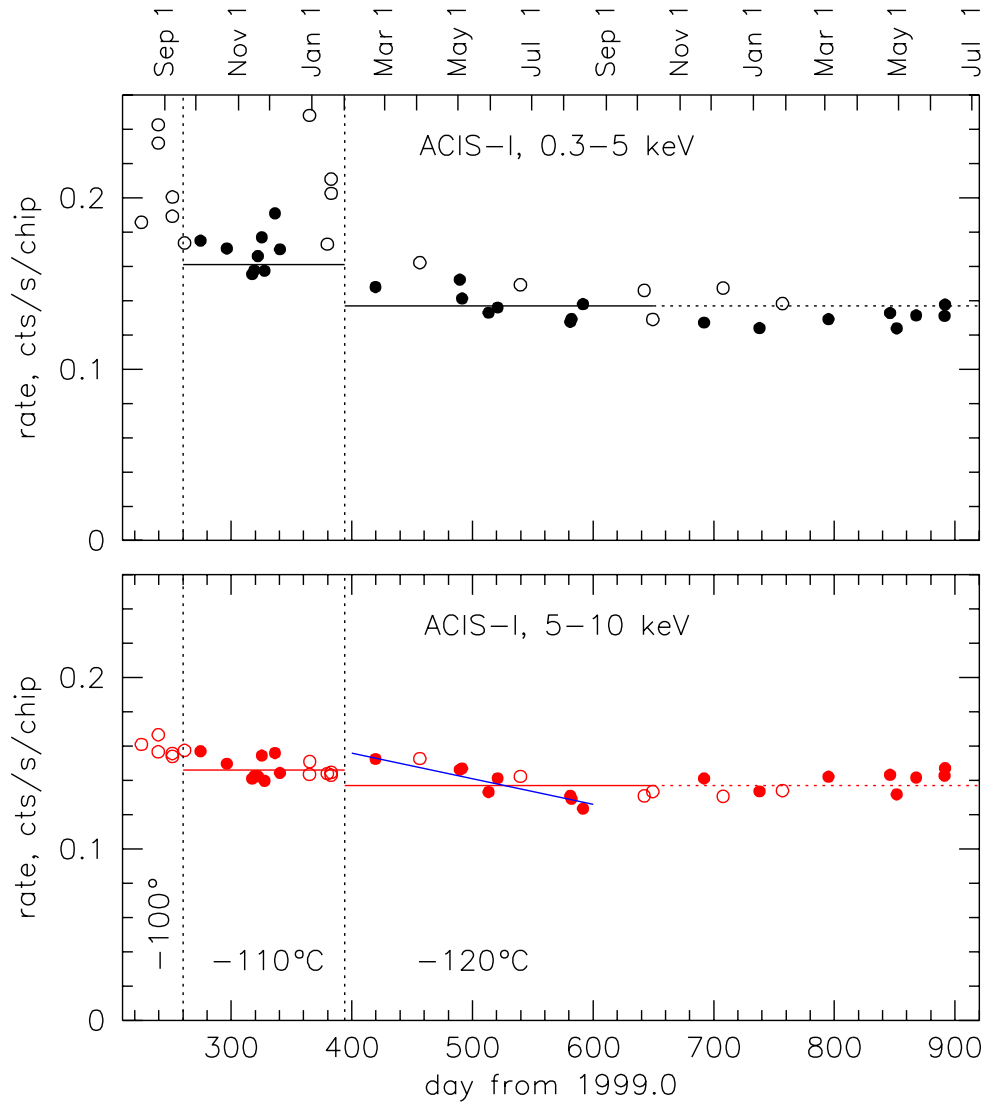


**Figure 4.11:** Long-term variation of background count rates of ACIS. The top panel shows the count rate of 0.3–5 keV that represents the CR component, while the bottom shows the rate of 5–10 keV that represents CXB. The CCD temperature is given at each period (Markevitch 2001<sup>[121]</sup>).

**Table 4.1:** Background count rate ( $\text{s}^{-1}$ ) of *Chandra* ACIS chips for five representative energy ranges (Markevitch 2001<sup>[121]</sup>). The rates in 0.5–8 keV were estimated using these values and the standard background spectrum (Figure 4.10).

chip	I2 <sup>a</sup>	I3 <sup>a</sup>	S1 <sup>b</sup>	S2 <sup>a</sup>	S3 <sup>b</sup>
0.3–10 keV	0.321	0.310	1.483	0.336	0.857
0.5–2 keV	0.083	0.076	0.168	0.086	0.160
0.5–7 keV	0.196	0.188	0.454	0.207	0.375
5–10 keV	0.153	0.154	1.038	0.162	0.506
10–12 keV	0.087	0.087	0.674	0.081	0.603
0.5–8 keV	0.226	0.220	.....	0.239	.....

<sup>a</sup> Front-illuminated chips.

<sup>b</sup> Back-illuminated chips.

for wide-field imaging and HRC-S designed to serve as a readout for the Low Energy Transmission Grating (LETG). HRI has no spectral resolution, but provides better temporal resolution than ACIS.

Each of the two instruments (ACIS and HRI) can be combined with one of the two gratings to conduct high-resolution ( $E/\Delta E \sim 100\text{--}1000$ ) spectroscopy. High Energy Transmission Grating (HETG) and LETG are respectively optimized for grating spectroscopy of the high and low energy X-rays.

## 4.2 University of Hawaii 88 inch (2.2 m) Telescope

### 4.2.1 Telescope

The University of Hawaii 88 inch (2.2 m) telescope (UH88) is one of the telescopes at the summit of Mauna Kea, Hawaii, U.S.A. It was constructed in 1970 and has been under operation of the University of Hawaii. The telescope utilizes the Ritchey-Crétien optics system and has the Cassegrain focus. The primary mirror has a diameter of 88.13 inch (2.24 m) with the focal length of 22.50 m (Fig. 4.13).

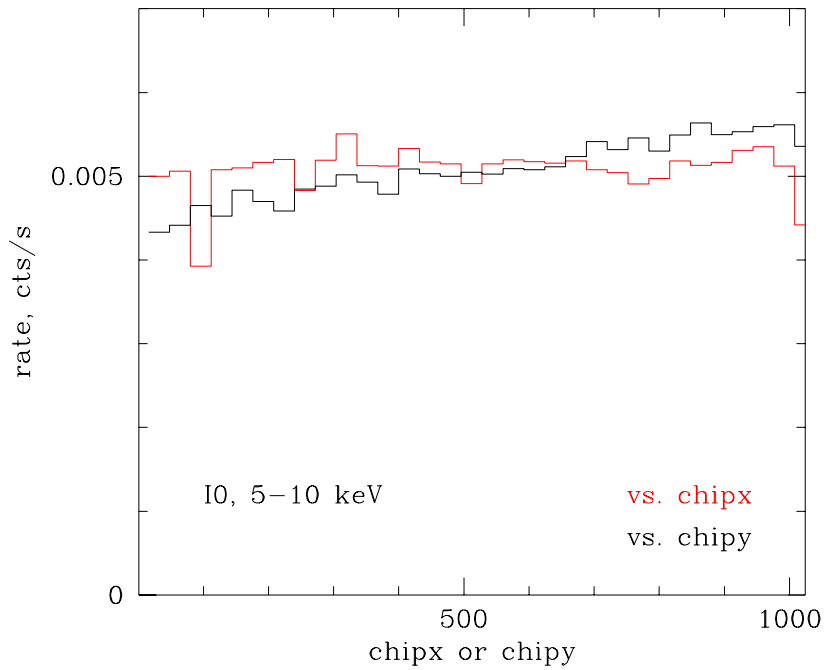


**Figure 4.12:** Spatial dependence of the background count rate of ACIS-I0. The profiles on the x-axis (*dotted*) and y-axis (*solid*) are shown. The count rate in the 5–10 keV range is used, where the CR component is dominant. The CXB component has no spatial dependence (Markevitch 2001<sup>[121]</sup>).

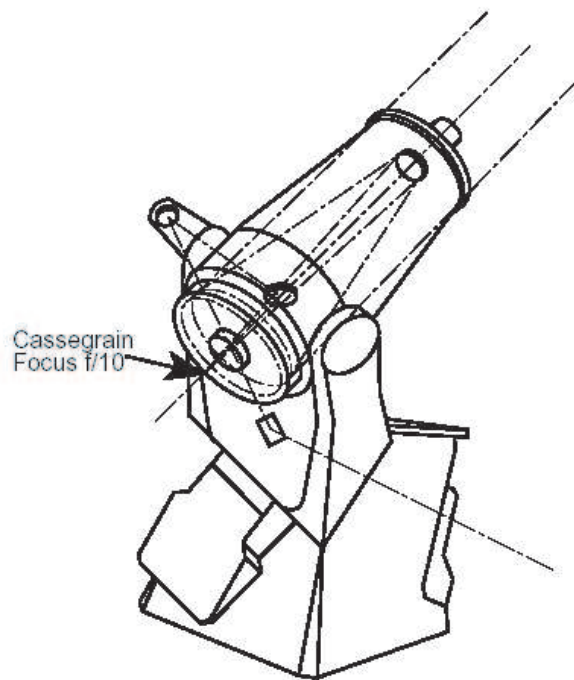


**Figure 4.13:** Schematic view of the University of Hawaii 88 inch (2.2 m) telescope. QUIRC is mounted on the Cassegrain focus of the telescope.

## 4.2.2 Instrument (QUIRC)

Quick Infrared Camera (QUIRC; Hodapp, Hora, & Metzger 1997<sup>[89]</sup>) is the only NIR camera mounted on the Cassegrain focus of the telescope. QUIRC has a HAWAII (HgCdTe Astronomical Wide Area Infrared Imaging) array produced by Rockwell Science Center. It consists of four quadrants, each of which has the format of  $512 \times 512$  pixels with the pixel size of  $18.5 \mu\text{m} \times 18.5 \mu\text{m}$ . It has two optics with different focal lengths ( $f/10$  and  $f/31$ ), which yields the pixel scale of  $0.1886'' \text{ pixel}^{-1}$  and  $0.0608'' \text{ pixel}^{-1}$ , and the FOV of  $193'' \times 193''$  and  $62'' \times 62''$ , respectively. In our observation, we used the  $f/10$  optics to maximize FOVs.

QUIRC is sensitive to the radiation from  $1 \mu\text{m}$  to  $2.5 \mu\text{m}$ . Two filter wheels with eight positions are combined to observe either in the broad-band ( $J$ ,  $H$ ,  $K$ ,  $K_s$ ,  $K'$ , and  $HK'$ ) or in the narrow-band ( $\text{H}_2 v = 1 - 0 \text{ S}(1)$ , Fe II, CO band head, Br  $\gamma$ , and their neighboring continuum). We used three broad-band ( $J$ ,  $H$ , and  $K$ ) and two narrow-band ( $\text{H}_2 v = 1 - 0 \text{ S}(1)$  at  $2.12 \mu\text{m}$  and  $K$ -continuum at  $2.26 \mu\text{m}$ ) filters. The transmissions of these filters are given in Figure 4.14.

The effective gain of the detector is  $1.85 \text{ electrons ADU}^{-1}$  and the linearity is kept better than 1% for values up to  $\sim 44000 \text{ ADUs}$ . The average detector dark current is  $\leq 0.8 \text{ electrons s}^{-1}$  and the readout noise is  $\leq 15 \text{ electrons (r.m.s.)}$ . The camera sensitivity is  $\sim 18.6 \text{ mag}$  ( $J$  band),  $\sim 17.8 \text{ mag}$  ( $H$  band), and  $\sim 16.2 \text{ mag}$  ( $K$  band), assuming one minute on-source integration time, a PSF of  $0.5''$  FWHM, and  $5 \sigma$  detection.

**Table 4.2:** Comparison of NIR imagers used in this thesis

telescopes .....	UH88	Subaru	IRTF
instruments .....	QUIRC	IRCS	NSFCam
format (pixels) .....	$1024 \times 1024$	$1024 \times 1024$	$256 \times 256$
pixel scale ( $'' \text{ pixel}^{-1}$ )	0.189	0.058	0.15
FOV ( $''$ ) .....	$193 \times 193$	$59.4 \times 59.4$	$76.8 \times 76.8$
filters used .....	$J, H, K, \text{H}_2, K\text{-cont.}$	$J, H, K, \text{H}_2, K\text{-cont.}$	$L'$
sensitivity (mag) <sup>a</sup> .....	$\sim 16$	$\sim 18$	$\sim 17$

<sup>a</sup> The  $5 \sigma$  detection limit in the  $K$  band with one minute on-source integration time.

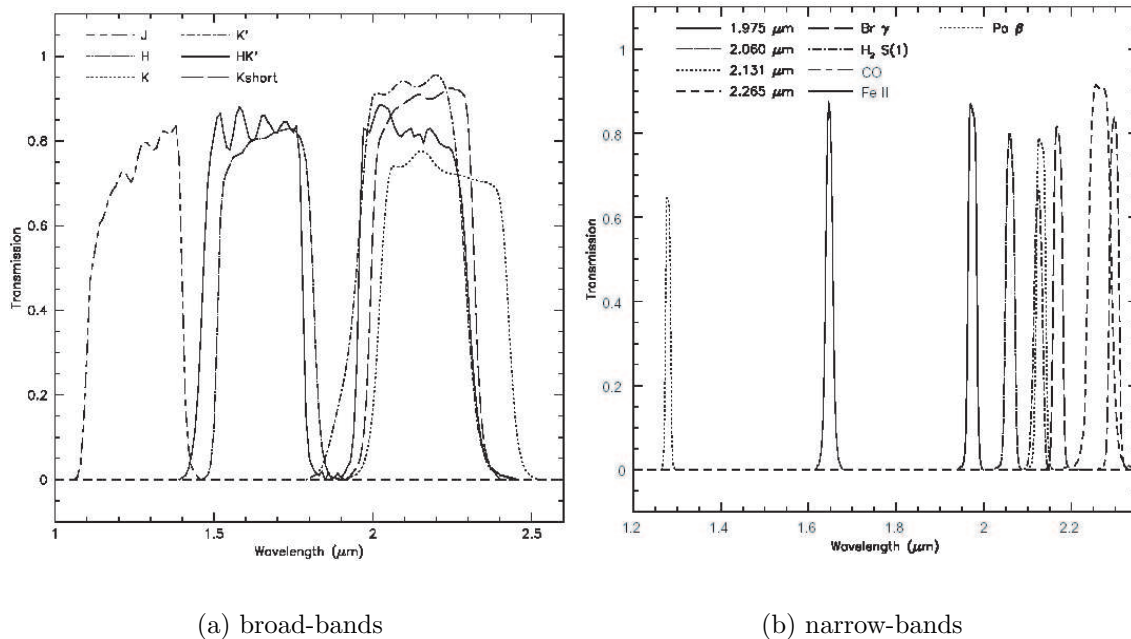


Figure 4.14: Transmissions of QUIRC filters; (a) broad-band and (b) narrow-band filters.

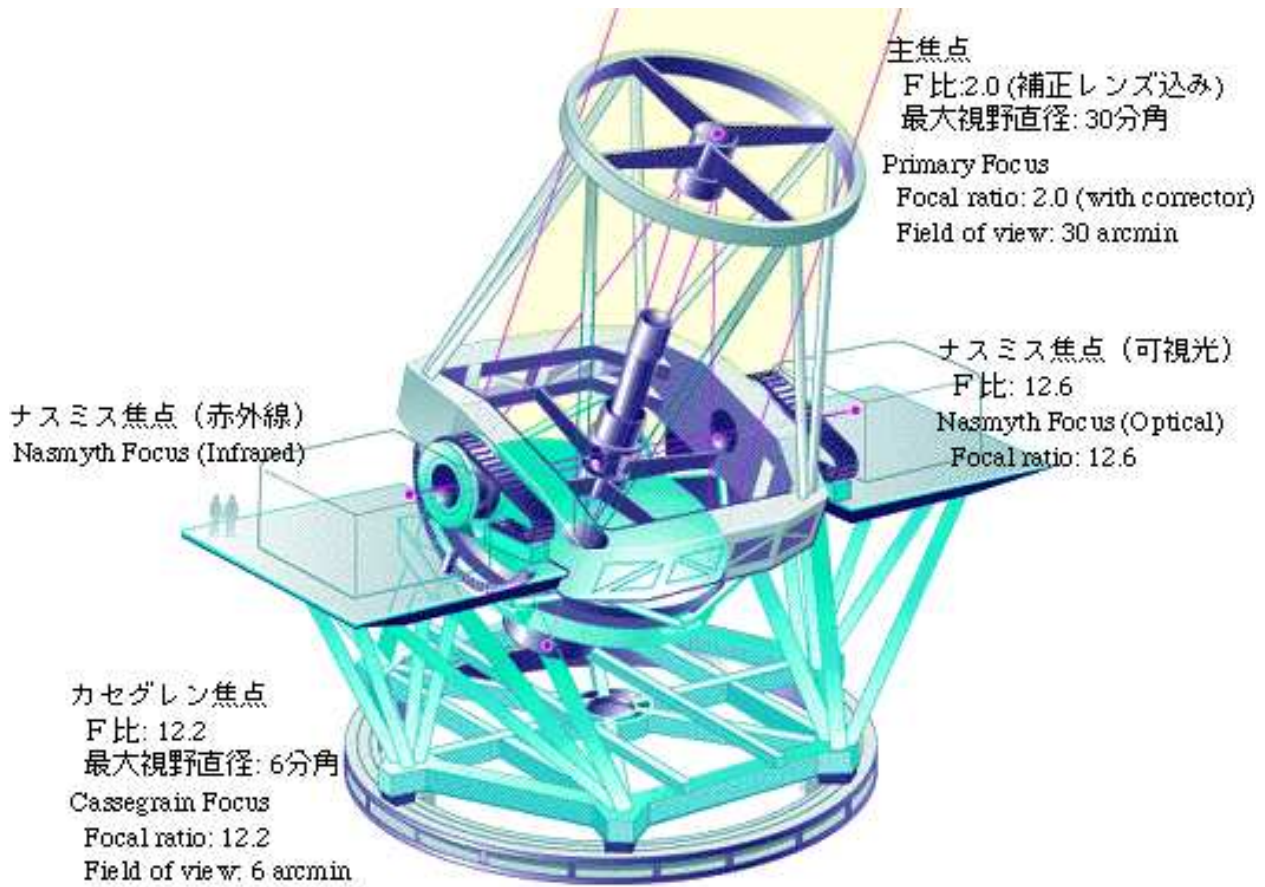
## 4.3 Subaru Telescope

### 4.3.1 Telescope

The Subaru telescope is also at the summit of Mauna Kea. It celebrated the first light in early 1999 and has been operated by National Astronomy Observatory of Japan (NAOJ). The telescope has the alto-azimuth mounting with four foci; the prime focus, the Cassegrain focus, and two Nasmyth foci for optical and infrared detectors (Fig. 4.15). It has the largest primary mirror among all the single mirrors facilitated in the telescopes around the world, with the diameter of 8.2 m and the focal length of 15 m.

### 4.3.2 Instrument (IRCS)

Infrared Camera and Spectrograph (IRCS) is a NIR imager and spectrometer for wide variety of usage (Tokunaga et al. 1998<sup>[184]</sup>; Kobayashi et al. 2000<sup>[105]</sup>). It has two ALADDIN II 1024 $\times$ 1024 pixel InSb arrays; one is for the imaging and the grism spectroscopy and the



遠藤孝悦・画 日経サイエンス1996年2月号より  
 Illustration by Takaetsu Endo, taken from *Nikkei Science* 1996

**Figure 4.15:** Schematic view of the Subaru telescope. IRCS is mounted on the Cassegrain focus of the telescope.



other for the echelle spectroscopy observations.

As an imager, it has two pixel scales of  $0.058'' \text{ pixel}^{-1}$  and  $0.023'' \text{ pixel}^{-1}$  with the corresponding FOV of  $59.4'' \times 59.4''$  and  $23.6'' \times 23.6''$ . They are optimized to be used with the tip-tilt and adaptive optics, respectively. The detector is sensitive at  $0.9\text{--}5.5 \mu\text{m}$  with the filters of  $J$ ,  $H$ ,  $K'$ ,  $K$ ,  $L'$ , and  $M'$  for the broad-band, and Fe II, Br  $\alpha$ , Br  $\gamma$ , H<sub>2</sub>  $v = 1 - 0 \text{ S}(1)$ ,  $2 - 1 \text{ S}(1)$ , etc. and their neighboring continuum for the narrow-band. The transmissions of broad-band filters are shown in Figure 4.16.

The detector gain is  $12.2 \text{ electrons ADU}^{-1}$  and the linearity is kept up to  $\sim 136000 \text{ ADUs}$ . The dark current and the readout noise are  $0.2\text{--}0.3 \text{ electrons s}^{-1}$  and  $67 \text{ electrons (r.m.s.)}$ , respectively. We used non-destructive readouts to decrease readout noise. The camera attains  $J \sim 23.6 \text{ mag}$ ,  $H \sim 22.8 \text{ mag}$ , and  $K \sim 22.3 \text{ mag}$  with one-hour integration time, a PSF of  $0.5'' \text{ FWHM}$ , and  $5 \sigma$  detection. In this observation, we used the ALLADIN II for the camera array, which was replaced with the ALLADIN III array with much superior sensitivity in September 2001.

IRCS camera also serves as a grism spectrograph providing a spectral resolving power of  $R = 100\text{--}2000$ . IRCS also has a separated echelle spectrograph providing a spectral resolving power of  $R = 5000\text{--}20000$ .

## 4.4 Infrared Telescope Facility

### 4.4.1 Telescope

The Infrared Telescope Facility (IRTF) is located at the summit of Mauna Kea. It is constructed in 1979 and is operated for NASA by the University of Hawaii. IRTF is optimized for NIR observations. It has the primary mirror of the  $3.0 \text{ m}$  in aperture and the Cassegrain focus.

### 4.4.2 Instrument (NSFCam)

NSFCam (Leggett & Denault 1996<sup>[115]</sup>) is a NIR camera mounted on the Cassegrain focus of the telescope. It employs an InSb array with the format of  $256 \times 256$  pixels. Three different magnifications can be selected that respectively yield the pixel scale of  $0.3'' \text{ pixel}^{-1}$ ,

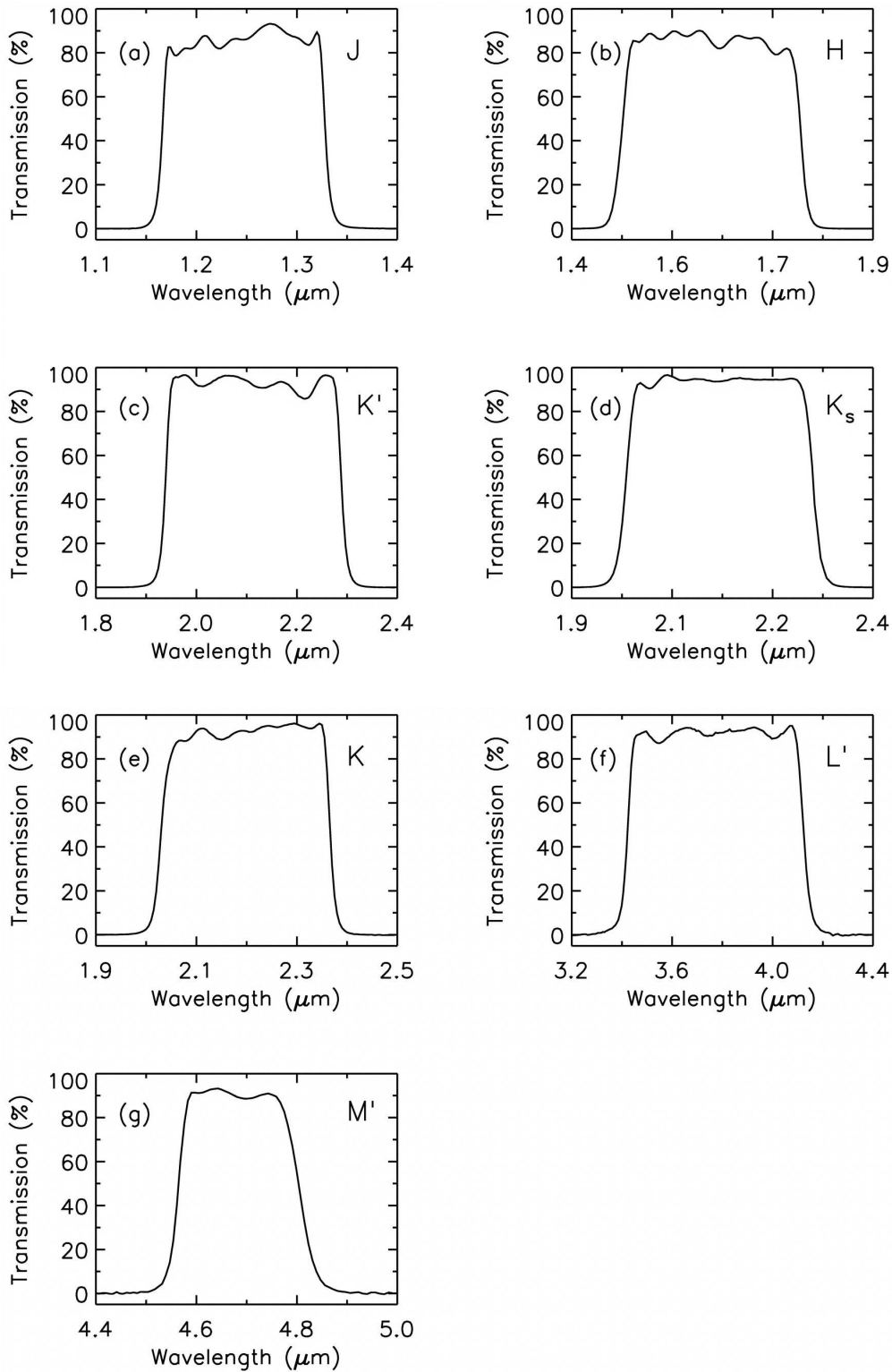


**Figure 4.16:** Broad-band filter transmissions of the Mauna Kea system advocated by Tokunaga, Simons, & Vacca (2002)<sup>[186]</sup>. Subaru IRCS and IRTF NSFCam comply with the system.

0.15'' pixel<sup>-1</sup> and 0.06'' pixel<sup>-1</sup> with the corresponding FOVs of 76.8''×76.8'', 37.9''×37.9'', and 14.1''×14.1''.

NSFCam has the sensitivity in 1–5 μm. By rotating its filter wheel, broad-band (*J*, *H*, *K*, *K'*, *L*, *L'*, and *M*) and narrow-band (He I, Fe II, H<sub>2</sub> *v* = 1 – 0 S(1), *v* = 2 – 1 S(1), CO band-head and their neighboring continuum) filters can be selected. We obtained the *L'*-band images with the pixel scale of 0.3'' pixel<sup>-1</sup> to complement the *J*-, *H*-, and *K*-band images taken with the Subaru telescope. The filters also comply with the Mauna Kea filter system (Fig. 4.16).

The camera can detect *J* ~ 20.6 mag, *H* ~ 18.9 mag, *K* ~ 18.8 mag, and *L'* = 13.6 mag with one-minute integration time, an aperture of 2''×2''box, and 3 σ detection.

## 4.5 Very Large Array

### 4.5.1 Telescope

Very Large Array (VLA) is the radio interferometer on Plains of San Agustin, New Mexico, U.S.A. It celebrated its first fringe in February 1976 and has been operated by National Radio Astronomy Observatory (NRAO). The interferometer consists of 27 antennae, which collaborate together for interferometry observations. The antennae have the size of 25 m in diameter and are positioned in the “Y” shape with nine antennae on each arm (Fig. 4.17).

Four configurations (A, B, C, and D) with different arm lengths are available and the configuration changes once in four months. The longer arm length configurations have longer baselines (distances between two antennae), thus have higher spatial resolution but are less sensitive to extended structures (Table 4.3). At the Cassegrain focus of each antenna, receivers in eight frequency bands are equipped (Table 4.4). Our observation was performed in 3.6 cm with the A configuration. Details on the radio interferometry and VLA can be found in Clark (1999)<sup>[36]</sup>, Thompson (1999)<sup>[180]</sup>, Napier (1999)<sup>[140]</sup>, Rommey (1999)<sup>[166]</sup>, and Perley & Taylor (2002)<sup>[151]</sup>.

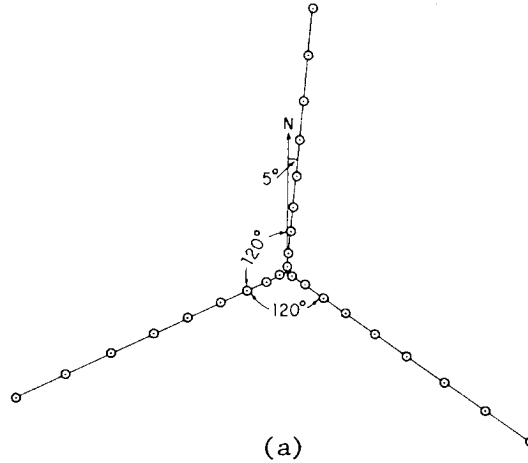


**Figure 4.17:** Configuration of VLA. The 27 antennae are laid out in the “Y” shape with the appropriate spacing to optimize the efficiency of  $u - v$  coverage.

**Table 4.3:** VLA configurations

configuration .....	A	B	C	D
min. baseline (km) .....	0.68	0.21	0.035	0.035
max. baseline (km) .....	36.4	11.4	3.4	1.03
synthesized beam width (") <sup>a</sup>	0.24	0.7	2.3	8.4

<sup>a</sup> The half power beam width at 3.6 cm.

**Table 4.4:** VLA frequency bands

band	frequency (Hz)	wavelength (cm)	resolution <sup>a</sup> (")
4	0.073–0.0745	400	24.0
P	0.30–0.34	90	6.0
L	1.34–1.73	20	1.4
C	4.5–5.0	6	0.4
X	8.0–8.8	3.6	0.24
U	14.4–15.4	2	0.14
K	22–24	1.3	0.08
Q	40–50	0.7	0.05

<sup>a</sup> The synthesized beam width of the A configuration.

### 4.5.2 Radio Interferometry

Let us suppose that the surface brightness of a celestial source is  $\epsilon_\nu(\mathbf{R})$  at the position of  $\mathbf{R}$  and at the frequency of  $\nu$ . The quasi-monochromatic component of the electric field that we receive at the position of  $\mathbf{r}$  can be expressed as

$$E_\nu(\mathbf{r}) = \int_S d\mathbf{R} \epsilon_\nu(\mathbf{R}) \frac{\exp(2\pi i\nu|\mathbf{R} - \mathbf{r}|/c)}{|\mathbf{R} - \mathbf{r}|}, \quad (4.1)$$

by integrating  $\epsilon_\nu(\mathbf{R})$  over the source region ( $S$ ). The spatial coherence function is defined as the product of  $E_\nu(\mathbf{r})$  at two different positions ( $\mathbf{r}_1$  and  $\mathbf{r}_2$ );

$$\begin{aligned} V_\nu(\mathbf{r}_1, \mathbf{r}_2) &= \langle E_\nu(\mathbf{r}_1)E_\nu(\mathbf{r}_2) \rangle \\ &= \left\langle \int_S d\mathbf{R}_1 \int_S d\mathbf{R}_2 \epsilon_\nu(\mathbf{R}_1)\epsilon_\nu^*(\mathbf{R}_2) \right. \\ &\quad \times \left. \left( \frac{\exp(2\pi i\nu|\mathbf{R}_1 - \mathbf{r}_1|/c)}{|\mathbf{R}_1 - \mathbf{r}_1|} \right) \left( \frac{\exp(-2\pi i\nu|\mathbf{R}_2 - \mathbf{r}_2|/c)}{|\mathbf{R}_2 - \mathbf{r}_2|} \right) \right\rangle. \end{aligned} \quad (4.2)$$

The surface brightness of the celestial source can be assumed to be coherent with each other at different positions with  $\langle \epsilon(\mathbf{R}_1)\epsilon(\mathbf{R}_2) \rangle \propto \delta(\mathbf{R}_1 - \mathbf{R}_2)$ . We can make a further approximation of  $1/|\mathbf{R} - \mathbf{r}| \approx 1/|\mathbf{R}|$  to transform the spatial coherence function into

$$V_\nu(\mathbf{r}_1, \mathbf{r}_2) = \int_S d\Omega I_\nu(\mathbf{s}) \exp(-2\pi i\nu\mathbf{s} \cdot (\mathbf{r}_1 - \mathbf{r}_2)/c), \quad (4.3)$$

where  $\mathbf{s} = \mathbf{R}/|\mathbf{R}|$ ,  $d\mathbf{R} = |\mathbf{R}|^2 d\Omega$ , and  $I_\nu(\mathbf{s}) = |\mathbf{R}|^2 \langle |\epsilon_\nu(\mathbf{s})|^2 \rangle$ . We introduce a new metric so that  $\mathbf{r}_1 - \mathbf{r}_2 = \lambda(u, v, w)$  in order to measure lengths in the unit of the wavelength;  $\lambda = c/\nu$ . By setting the  $w$ -axis in the direction of  $\mathbf{r}_1 \times \mathbf{r}_2$ ,  $w = 0$ . Then,

$$\begin{aligned} V_\nu(u, v) &= \int du' \int dv' I_\nu(u', v') \frac{\exp(-2\pi i(uu' + vv'))}{\sqrt{(1 - u'^2 - v'^2)}} \\ &\approx \int du' \int dv' I_\nu(u', v') \exp(-2\pi i(uu' + vv')). \end{aligned} \quad (4.4)$$

Here,  $\sqrt{(1 - u'^2 - v'^2)} \approx 1$  is assumed for simplicity. By considering the vignetting effect  $A_\nu(u', v')$  of the telescope,

$$V_\nu(u, v) = \int du' \int dv' A_\nu(u', v') I_\nu(u', v') \exp(-2\pi i(uu' + vv')). \quad (4.5)$$

The surface brightness distribution of the source  $I_\nu(u, v)$  is thus derived by Fourier-converting  $V_\nu(u, v)$ .

When the spatial coherence function is applied to the simplest interferometer with two antennae at  $\mathbf{r}_1$  and  $\mathbf{r}_2$ , the visibility function is obtained as

$$V = |V| \exp(i\phi) \quad (4.6)$$

$$= \int_S d\Omega A(\mathbf{s}') I(\mathbf{s}') \exp(-2\pi i \nu \mathbf{b} \cdot \mathbf{s}' / c), \quad (4.7)$$

where  $\mathbf{b} = \mathbf{r}_1 - \mathbf{r}_2$  is the baseline vector in the  $u$ - $v$  plane and  $\mathbf{s}' = \mathbf{s} - \mathbf{s}_0$  with  $\mathbf{s}_0$  being the unit vector pointing at the phase tracking center.

The value of the visibility function over the  $u$ - $v$  plane can be obtained through the correlator outputs. The correlator multiplies the voltages from two antennae ( $V_1(t)$  and  $V_2(t)$ ) and integrates it for a given period of time ( $T$ ). As  $V_1(t)$  and  $V_2(t)$  have different phases stemming from their geometrical distance to the source;

$$V_1(t) = V_1 \cos(2\pi\nu(t - \mathbf{b} \cdot \mathbf{s}/c)) \quad (4.8)$$

$$V_2(t) = V_2 \cos(2\pi\nu t). \quad (4.9)$$

The correlator output is described as

$$\begin{aligned} r &\propto \frac{1}{T} \int_0^T dt V_1(t) V_2(t) \\ &\longrightarrow V_1 V_2 \cos(2\pi\nu \mathbf{b} \cdot \mathbf{s}/c) \quad (T \longrightarrow \infty) \end{aligned} \quad (4.10)$$

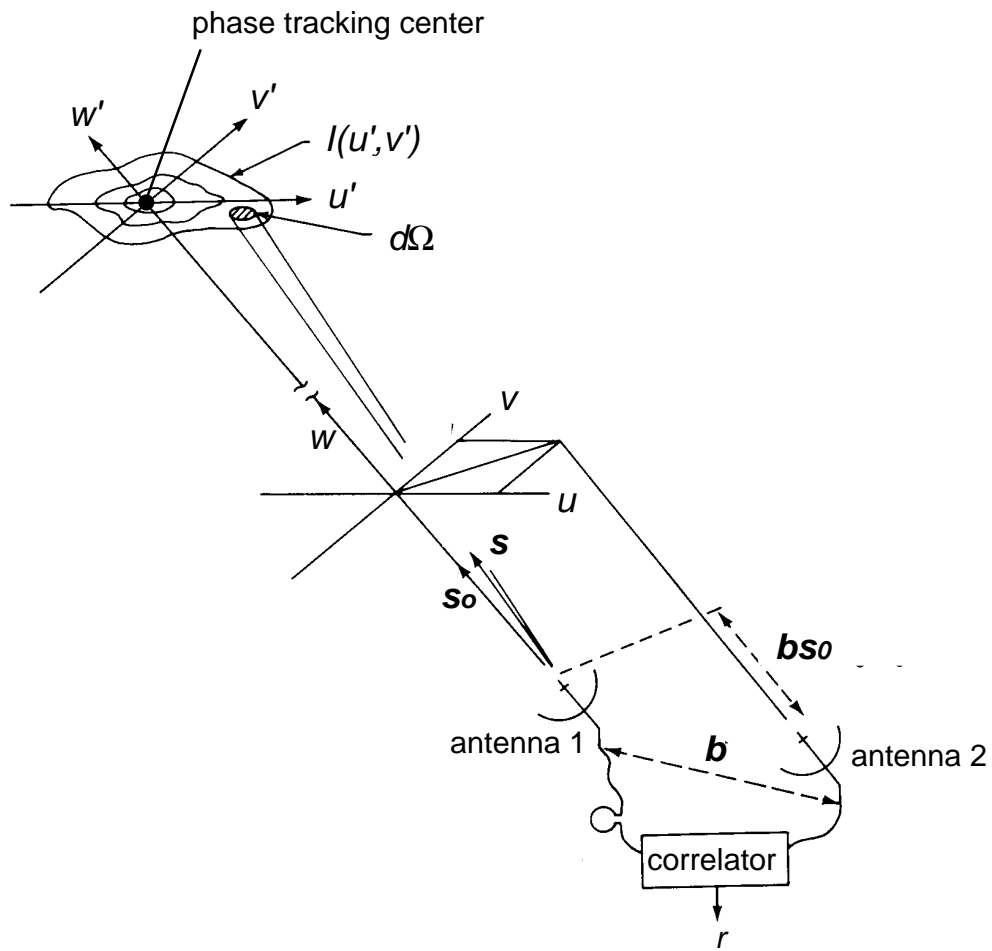


Figure 4.18: Schematic view of the radio interferometry (Rohlfs & Wilson 1999<sup>[165]</sup>).

The output is also proportional to the power that an antenna receives;  $A(\mathbf{s})I(\mathbf{s})\Delta\nu\Delta\Omega$ . Therefore, by integrating  $\mathbf{s}$  over the antenna beam width, the correlator output is

$$r = \Delta\nu \int_S A(\mathbf{s})I(\mathbf{s}) \cos(2\pi\nu\mathbf{b} \cdot \mathbf{s}/c) \quad (4.11)$$

When we substitute  $\mathbf{s}$  with  $\mathbf{s}' + \mathbf{s}_0$ , we obtain

$$\begin{aligned} r &= \Delta\nu \cos(2\pi\nu\mathbf{b} \cdot \mathbf{s}_0/c) \int_S d\Omega A(\mathbf{s}')I(\mathbf{s}') \cos(2\pi\nu\mathbf{b} \cdot \mathbf{s}'/c) \\ &\quad - \Delta\nu \sin(2\pi\nu\mathbf{b} \cdot \mathbf{s}_0/c) \int_S d\Omega A(\mathbf{s}')I(\mathbf{s}') \sin(2\pi\nu\mathbf{b} \cdot \mathbf{s}'/c) \end{aligned} \quad (4.12)$$

The real and imaginary part of the visibility function;

$$\Re[V] = |V| \cos(\phi) = \int_S d\Omega A(\mathbf{s}')I(\mathbf{s}') \cos(2\pi\nu\mathbf{b} \cdot \mathbf{s}'/c) \quad (4.13)$$

$$\Im[V] = |V| \sin(\phi) = - \int_S d\Omega A(\mathbf{s}')I(\mathbf{s}') \sin(2\pi\nu\mathbf{b} \cdot \mathbf{s}'/c) \quad (4.14)$$

$$(4.15)$$

appears in  $r$ , which connects  $r$  and  $V$  as

$$r = \Delta\nu|V| \cos(2\pi\nu\mathbf{b} \cdot \mathbf{s}_0/c - \phi). \quad (4.16)$$

By measuring the amplitude and the phase of  $r$ , the value of the visibility function is derived at a given point of the  $u$ - $v$  plane. With  $N$  antennae,  ${}_N C_2$  correlations can be obtained, which are all used to derive the value of the visibility function at  ${}_N C_2$  points. These points move around the  $u$ - $v$  plane as the earth rotates and  $\mathbf{s}_0$  changes from time to time. The visibility function  $V(u, v)$  is obtained after gridding the data points over the  $u$ - $v$  plane, then is Fourier-converted to derive the surface brightness distribution.



# Chapter 5

## *Chandra* and QUIRC Observations

### Contents

---

<b>5.1</b>	<b>X-ray Observation with <i>Chandra</i>/ACIS . . . . .</b>	<b>94</b>
5.1.1	Observation . . . . .	94
5.1.2	Data Reduction . . . . .	94
5.1.3	Source Extraction . . . . .	96
5.1.4	2MASS Counterpart of <i>Chandra</i> Sources . . . . .	96
5.1.5	Results . . . . .	101
<b>5.2</b>	<b>NIR Observation with UH88/QUIRC . . . . .</b>	<b>104</b>
5.2.1	Observation . . . . .	104
5.2.2	Data Reduction . . . . .	106
5.2.3	Source Extraction and Photometry . . . . .	107
5.2.4	2MASS Counterpart of QUIRC Sources . . . . .	109
5.2.5	Results . . . . .	109
5.2.6	QUIRC Counterpart of <i>Chandra</i> Sources . . . . .	114

---

In this chapter, we describe our X-ray and NIR observations on OMC-2 and OMC-3, and their data reduction and results. We conducted a deep-exposure *Chandra*/ACIS observation and detected  $\sim 400$  X-ray sources in this field. These X-ray sources were first correlated with the 2MASS catalog to identify the NIR counterpart (Sect. 5.1). The 2MASS catalog, which covers brighter NIR sources than  $K = 14$  mag, was found not to be deep enough to match the *Chandra* depth. In order to complement 2MASS with fainter sources, we made a follow-up NIR observation deeper on the *Chandra* field (Sect. 5.2) using QUIRC mounted on the University of Hawaii 88 inch (2.2 m) telescope. The *Chandra* sources that have no 2MASS counterpart were further correlated with the QUIRC sources to find their NIR counterpart. The X-ray and NIR source lists are separately given in Tables A.1 and B.1.

## 5.1 X-ray Observation with *Chandra*/ACIS

### 5.1.1 Observation

The *Chandra* observation on OMC-2 and OMC-3 was carried out on January 1–2, 2000 with a nominal exposure time of 88.4 ks. We used the four ACIS-I chips (I0, I1, I2, and I3) and one ACIS-S chip (S2) on the focal plane of the mirror system. The four ACIS-I chips cover a field of  $\sim 17' \times 17'$  and the ACIS-S chip of  $\sim 8.5' \times 8.5'$ . The nominal center was set at R.A. (right ascension) =  $05^{\text{h}}35^{\text{m}}20.792^{\text{s}}$  and decl. (declination) =  $-05^{\circ}05'46.95''$  (the equinox J2000.0) so that the ACIS-I FOV covers the whole OMC-2 and OMC-3 (Fig. 5.1). The timed exposure mode was used as the operating mode with the frame time of 3.2 s.

### 5.1.2 Data Reduction

For data reduction, we used the level 2 data “reprocessed” at the *Chandra* X-ray Center (CXC). This version improves the aspect solution and restores the degradation of the energy gain and resolution due to the increase of the charge transfer inefficiency (CTI) of ACIS<sup>1</sup>. We also applied the `acis_process_events` program to the data in order to eliminate “spikings” in X-ray spectra reported by CXC<sup>2</sup>. For data manipulation, we used CIAO version 2.2<sup>3</sup> and

---

<sup>1</sup>See <http://asc.harvard.edu/udocs/reprocessing.html>.

<sup>2</sup>See [http://asc.harvard.edu/ciao/caveats/acis\\_pi.html](http://asc.harvard.edu/ciao/caveats/acis_pi.html).

<sup>3</sup>See <http://asc.harvard.edu/ciao/>.

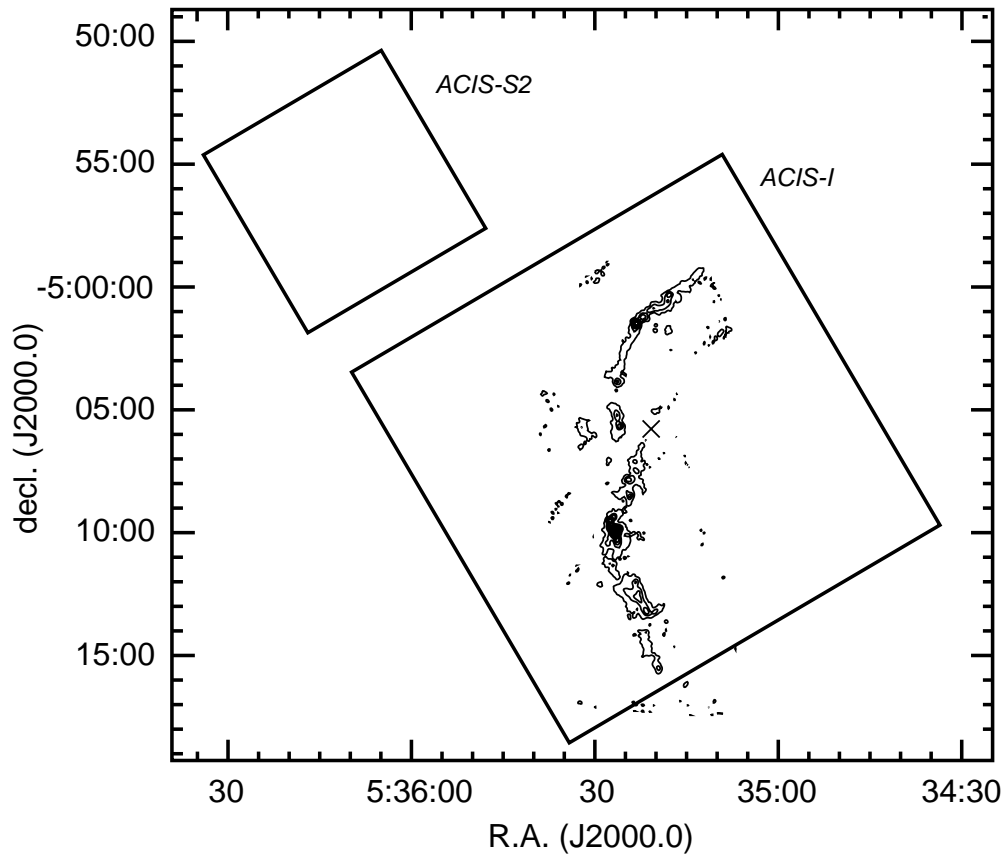


**Figure 5.1:** FOV of *Chandra*. The larger and smaller squares indicate the FOVs of ACIS-I and ACIS-S2, respectively. The aim point is shown with the cross. The contours are the 1.3 mm intensity (Chini et al. 1997<sup>[35]</sup>).

HEASoft version 5.2<sup>4</sup>. Throughout this thesis, we used X-ray photons in the 0.5–8.0 keV energy band unless otherwise noted. Photons of each source were accumulated from an elliptical region. The major and minor axis lengths and the position angles were derived from the wavdetect program. For some sources with bright neighbors, we manually shifted their accumulation region to avoid contamination. Background photons were accumulated from the standard background data provided by the ACIS team<sup>5</sup>, which combine some observations of relatively empty fields at high galactic latitudes. The pseudo-color image is shown in Figure 5.2. The *Chandra* PSF radius increases as the off-axis angle becomes larger (Fig. 4.6), which causes off-axis sources to appear extended.

### 5.1.3 Source Extraction

For source detection, we used the wavdetect program with the significance threshold of  $1 \times 10^{-5}$  (one false recognition of event pixels is expected in a  $10^5$  pixel image) and the wavelet scales ranging from 1 to 16 pixels in multiples of  $\sqrt{2}$ . We removed spurious sources through careful inspection by eye. We then detected 365 sources in the 0.5–8.0 keV band image (I1–I354 from ACIS-I and S1–S11 from ACIS-S). In order to pick up either highly absorbed (hard) or less absorbed (soft) sources more effectively, we also applied the same detection algorithm to the 2.0–8.0 keV (hard) and 0.5–2.0 keV (soft) band images. Then, 17 (I355–I369 and S11–S12) and 16 (I370–I385) sources were additionally found, respectively. In total, we detected 398 *Chandra* sources in the ACIS-I and ACIS-S FOVs. For each detected source, we calculated the X-ray photon counts (0.5–8.0 keV) and the hardness ratio (HR), which is defined as  $(H - S)/(H + S)$ , where  $H$  and  $S$  are the photon counts in the hard and soft band, respectively (Table A.1).

### 5.1.4 2MASS Counterpart of *Chandra* Sources

#### 2MASS Database

The Two Micron All Sky Survey (2MASS)<sup>6</sup> is a joint project among NASA Infrared Processing and Analysis Center (IPAC), Jet Propulsion Laboratory (JPL), the University of

<sup>4</sup>See <http://heasarc.gsfc.nasa.gov/docs/software/lheasoft/>.

<sup>5</sup>See <http://cxc.harvard.edu/contrib/maxim/bg/index.html>.

<sup>6</sup>See <http://www.ipac.caltech.edu/2mass/> for more details.

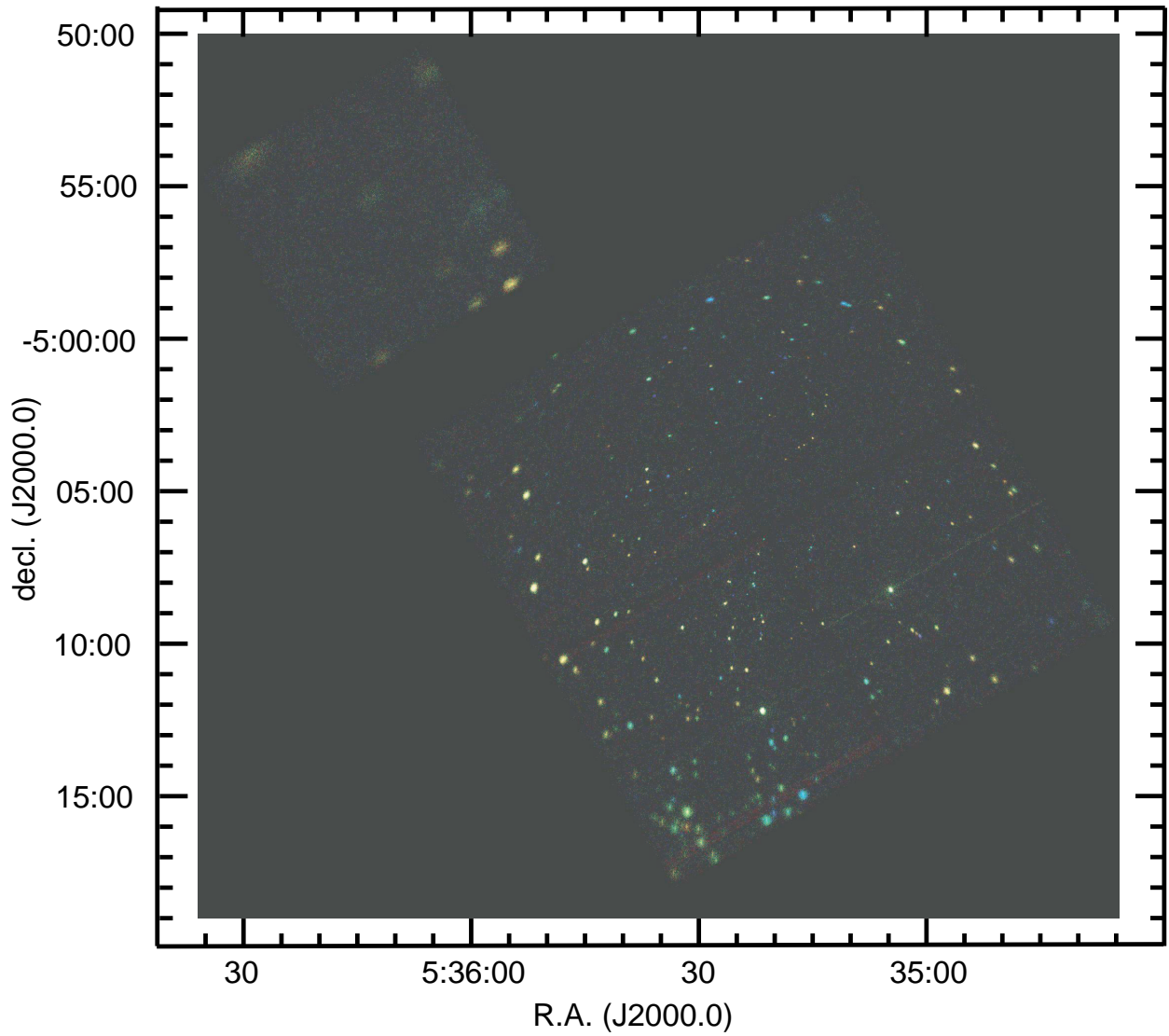


**Figure 5.2:** Three-color image of *Chandra* observations. Red, green, and blue are for photons in the 0.2–1.0 keV, 1.0–2.5 keV, and 2.5–8.0 keV, respectively.

Massachusetts, and California Institute of Technology (CIT), which aims to provide imaging data of the all sky in the  $J$  ( $1.25 \mu\text{m}$ ),  $H$  ( $1.65 \mu\text{m}$ ), and  $K_s$  ( $2.17 \mu\text{m}$ ) bands. Two telescopes; one at Mt. Hopkins, Arizona, U.S.A. and another at Cerro Tololo, Chile, are exclusively devoted for this project to cover the northern and southern sky, respectively. The identical NICMOS3 arrays are used for three bands at two telescopes. The  $J$ -,  $H$ -, and  $K_s$ -band observations are conducted simultaneously with a 7.8 s exposure per frame. The FOV is  $8.5' \times 8.5'$  with the pixel scale of  $1'' \text{ pixel}^{-1}$ .

The Second Incremental Data Release of 2MASS, which was released in March 2000, consists of two data sets; the Point Source Catalog (PSC) and the Extended Source Catalog (XSC). The release covers 19680.8 square degrees ( $\sim 47\%$  of the all sky; Fig. 5.3). OMC-2 and OMC-3 are fully covered.

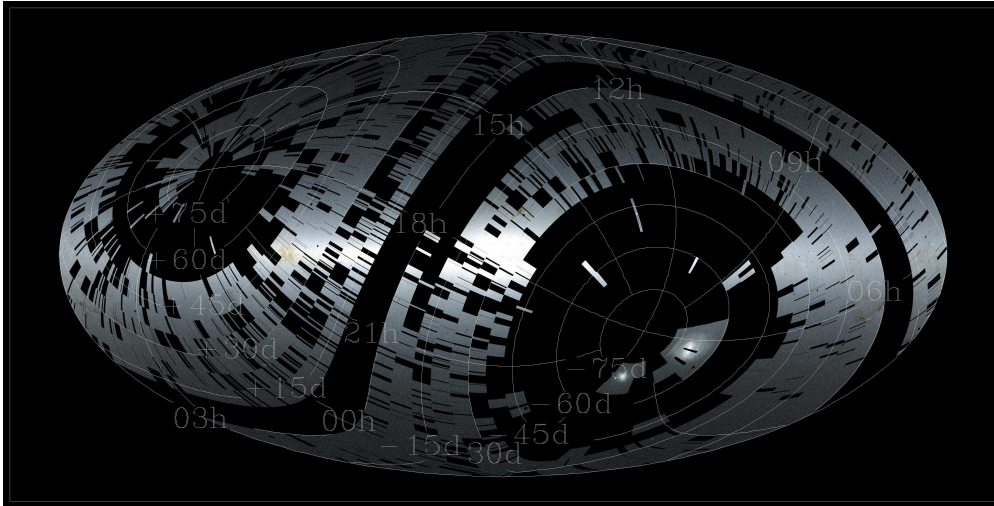


**Figure 5.3:** Sky coverage by the 2MASS Second Incremental Data Release. It covers  $\sim 47\%$  of the all sky (the shining parts of the map; <http://www.ipac.caltech.edu/2mass>). OMC-2 and OMC-3 are fully covered at R.A.  $\sim 5^{\text{h}}30^{\text{m}}$  and decl.  $\sim -5^{\circ}$ .

The PSC contains the position and the magnitude of 157,820,597, 149,650,034, and 130,337,158 sources in the  $J$ ,  $H$ , and  $K_s$  band, respectively. The astrometric accuracy is  $\sim 0.1''$  both in the R.A. and decl. directions with a negligible systematic offset from the Astrographic Catalog/Tyco (ACT) catalog (Fig. 5.4). The photometric accuracy is given in Figure 5.5, where the uncertainties in magnitudes are less than 0.1 mag for the  $J$ -,  $H$ -, and  $K_s$ -band sources brighter than 15.8 mag, 15.1 mag, and 14.3 mag, respectively.

We consulted the PSC and found that  $\sim 600$  sources are in the FOV of *Chandra*. These

sources are correlated with QUIRC and *Chandra* sources, and were used to evaluate their astrometric and photometric accuracy.

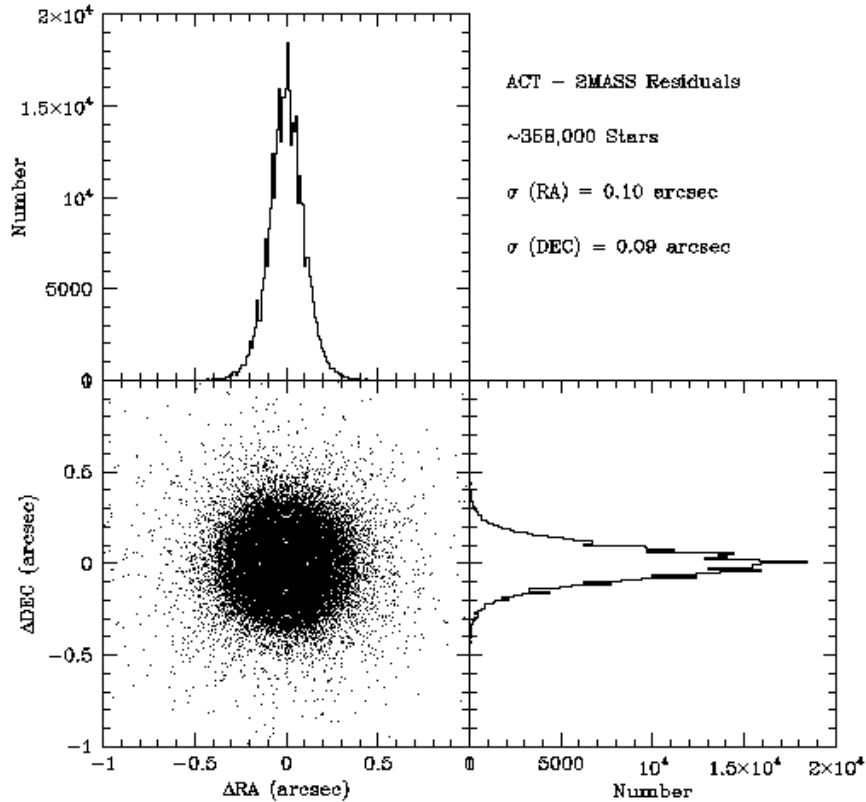


**Figure 5.4:** Distribution of the R.A. and decl. differences of  $\sim 358,000$  sources between 2MASS PSC and ACT (*bottom left*) and its profiles on R.A. (*top left*) and decl. (*bottom right*) axes. The  $1\sigma$  values for both profiles (=the typical astrometric accuracy of 2MASS PSC) are  $\sim 0.1''$  (<http://www.ipac.caltech.edu/2mass>).

## 2MASS Counterpart of *Chandra* Sources

We searched for the 2MASS counterpart of the *Chandra* sources in the following manner. In the ACIS-I and ACIS-S FOVs, we found 638 2MASS sources. First, we searched for the 2MASS source closest to each *Chandra* source within a  $3''$  radius. Second, we conversely searched for the *Chandra* source closest to each 2MASS source within a  $3''$  radius. Thus we picked up the closest *Chandra*-2MASS pairs. The systematic position offset of the *Chandra* sources from their 2MASS counterpart was found to be  $-0.18''$  and  $0.21''$  in the direction

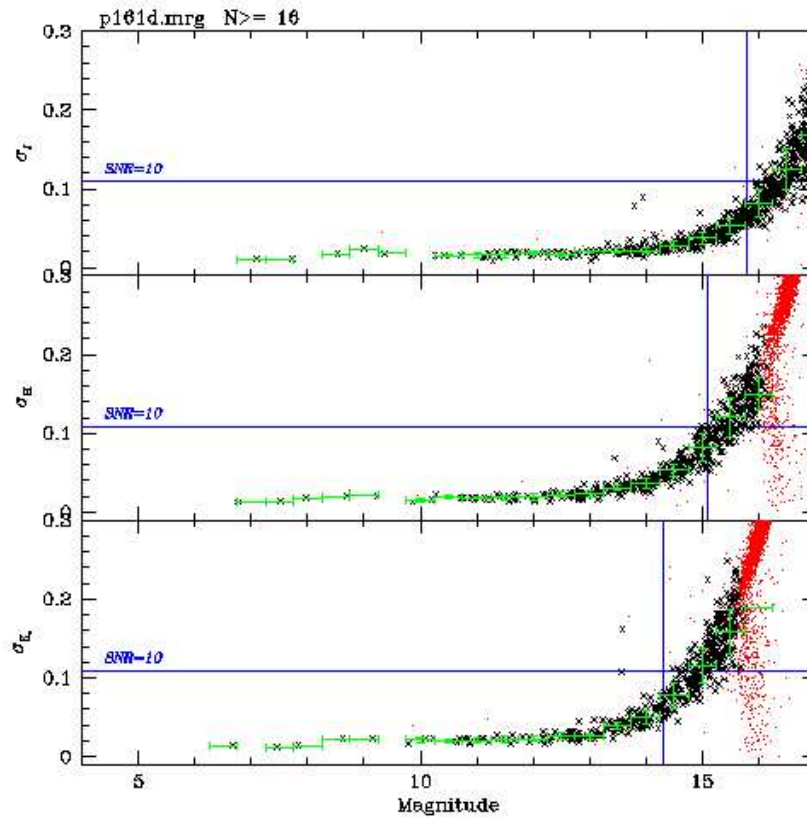


**Figure 5.5:** Photometric accuracy of sources detected in a calibration field. The uncertainty in magnitudes (*vertical axis*) versus the mean magnitude (*horizontal axis*) is plotted in black (sources detected at least 16 out of the 18 trials) and in red (sources detected fewer than 16 times) separately for the  $J$  (*top*),  $H$  (*middle*), and  $K_s$  (*bottom*) band. The dotted bars indicate the r.m.s. averaged in each 0.5 mag bin (<http://www.ipac.caltech.edu/2mass>).



of R.A. and decl., respectively. After correcting the *Chandra* positions for the systematic offsets, we repeated the same procedure for the 2MASS counterpart search. Finally, we found that 237 out of 398 ( $\sim 60\%$ ) *Chandra* sources have the 2MASS counterpart.

### 5.1.5 Results

#### Source List

The results of the X-ray imaging analysis are compiled in Table A.1 with the X-ray source numbers, positions corrected for the systematic offset from the 2MASS frame, detector raw counts, and HRs. The X-ray sources can be referred following the International Astronomical Union (IAU) convention; e.g., CXOU J05343860–0508428 for the source No. 1.

#### Astrometric Accuracy

Figure 5.6 shows the differences between the *Chandra* and 2MASS positions both in the R.A. and decl. directions. We found that  $\Delta\text{R.A.} = 0.00'' \pm 0.40''$  ( $1\sigma$ ) and  $\Delta\text{decl.} = 0.01'' \pm 0.36''$  ( $1\sigma$ ), which indicates that the *Chandra* positions are determined with the accuracy of the size of a *Chandra* pixel ( $0.492''$ ) and the systematic offset between *Chandra* and 2MASS positions is negligible.

#### Survey Depth

Figure 5.7 shows the histogram of X-ray counts. The peak of the histogram ( $10^{1.5} = 32$  counts) roughly corresponds to the completeness limit of this observation, while the minimum number of counts (3 counts) gives the flux of the faintest detected sources. To convert the X-ray counts into the X-ray flux or luminosity, we made an empirical relation between these two parameters using the result of the spectral fitting of bright *Chandra* sources (Figs. 7.22 and 7.23). The completeness limit was estimated to be  $\sim 10^{-14.5}$  ergs s $^{-1}$  cm $^{-2}$  in flux and  $\sim 10^{29.1}$  ergs s $^{-1}$  in luminosity in the 0.5–8.0 keV range. The X-ray flux and the luminosity of the faintest detected source were  $\sim 10^{-15.5}$  ergs s $^{-1}$  cm $^{-2}$  and  $\sim 10^{28.1}$  ergs s $^{-1}$ , respectively.

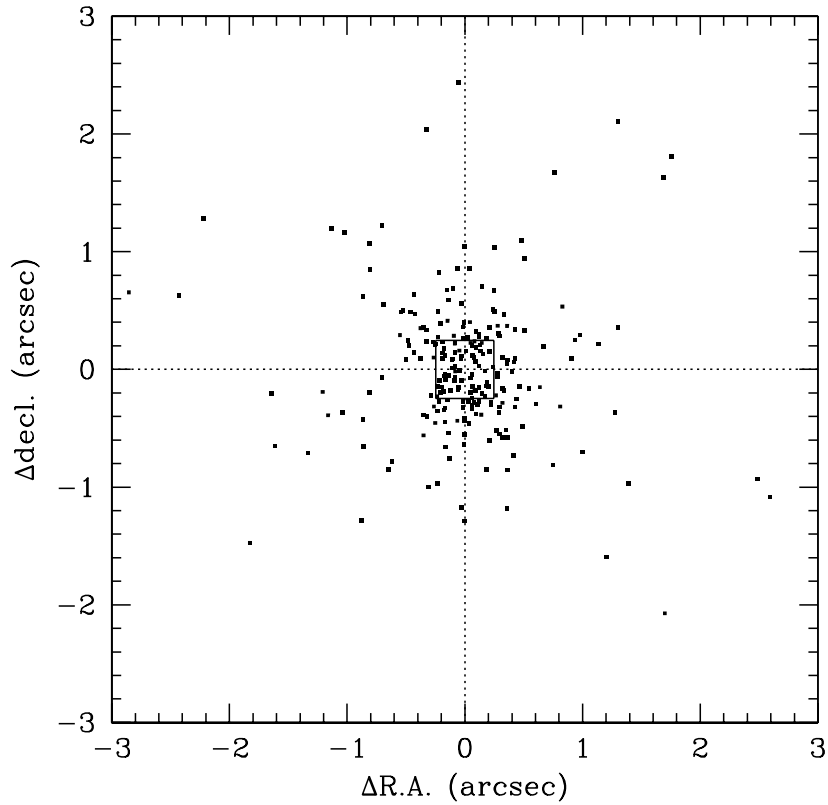


**Figure 5.6:** Astrometric accuracy of *Chandra* sources. The difference of R.A. and decl. in the *Chandra* and 2MASS positions ( $\Delta R.A.$  and  $\Delta decl.$ , respectively) is plotted for *Chandra*-2MASS counterpart pairs. The solid square at the center represents the size of a *Chandra* pixel of  $0.492'' \times 0.492''$ .

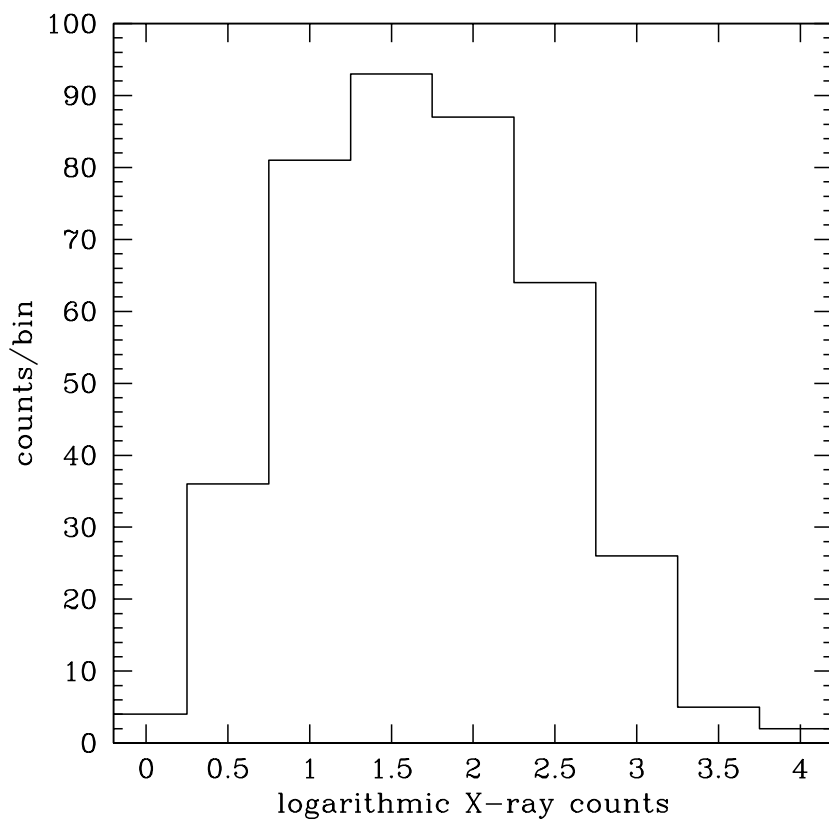


**Figure 5.7:** Histogram of *Chandra* counts of all detected sources.

## 5.2 NIR Observation with UH88/QUIRC

### 5.2.1 Observation

In two points, the 2MASS data are not sufficient to find the NIR counterpart of our X-ray sources and to identify their nature. One point is that the 2MASS data sometimes lack  $J$ -,  $H$ -, or both band detections in star-forming regions, where the extinction by dense ISM makes sources heavily reddened. Another point is that the 2MASS depth is not deep enough to match the depth of our *Chandra* observation. Casanova et al. (1995)<sup>[29]</sup> derived an empirical relation between the un-dereddened  $J$ -band magnitude ( $J$ ) and the X-ray flux ( $F_X$ ) in the 1.0–2.4 keV band using T Tauri star samples in the  $\rho$  Ophiuchi cloud ( $D = 160$  pc) detected by *ROSAT*, which is expressed as

$$\log F_X(4\pi D)^2 \sim -0.30J + 32. \quad (5.1)$$

The faintest detected sources of our *Chandra* observation have  $F_X \sim 10^{-15.5}$  ergs s<sup>-1</sup> cm<sup>-2</sup> in 0.5–8.0 keV at the distance of  $D = 450$  pc, which can be converted to  $F_X \sim 2 \times 10^{-16}$  ergs s<sup>-1</sup> cm<sup>-2</sup> in the 1.0–2.4 keV band assuming a thin-thermal plasma spectrum of 1 keV temperature. If the equation (5.1) can be applied to other YSOs, the required NIR detection limit would be  $J \sim 17$  mag. In order to complement the 2MASS data with fainter sources than the 2MASS limit, we conducted deeper NIR observations in OMC-2 and OMC-3 with the  $J$ -band integration time twice longer than that of the  $H$  and  $K$  bands.

We used QUIRC mounted on the Cassegrain focus of the University of Hawaii 88 inch (2.2 m) telescope (UH88; Hodapp et al. 1997<sup>[89]</sup>). QUIRC provides a 3.2' × 3.2' FOV with the pixel scale of 0.189" pixel<sup>-1</sup>. The smaller pixel scale than that of the 2MASS detectors is more appropriate to pick up sources contaminated by diffuse emissions, particularly in the southern half of our study field (Fig. 5.9).

We conducted a mosaic mapping observation to sweep the *Chandra* ACIS-I FOV (Fig. 5.8). We first covered the uppermost row (frame Nos. 1–5) of the mosaic by shifting the field center by 1.6' (half of the side of the QUIRC FOV) from east to west. Then, we moved 1.6' southward and covered the second uppermost row (frame Nos. 6–13) by inversely shifting from west to east. We continued these raster scans to reach the lowermost row of the mosaic. In this way, we can minimize dead times due to the shifts of field center and reduce the effect of ghost signals caused by residual electrons in detector pixels. In total, we swept the *Chandra* FOV with 169 QUIRC FOVs that amount to  $\sim 512$  arcmin<sup>2</sup>.

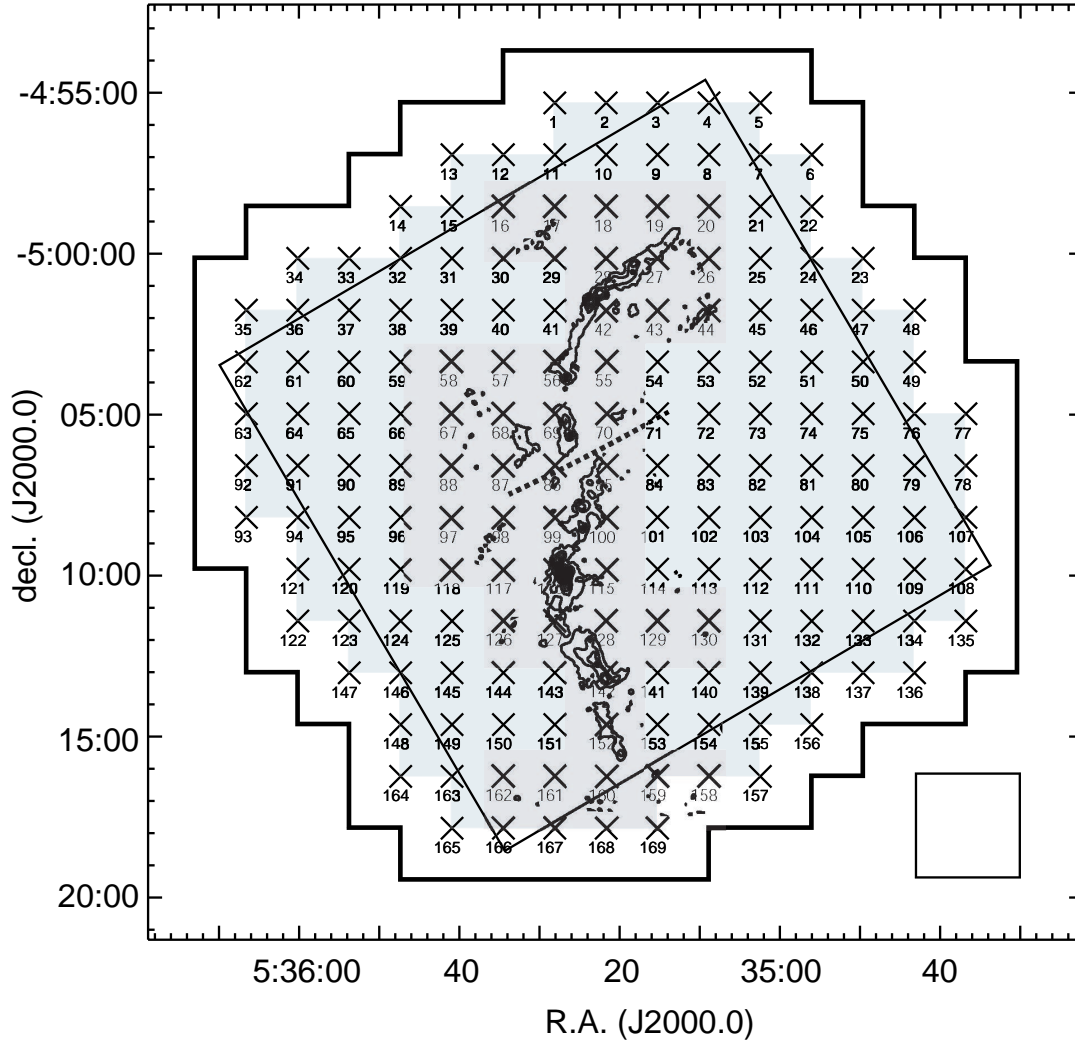


**Figure 5.8:** Configuration of our QUIRC mosaic mapping observations. The positions of 169 frame centers are marked with crosses with the relevant frame number. The frames are tiled at the intervals of  $1.6'$  to sweep the *Chandra* ACIS-I FOV (*solid oblique square*). Each frame covers a  $3.2' \times 3.2'$  square region (the size is shown at the right bottom) centered on each cross. When the all frames are combined, any point in the thick lines ( $\sim 512 \text{ arcmin}^2$ ) is covered at least by one frame, while that in the gray region ( $\sim 360 \text{ arcmin}^2$ ) is covered by four frames. The contours show the 1.3 mm intensity (Chini et al. 1997<sup>[35]</sup>). OMC-2 and OMC-3 are separated by the dashed line into the southern and northern part of the integral-shaped ridge, respectively.

Each 169 frame was exposed for 60 s. We conducted the mosaic mapping once in the  $H$  and  $K$  band and twice in the  $J$  band, spending six half-nights of February 4–6 and March 11–13, 2001 (Table 5.1). All nights were photometric with the seeing of  $0.7''$ – $1.1''$ . In one sweep, any region inside the *Chandra* field except for edges (the gray region in Fig. 5.8) was covered four times, which makes the nominal exposure time to be 240 s in the  $H$  and  $K$  band and 480 s in the  $J$  band.

**Table 5.1:** QUIRC observation log

date	band	frame numbers <sup>a</sup>
2001 Feb. 04	$K$	Nos. 1–169
2001 Feb. 05	$J$	Nos. 1–52
2001 Feb. 06	$H$	Nos. 1–169
2001 Mar. 11	$J$	Nos. 1, 51–169
2001 Mar. 12	$J$	Nos. 1–129
2001 Mar. 13	$J$	Nos. 1, 107–169

<sup>a</sup> The frame numbers (see Fig. 5.8) covered in each night. In the  $J$ -band sweep, for which we spent four nights, some frames are duplicated; i.e., the frame No. 1 at the beginning of every run to check the telescope positioning accuracy, and frame Nos. 51–52 and 107–129 to check any difference of image quality in different nights. All these duplicated frames were confirmed to have similar quality and were combined equally into the final  $J$ -band image with the correction for the exposure time.

## 5.2.2 Data Reduction

All QUIRC frames were reduced following the standard procedures using IRAF<sup>7</sup>; i.e., dark subtraction, flat fielding, sky subtraction, and bad pixel removal. Dark frames with a 60 s integration time were taken at the end of each night for each filter, and were used to subtract dark current signals of source images. Flat frames were also taken at each night for each filter by observing the telescope dome, and were used to correct for the pixel-to-pixel variation in quantum efficiency. Sky frames were constructed for each frame set of a mosaic image by adopting the median of 169 ADU values at a given pixel. SExtractor (Bertin & Arnouts 1996<sup>[21]</sup>) was used for source extraction and photometry.

For the purpose of the astrometric and photometric calibration of all frames, we consulted the 2MASS catalog. We tentatively extracted sources from each frame and correlated

<sup>7</sup>See <http://iraf.noao.edu/>.

them with the 2MASS sources using WCSTools<sup>8</sup>. We found that all QUIRC frames have 18–145 sources including 4–51 sources with the 2MASS counterpart. Using the QUIRC–2MASS counterpart pairs, we first shifted each QUIRC frame so that the mean separation between QUIRC sources and their 2MASS counterpart in the frame reaches the minimum. Second, we multiplied each QUIRC frame with a constant value that was derived by the least-square method in order to match the QUIRC photometry with the 2MASS photometry of QUIRC–2MASS counterpart pairs. In this way, we used the 2MASS sources as standard stars. Sources brighter than 11 mag or fainter than 16 mag were not used for this procedure because of the unguaranteed linearity of QUIRC or because of the large uncertainty in the 2MASS photometry.

All the frames, which were thus corrected for astrometry and photometry, were combined into three large mosaic images of the  $J$ ,  $H$ , and  $K$  bands. The pseudo-color image is shown in Figure 5.9. Some discontinuities are left in the image because of the difficulty in determining the background intensity level, particularly in regions contaminated by diffuse emissions.

### 5.2.3 Source Extraction and Photometry

Prior to source detection, all the mosaic images were binned with neighboring  $2 \times 2$  pixels and smoothed with a Gaussian function to attain better signal-to-noise ratio. For the  $K$ -band mosaic image thus improved, we extracted NIR sources above  $3 \sigma$  level. In SExtractor, we can choose any convolution masks  $\phi(x, y)$  in peak finding procedures to increase detectability of faint sources. The two dimensional Gaussian mask  $\phi_G(x, y)$  is routinely used, where

$$\phi_G(x, y) = \frac{1}{2\pi\sigma_x\sigma_y} \exp\left(-\frac{1}{2\sigma_x^2} - \frac{1}{2\sigma_y^2}\right). \quad (5.2)$$

However, we adopted the Mexican hat function  $\phi_{MH}(x, y)$  for the mask; i.e.,

$$\begin{aligned} \phi_{MH}(x, y) &= \left[ \left( x \frac{\partial}{\partial x} + 1 \right) + \left( y \frac{\partial}{\partial y} + 1 \right) \right] \phi_G(x, y) \\ &= \frac{1}{2\pi\sigma_x\sigma_y} \left( 2 - \frac{x^2}{\sigma_x^2} - \frac{y^2}{\sigma_y^2} \right) \exp\left(-\frac{x^2}{2\sigma_x^2} - \frac{y^2}{2\sigma_y^2}\right). \end{aligned} \quad (5.3)$$

This function has a positive kernel surrounded by a negative annulus. The limited spatial extent of the kernel favors sources with intrinsically or instrumentally broadened size of

---

<sup>8</sup>See <http://tdc-www.harvard.edu/software/wcstools/> for more details.

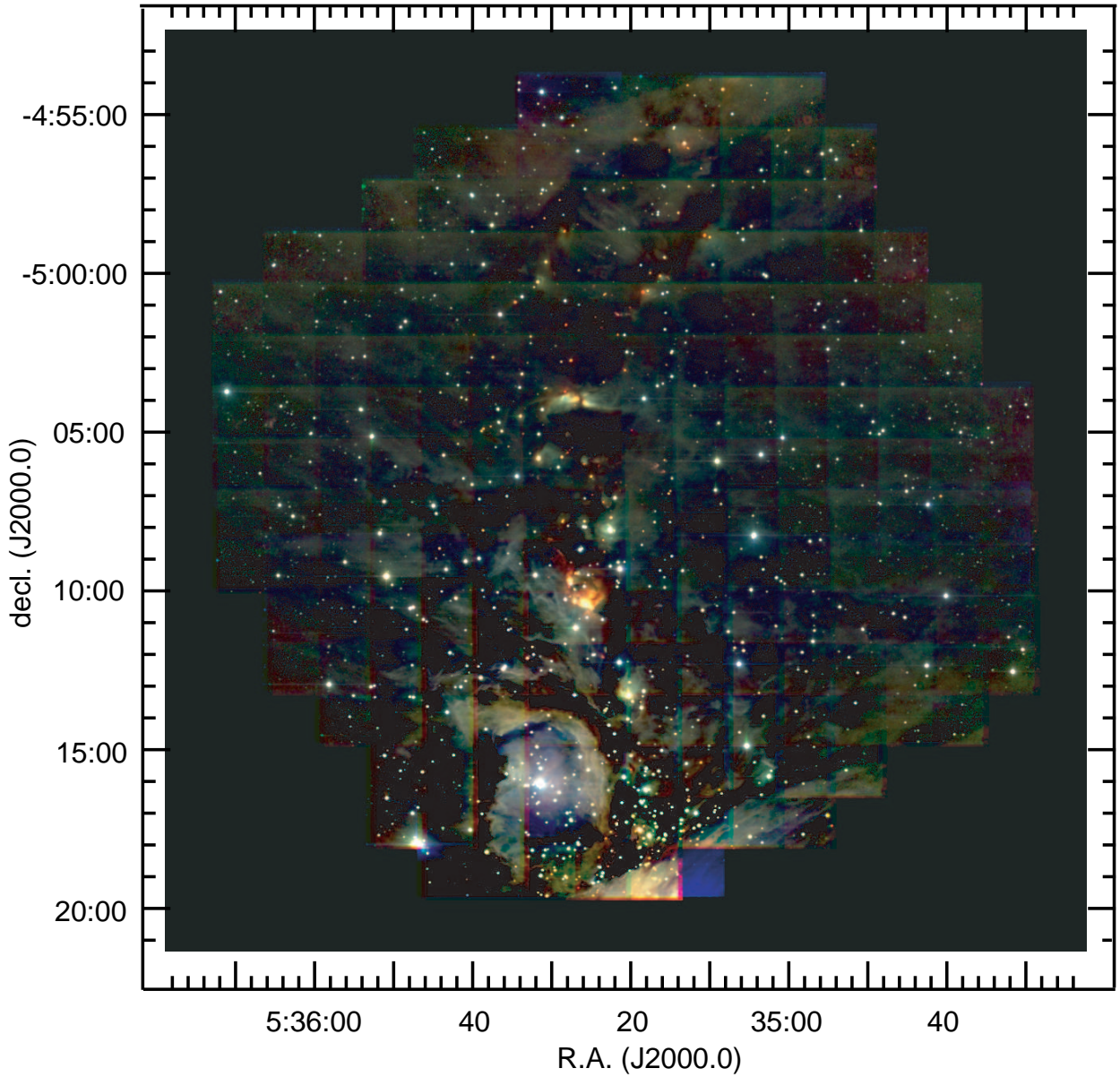


**Figure 5.9:** Three-color image of QUIRC observations. The neighboring  $8 \times 8$  pixels are binned. Red, green, and blue are for the  $K$ -,  $H$ -, and  $J$ -band intensity, respectively.



about  $(\sigma_x, \sigma_y)$  to be detected. We confirmed that a Mexican hat function of the seeing size radius gives the most robust result among several masks with various radii we examined, particularly in regions contaminated with diffuse emissions. With careful visual inspections on the output, we removed (1) sources at the edge of the mosaic images, (2) ghosts of bright sources, and (3) spurious detections (in most cases, diffuse structures were identified as point-like sources). As a result, we picked up 1448  $K$ -band sources.

For each  $K$ -band detected source, we derived the  $J$ -,  $H$ -, and  $K$ -band magnitude with the adaptive aperture photometry. For source with less than a  $3\sigma$  detection in the  $J$ ,  $H$ , or both bands, we calculated the  $3\sigma$  upper limit of their magnitudes.

#### 5.2.4 2MASS Counterpart of QUIRC Sources

We correlated all the QUIRC sources with the 2MASS catalog with the `imtmc` command in the `WCSTools` package and found that 692 ( $\sim 48\%$ ) have the 2MASS counterpart.

#### 5.2.5 Results

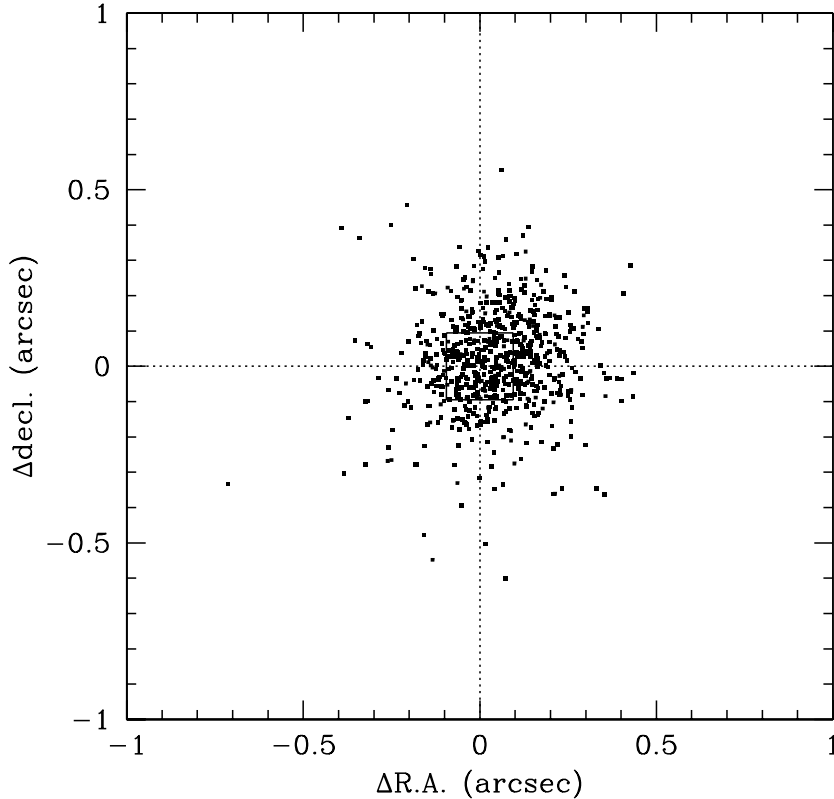
##### Source List

Table B.1 lists the QUIRC sources with their source number, position,  $J$ -,  $H$ -, and  $K$ -band magnitudes, and their 2MASS counterpart. Hereafter, we refer these sources following the IAU convention; e.g., TKK J05342894–0508387 for the source No.1. Note that all the magnitudes in the list are in the 2MASS color system. For sources that lack the  $J$ ,  $H$ , or both band detections, we listed the  $3\sigma$  upper limit of the flux (lower limit of the magnitude) and labeled them with “ $>$ ”. For QUIRC magnitudes brighter than 11 mag, we replaced them with the 2MASS magnitudes with the label “ $\dagger$ ” if they have the 2MASS counterpart. If they do not have the 2MASS counterpart, we labeled the magnitudes with “ $<$ ” and recognized them as the lower limit of the flux (the upper limit of the magnitude).

##### Astrometric and Photometric Accuracy

Using the QUIRC–2MASS counterpart pairs, we evaluated the accuracy of the QUIRC astrometry and photometry in the following way.

In Figure 5.10, we plotted differences between the QUIRC and 2MASS positions both in the R.A. and decl. directions. We found that  $\Delta\text{R.A.} = 0.048'' \pm 0.161''$  ( $1 \sigma$ ) and  $\Delta\text{decl.} = 0.022'' \pm 0.148''$  ( $1 \sigma$ ), which indicates that the QUIRC positions are determined with the accuracy of the size of a QUIRC pixel ( $0.189''$ ) and the systematic offset between QUIRC and 2MASS positions is negligible.



**Figure 5.10:** Astrometric accuracy of QUIRC sources. The difference of R.A. and decl. in the QUIRC and 2MASS positions ( $\Delta\text{R.A.}$  and  $\Delta\text{decl.}$ , respectively) are plotted for each QUIRC–2MASS pair. The solid square at the center represents a QUIRC pixel size of  $0.189'' \times 0.189''$ .

In Figure 5.11, we plotted the QUIRC and 2MASS magnitudes of QUIRC–2MASS counterpart pairs separately for each band. The linear relations (2MASS magnitudes equal QUIRC magnitudes) are violated at the brighter side than  $\sim 11$  mag due to the unguaranteed linearity of QUIRC, where its saturation limit of 44000 ADU counts corresponds to  $\sim 11$  mag in our observations. For sources fainter than 11 mag in the QUIRC and 2MASS magnitudes, we calculated the difference between these magnitudes for each band ( $\Delta m_J$ ,  $\Delta m_H$ , and

$\Delta m_K$ ). We found that  $\Delta m_J = -0.06 \pm 0.22$  mag ( $1 \sigma$ ),  $\Delta m_H = -0.07 \pm 0.19$  mag ( $1 \sigma$ ), and  $\Delta m_K = -0.04 \pm 0.18$  mag ( $1 \sigma$ ), indicating that the QUIRC photometry fainter than 11 mag is consistent with the 2MASS photometry within  $\sim 0.2$  mag.

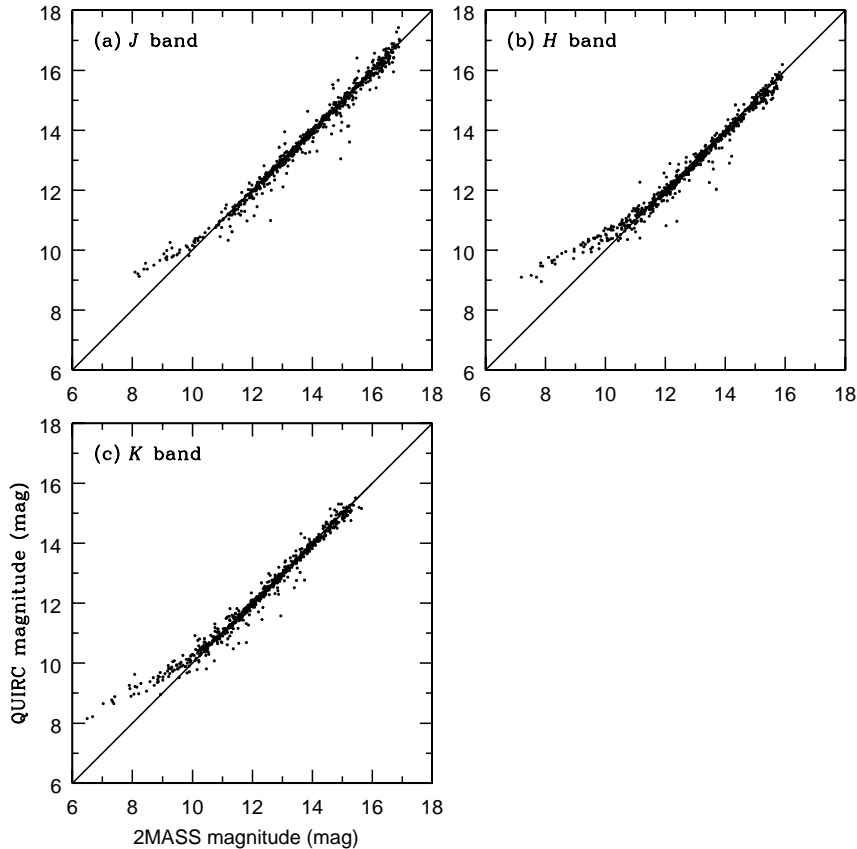


**Figure 5.11:** Photometric accuracy of QUIRC sources. The 2MASS and QUIRC magnitudes of the counterpart pairs are plotted separately for the (a) *J*, (b) *H*, and (c) *K* bands. Solid lines represent that the 2MASS magnitudes equal to the QUIRC magnitudes).

## Survey Depth

We estimated the survey depth of our QUIRC observations in the following manner. First, we embedded 500 artificial sources with 13.0–13.5 mag in the *J*-, *H*-, and *K*-band mosaic images. The same source detection algorithm was employed to detect these artificial sources, then the detection rate of sources with 13.0–13.5 mag was derived. The same procedure was repeated for sources of different magnitudes from 13.0 to 20.0 mag with 0.5 mag bins. The

detection rate at each magnitude bin is given in Figure 5.12 for the  $K$  (solid),  $H$  (long-dashed), and  $J$  (short-dashed) band, respectively. The 90% completeness limit ( $3\sigma$ ) was thus estimated to be  $K \sim 16.0$  mag,  $H \sim 16.5$  mag, and  $J \sim 17.5$  mag.

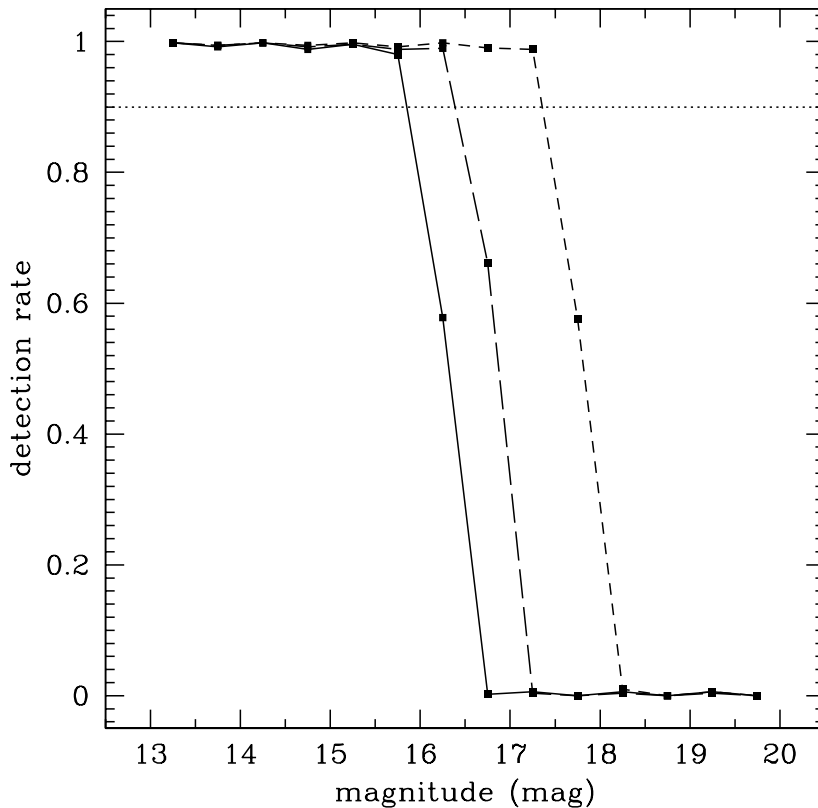


**Figure 5.12:** Completeness limit of QUIRC observations. The fractions of detected artificial sources are shown with the solid ( $K$ ), long-dashed ( $H$ ), and short-dashed ( $J$ ) lines. The 90% (dotted line) completeness limit is  $K \sim 16.0$  mag,  $H \sim 16.5$  mag, and  $J \sim 17.5$  mag.

In order to compare the depth of our observation with that of 2MASS, we made a histogram of the number counts of the  $K$ -band detected sources at each magnitude (Fig. 5.13). The short- and long-dashed histograms respectively represent the number of the QUIRC sources with and without the 2MASS counterpart, while the total is given in the solid histogram. The 2MASS catalog fails to detect some bright sources even in  $K < 14$  mag, which is mainly due to the contamination by diffuse emission or to their binarity. This was confirmed by plotting the 2MASS source list on the 2MASS image.

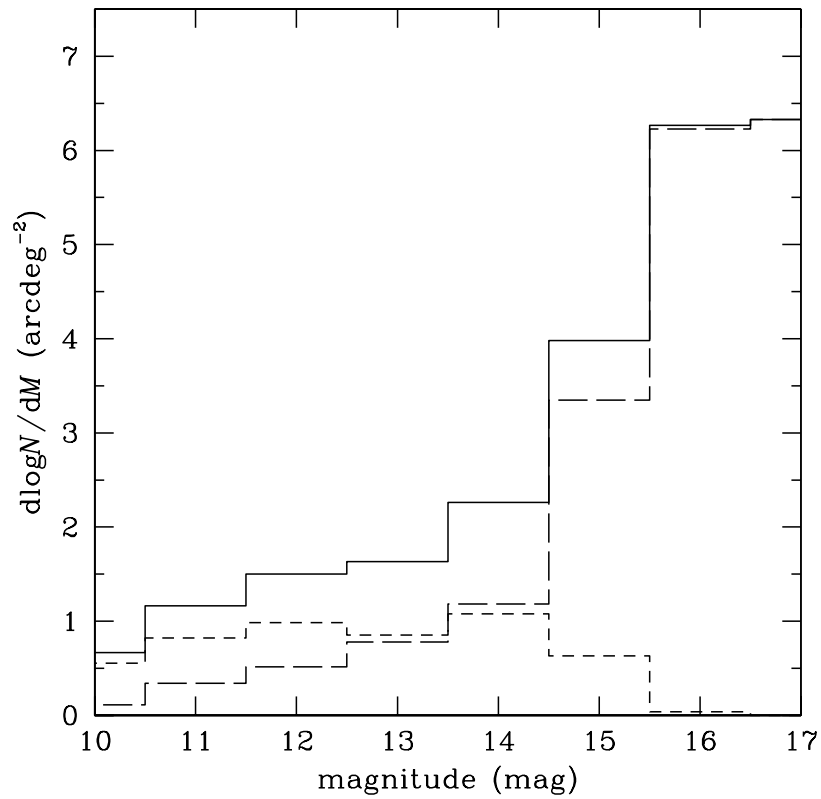


**Figure 5.13:** Source counts ( $d \log N / dM$ ) of QUIRC  $K$ -band detected sources, where  $M$  is the magnitude and  $N$  is the number of sources fainter than  $M$  mag. The solid histogram is the counts of all the QUIRC  $K$ -band sources, while the short- and long-dashed histograms are those with and without the 2MASS counterpart, respectively.

### 5.2.6 QUIRC Counterpart of *Chandra* Sources

Among 237 *Chandra* sources with the 2MASS counterpart, 30 sources lack either 2MASS  $J$ -,  $H$ -, or  $K_s$ -band detections. Together with 161 *Chandra* sources that have no 2MASS counterpart, we hereafter call them the “2MASS-unIDed” *Chandra* sources. There are 183 and 9 2MASS-unIDed sources in the ACIS-I and ACIS-S2 FOVs. Using the QUIRC source list (Table B.1), we searched for the NIR counterpart of 183 2MASS-unIDed ACIS-I sources with a more elaborated procedure as follows.

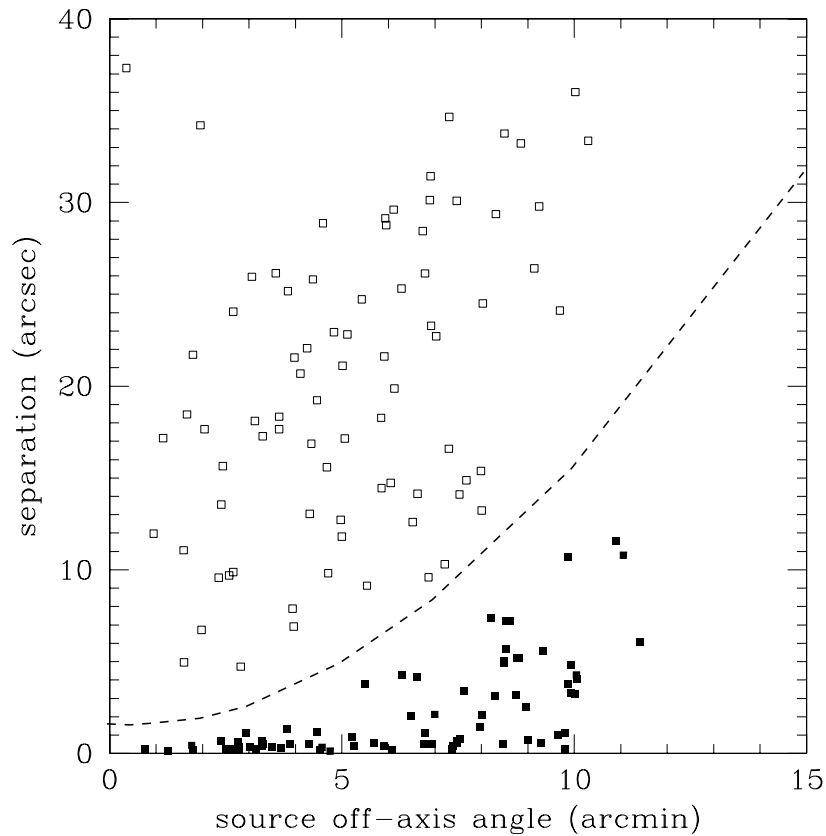


**Figure 5.14:** Closest QUIRC–*Chandra* pairs with their separation and the X-ray off-axis angle on the vertical and the horizontal axis, respectively. The dotted curve is the 90% encircled energy radius ( $r_{90}$ ) of 1.49 keV X-rays at a given off-axis angle. Filled squares, which are below the dotted curve, are recognized as the counterpart pairs. Open squares, which are above the dotted curve, are recognized as non-associated pairs.

The *Chandra* PSF radii differ by more than an order of magnitude between on-axis sources and those at the field edge, which deteriorates the position accuracy of sources

at large off-axis angles. Therefore, in identifying the QUIRC counterpart of the *Chandra* sources, we took the off-axis angle into account. First, we searched for the QUIRC source closest to each *Chandra* source. Second, we conversely searched for the *Chandra* source closest to each QUIRC source. Then, we picked up 159 QUIRC–*Chandra* pairs that are the closest to each other. These pairs include those of physically associated (“counterpart pairs”) and those of no physical association (“non-associated pairs”). In Figure 5.14, we plotted the separation between the closest QUIRC–*Chandra* pairs as a function of the off-axis angle of the *Chandra* source. We showed two groups by the filled and open squares, which are well separated by the dotted curve indicating the 90% encircled energy radius ( $r_{90}$ ;  $\sim 0.9$  times FWHM of a Gaussian PSF) of 1.49 keV X-rays as a function of the off-axis angle<sup>9</sup>. Since  $r_{90}$  is the radius in which the 90% of incident X-ray photons are accumulated, it also represents the position accuracy of the *Chandra* sources at each off-axis angle. We therefore regard the closest QUIRC–*Chandra* pairs with the separation angle less than  $r_{90}$  (*filled squares*) to be counterpart pairs, while those with larger separation angle of more than  $r_{90}$  (*open squares*) as non-associated pairs. As a result, 75 2MASS-unIDed *Chandra* sources were newly found to have the QUIRC counterpart (hereafter we call them “QUIRC-IDed” sources). The 2MASS and QUIRC counterpart of *Chandra* sources and their NIR colors are given in Table A.1. Note that the NIR colors are converted to the CIT color system (Sect. 6.2).

A (203)	B (29)	C (153)
A (203)	D (75)	E (107)

**Figure 5.15:** NIR identifications of *Chandra* ACIS-I sources. (*top*) 2MASS identifications. Those with the 2MASS  $J$ -,  $H$ -, and  $K_s$ -band detections (“2MASS-IDed”) are in A, those lack at least one detection in these three bands are in B, and those with no 2MASS counterpart are in C. B and C are called “2MASS-unIDed” sources, for which the QUIRC counterpart is searched. (*bottom*) QUIRC identifications. Those with the QUIRC counterpart (“QUIRC-IDed”) are in D, while those without 2MASS nor QUIRC counterpart (“NIR-unIDed”) are in E. 2MASS-IDed and QUIRC-IDed sources (A and D) are collectively called “NIR-IDed” sources. The number of sources are shown in parentheses.

<sup>9</sup>See <http://asc.harvard.edu/udocs/docs/POG/MPOG/index.html>.





# Chapter 6

## NIR-IDed X-ray Sources: (1) NIR Properties

### Contents

---

<b>6.1</b>	<b>NIR Sources</b>	<b>118</b>
6.1.1	<i>K</i> -band Luminosity Function	118
6.1.2	Color-color Diagram of QUIRC Sources	119
6.1.3	Color-magnitude Diagram of QUIRC Sources	120
<b>6.2</b>	<b>The NIR-IDed X-ray Sources</b>	<b>124</b>
6.2.1	Cloud Membership	124
6.2.2	Evolutional Class Estimates	124
6.2.3	Mass and Bolometric Luminosity Estimates	127

---

In this chapter, the NIR properties of the QUIRC sources and NIR-IDed X-ray sources are discussed. Using color-color and color-magnitude diagrams of the  $J$ ,  $H$ , and  $K$  bands, ample information on physical parameters of YSOs can be obtained such as the evolutionary class, disk existence, stellar mass, bolometric luminosity and amount of extinction. In Sect. 6.1, we examine the NIR colors of all QUIRC sources and describe the overall features of OMC-2 and OMC-3. In Sect. 6.2, we zoom in to the NIR-IDed X-ray sources (=NIR sources with the X-ray counterpart), and estimate their mass and evolutionary class to classify them into several groups.

## 6.1 NIR Sources

### 6.1.1 $K$ -band Luminosity Function

We made a histogram of the  $K$ -band-detected QUIRC sources at each  $K$ -band magnitude ( $K$ -band luminosity function; KLF) in Figure 6.1. The short- and long-dashed histograms respectively represent the KLF of QUIRC sources with and without the 2MASS counterpart, while the total is given in the solid histogram. The dashed-and-dotted histogram is the KLF of NIR-IDed X-ray sources normalized to the area of QUIRC FOV. In the KLF, we can estimate the back- and foreground source contamination. The dotted curve shows the back- and foreground source counts predicted by a Galactic star count model (the SKY model; Cohen 1993<sup>[38]</sup>; Cohen 1994<sup>[39]</sup>; Cohen, Sasseen, & Bowyer 1994<sup>[40]</sup>; Cohen 1995<sup>[41]</sup>) assuming no interstellar extinction. There is an overall extinction of  $A_K \sim 1$  mag in this region (Fig. 6.4; see the relevant discussion in the text), which shifts the dotted curve rightward by  $\sim 1$  mag to the dashed curve. The contamination is not negligible for sources fainter than  $K \sim 15$  mag. For brighter sources, however, we can assume that most of them are cloud members.

The peak of KLF for all the QUIRC sources (*solid histogram*) at 12–13 mag is a real feature when the completeness limit ( $K \sim 16$  mag) and back- and foreground contamination are taken into consideration. This has been inferred by Jones et al. (1994)<sup>[101]</sup>, who studied the KLF of OMC-2 sources. The peak of KLF is often seen in the young associations like the Orion Nebula Cluster (Ali & DePoy 1995<sup>[2]</sup>; Hillenbrand & Carpenter 2000<sup>[86]</sup>) and can be explained in terms of difference in the mass-to-luminosity relation between main sequence and pre-main-sequence sources (Muench, Lada, & Lada 2000<sup>[137]</sup>). The peak magnitude is

consistent with the cloud age of  $\sim 1$  Myr (Ali & DePoy 1995<sup>[2]</sup>), which was also confirmed by other methods (Sect. 3.1).

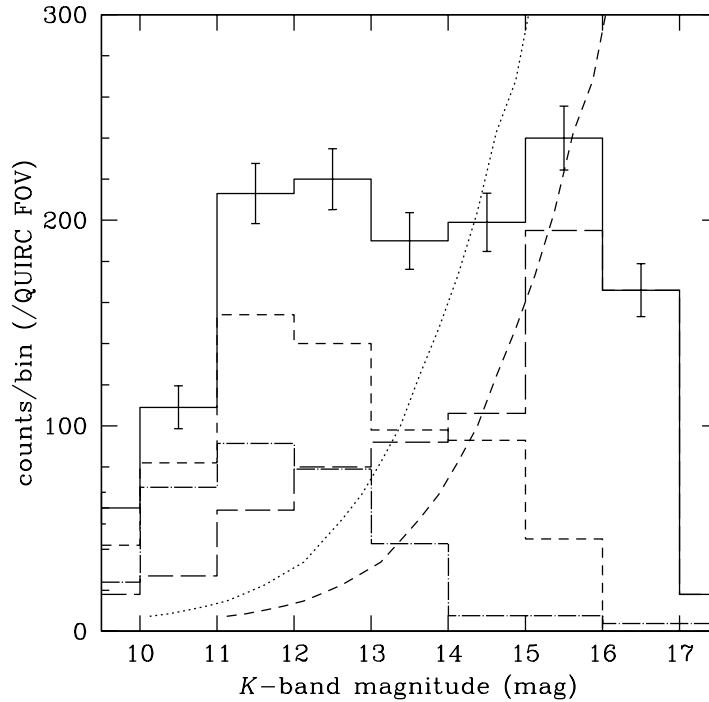


**Figure 6.1:** QUIRC  $K$ -band-detected source counts at each magnitude in the 2MASS color system. The solid histogram is the counts of all the QUIRC  $K$ -band sources, while the short- and long-dashed histograms are those with and without the 2MASS counterpart, respectively. The dashed-and-dotted histogram is the KLF of the NIR-IDed X-ray sources normalized to the area of QUIRC FOV. The uncertainty of  $\sqrt{\text{counts bin}^{-1}}$  is given for the solid histogram. The dotted curve shows the back- and foreground source counts predicted by a Galactic star count model assuming no extinction. When a uniform extinction of 1 mag is assumed, this curve should be shifted rightward by 1 mag to the dashed curve.

### 6.1.2 Color-color Diagram of QUIRC Sources

We first converted the  $J$ -,  $H$ -, and  $K$ -band magnitudes in the 2MASS color system in Table B.1 ( $J_{2\text{MASS}}$ ,  $H_{2\text{MASS}}$ , and  $K_{2\text{MASS}}$ ) to the CIT color system ( $J_{\text{CIT}}$ ,  $H_{\text{CIT}}$ , and  $K_{\text{CIT}}$ ) using the following conversion formula (Carpenter 2001<sup>[27]</sup>):

$$J_{\text{CIT}} = 0.947J_{2\text{MASS}} + 0.053K_{2\text{MASS}} + 0.036 \quad (6.1)$$

$$(J - H)_{\text{CIT}} = 0.929(J - H)_{2\text{MASS}} + 0.040 \quad (6.2)$$

$$(H - K)_{\text{CIT}} = 0.975(H - K)_{2\text{MASS}} - 0.027 \quad (6.3)$$

The color-color diagram (Lada & Adams 1992<sup>[114]</sup>) was made using all QUIRC sources with significant  $J$ -,  $H$ -, and  $K$ -band detections (1305 out of 1448 sources). Figure 6.2 shows the  $(J-H)/(H-K)$  diagram, where QUIRC sources with and without the 2MASS counterpart are respectively shown with open and filled symbols. The intrinsic colors of giants and dwarfs are given by the thick solid curves (Tokunaga 2000<sup>[185]</sup>). The emission from the circumstellar disks of cTTSs gives NIR excess on the giant and dwarf colors, hence cTTSs are aligned from bottom left to top right along the cTTS locus in the thick solid line (Meyer, Calvet, & Hillenbrand 1997<sup>[130]</sup>). These colors change their position along the reddening vector as increasing interstellar and circumstellar medium. Therefore, sources between the right and middle reddening lines are reddened cTTSs (*diamonds*), while those between the middle and left reddening lines are reddened wTTSs and some fraction of cTTSs (*triangles*). Sources located to the right of the right reddening line are surrounded by extended envelopes in addition to the disks, hence they are reddened more than disks alone (Strom, Kepner, & Strom 1995<sup>[177]</sup>). These sources (*hexagons*) are classified to be class I protostars.

Cares should be taken that back- and foreground sources are included in our NIR source samples. However, sources with NIR excess (protostars and cTTSs; hexagons and diamonds in Fig. 6.2) can be safely assumed to be YSOs, namely cloud members.

### 6.1.3 Color-magnitude Diagram of QUIRC Sources

In order to estimate the stellar mass and extinction of NIR sources, we employed the  $J/(J-H)$  color-magnitude diagram (Fig. 6.3), where QUIRC sources with significant  $J$ - and  $H$ -band detections are shown in squares. Among them, filled squares are those with NIR excess. All sources are assumed to be at the distance of 450 pc. The intrinsic colors of sources at the age of 1 Myr are shown in the solid curves for the mass range of 0.002–1.4  $M_{\odot}$  (Baraffe et al. 1998<sup>[16]</sup>) and 1.4–7.0  $M_{\odot}$  (Siess, Dufour, & Forestini 2000<sup>[171]</sup>). As a result of the extinction, these intrinsic colors are reddened in the direction of the reddening vector at the top right of Figure 6.3. By moving the position of squares backward along the reddening vector to the 1 Myr isochrone curves, the mass and amount of extinction ( $A_V$ ) can be estimated for each source.

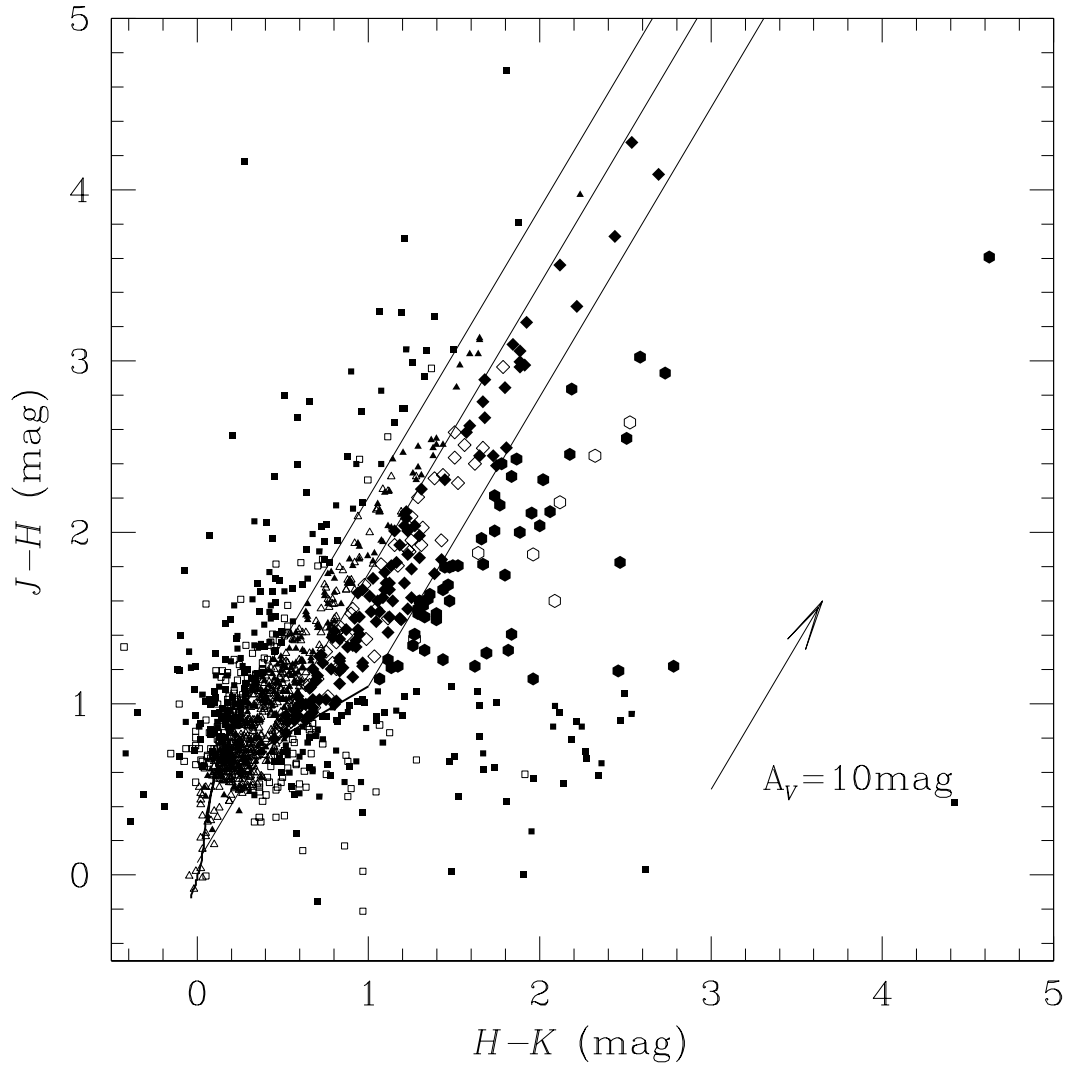


**Figure 6.2:** Color-color diagram of QUIRC sources with significant  $J$ -,  $H$ - and  $K$ -band detections. Open and filled symbols are QUIRC sources with and without 2MASS counterpart, respectively. Hexagons and diamonds are classified as protostars and cTTSs, while triangles are the mixture of main sequence, wTTSs, and cTTSs. Squares are in none of these classifications. The intrinsic colors of dwarfs and giants are given with thick solid curves, while the cTTS locus is with the thick solid line. The arrow at the bottom right gives the reddening vector of  $A_V = 10 \text{ mag}$ . The slope of the reddening lines is assumed to be  $E(J-H)_{\text{reddening}}/E(H-K)_{\text{reddening}} = 1.69$  (Meyer et al. 1997<sup>[130]</sup>). The typical uncertainty of colors is roughly  $\pm 0.1 \text{ mag}$ .

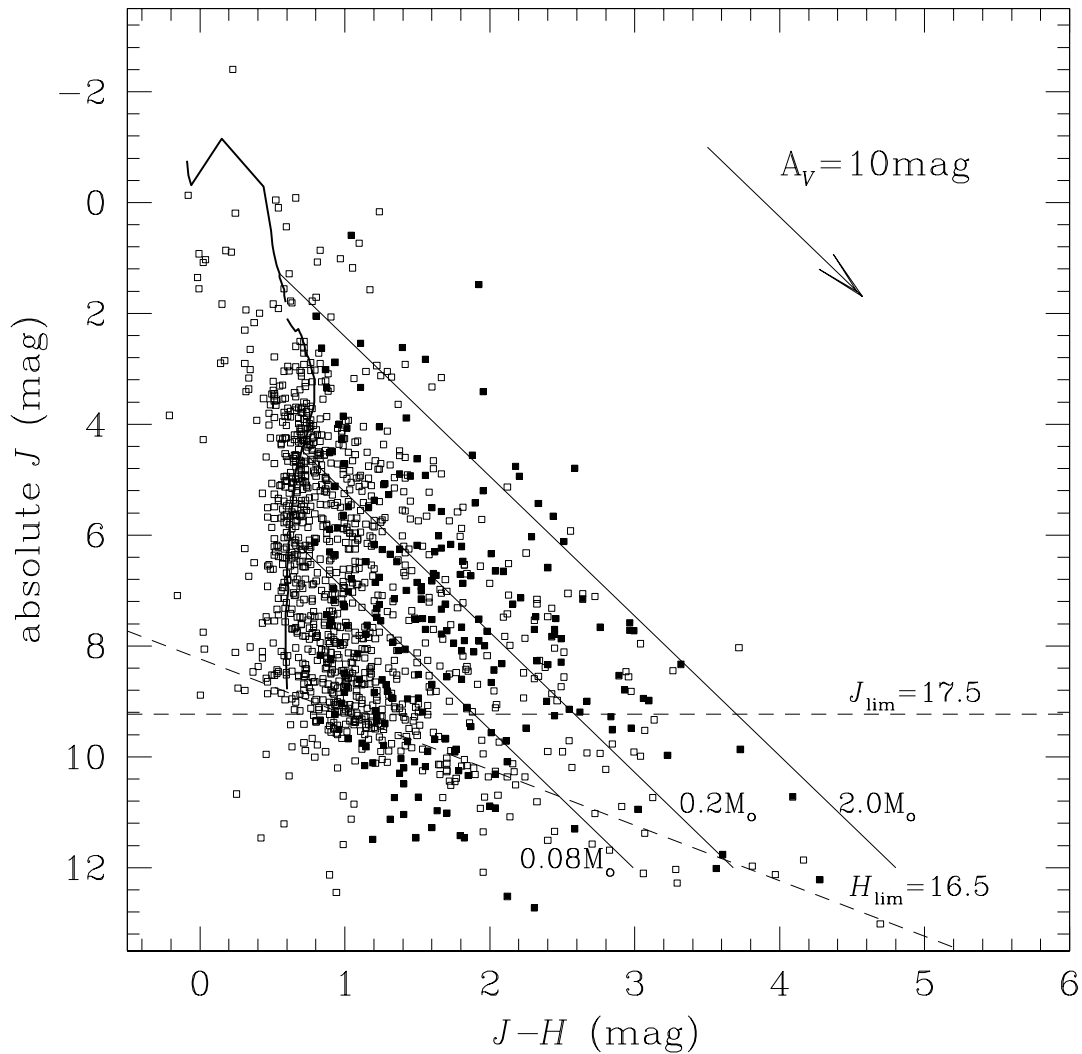


**Figure 6.3:** Color-magnitude diagram of QUIRC sources with significant  $J$ - and  $H$ -band detections (squares). Among them, filled are those with NIR excess. The 1 Myr isochrone curves (thick solid curves) are from Baraffe et al. (1998)<sup>[16]</sup> for  $0.002 M_{\odot} \leq M \leq 1.4 M_{\odot}$  and Siess et al. (2000)<sup>[171]</sup> for  $1.4 M_{\odot} \leq M \leq 7.0 M_{\odot}$ . Two dashed lines show the detection limit of  $J = 17.5$  mag and  $H = 16.5$  mag. The arrow at the top right indicates the reddening vector of  $A_V = 10$  mag. Reddening lines for  $2.0 M_{\odot}$ ,  $0.2 M_{\odot}$ , and  $0.08 M_{\odot}$  are given with solid lines. The typical uncertainty of colors and magnitudes is roughly  $\pm 0.1$  mag.

To examine the distribution of NIR extinction, we made the histogram of the  $K$ -band extinction ( $A_K$ ) in Figure 6.4. The  $A_K$  value of each source was converted from  $A_V$  using  $A_K/A_V = 0.125$  (Mathis 2000<sup>[123]</sup>). Sources in the mass range of  $0.2 M_\odot \leq M \leq 2.0 M_\odot$  and  $J > 17.5$  mag (Fig. 6.3) are used to construct the histogram. The observational bias in favor of low extinction sources is thus avoided for  $A_V < 20$  mag ( $A_K < 2.5$  mag). The typical  $A_K$  was estimated to be  $\sim 1$  mag.

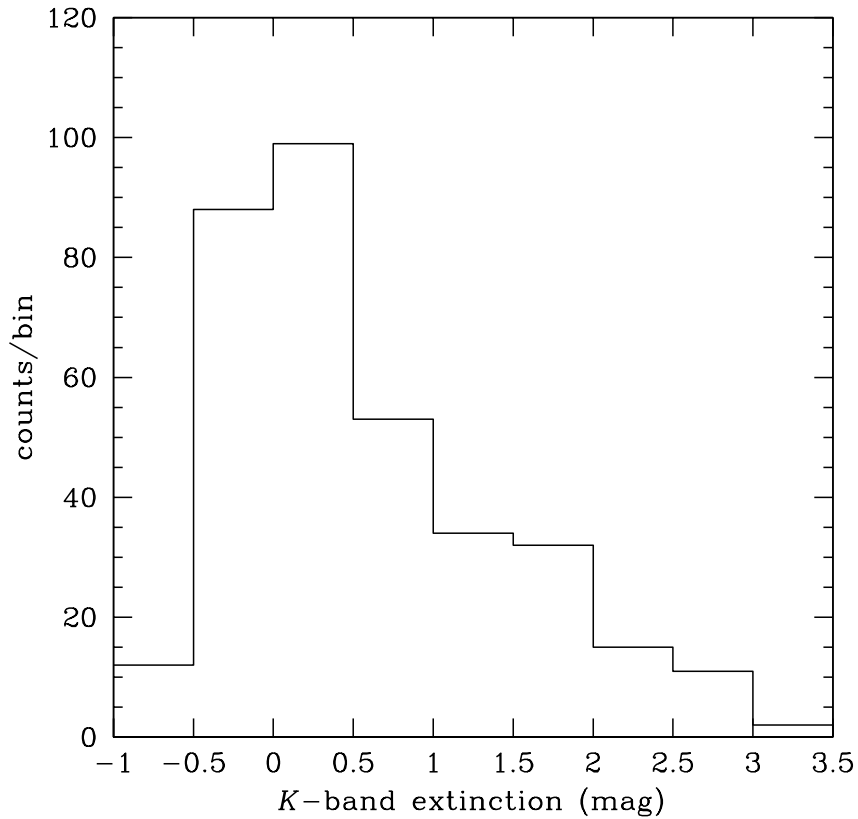


**Figure 6.4:** Histogram of the  $K$ -band extinction ( $A_K$ ) derived from NIR sources in the mass range of  $0.2 M_\odot < M < 2.0 M_\odot$  and  $J > 17.5$  mag. The  $A_V$  value of each source was estimated from Figure 6.3, and converted to  $A_K$  using  $A_K/A_V = 0.125$  (Mathis 2000<sup>[123]</sup>). The histogram was fitted with an exponential function in the positive  $A_K$  region to derive the typical value of  $A_K \sim 1$  mag.

## 6.2 The NIR-IDed X-ray Sources

### 6.2.1 Cloud Membership

Krishnamurthi et al. (2001)<sup>[108]</sup> observed the core of the Pleiades star cluster with *Chandra* for 36 ks and found that a significant fraction of X-ray sources are likely to be AGNs. We examined the contamination of our X-ray samples by AGNs and concluded that there is only a negligible number of AGNs among NIR-IDed X-ray sources for the following reason.

The number count of galaxies ( $N$ ) per square degree per magnitude at a certain  $K$ -band magnitude ( $K$ ) is given by

$$\frac{dN}{dK} = 4000 \times 10^{\alpha(K-17)}, \quad (6.4)$$

where  $\alpha = 0.67$  for  $10 \text{ mag} < K < 17 \text{ mag}$  (Tokunaga 2000<sup>[185]</sup>). The number of galaxies in the range of  $K_{min} \text{ mag} < K < K_{max} \text{ mag}$  is then estimated by

$$\int_{K_{min}}^{K_{max}} \frac{dN}{dK} dK = \frac{4000}{\alpha \log 10} \{10^{\alpha(K_{max}-17)} - 10^{\alpha(K_{min}-17)}\}. \quad (6.5)$$

The NIR counterparts of the *Chandra* sources have a  $K$ -band magnitude in  $6 \text{ mag} < K < 15 \text{ mag}$ . We substituted  $K_{min} = 6$  and  $K_{max} = 15$  for simplicity, though the equation (6.5) is valid only for  $K_{min} > 10 \text{ mag}$ . Still, this gives us a good estimate since the second term of the right-hand side is negligible compared to the first term in this case. Considering the *Chandra* FOV, the estimated number of galaxies in the range of  $6 \text{ mag} < K < 15 \text{ mag}$  is  $\sim 12$ . This is only  $\sim 0.8\%$  of all the NIR sources in the same magnitude range. Moreover, the background galaxies in this direction suffer a significant extinction due to dense ISM, which makes the contribution of extragalactic sources to our NIR samples even smaller. This excludes the possibility of NIR-IDed X-ray sources to be extragalactic AGNs.

The KLF of NIR-IDed X-ray sources (Fig. 6.1) indicates that most of the X-ray sources have the  $K$ -band magnitude of  $K < 14 \text{ mag}$ , where the contamination by back- and foreground galactic sources is negligible. We hereafter regard all the NIR-IDed X-ray sources as cloud members.

### 6.2.2 Evolutional Class Estimates

Table A.1 lists the  $J$ -band magnitude and  $(J-H)$  and  $(H-K)$  colors of NIR-IDed *Chandra* sources in the CIT color system. Using these colors, we first made the  $(J-H)/(H-K)$



color-color diagram (Fig. 6.5), where NIR-IDed *Chandra* sources are plotted. Filled and open symbols are QUIRC-IDed and 2MASS-IDed *Chandra* sources. The arrows on symbols indicate the lower limit of colors; i.e., the upward arrows are due to the lack of the *J*-band detections and the rightward arrows are due to the saturation in the *K* band. Following the classification scheme addressed in the previous section, we picked up protostars, cTTSs, and wTTSs (*hexagons*, *diamonds*, and *triangles*). Some sources can not be classified in any of these classes either because they are out of the three regions (*squares*) or they have no *J*-, *H*-, or both band detections.

We have to keep in mind that the *K*-band magnitude is not always sensitive enough to detect excess emissions from circumstellar disks. Recent *Infrared Space Observatory* observations on R Coronae Australis, Chamaeleon, and  $\rho$  Ophiuchi dark clouds indicate that the classification based only on the *J*, *H*, and *K*-band data underestimates the number of YSOs with disks (Olofsson et al. 1999<sup>[144]</sup>; Persi et al. 2000<sup>[152]</sup>; Bontemps et al. 2001<sup>[24]</sup>). Haisch et al. (2001)<sup>[76]</sup> combined the MIR with NIR photometry on NGC 2024 and reported that about one-third of class II sources are recognized not to have excess emissions with the  $(J-H)/(H-K)$  diagram alone, hence are classified as class III sources.

In classifying the NIR-IDed X-ray sources, therefore, we additionally used  $H_\alpha$  emission (Herbig & Bell 1988<sup>[83]</sup>) and *UV* excess (Rebull et al. 2000<sup>[160]</sup>) data to complement the NIR excess data. The  $H_\alpha$  emission line is directly related to disks and its equivalent width is used to discriminate cTTSs ( $>10 \text{ \AA}$ ) and wTTSs ( $<10 \text{ \AA}$ ). The NIR and UV excess data work complementarily. The former is sensitive to disks of earlier-type sources with higher photospheric temperature, while the latter is sensitive to later-type sources with lower temperature, because of the contrast between the photosphere and disk colors. The UV excess of cTTSs is considered to originate from the boundary layer of an accretion disk (Hartigan et al. 1991<sup>[79]</sup>), making it another indicator of disk existence.

Among sources classified as wTTSs in the  $(J-H)/(H-K)$  color-color diagram, four (I13, I248, I324, and I334) and eleven (I111, I122, I150, I200, I237, I308, I319, I322, I328, I332, and S4) sources are reclassified into cTTSs based respectively on their  $H_\alpha$  and *UV* excess emissions. Consequently, we identified 13 protostars, 59 cTTSs, and 170 wTTSs among 278 NIR-IDed X-ray sources. The result of the classification is summarized in Table A.1.

We examined the position of *Chandra* sources separately for each class (Fig. 6.6). Protostars are clearly concentrated along the 1.3 mm ridge. Since cores seen in the millimeter continuum are the sites of on-going star formation, this reinforces the idea that they are

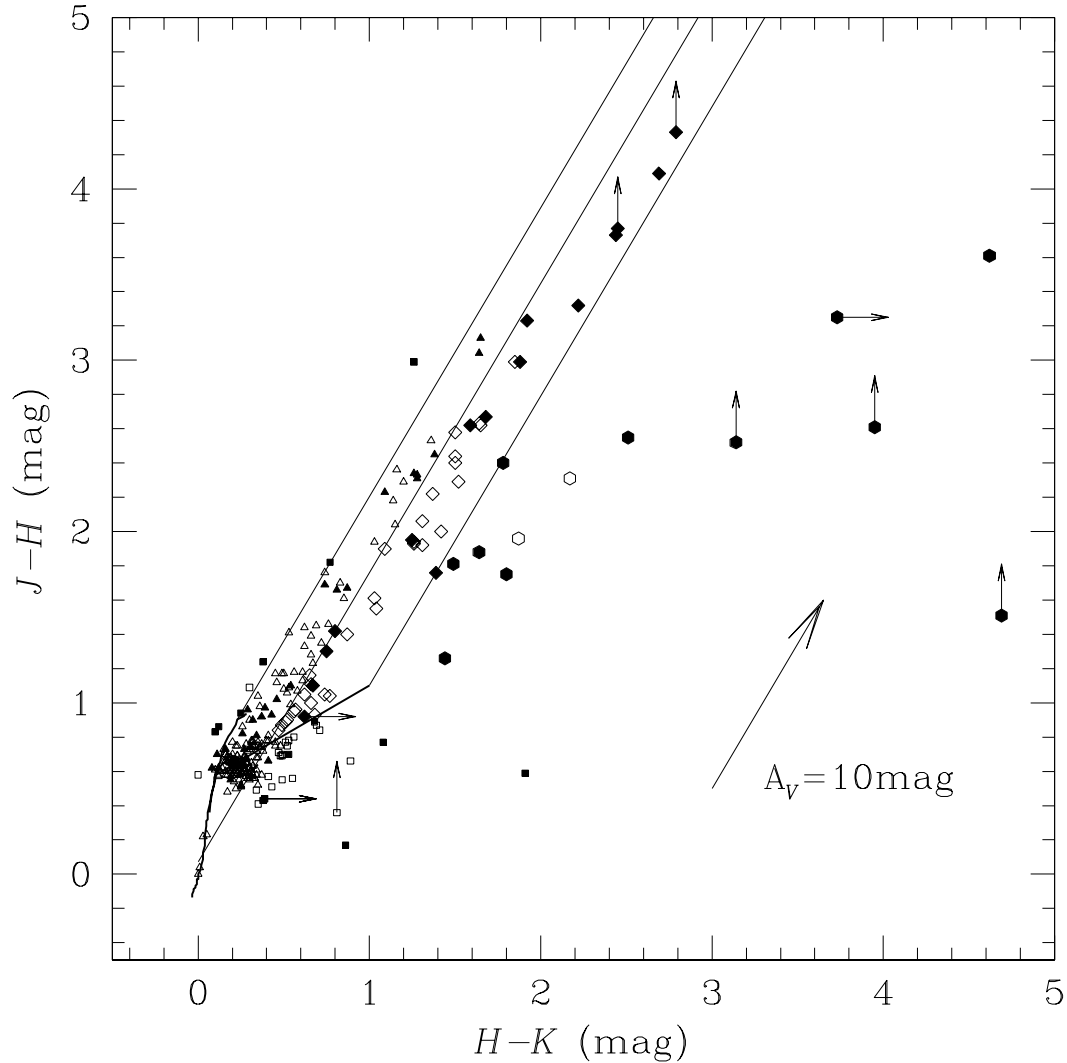


**Figure 6.5:** Color-color diagram of NIR-IDed X-ray sources. The 2MASS-IDed and QUIRC-IDed *Chandra* sources are plotted with open and filled symbols, respectively. Hexagons, diamonds, and triangles are classified to be protostars, cTTSs, and wTTSs, while squares are in none of these classes. The intrinsic colors of dwarfs and giants are given with solid curves, while the cTTS locus is with solid line. The arrow at the bottom right gives the reddening vector of  $A_V = 10$  mag. The slope of the reddening lines is assumed to be  $E(J-H)_{\text{reddening}}/E(H-K)_{\text{reddening}} = 1.69$  (Meyer et al. 1997<sup>[130]</sup>). The typical uncertainty is roughly  $\pm 0.1$  mag.

YSOs at the very early stage. Most of protostars also accompany apparent NIR nebulosity in the  $K$ -band image, which indicates that they are deeply embedded sources. The spatial distribution of cTTSs is also correlated with the ridge, although wTTSs and X-ray sources with no NIR counterpart (Fig. 6.8) are not.

### 6.2.3 Mass and Bolometric Luminosity Estimates

We next made the  $J/(J-H)$  color-magnitude diagram (Fig. 6.7), where NIR-IDed *Chandra* sources are shown in squares. Among them, filled squares are those with NIR excess. Squares with the rightward arrows indicate the saturation in the  $H$  band, and those with both the rightward and the downward arrows have  $H$ - but not  $J$ -band detection.

We categorized the NIR-IDed X-ray sources into four groups based on their mass. Using this diagram, we can estimate the mass with the  $J$ -band magnitude because nearly all the emission in this band is photospheric for late-type pre-main-sequence stars (Strom & Strom 1994<sup>[176]</sup>). Magnitudes in the longer wavelengths are affected by NIR excess emissions from circumstellar dust, while those in the shorter wavelengths are by UV excess emissions from the disk-boundary layer, giving a significant overestimate of the mass (Gagné et al. 1995<sup>[61]</sup>).

Using the theoretical calculations of isochrone curves by Baraffe et al. (1998)<sup>[16]</sup> for sources in  $0.002 M_{\odot} \leq M \leq 1.4 M_{\odot}$  and Siess et al. (2000)<sup>[171]</sup> in  $1.4 M_{\odot} \leq M \leq 7.0 M_{\odot}$ , we estimated the mass (Table A.1), which is quantized depending on the grid of these computations. The bolometric luminosity is also derived for each source in the same way.

Among 278 NIR-IDed X-ray sources, 268 have significant  $J$ - and  $H$ -band detections. These sources are separated into high mass (HM) with  $M > 10 M_{\odot}$ , intermediate mass (IM) with  $10 M_{\odot} > M > 2.0 M_{\odot}$ , low mass (LM) with  $2.0 M_{\odot} > M > 0.2 M_{\odot}$ , and very low mass (VLM) sources with  $M < 0.2 M_{\odot}$ . For sources with  $M > 4.0 M_{\odot}$ , where the  $J$ -band magnitude is insensitive to the mass, we assumed that they have  $M = 4.0 M_{\odot}$  except for I242, which we classified into HM based on its spectroscopy observations (Kukarkin et al. 1971<sup>[111]</sup>). As a consequence, we found 1 HM, 21 IM, 139 LM, and 107 VLM sources. The spatial distributions of these sources are given separately for each mass range in Figure 6.8.

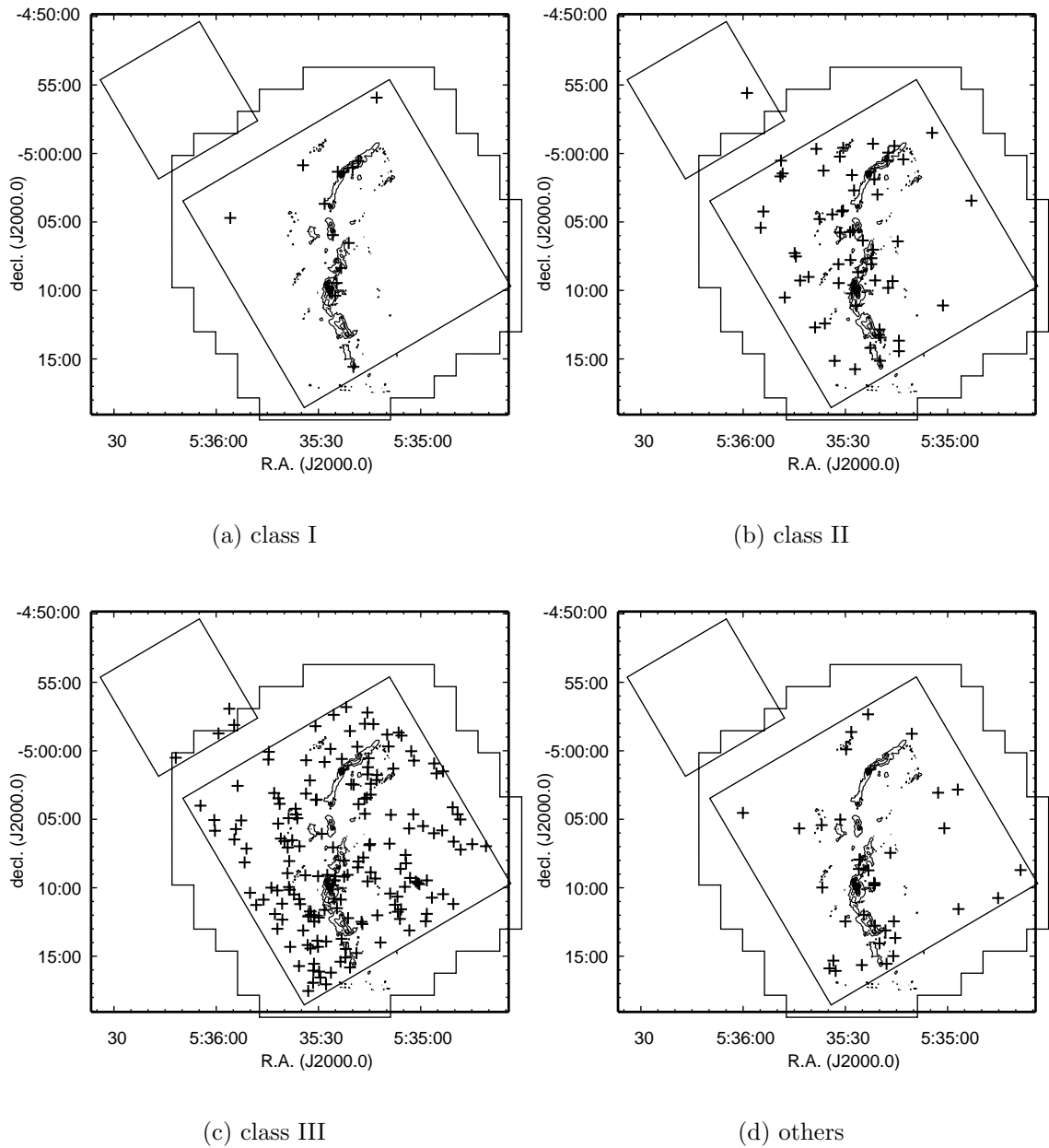


**Figure 6.6:** Spatial distribution of *Chandra* sources (*pluses*) separately for (a) class I (protostars), (b) class II (cTTs), (c) class III (wTTs), and (d) NIR-Ided sources that are classified into none of these three classes. The FOVs of ACIS and QUIRC are shown with solid lines. The contours in each panel are the 1.3 mm intensity (Chini et al. 1997<sup>[35]</sup>).

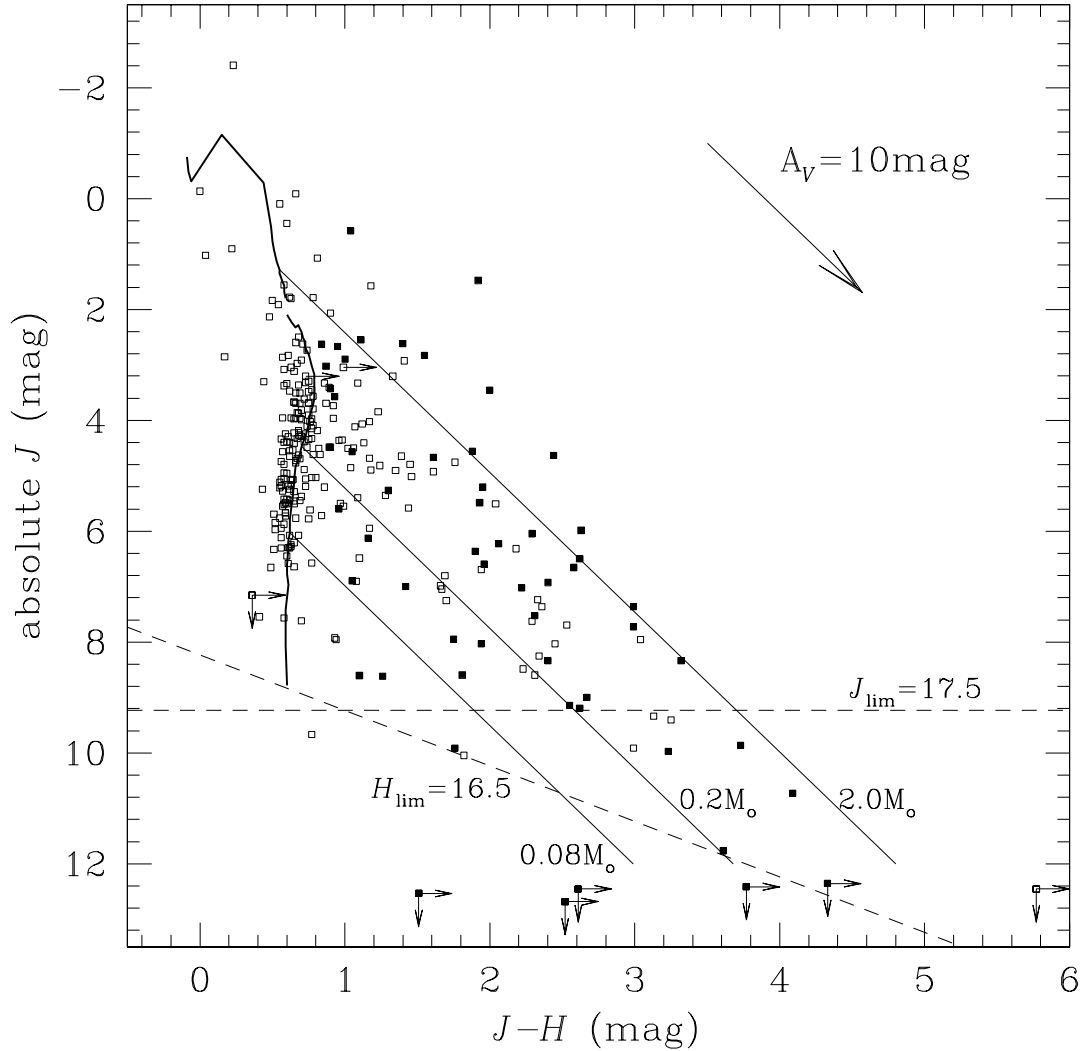


**Figure 6.7:** Color-magnitude diagram of NIR-IDed *Chandra* sources (squares). Among them, filled ones are those with NIR excess. The 1 Myr isochrone curves (thick solid curves) are from Baraffe et al. (1998)<sup>[16]</sup> for  $0.002 M_{\odot} \leq M \leq 1.4 M_{\odot}$  and from Siess et al. (2000)<sup>[171]</sup> for  $1.4 M_{\odot} \leq M \leq 7.0 M_{\odot}$ . Two dashed lines show the detection limit of  $J = 17.5$  mag and  $H = 16.5$  mag. The arrow at the top right indicates the reddening vector of  $A_V = 10$  mag. The reddening lines for  $2.0 M_{\odot}$ ,  $0.2 M_{\odot}$ , and  $0.08 M_{\odot}$  are given with solid lines. The typical uncertainty is roughly  $\pm 0.1$  mag.

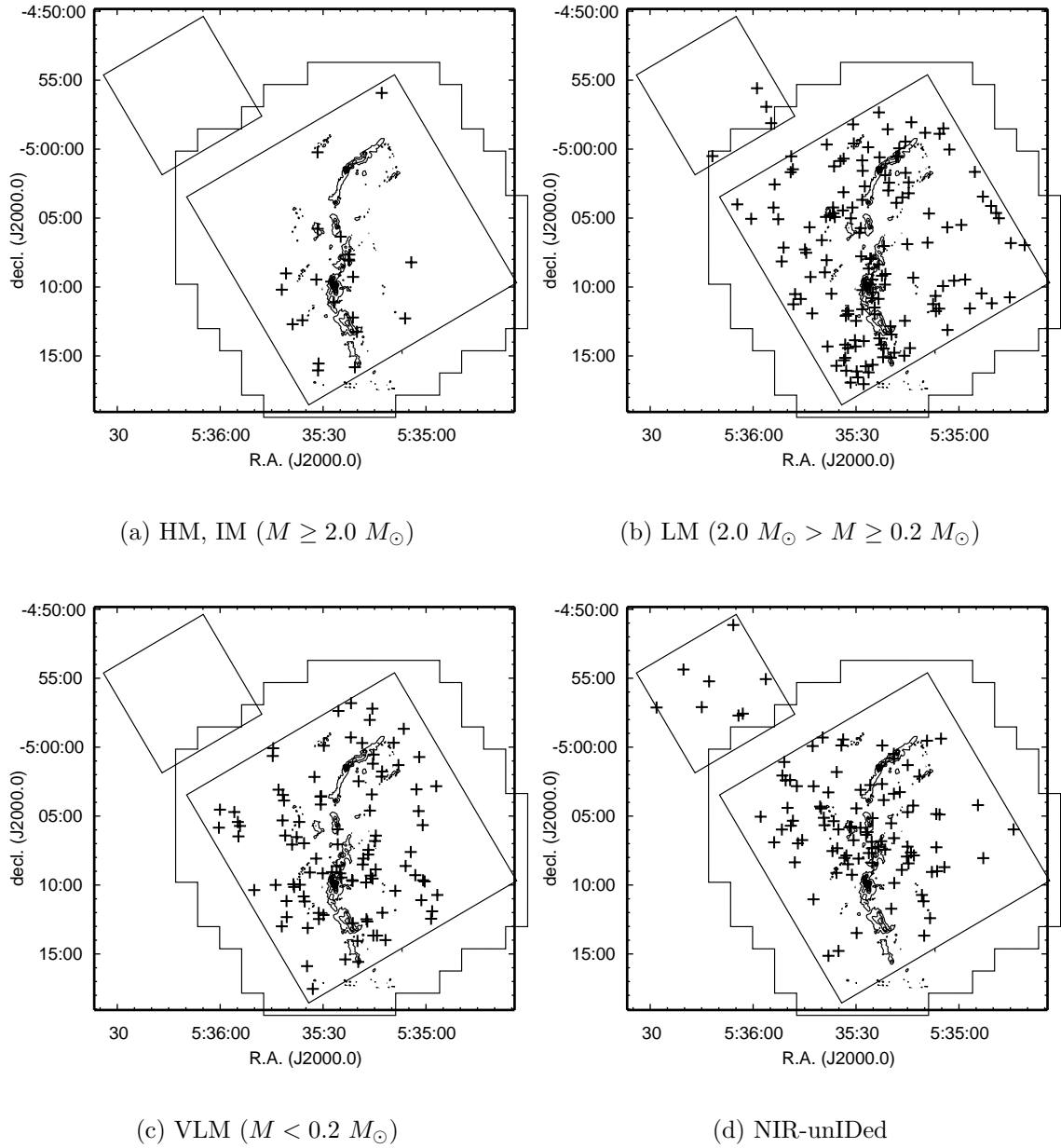


**Figure 6.8:** Spatial distribution of *Chandra* sources (*pluses*) separately for (a) HM and IM ( $M \geq 2.0 M_{\odot}$ ) (b) LM ( $2.0 M_{\odot} > M \geq 0.2 M_{\odot}$ ), (c) VLM ( $M < 0.2 M_{\odot}$ ), and (d) NIR-unIDed X-ray sources. The FOVs of ACIS and QUIRC are shown with solid lines. The contours in each panel are the 1.3 mm intensity (Chini et al. 1997<sup>[35]</sup>).

# Chapter 7

## NIR-IDed X-ray Sources: (2) X-ray Properties

### Contents

---

<b>7.1</b>	<b>Temporal Analysis</b> . . . . .	<b>132</b>
<b>7.2</b>	<b>Spectral Analysis</b> . . . . .	<b>139</b>
7.2.1	Spectrum Models and Fittings . . . . .	139
7.2.2	One-temperature Plasma Fittings . . . . .	140
7.2.3	Two-temperature Plasma Fittings . . . . .	151
7.2.4	Time-sliced Spectroscopy . . . . .	159
<b>7.3</b>	<b>Relations between Parameters</b> . . . . .	<b>162</b>
7.3.1	X-ray absorption versus NIR extinction . . . . .	162
7.3.2	X-ray counts versus X-ray flux . . . . .	162
7.3.3	X-ray counts versus X-ray luminosity . . . . .	162

---

In this chapter, we discuss the X-ray properties of NIR-IDed *Chandra* sources. In order to concentrate on sources with enough statistics, we deal with bright ACIS-I sources in this and the following chapters. In Sect. 7.1, we conduct temporal analysis and illustrate that about half of them show flux variability including flares. In Sect. 7.2, we perform spectral analysis. By fitting with one-temperature thin-thermal plasma model, we derive the plasma temperature ( $k_{\text{B}}T$ ), X-ray luminosity ( $L_{\text{X}}$ ), and the amount of absorption ( $N_{\text{H}}$ ). When rejected, we apply two-temperature plasma model to fit the spectra. About 90% of sources are fit with either by one-temperature or two-temperature plasma model. Finally, in Sect. 7.3, we examine the relations among these parameters.

## 7.1 Temporal Analysis

One of the most notable characteristics of the X-ray emissions from YSOs is rapid variability of their X-ray light curves. Flare episodes of fast rise and slow decay are often observed. In order to pick up X-ray sources with variability, we applied a simple temporal analysis for the *Chandra* sources. The XRONOS package<sup>1</sup> was used for the following procedures.

We concentrated our temporal analysis on bright ACIS-I sources so that we can ignore the backgrounds. Figure 7.1 shows the distribution of X-ray counts (0.5–8.0 keV) and  $S/N$ , where  $S$  and  $N$  are the source and background counts in the 0.5–8.0 keV range. The background counts were derived using the values in Table 4.1 and normalized by the area of source accumulation region and the exposure time. We picked up sources with more counts than 100 and higher  $S/N$  than 10 as the samples for temporal analysis. We hereafter call them “bright (T)” sources, while the remaining sources are called “faint (T)” sources. Among 278 NIR-IDed ACIS-I sources, 120 are bright (T) and 158 are faint (T).

The X-ray counts of bright (T) sources were binned with three binning sizes (100 s bin<sup>-1</sup>, 1000 s bin<sup>-1</sup>, and 10000 s bin<sup>-1</sup>) to construct light curves. These light curves were fitted with a constant flux model. The  $\chi^2$  value was derived for each fitting with

$$\chi^2 = \sum_{i=1}^N \left( \frac{F_{\text{data}}^{(i)} - F_{\text{model}}^{(i)}}{\Delta F_{\text{data}}^{(i)}} \right)^2, \quad (7.1)$$

where  $F_{\text{data}}^{(i)}$  and  $F_{\text{model}}^{(i)}$  are the count rate of the data and the model in the  $i$ 'th time bin, and  $\Delta F_{\text{data}}^{(i)}$  is the uncertainty of  $F_{\text{data}}^{(i)}$ . The  $\chi^2$  value follows the chi square distribution of

<sup>1</sup>See <http://heasarc.gsfc.nasa.gov/docs/xanadu/xronos/xronos.html>.



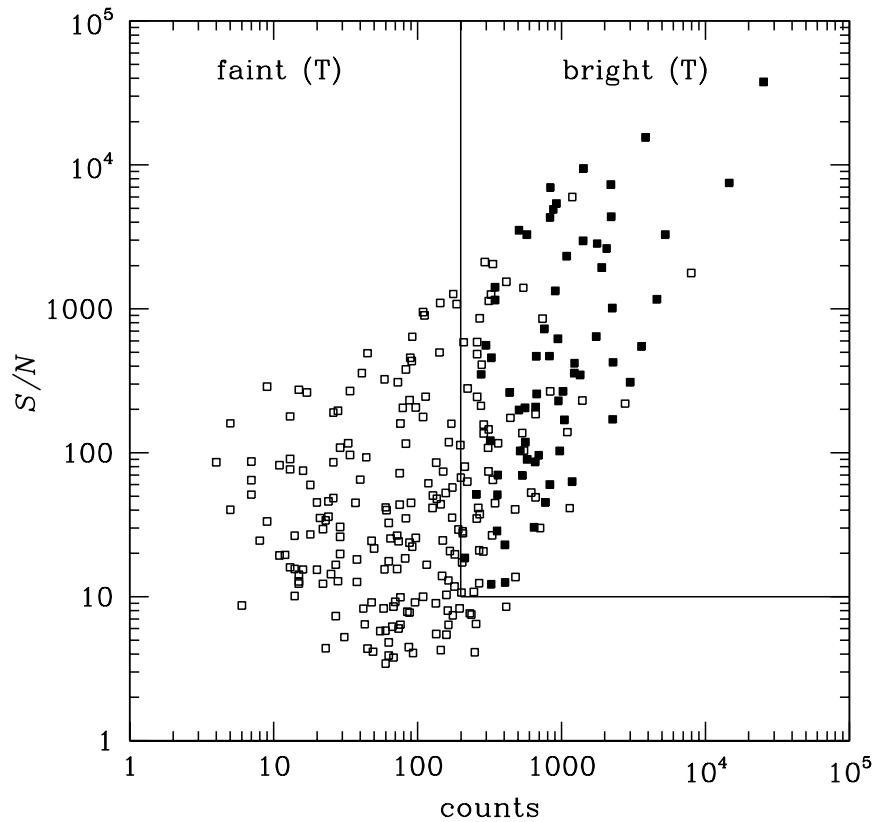


**Figure 7.1:** X-ray counts (0.5–8.0 keV) and  $S/N$  (0.5–8.0 keV) of NIR-IDed ACIS-I sources. Sources with more counts than 200 and higher  $S/N$  than 10 (120 sources) are bright (T) sources, for which the temporal analysis was conducted. The remaining 158 sources are faint (T) sources. Variable sources among bright (T) sources are marked filled.

$(N - 1)$  degrees of freedom;  $\chi_{N-1}^2(x)$ . The upper probability for the null hypothesis ( $\alpha$ ) was thus calculated as

$$\alpha = \int_{\chi^2}^{\infty} \chi_{N-1}^2(x) dx. \quad (7.2)$$

We recognized the null hypothesis (the constant count rate) is rejected; i.e., the light curve is variable, if  $\alpha < 0.01$  in at least one binning size. Consequently, we picked up 66 (55%) variable light curves among bright (T) sources.

Figures 7.2–7.6 show the background-unsubtracted light curves of all the variable X-ray sources. Note that the background count rate is less than the total count rate by more than 10 times. Many of the light curves show typical flare-like events.

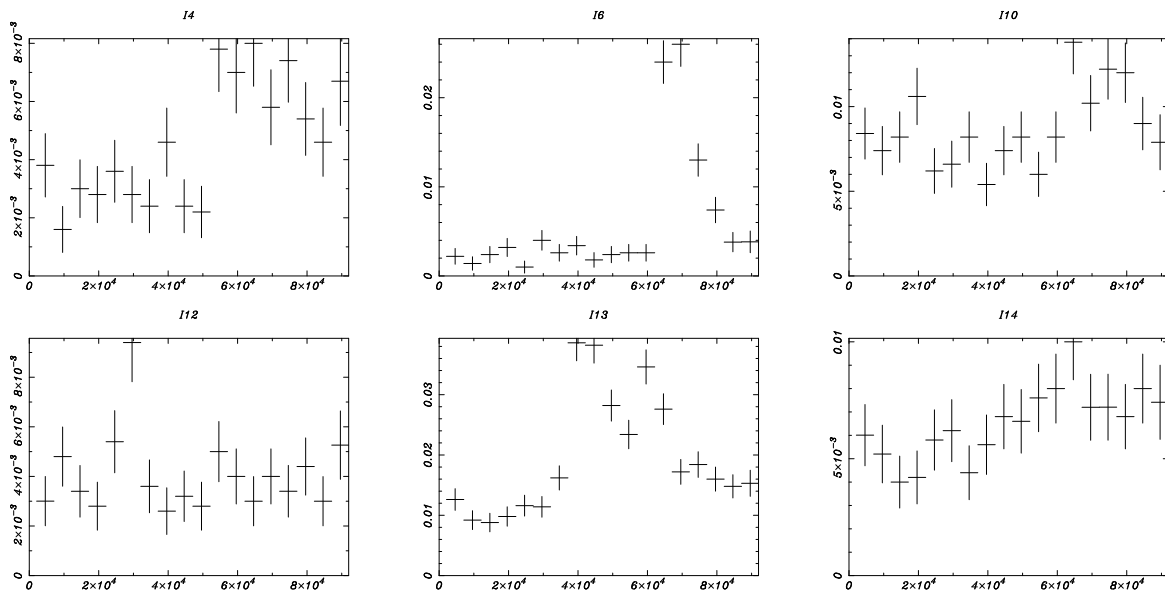


**Figure 7.2:** Light curves of variable bright (T) NIR-IDed *Chandra* sources (I4–I14) with the binning of  $5000 \text{ s bin}^{-1}$ . Light curves are plotted over the count rate ( $\text{s}^{-1}$ ; *vertical axis*) versus the time from the start of the observation (s; *horizontal axis*) plane.

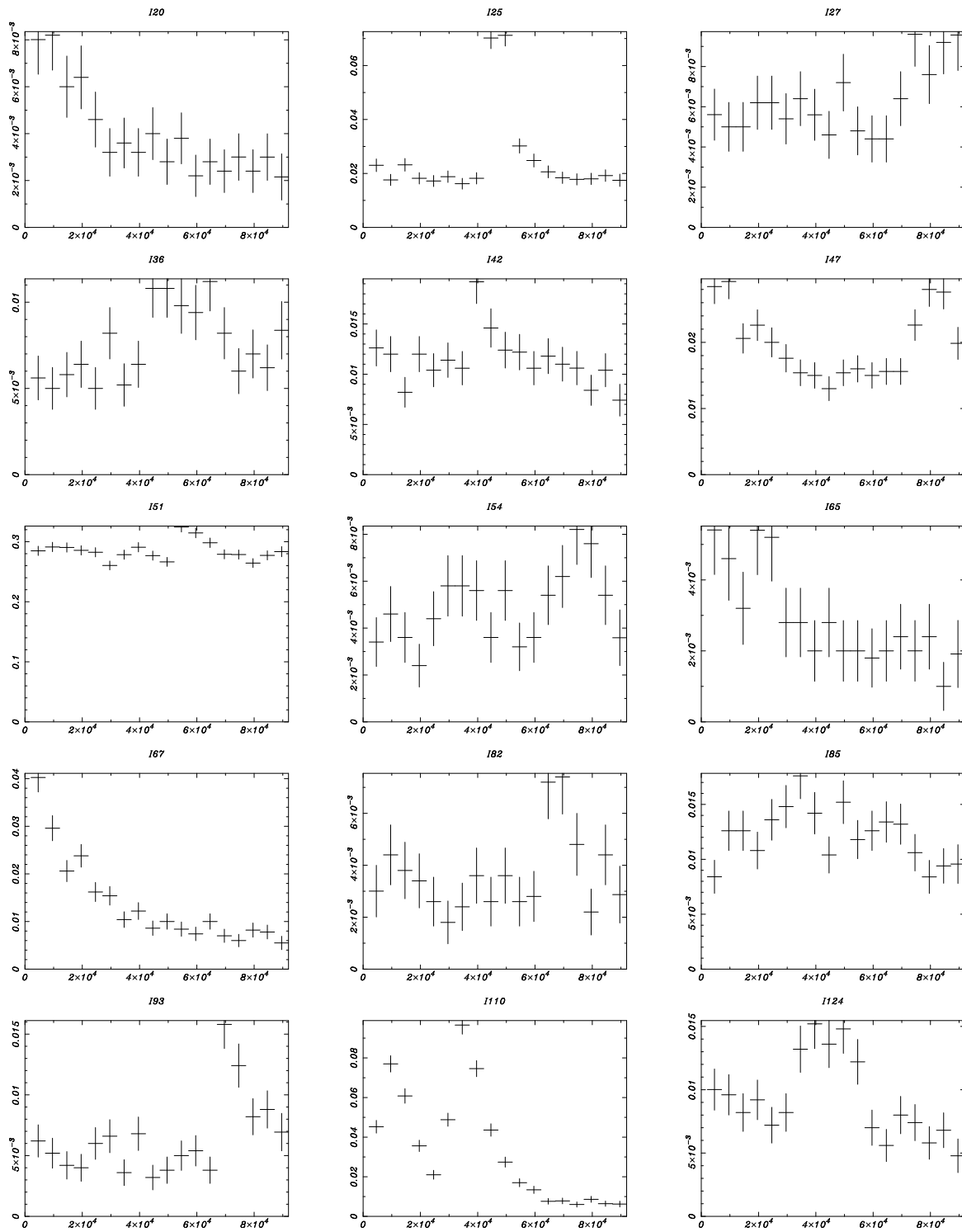


**Figure 7.3:** Light curves of variable bright (T) NIR-IDed *Chandra* sources (I20–I124).

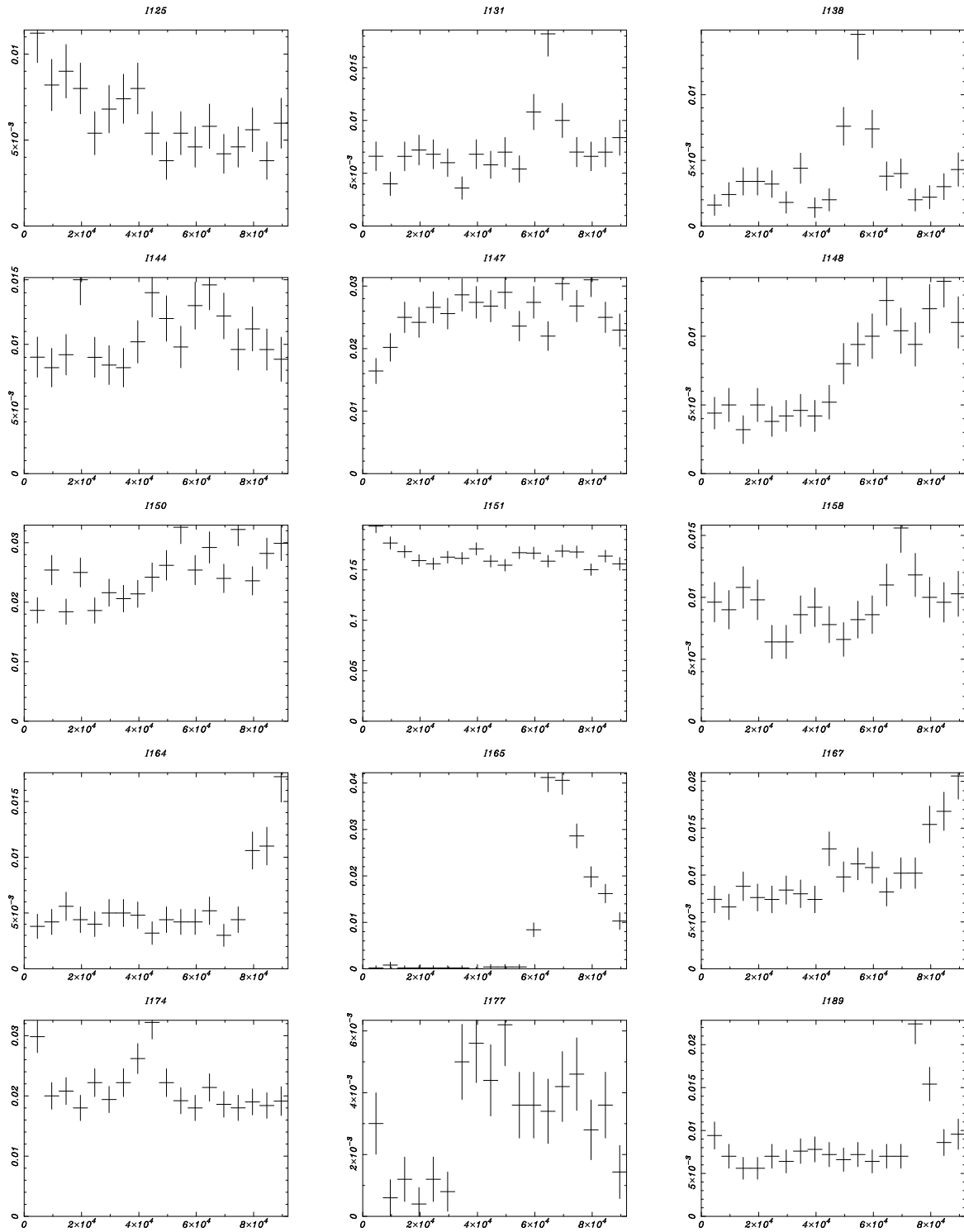


**Figure 7.4:** Light curves of variable bright (T) NIR-IDed *Chandra* sources (I125–I189).

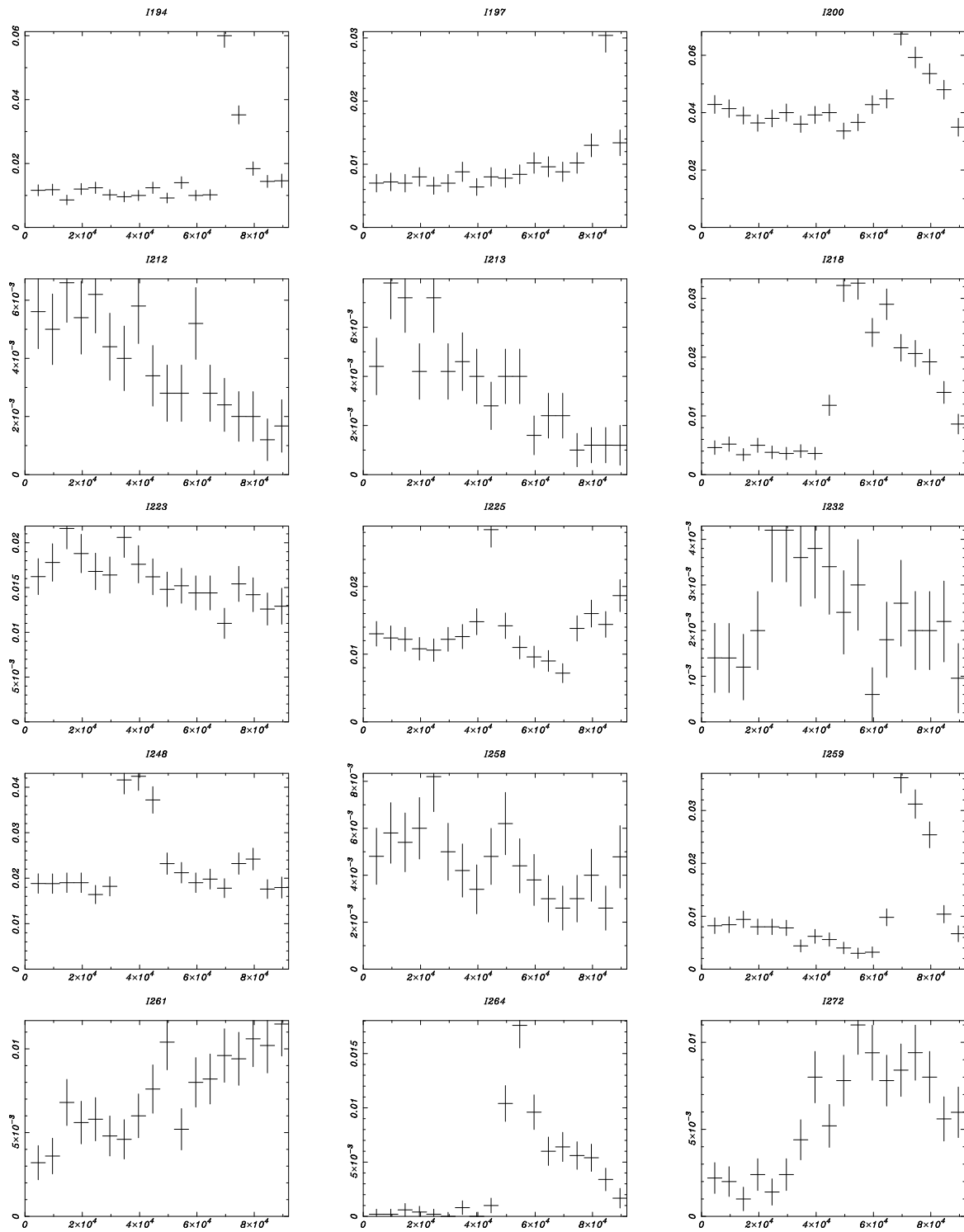


**Figure 7.5:** Light curves of variable bright (T) NIR-IDed *Chandra* sources (I194–I272).

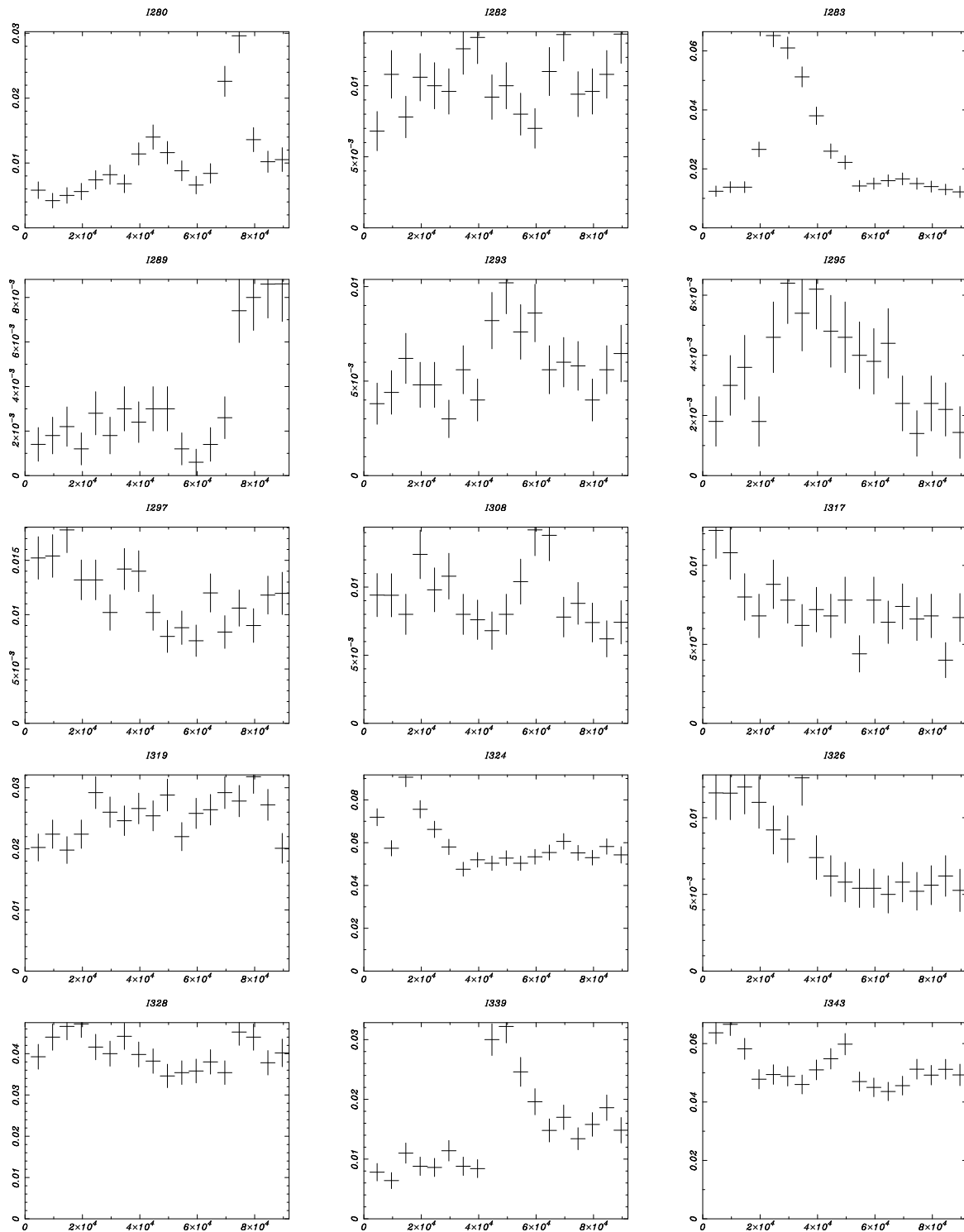


**Figure 7.6:** Light curves of variable bright (T) NIR-IDed *Chandra* sources (1280–1343).

## 7.2 Spectral Analysis

### 7.2.1 Spectrum Models and Fittings

As almost all the NIR-IDed X-ray sources are considered to be YSOs and the X-ray emissions from YSOs are of plasma origin (Feigelson & Montmerle 1999<sup>[53]</sup>), we fitted the X-ray spectra of NIR-IDed sources with the mekal model convolved with the wabs model.

The mekal model implements the X-ray emissions from thermal plasma at the optically thin limit; i.e., the plasma is transparent to its own X-ray radiation. The plasma consists of electrons and collisionally ionized and excited atoms. When an electron is accelerated by the electric field around an atom, it emits X-rays known as “bremsstrahlung”. When the bremsstrahlung is integrated over all electrons at a thermal equilibrium with a Maxwellian velocity distribution, the intensity of the radiation  $I(E, T)$  at the energy  $E$  and the plasma temperature  $T$  is expressed as

$$I(E, T) \propto g(E, T) Z^2 n_e n_i (k_B T)^{-\frac{1}{2}} \exp\left(-\frac{E}{k_B T}\right), \quad (7.3)$$

where  $n_e$  and  $n_i$  are the number density of the electrons and the ions,  $Z$  is the charge of the ion, and  $g(E, T)$  is the Gaunt factor having a weak dependence on  $E$  and  $T$ . Line emissions from excited and ionized atoms are added on the continuum radiation. The calculation of thin-thermal plasma spectrum in the mekal model is based on Mewe, Gronenschild, & van den Oord (1985)<sup>[127]</sup>, Mewe, Lemen, & van den Oord (1986)<sup>[128]</sup>, and Kaastra (1992)<sup>[102]</sup> with Fe L-shell line emissions improved by Liedahl, Osterheld, & Goldstein (1995)<sup>[116]</sup>. The continuum emissions as well as line emissions from atoms (C, N, O, Ne, Na, Mg, Al, Si, S, Ar, Ca, Fe, and Ni) are included. Free parameters of the model are the electron temperature ( $k_B T$  keV), metallicity of elements ( $Z_C$ ,  $Z_N$ ,  $Z_O$ , and so on), and emission measure ( $EM = \int n_e n_H dV$  cm<sup>-3</sup> where  $n_e$  and  $n_H$  are the electron and hydrogen density and  $V$  is the emitting volume). Given the values of  $k_B T$ ,  $EM$ , and the distance to the source (450 pc), the X-ray luminosity ( $L_X$  ergs s<sup>-1</sup>) is determined.

The wabs model implements the photoelectric absorption by cold interstellar medium and is used to derive the amount of interstellar absorption using absorption lines in the X-ray spectra. In most cases, C, N, and O lines in the soft X-ray band dominate fittings. The calculation is based on the Wisconsin cross-sections that include photoelectric absorption cross-sections of major cosmic elements (Morrison & McCammon 1983<sup>[136]</sup>). Neither

Thomson nor Compton scattering is considered. The spectral intensity of the model ( $M$ ) at a given energy ( $E$ ) is described as

$$M(E) = \exp(-p_1\sigma(E)), \quad (7.4)$$

where  $\sigma(E)$  is the effective photoelectric absorption cross-section that is derived by converting all the cross-sections of major elements into the hydrogen equivalent and averaging them out. The amount of absorption ( $p_1$ ) is thus determined as the equivalent hydrogen column density ( $N_{\text{H}} \text{ cm}^{-2}$ ).

The cosmic abundances used in the mekal and wabs models are respectively based on the results by Anders & Grevesse (1989)<sup>[4]</sup> and Anders & Ebihara (1982)<sup>[3]</sup>, who derived values with meteorites and chondrites in the solar system and the solar photosphere and corona.

The combined model of mekal and wabs is further convolved with the optics and detector responses (Auxiliary Response Function [ARF] and Redistribution Matrix Function [RMF], respectively). Both of ARF and RMF for *Chandra*/ACIS are provided by *Chandra* X-ray Center. This convolution is fitted to the spectra that were constructed by binning the X-ray photons along the energy with 20 counts  $\text{bin}^{-1}$  (for sources of more than 200 counts) or 10 counts  $\text{bin}^{-1}$  (for sources of less than 200 counts). Again, the  $\chi^2$  value was calculated for each fitting trial as

$$\chi^2 = \sum_{i=1}^N \left( \frac{E_{data}^{(i)} - E_{model \otimes ARF \otimes RMF}^{(i)}}{\Delta E_{data}^{(i)}} \right)^2, \quad (7.5)$$

where  $E_{data}^{(i)}$  and  $E_{model \otimes ARF \otimes RMF}^{(i)}$  are the spectrum intensity ( $\text{s}^{-1} \text{ keV}^{-1}$ ) of background-subtracted data and the convolution of the model, ARF, and RMF in the  $i$ 'th energy bin.  $\Delta E_{data}^{(i)}$  is the uncertainty of  $E_{data}^{(i)}$  and is calculated as  $\sqrt{E_{data}^{(i)}}$ . The upper probability for the null hypothesis ( $\alpha$ ) for the minimum  $\chi^2$  value was used to discriminate whether a fitting is acceptable or not. The XSPEC package<sup>2</sup> was used for all these procedures.

## 7.2.2 One-temperature Plasma Fittings

We concentrated our spectral analysis on bright ACIS-I sources in the same way as our temporal analysis. Figure 7.7 shows the distribution of X-ray counts (0.5–8.0 keV) and  $S/N$  (2.0–8.0 keV), which is defined as the ratio of the source and the background counts in

<sup>2</sup>See <http://heasarc.gsfc.nasa.gov/docs/xanadu/xspec/index.html>.



the 2.0–8.0 keV range. Unlike Figure 7.1, we used the  $S/N$  values in the hard band (2.0–8.0 keV). This is because the spectrum in this energy range is important to see whether a source has hard X-ray component in addition to the soft component, nevertheless the source spectrum can be more easily contaminated by the background spectrum in this band. We defined “bright (S)” sources for those with more counts than 50 and larger  $S/N$  than 10 and “faint (S)” for the remaining sources among the 278 NIR-IDed ACIS-I sources. The former consists of 142 (51%) samples while the latter of 136 (49%).

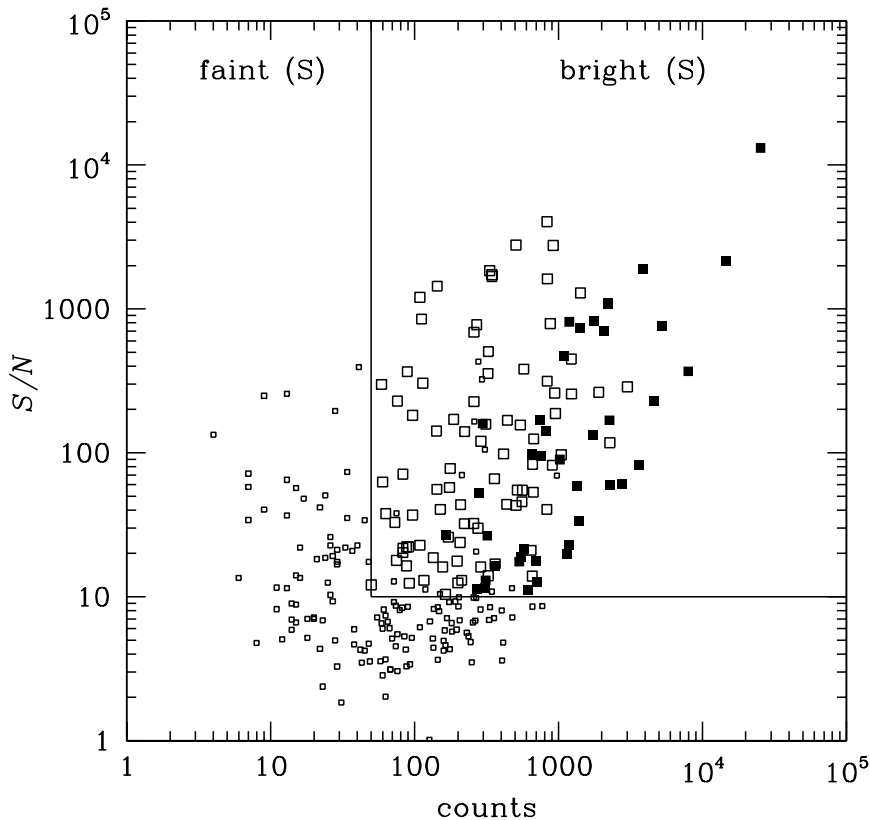


**Figure 7.7:** X-ray counts (0.5–8.0 keV) and  $S/N$  (2.0–8.0 keV) of NIR-IDed ACIS-I sources. Sources with more counts than 50 and higher  $S/N$  than 10 (142 sources) are bright (S) sources, for which the spectral analysis was conducted. Larger squares indicate sources fitted by thin-thermal plasma models; open for one-temperature model and filled for two temperature model.

First, for bright (S) sources, we applied one-temperature thin-thermal plasma model (the mekal model) convolved with the ISM absorption (the wabs model). The metallicity of all elements is fixed to 0.3 solar based on previous works (e.g., Imanishi et al. 2001<sup>[91]</sup>).

When  $\alpha$  is less than 0.05 or the best-fit parameters are unphysical (e.g.,  $k_{\text{B}}T > 10$  keV), we recognized that the model was rejected. Among fitted samples, 87 (61%) sources had an acceptable fit. Using the best-fit parameters, we compiled  $N_{\text{H}}$ ,  $k_{\text{B}}T$ , and  $L_{\text{X}}$  in Table 7.1. The spectra and the best-fit models of these sources are tiled in Figures 7.8–7.13.

Table 7.1: One-temperature plasma fittings of bright NIR-IDed *Chandra* sources

ID	counts <sup>a</sup>	$S/N^b$	$N_{\text{H}}^c$ ( $10^{22}$ cm <sup>-2</sup> )	$k_{\text{B}}T^c$ (keV)	$L_{\text{X}}^a$ (ergs s <sup>-1</sup> )
I21	276	29.9	0.00 (0.00–0.07)	1.18 (1.00–1.31)	3.65e+29
I27	558	45.7	0.03 (0.00–0.15)	1.58 (1.34–1.79)	9.84e+29
I34	135	18.7	0.00 (0.00–0.07)	1.26 (0.99–1.67)	1.70e+29
I36	670	53.2	0.07 (0.01–0.15)	1.09 (1.01–1.22)	1.04e+30
I38	83	21.7	0.72 (0.39–1.24)	0.63 (0.22–0.97)	5.32e+29
I54	437	43.9	0.45 (0.00–0.31)	0.84 (0.98–1.42)	7.04e+29
I58	92	12.4	0.40 (0.00–1.15)	6.39 (2.42–79.9)	3.62e+29
I65	257	32.3	0.77 (0.41–1.25)	2.72 (1.67–5.06)	1.26e+30
I66	200	12.5	0.09 (0.00–0.53)	0.97 (0.60–1.17)	3.23e+29
I67	1232	256.5	0.81 (0.66–0.93)	2.74 (2.35–3.45)	6.36e+30
I74	442	168.5	2.25 (1.84–2.77)	2.21 (1.74–2.82)	4.28e+30
I77	835	314.7	3.20 (2.83–3.63)	3.16 (2.51–4.13)	1.02e+31
I82	325	14.0	2.67 (2.13–3.44)	4.19 (2.41–6.80)	3.47e+30
I83	109	22.8	0.71 (0.46–0.99)	0.46 (0.30–0.67)	9.44e+29
I87	207	23.8	1.93 (1.04–2.47)	2.06 (1.32–3.93)	1.97e+30
I90	116	13.0	0.65 (0.00–1.39)	7.09 (2.79–79.9)	5.64e+29
I92	313	157.9	0.55 (0.36–0.72)	0.60 (0.45–0.83)	1.55e+30
I93	574	382.2	0.00 (0.00–0.07)	1.20 (1.00–1.12)	7.16e+29
I96	333	1845.7	1.93 (1.38–2.53)	2.48 (1.83–3.66)	2.62e+30
I99	112	849.6	2.79 (1.55–4.30)	1.91 (1.19–3.75)	1.25e+30
I106	151	40.4	1.46 (1.15–2.08)	1.42 (1.00–1.76)	1.02e+30
I109	177	77.9	0.65 (0.35–0.93)	0.37 (0.22–0.69)	1.70e+30
I110	3013	287.9	1.23 (1.12–1.35)	7.69 (6.01–10.4)	2.24e+31
I111	88	16.4	0.44 (0.00–1.10)	0.41 (0.11–0.88)	2.04e+29
I121	259	227.2	2.69 (1.77–3.71)	1.70 (1.18–3.00)	3.28e+30
I124	830	40.4	0.72 (0.60–0.87)	4.41 (3.80–6.03)	5.04e+30

(cont.)

ID	counts <sup>a</sup>	$S/N^b$	$N_{\text{H}}^c$	$k_{\text{B}}T^c$	$L_{\text{X}}^a$
I125	561	54.9	0.33 (0.19–0.51)	3.25 (2.34–4.59)	1.96e+30
I128	60	62.7	12.7 (0.46–49.2)	3.05 (0.72–79.9)	1.55e+31
I131	662	83.3	0.10 (0.00–0.23)	3.19 (2.35–4.48)	1.42e+30
I138	359	66.0	3.22 (2.21–4.28)	7.52 (3.54–79.9)	3.96e+30
I140	259	689.2	6.22 (4.36–12.4)	3.12 (1.32–5.84)	6.32e+30
I142	97	36.9	11.6 (3.75–21.1)	1.07 (0.54–3.56)	4.84e+30
I143	143	55.8	1.60 (0.88–2.41)	2.99 (1.77–6.40)	1.03e+30
I144	953	187.5	1.68 (1.48–1.89)	2.55 (2.13–3.10)	8.08e+30
I145	73	32.9	0.00 (.....–.....)	1.00 (.....–.....)	8.76e+28
I147	2276	117.4	1.04 (0.95–1.15)	2.78 (2.45–3.20)	1.46e+31
I148	673	125.0	0.50 (0.32–0.65)	2.76 (2.17–3.93)	2.68e+30
I149	109	1204.9	5.32 (3.23–9.10)	1.48 (0.75–3.02)	5.84e+30
I153	142	141.8	1.38 (1.11–2.21)	0.88 (0.43–1.13)	1.73e+30
I154	97	182.1	1.91 (1.23–3.54)	2.30 (1.18–4.34)	7.64e+29
I155	76	229.1	7.90 (.....–.....)	1.99 (.....–.....)	1.27e+30
I158	838	1617.2	0.49 (0.20–0.42)	1.09 (1.19–1.46)	1.96e+30
I164	507	2778.6	2.06 (1.71–2.46)	1.80 (1.48–2.27)	4.52e+30
I165	833	4039.7	1.40 (1.14–1.70)	4.78 (3.34–7.87)	5.48e+30
I166	415	98.2	0.77 (0.65–0.92)	0.30 (0.23–0.48)	7.36e+30
I167	921	2759.8	0.45 (0.31–0.57)	3.12 (2.56–4.13)	3.37e+30
I170	164	10.4	0.50 (0.16–0.99)	7.01 (3.40–36.9)	6.08e+28
I173	59	298.2	1.64 (.....–.....)	2.92 (.....–.....)	3.74e+29
I174	1908	263.3	0.00 (0.00–0.02)	1.30 (1.24–1.34)	2.74e+30
I178	83	20.3	0.21 (0.00–1.01)	8.93 (2.16–79.9)	2.82e+29
I179	363	16.9	0.43 (0.28–0.53)	0.61 (0.51–0.74)	1.59e+30
I181	144	1437.5	2.97 (1.39–4.70)	7.54 (2.94–79.9)	1.23e+30
I187	544	156.1	0.00 (0.00–0.06)	1.24 (1.06–1.32)	7.84e+29
I192	324	355.7	0.64 (0.32–0.82)	0.94 (0.78–1.14)	1.34e+30
I197	878	790.1	0.01 (0.00–0.05)	1.38 (1.30–1.60)	1.29e+30
I198	83	71.1	0.18 (0.00–1.02)	0.76 (0.14–1.11)	1.61e+29
I202	88	22.2	2.82 (1.43–4.57)	2.00 (1.07–3.55)	1.04e+30
I204	289	120.3	1.97 (1.50–2.51)	2.62 (1.83–3.40)	2.28e+30
I208	270	775.9	1.46 (1.02–2.30)	4.24 (2.10–21.9)	1.95e+30

(cont.)

ID	counts <sup>a</sup>	$S/N^b$	$N_{\text{H}}^c$	$k_{\text{B}}T^c$	$L_{\text{X}}^a$
I212	345	1727.6	3.67 (2.60–5.00)	2.35 (1.60–3.89)	4.16e+30
I213	326	504.9	3.16 (2.18–4.27)	2.02 (1.38–3.49)	4.20e+30
I216	172	25.9	0.17 (0.00–0.46)	1.02 (0.88–1.32)	3.06e+29
I217	50	12.1	0.43 (0.00–2.34)	3.15 (0.81–79.9)	1.65e+29
I218	1228	448.2	3.63 (3.24–4.10)	3.10 (2.49–3.95)	1.80e+31
I219	89	366.8	1.31 (0.00–3.11)	1.50 (0.87–7.35)	6.60e+29
I229	157	16.1	0.88 (0.01–0.33)	1.06 (1.70–3.35)	4.28e+28
I223	1424	1291.3	0.07 (0.04–0.11)	1.22 (1.02–1.28)	2.20e+30
I232	213	13.0	1.47 (0.94–2.18)	1.75 (1.14–2.87)	1.52e+30
I234	222	32.2	1.15 (0.85–1.73)	1.49 (1.00–2.84)	1.30e+30
I237	91	22.2	0.46 (0.14–0.99)	0.42 (0.12–0.65)	4.52e+30
I243	187	170.8	0.00 (0.00–0.11)	1.20 (1.04–1.40)	2.23e+29
I246	63	37.8	2.51 (0.46–7.60)	5.68 (1.43–79.9)	6.12e+29
I251	175	57.5	2.08 (1.44–2.84)	3.14 (2.06–5.65)	1.41e+30
I261	646	21.0	0.50 (0.37–0.65)	8.64 (5.85–17.9)	3.08e+30
I263	223	140.6	1.48 (0.50–2.03)	1.26 (0.83–4.09)	1.97e+30
I264	346	1681.7	7.14 (3.82–10.7)	5.48 (3.05–79.9)	5.56e+30
I272	507	43.1	0.00 (0.00–0.04)	1.75 (1.57–2.21)	8.48e+29
I274	209	43.6	0.59 (0.36–0.99)	0.62 (0.80–1.31)	2.78e+29
I279	114	304.4	4.00 (2.16–6.27)	2.52 (1.37–5.85)	1.36e+30
I280	943	260.1	0.33 (0.21–0.43)	2.70 (2.24–3.50)	3.42e+30
I282	908	82.1	0.02 (0.00–0.08)	1.02 (0.95–1.08)	1.24e+30
I293	518	55.1	0.54 (0.30–0.75)	3.01 (2.14–5.36)	2.26e+30
I297	1048	96.8	0.53 (0.43–0.59)	3.45 (2.91–4.36)	4.48e+30
I299	198	17.7	0.03 (0.00–0.14)	1.35 (1.16–1.70)	8.96e+28
I303	75	17.9	0.66 (0.00–1.23)	0.98 (0.46–3.07)	3.28e+30
I317	657	13.9	0.00 (0.00–0.05)	1.30 (1.22–1.38)	1.09e+30
I322	288	16.1	0.34 (0.00–0.16)	0.68 (0.84–1.07)	3.78e+29

<sup>a</sup> Values in the 0.5–8.0 keV range.

<sup>b</sup> Values in the 2.0–8.0 keV range.

<sup>c</sup> The lower and upper limit ( $1 \sigma$ ) are given in parentheses. Three sources (I145, I155, and I173) have too few spectral bins to derive the uncertainty of their best-fit parameters.

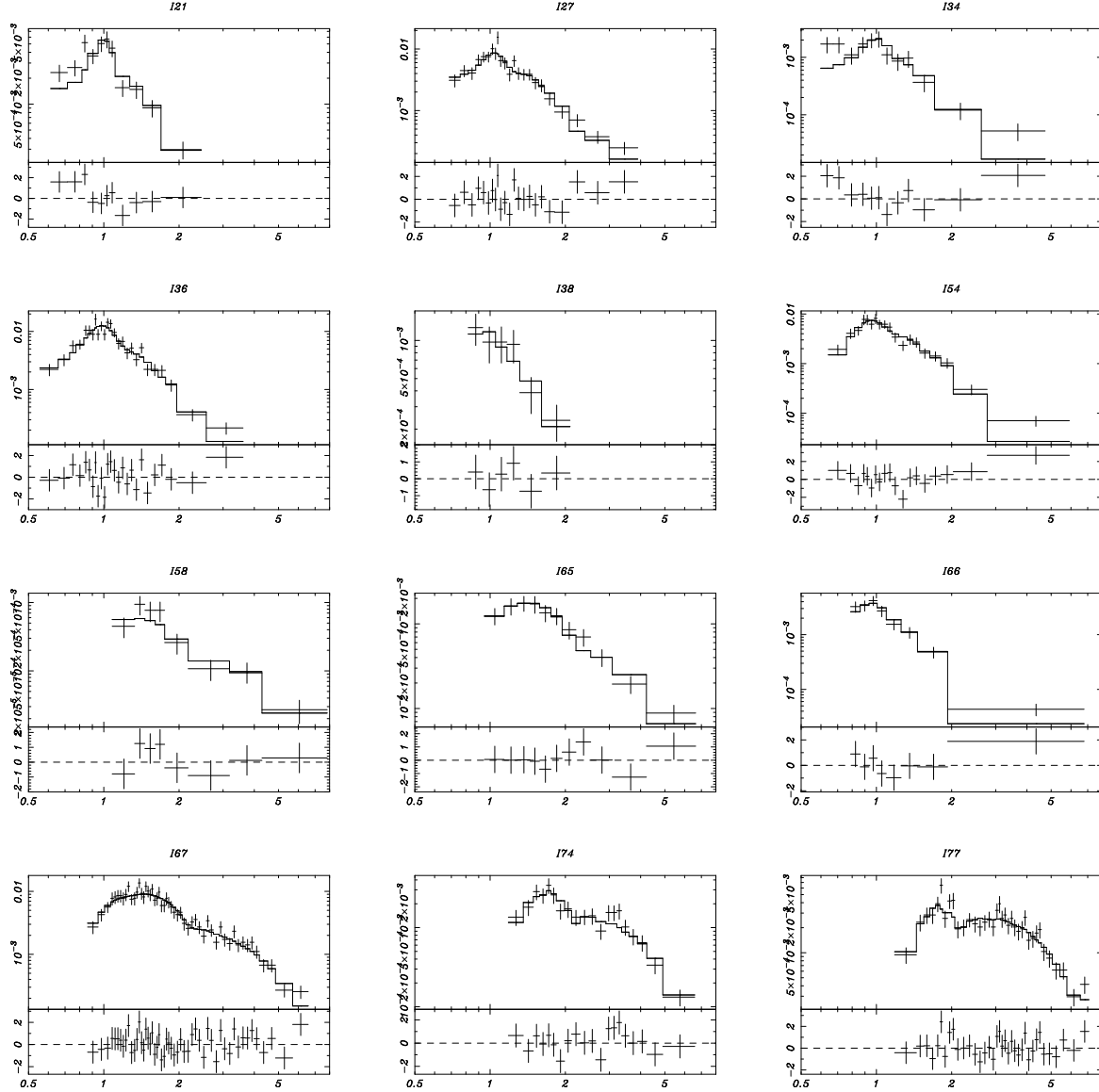


**Figure 7.8:** Spectra and the best-fit models of one-temperature thin-thermal plasma fittings of bright (S) NIR-IDed *Chandra* sources (I21–I77). The metallicity of all elements is fixed to be 0.3 solar. In the upper panels, the data (*pluses*) and the best-fit model (*solid steps*) are plotted over the energy (keV; *horizontal axis*) versus normalized spectral intensity (count rate keV<sup>-1</sup>; *vertical axis*) plane. The response functions of the optics and the detector are convolved into the model. In the lower panels, the residuals between the background-subtracted data and the best-fit model are plotted over the energy (keV; *horizontal axis*) versus  $\chi^{(i)} = (E_{data}^{(i)} - E_{model \otimes ARF \otimes RMF}^{(i)}) / \Delta E_{data}^{(i)}$  (*vertical axis*) plane.

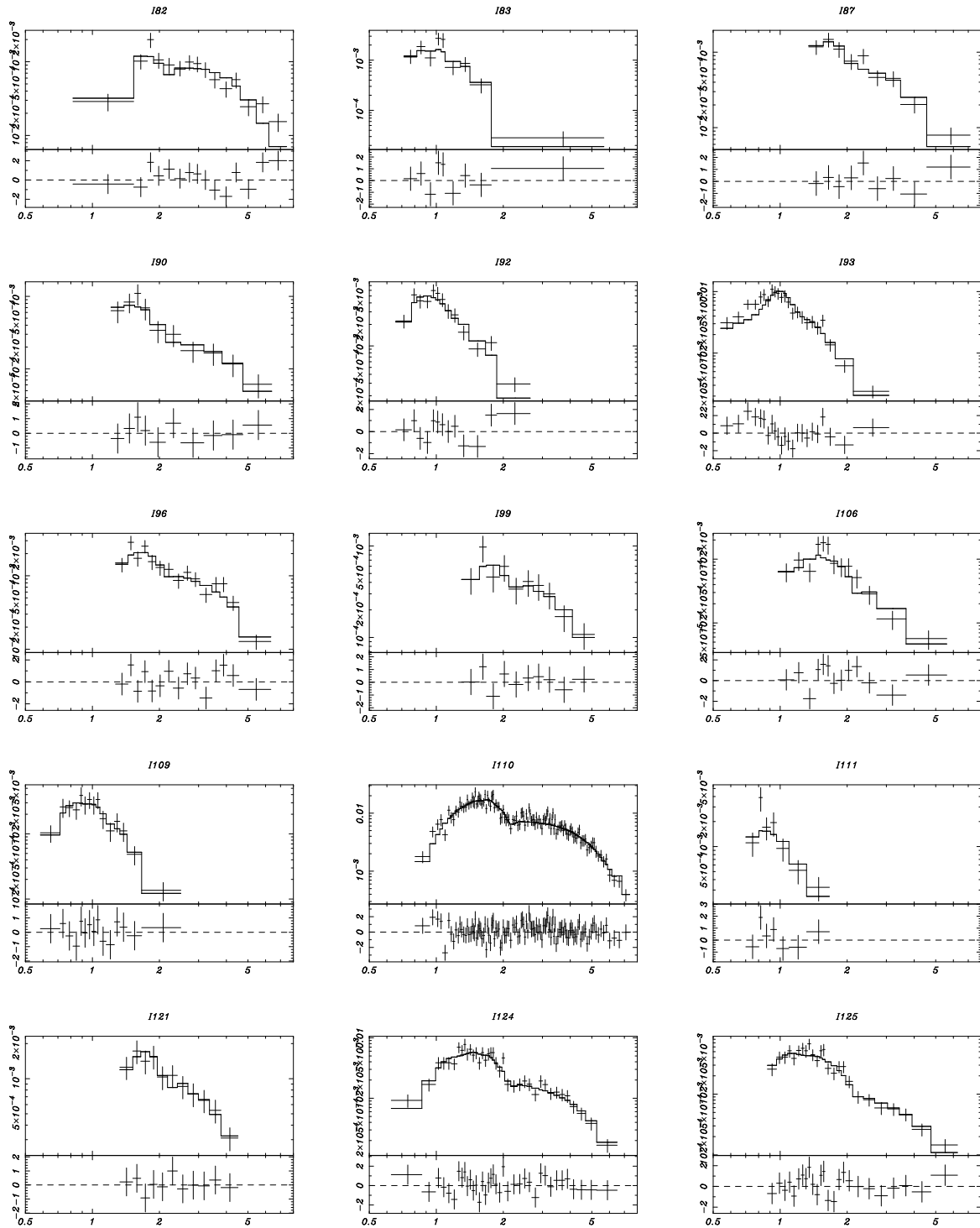


**Figure 7.9:** Spectra and the best-fit models of one-temperature thin-thermal plasma fittings of bright (S) NIR-IDed *Chandra* sources (I82–I125).

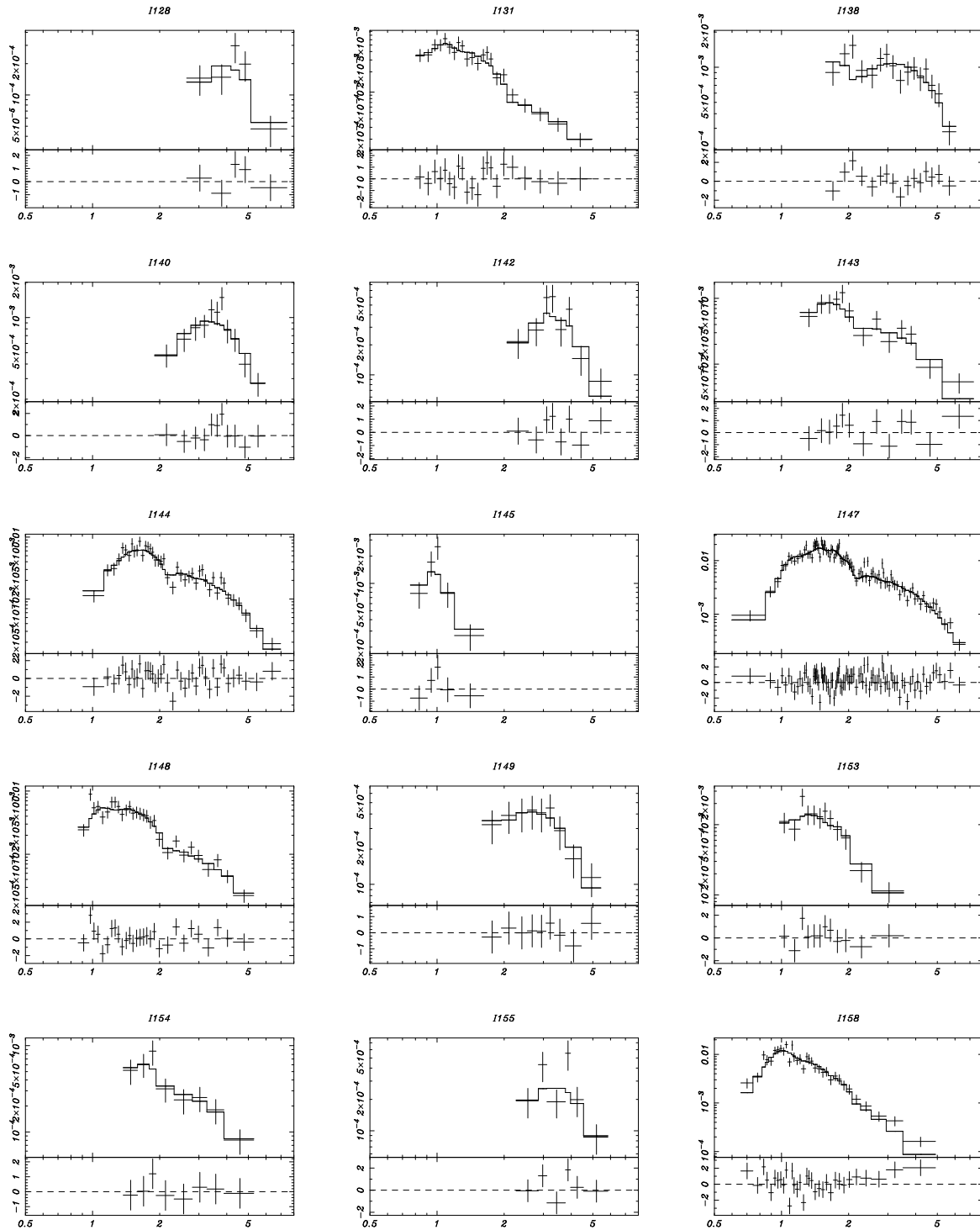


**Figure 7.10:** Spectra and the best-fit models of one-temperature thin-thermal plasma fittings of bright (S) NIR-IDed *Chandra* sources (I128–I158).

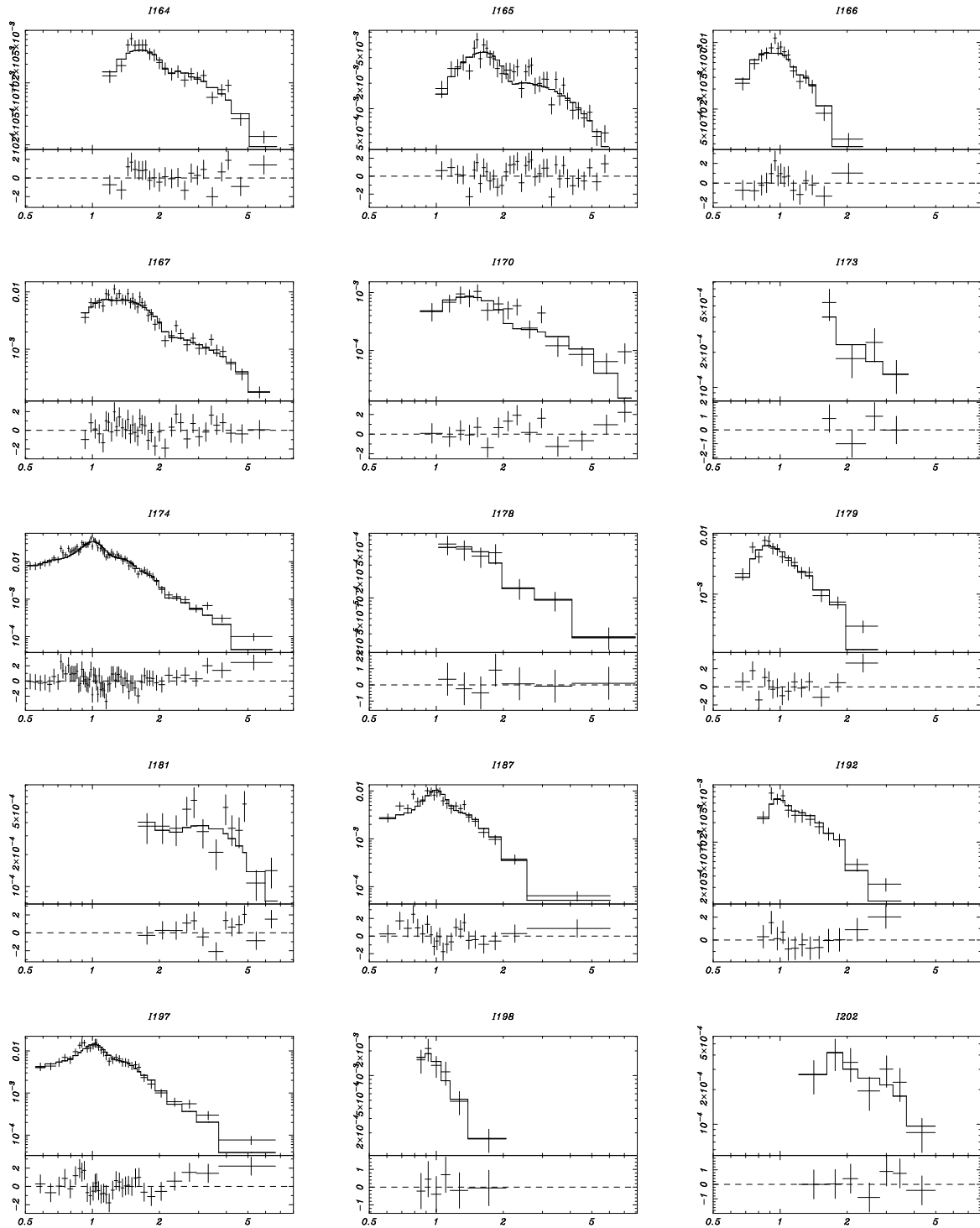


**Figure 7.11:** Spectra and the best-fit models of one-temperature thin-thermal plasma fittings of bright (S) NIR-IDed *Chandra* sources (I164–I202).



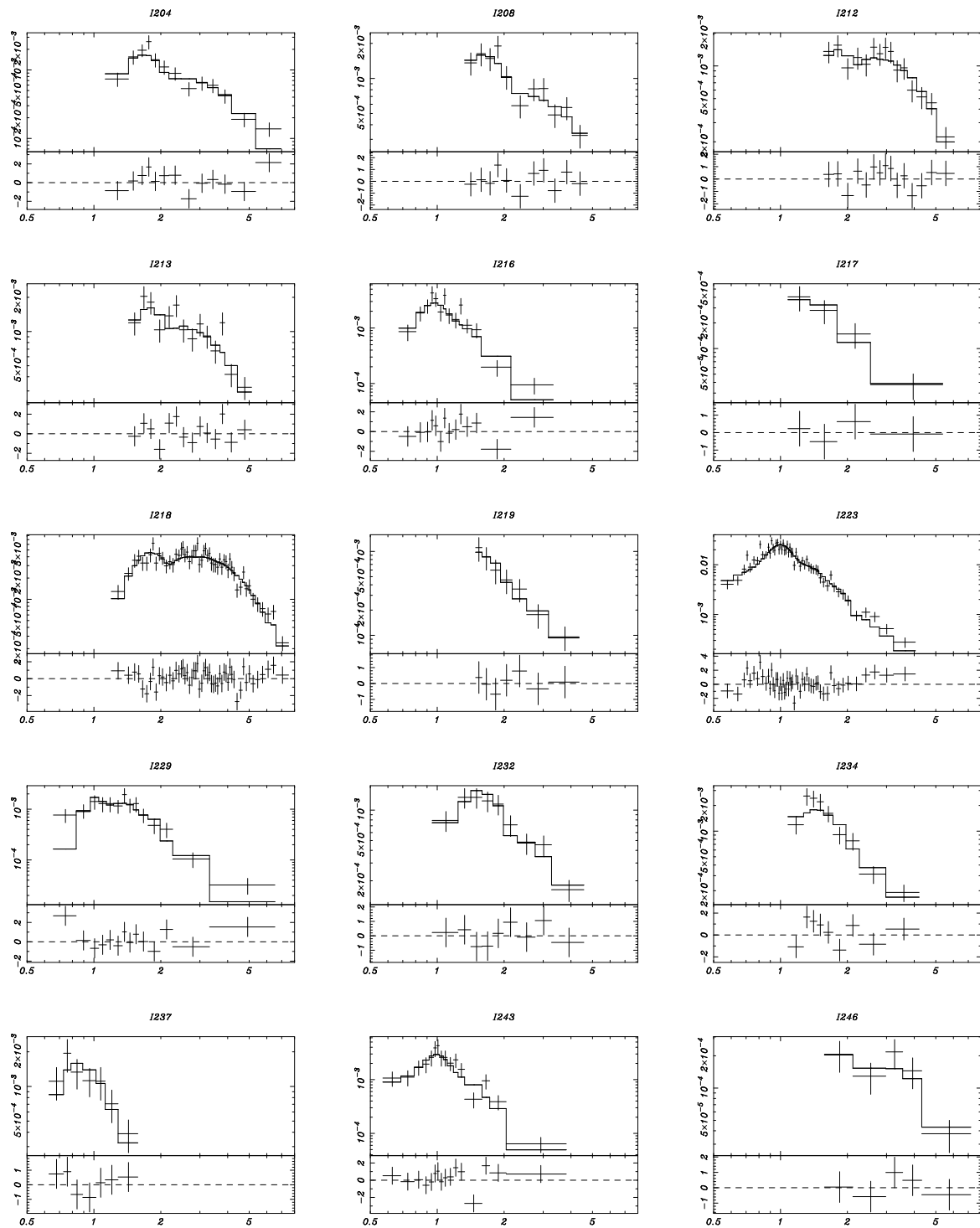


**Figure 7.12:** Spectra and the best-fit models of one-temperature thin-thermal plasma fittings of bright (S) NIR-IDed *Chandra* sources (I204–I246).

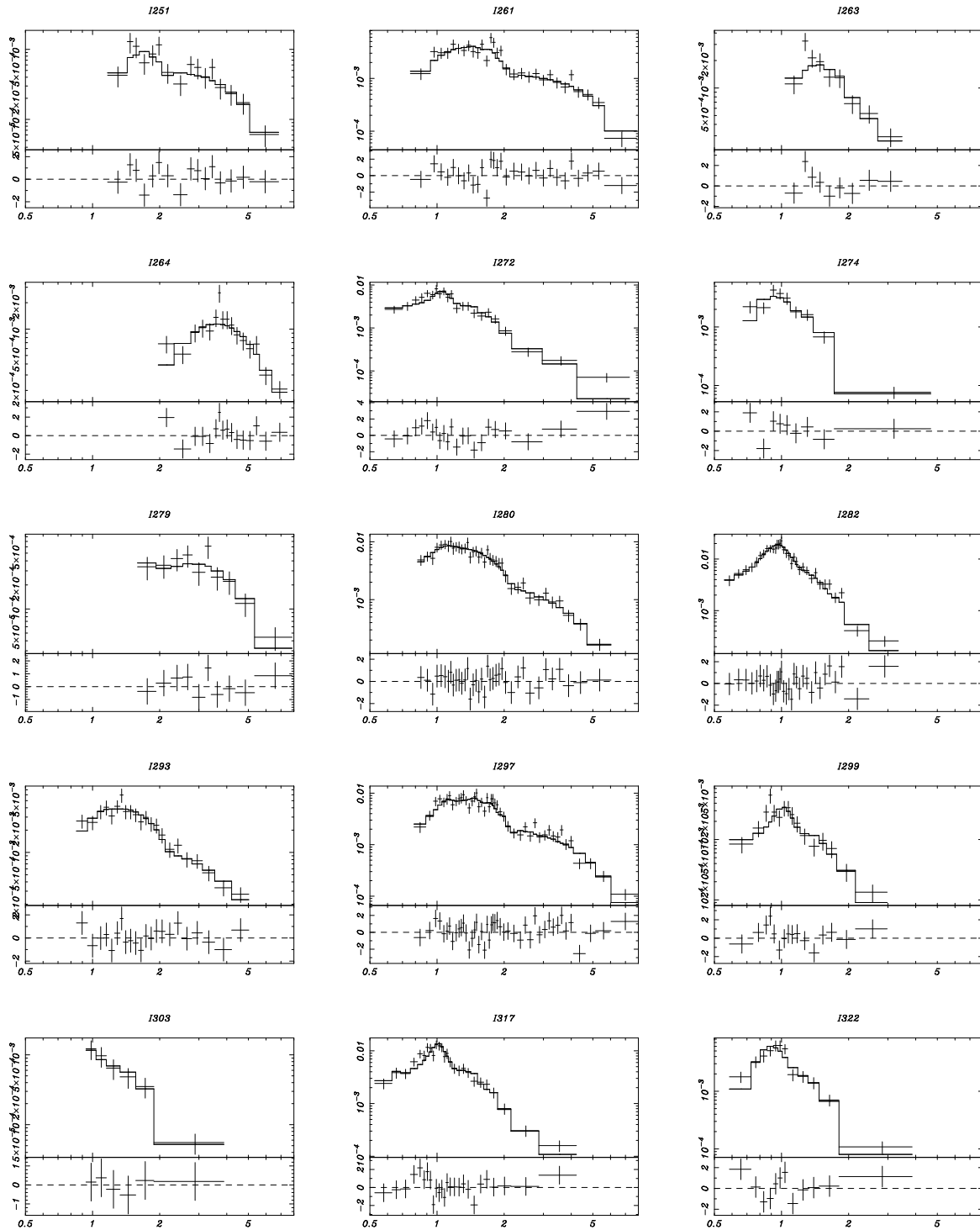


**Figure 7.13:** Spectra and the best-fit models of one-temperature thin-thermal plasma fittings of bright (S) NIR-ided *Chandra* sources (I251–I322).

### 7.2.3 Two-temperature Plasma Fittings

Second, for 55 bright (S) sources that rejected one-temperature plasma model, we applied two-temperature plasma model (two mekal models with different temperatures) convolved with wabs, resulting 32 (23%) sources to have an acceptable fit with  $\alpha \geq 0.05$ . Both components were assumed to have the same  $N_{\text{H}}$  value. The metallicity of all elements was again fixed to 0.3 solar. In Table 7.2, we compiled the best-fit values of  $k_{\text{B}}T$  and  $L_{\text{X}}$  of the higher temperature component ( $k_{\text{B}}T_1$  and  $L_{\text{X}1}$ ) as well as those of the lower temperature component ( $k_{\text{B}}T_2$  and  $L_{\text{X}2}$ ) along with  $N_{\text{H}}$  and the total  $L_{\text{X}}$  of both components. The spectra and the best-fit models are tiled in Figures 7.15–7.17.

We still have 23 bright (S) sources not to be fitted with either one-temperature or two-temperature plasma models with 0.3 solar metallicity. Nine sources, which were globally well fitted with two-temperature plasma model, show excess emission lines that decrease the  $\alpha$  value. We therefore fitted these spectra with two-temperature plasma model with variable metallicity for elements with prominent line emissions (two vmekal models), resulting that all of them have an acceptable fit. Table 7.3 lists the best-fit values of continuum emissions ( $k_{\text{B}}T$  and  $L_{\text{X}}$  values of the higher and lower temperature component,  $N_{\text{H}}$  and the total  $L_{\text{X}}$ ), while Table 7.4 shows the best-fit values of line emissions (the metallicity of each element). The spectra and the best-fit models are given in Figure 7.18.



**Figure 7.14:** Breakdown of best-fit models of 142 bright (S) NIR-IDed ACIS-I sources. A and B are for the spectra fitted with one-temperature and two-temperature plasma model with the metallicity fixed to be 0.3 solar, while C is for the spectra fitted with two-temperature plasma with variable metallicity values. D is for those fitted by none of these models. The number of sources are shown in parentheses.

Table 7.2: Two-temperature plasma fittings of bright NIR-IDed *Chandra* sources (1)

ID	counts <sup>a</sup>	$S/N^b$	$N_H^c$ ( $10^{22}$ cm <sup>-2</sup> )	$k_B T_1^{cd}$ (keV)	$L_{X1}^{ad}$ (ergs s <sup>-1</sup> )	$k_B T_2^{ce}$ (keV)	$L_{X2}^{ae}$ (ergs s <sup>-1</sup> )	$L_{X1+2}^{af}$ (ergs s <sup>-1</sup> )
I7	549	18.8	0.02 (0.00-0.15)	1.68 (1.34-3.26)	4.04e+29	0.74 (0.60-0.86)	2.67e+29	6.71e+29
I12	361	16.3	0.00 (0.00-0.23)	3.15 (0.66-13.8)	5.56e+29	1.04 (0.63-1.37)	1.88e+29	7.44e+29
I14	579	21.3	0.00 (0.00-0.04)	3.49 (2.27-9.44)	7.04e+29	0.88 (0.76-1.06)	3.34e+29	1.04e+30
I17	534	17.5	0.00 (0.00-0.14)	1.94 (1.44-2.77)	5.68e+29	0.77 (0.58-0.87)	2.80e+29	8.48e+29
I25	2287	59.5	0.00 (0.00-0.02)	4.61 (2.48-13.0)	1.61e+30	1.00 (0.87-1.06)	2.24e+30	3.85e+30
I31	740	169.2	0.80 (0.54-1.34)	1.24 (1.01-1.41)	2.51e+30	0.13 (0.09-0.15)	5.68e+31	5.93e+31
I42	1023	89.9	0.90 (0.62-1.07)	1.31 (1.22-1.56)	8.48e+29	0.10 (0.09-0.18)	2.26e+30	3.11e+30
I47	1771	828.8	0.36 (0.27-0.48)	2.45 (2.13-3.07)	3.66e+30	0.84 (0.71-1.03)	1.90e+30	5.56e+30
I71	1191	814.1	0.08 (0.02-0.12)	2.03 (1.15-4.66)	9.44e+29	0.79 (0.67-0.87)	1.06e+30	2.00e+30
I85	1088	471.3	0.02 (0.00-0.07)	4.05 (2.40-6.40)	2.36e+30	1.05 (0.81-1.27)	1.74e+30	4.10e+30
I130	165	26.8	1.00 (0.69-1.15)	2.93 (1.46-50.1)	2.78e+29	0.21 (0.14-1.09)	8.48e+30	8.76e+30
I150	2201	1080.8	0.22 (0.16-0.27)	8.28 (3.86-79.9)	1.26e+30	0.84 (0.78-0.88)	4.00e+30	5.26e+30
I151	14667	2164.2	0.33 (0.31-0.35)	2.80 (2.52-3.34)	2.61e+31	1.10 (1.06-1.21)	1.94e+31	4.55e+31
I189	761	95.0	0.00 (0.00-0.11)	1.47 (1.34-1.75)	8.76e+29	0.55 (0.41-0.70)	2.37e+29	1.11e+30
I194	1411	741.5	0.26 (0.18-0.36)	3.14 (1.73-6.20)	1.80e+30	1.04 (0.79-1.14)	1.76e+30	3.56e+30
I200	3840	1896.2	0.01 (0.00-0.03)	2.45 (2.00-2.75)	2.94e+30	0.87 (0.83-0.91)	3.17e+30	6.11e+30
I211	711	12.6	0.26 (0.17-0.36)	5.67 (3.29-15.8)	2.22e+30	1.21 (1.06-1.34)	1.04e+30	3.26e+30
I225	1189	22.9	0.23 (0.16-0.26)	5.72 (3.76-7.12)	4.36e+30	1.00 (0.84-1.11)	9.32e+29	5.29e+30
I238	311	11.5	0.47 (0.21-1.01)	0.71 (0.45-0.84)	9.88e+29	0.10 (0.08-0.21)	5.88e+30	6.87e+30
I240	2772	60.7	0.43 (0.37-0.50)	2.53 (1.97-3.32)	5.40e+30	1.02 (0.83-1.10)	5.00e+30	1.04e+31
I248	2062	707.9	0.24 (0.19-0.32)	3.01 (2.52-3.61)	3.67e+30	0.85 (0.76-0.97)	1.97e+30	5.64e+30
I256	1143	19.7	0.85 (0.35-1.03)	3.57 (2.80-5.29)	4.04e+30	0.62 (0.48-1.10)	4.60e+30	8.64e+30

(cont.)

ID	counts <sup>a</sup>	$S/N^b$	$N_H^c$	$k_B T_1^{cd}$	$L_{X1}^{ad}$	$k_B T_2^{ce}$	$L_{X2}^{ae}$	$L_{X1+2}^{af}$
I278	270	11.4	0.21 (.....)	6.89 (.....)	3.67e+29	0.63 (.....)	3.42e+29	7.09e+29
I287	312	13.0	0.66 (0.35-0.92)	1.11 (0.38-0.63)	4.56e+29	0.21 (0.08-0.30)	1.09e+30	1.55e+30
I289	298	159.8	0.25 (0.00-1.08)	2.21 (1.52-4.26)	7.20e+29	0.18 (0.08-11.2)	6.28e+29	1.35e+30
I298	279	52.4	0.03 (0.00-0.82)	1.38 (1.04-1.80)	3.14e+29	0.35 (0.18-0.68)	1.39e+29	4.53e+29
I308	825	141.5	0.35 (0.23-0.45)	2.80 (1.80-5.16)	2.39e+30	1.06 (0.71-1.41)	1.22e+30	3.61e+30
I313	660	97.8	1.04 (0.74-1.28)	2.82 (2.11-4.45)	2.42e+30	0.85 (0.60-1.06)	2.28e+30	4.70e+30
I314	617	11.2	0.08 (0.03-0.21)	3.79 (1.91-5.78)	8.44e+29	0.95 (0.76-1.05)	5.44e+29	1.39e+30
I319	2262	168.3	0.00 (0.00-0.04)	2.41 (1.90-3.23)	2.99e+30	0.95 (0.80-1.05)	9.96e+29	3.99e+30
I324	5270	757.1	0.09 (0.07-0.11)	2.92 (2.71-3.40)	8.48e+30	0.99 (0.86-1.06)	3.25e+30	1.17e+31
I326	695	17.8	0.21 (0.08-0.41)	2.66 (1.76-10.4)	8.84e+29	0.65 (0.57-0.83)	9.72e+29	1.86e+30

<sup>a</sup> Values in the 0.5–8.0 keV range.

<sup>b</sup> Values in the 2.0–8.0 keV range.

<sup>c</sup> The lower and upper limit ( $1\sigma$ ) are given in parentheses. I278 has too few spectral bins to derive the uncertainty of its best-fit parameters.

<sup>d</sup> Best-fit parameters of the higher temperature component are given.

<sup>e</sup> Best-fit parameters of the lower temperature component are given.

<sup>f</sup> The total luminosity of two components is given.

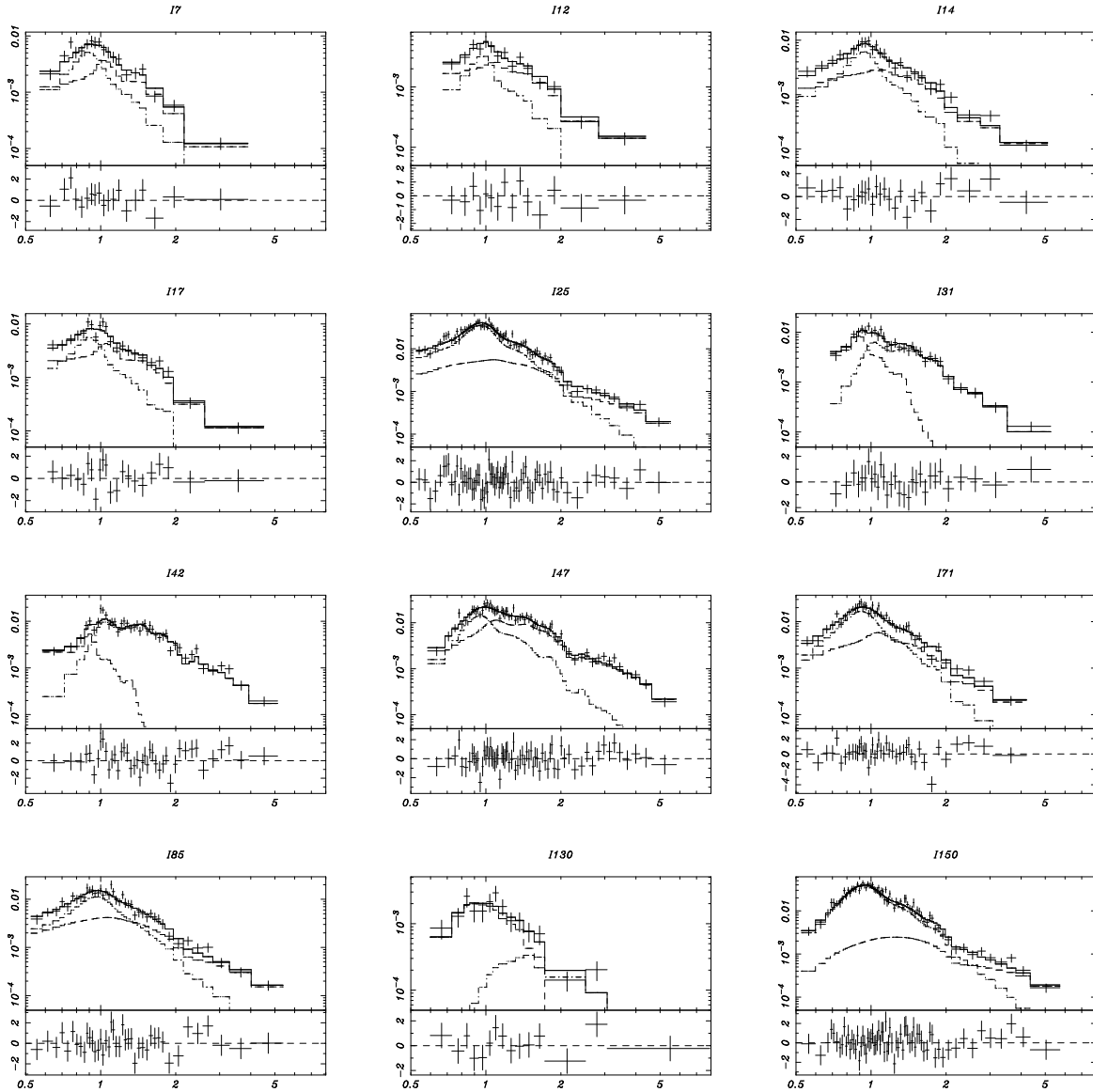


**Figure 7.15:** Spectra and the best-fit models of two-temperature thin-thermal plasma fittings of bright (S) NIR-ided *Chandra* sources (I7–I150). The metallicity of all elements is fixed to be 0.3 solar. In the upper panels, the data (*pluses*) and the best-fit model (*solid steps*) are plotted over the energy (keV; *horizontal axis*) versus normalized spectral intensity (count rate keV<sup>-1</sup>; *vertical axis*) plane. The dashed and dashed-and-dotted steps represent each spectral component. The response functions of the optics and the detector are convolved into the model. In the lower panels, the residuals between the background-subtracted data and the best-fit model are plotted over the energy (keV; *horizontal axis*) versus  $\chi^{(i)} = (E_{data}^{(i)} - E_{model \otimes ARF \otimes RMF}^{(i)}) / \Delta E_{data}^{(i)}$  (*vertical axis*) plane.

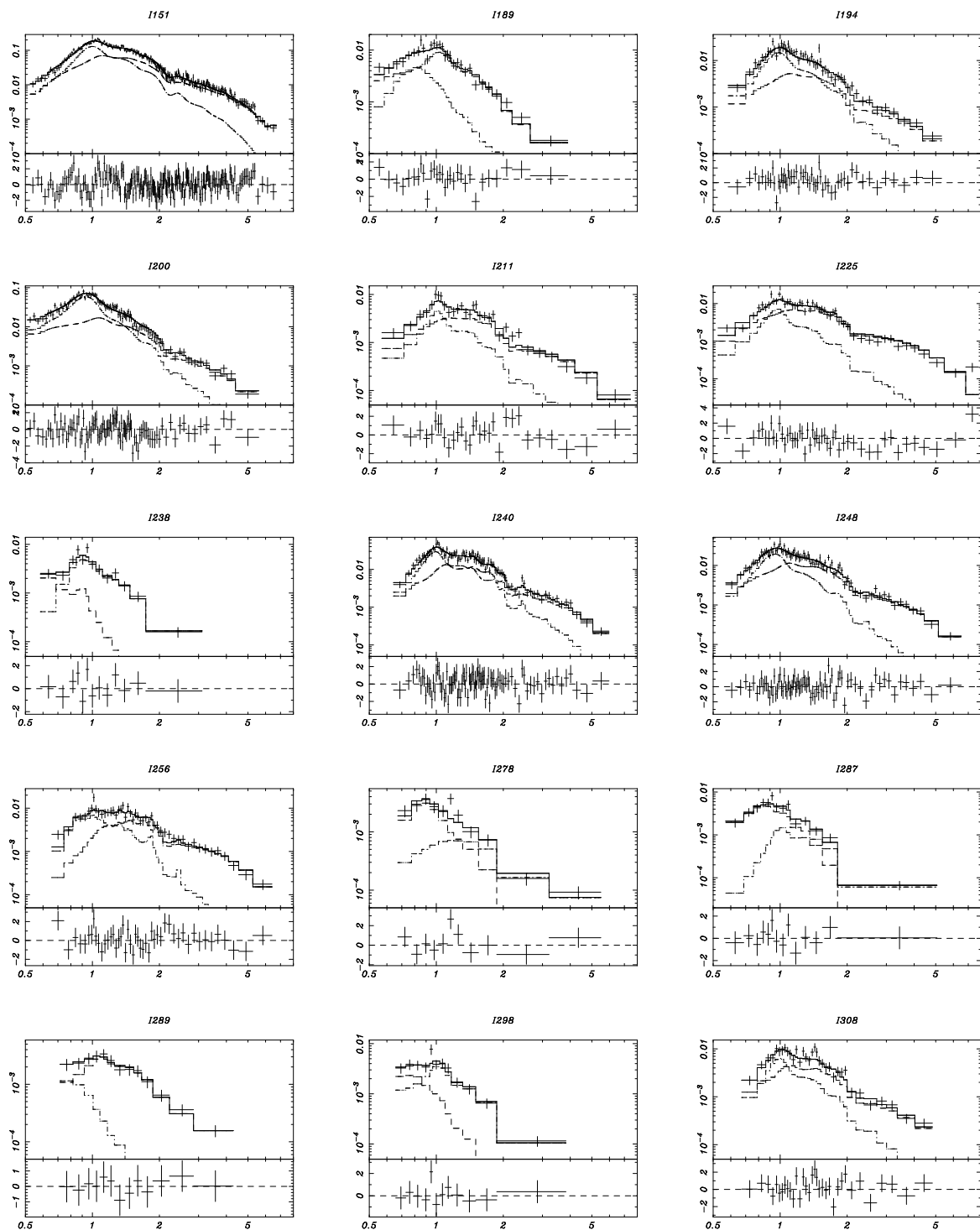


**Figure 7.16:** Spectra and the best-fit models of two-temperature thin-thermal plasma fittings of bright (S) NIR-IDed *Chandra* sources (I151–I308).

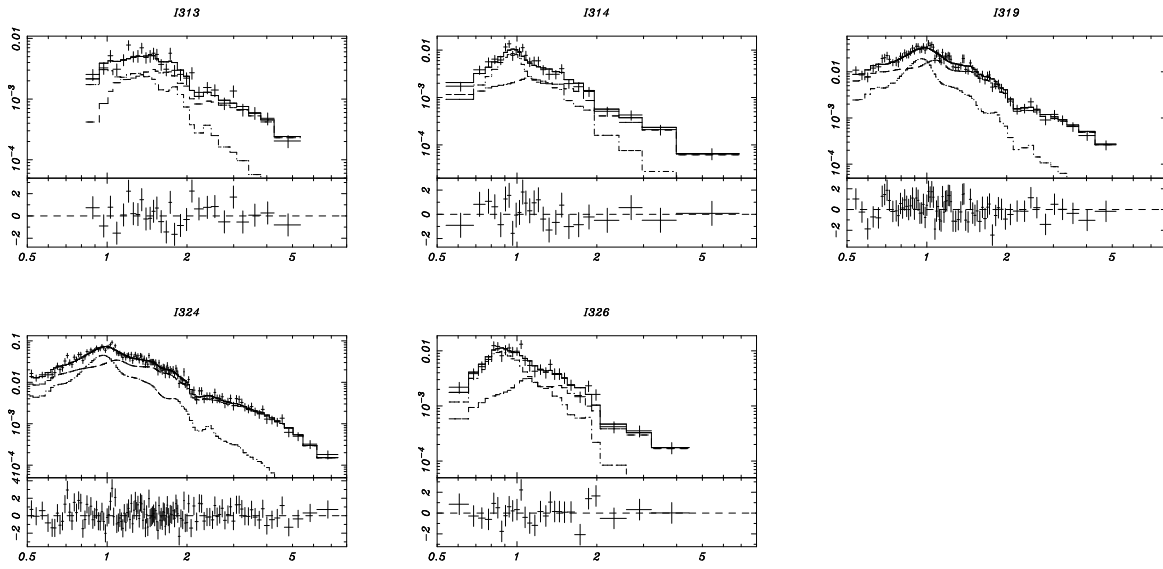


**Figure 7.17:** Spectra and the best-fit models of two-temperature thin-thermal plasma fittings of bright (S) NIR-IDed *Chandra* sources (I313–I326).



Table 7.3: Two-temperature plasma fittings of bright NIR-IDed *Chandra* sources (2)

ID	counts <sup>a</sup>	$S/N^b$	$N_H^c$ ( $10^{22}$ cm <sup>-2</sup> )	$k_B T_{1}^{cd}$ (keV)	$L_{X1}^{ad}$ (ergs s <sup>-1</sup> )	$k_B T_{2}^{ce}$ (keV)	$L_{X2}^{ae}$ (ergs s <sup>-1</sup> )	$L_{X1+2}^{af}$ (ergs s <sup>-1</sup> )
I13	1747	133.5	0.02 (0.00-0.10)	3.29 (2.73-4.06)	2.52e+30	0.70 (0.63-0.79)	8.48e+29	3.37e+30
I51	25400	13166.7	0.20 (0.18-0.22)	2.90 (2.79-3.09)	6.12e+31	0.73 (0.65-0.87)	6.84e+30	6.80e+31
I283	2221	1102.3	0.04 (0.00-0.09)	3.27 (2.55-4.37)	3.83e+30	1.00 (0.81-1.23)	7.04e+29	4.53e+30
I295	320	26.5	0.05 (0.00-0.38)	3.43 (2.48-8.55)	4.92e+29	0.82 (0.60-0.96)	1.43e+29	6.34e+29
I328	3603	82.1	0.07 (0.04-0.12)	1.85 (1.45-1.72)	4.16e+30	0.67 (0.34-0.51)	2.38e+30	6.54e+30
I339	1348	58.4	0.04 (0.00-0.09)	2.38 (1.85-5.58)	1.65e+30	0.95 (0.76-1.11)	8.24e+29	2.47e+30
I342	7968	368.7	0.10 (0.08-0.13)	2.29 (2.12-2.51)	1.44e+31	0.67 (0.61-0.75)	5.12e+30	1.95e+31
I343	4600	228.6	0.21 (0.17-0.27)	1.97 (1.82-2.14)	8.28e+30	0.64 (0.57-0.69)	5.20e+30	1.35e+31
I346	1399	33.4	0.02 (0.00-0.11)	2.11 (1.72-2.55)	1.50e+30	0.73 (0.63-0.85)	8.64e+29	2.36e+30

<sup>a</sup> Values in the 0.5–8.0 keV range.

<sup>b</sup> Values in the 2.0–8.0 keV range.

<sup>c</sup> The lower and upper limit ( $1\sigma$ ) are given in parentheses.

<sup>d</sup> Best-fit parameters of the higher temperature component are given.

<sup>e</sup> Best-fit parameters of the lower temperature component are given.

<sup>f</sup> The total luminosity of two components is given.

Table 7.4: Two-temperature plasma fittings of bright NIR-IDed *Chandra* sources (3)

ID	N <sup>a</sup> (solar)	O <sup>a</sup> (solar)	Ne <sup>a</sup> (solar)	Mg <sup>a</sup> (solar)	Si <sup>a</sup> (solar)	S <sup>a</sup> (solar)	Ar <sup>a</sup> (solar)	Fe <sup>a</sup> (solar)
I13	0.3	0.80 (0.30-1.76)	0.26 (0.00-0.85)	0.3	0.3	0.3	0.3	0.29 (0.15-0.53)
I51	0.3	0.3	1.52 (0.80-2.01)	0.3	0.31 (0.15-0.39)	0.93 (0.69-1.19)	0.78 (0.18-1.38)	0.26 (0.20-0.32)
I283	0.3	0.3	0.3	1.86 (0.41-5.13)	0.3	2.57 (1.17-5.17)	0.3	0.82 (0.30-1.93)
I295	0.3	0.3	0.66 (0.00- )	0.89 (0.00- )	0.3	0.3	0.3	1.05 (0.41- )
I328	0.3	0.21 (0.05-0.28)	1.05 (0.59-1.25)	0.31 (0.10-0.57)	0.3	0.3	0.3	0.13 (0.06-0.16)
I339	0.3	0.3	0.37 (0.00-1.72)	0.3	0.3	0.3	0.3	0.25 (0.18-0.39)
I342	5.15 (0.00-12.7)	0.3	1.05 (0.82-1.31)	0.3	0.3	0.55 (0.29-0.82)	0.40 (0.00-1.14)	0.13 (0.09-0.19)
I343	41.3 (24.3-73.8)	0.3	1.38 (0.88-2.12)	0.3	0.3	0.3	0.3	0.36 (0.26-0.55)
I346	0.3	0.3	1.34 (0.12-2.57)	0.3	0.3	0.3	0.3	0.30 (0.14-0.53)

<sup>a</sup> The lower and upper limit ( $1\sigma$ ) are given in parentheses for free parameters. Others are fixed to be 0.3 solar.

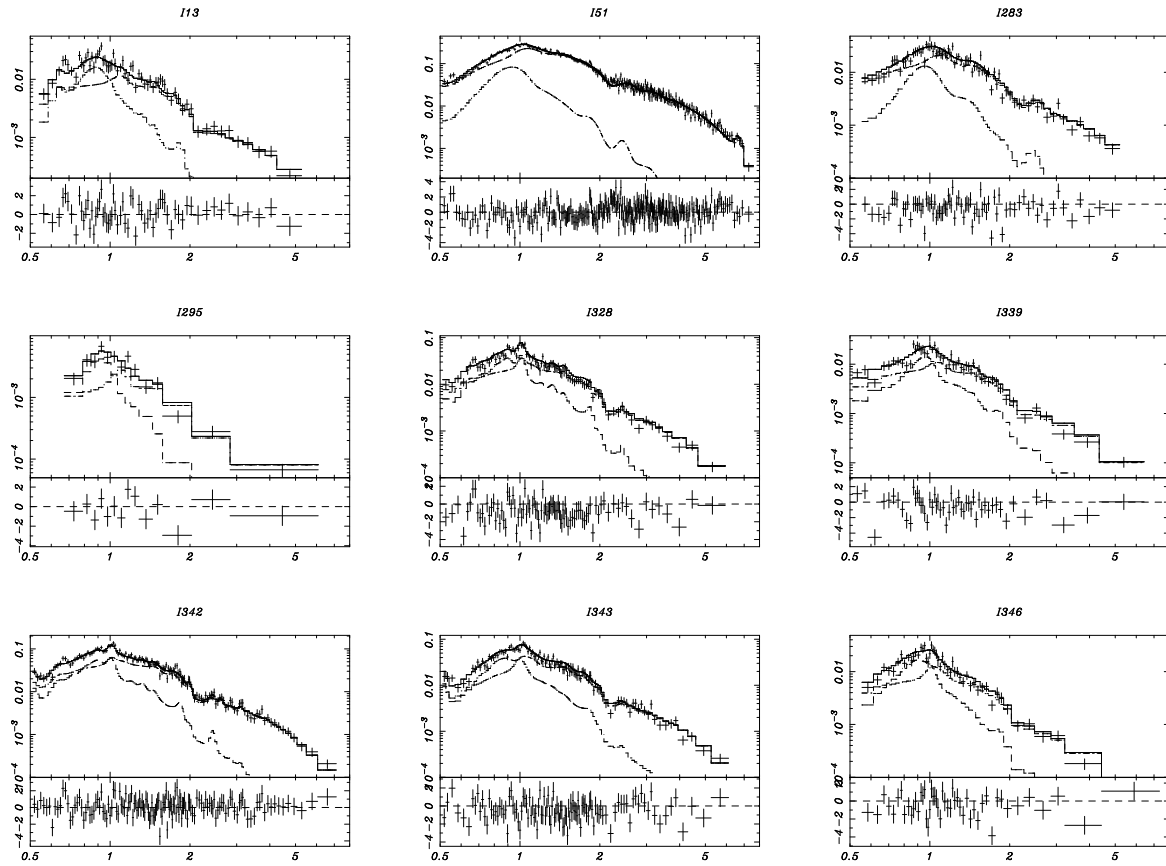


**Figure 7.18:** Spectra and the best-fit models of two-temperature thin-thermal plasma fittings of bright (S) NIR-IDed *Chandra* sources (I13–I346). The metallicity of all elements is fitted for elements with prominent line emissions. In the upper panels, the data (*pluses*) and the best-fit model (*solid steps*) are plotted over the energy (keV; *horizontal axis*) versus normalized spectral intensity (count rate keV<sup>-1</sup>; *vertical axis*) plane. The dashed and dashed-and-dotted steps represent each spectral component. The response functions of the optics and the detector are convolved into the model. In the lower panels, the residuals between the background-subtracted data and the best-fit model are plotted over the energy (keV; *horizontal axis*) versus  $\chi^{(i)} = (E_{data}^{(i)} - E_{model \otimes ARF \otimes RMF}^{(i)}) / \Delta E_{data}^{(i)}$  (*vertical axis*) plane.

### 7.2.4 Time-sliced Spectroscopy

Finally, we conducted the time-sliced spectroscopy of the bright variable sources. We confined this analysis to those with flare-like variability and more counts than 500 in each slice. Six sources (I25, I51, I110, I200, I248, and I324) meet these criteria. We sliced their light curves (Figs. 7.19 and 7.20) into flare and quiescent phases, and fitted the spectrum of each slice with thin-thermal plasma models. Both slices of I110 were well fitted with one-temperature plasma model. Other slices were not fitted with one-temperature plasma with  $\alpha < 0.05$  or a systematic residual, so two-temperature plasma model was used to fit these spectra. The best-fit values are summarized in Table 7.5.

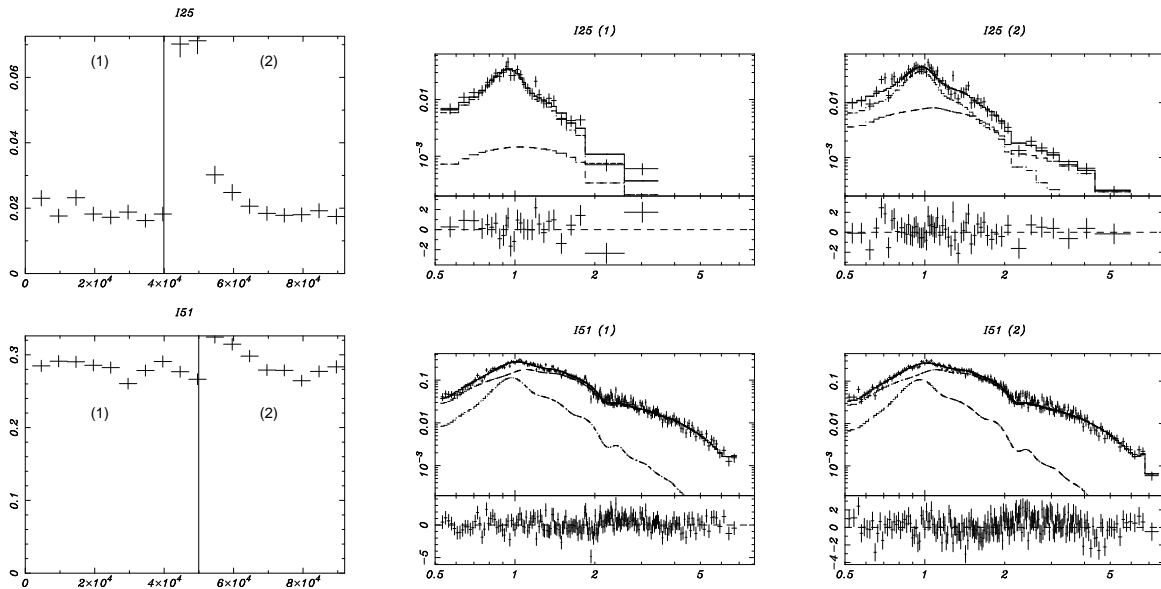


**Figure 7.19:** Time-sliced spectroscopy of some bright variable NIR-IDed *Chandra* sources (I25–I51). The light curves and the time slices are in the panels of the left column. The time-sliced spectra and the best-fit models of thin-thermal plasma fittings are in the middle and the right column. The metallicity of all elements is fixed to be 0.3 solar. In the upper panels, the data (*pluses*) and the best-fit model (*solid steps*) are plotted over the energy (keV; *horizontal axis*) versus normalized spectral intensity (count rate keV<sup>-1</sup>; *vertical axis*) plane. The dashed and dashed-and-dotted steps represent each spectral component. The response functions of the optics and the detector are convolved into the model. In the lower panels, the residuals between the background-subtracted data and the best-fit model are plotted over the energy (keV; *horizontal axis*) versus  $\chi^{(i)} = (E_{data}^{(i)} - E_{model \otimes ARF \otimes RMF}^{(i)}) / \Delta E_{data}^{(i)}$  (*vertical axis*) plane.

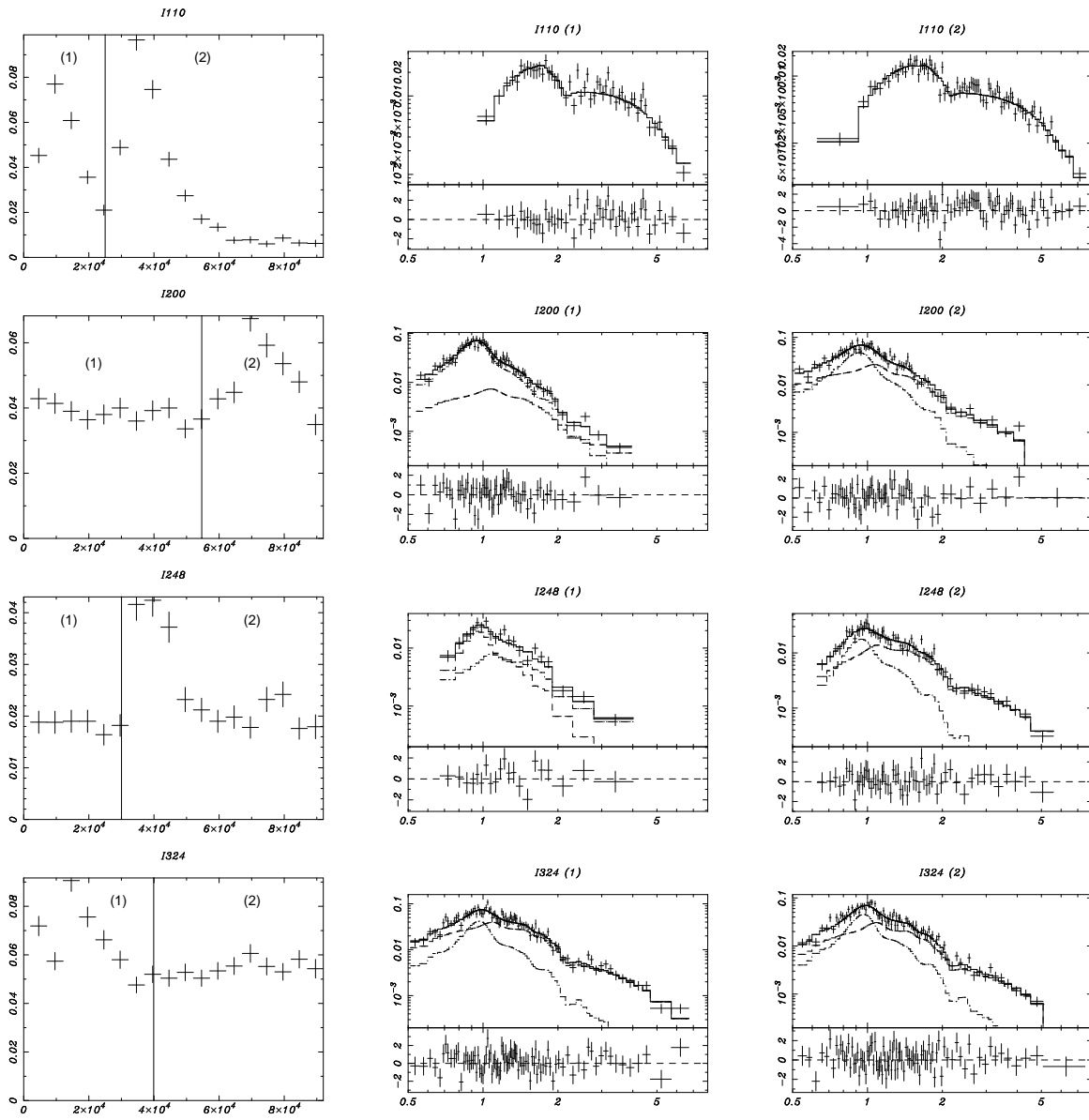


**Figure 7.20:** Time-sliced spectroscopy of some bright variable NIR-ILED *Chandra* sources (I110–I324).

Table 7.5: Time-sliced spectroscopy of bright NIR-IDed *Chandra* sources (1)

ID	phase <sup>a</sup>	counts <sup>b</sup>	$N_{\text{H}}^c$ ( $10^{22} \text{ cm}^{-2}$ )	$k_{\text{B}}T_{\text{I}}^{\text{cd}}$ (keV)	$EM_{\text{I}}^d$ ( $\text{cm}^{-3}$ )	$k_{\text{B}}T_{\text{2}}^{\text{e}}$ (keV)	$EM_{\text{2}}^e$ ( $\text{cm}^{-3}$ )
I25	1 (Q)	715	0.00 (0.00-0.06)	9.71 (0.21-79.9)	3.71 (1.04-9.14)	e+52	2.15 (0.07-2.50)
	2 (F)	1572	0.01 (0.00-0.04)	4.83 (2.61-8.77)	1.79 (1.12-2.50)	e+53	2.78 (2.01-3.49)
I51	1 (Q)	13470	0.19 (0.17-0.20)	3.28 (3.01-3.60)	4.66 (4.28-24.6)	e+54	1.23 (0.92-1.52)
	2 (F)	11930	0.20 (0.18-0.23)	3.23 (2.95-3.53)	5.04 (4.62-25.0)	e+54	1.14 (0.88-1.46)
I110	1 (F)	1154	1.52 (1.29-1.77)	6.82 (4.59-12.0)	2.55 (2.20-3.07)	e+54	.....
	2 (F)	1859	1.03 (0.91-1.15)	7.89 (5.85-11.6)	1.11 (1.02-1.23)	e+54	.....
I200	1 (Q)	2037	0.04 (0.00-0.08)	2.65 (1.73-9.42)	1.35 (0.70-2.03)	e+53	4.19 (3.45-4.98)
	2 (F)	1803	0.00 (0.00-0.03)	2.27 (1.86-2.83)	4.32 (3.59-5.29)	e+53	2.73 (2.05-3.32)
I248	1 (Q)	511	0.20 (0.04-0.78)	2.52 (0.50-27.4)	1.95 (0.77-4.08)	e+53	1.91 (0.89-7.43)
	2 (F)	1551	0.22 (0.14-0.32)	3.07 (2.53-3.79)	3.82 (3.08-4.42)	e+53	1.84 (1.17-2.90)
I324	1 (F)	2495	0.07 (0.05-0.10)	3.17 (2.61-3.99)	8.73 (7.21-10.2)	e+53	3.27 (2.20-4.59)
	2 (Q)	2775	0.11 (0.08-0.16)	2.63 (1.96-3.26)	6.70 (5.31-8.60)	e+53	3.80 (2.63-5.06)

<sup>a</sup> Q for the quiescent phases and F for the flare phases.

<sup>b</sup> Values in the 0.5–8.0 keV range.

<sup>c</sup> The lower and upper limit ( $1 \sigma$ ) are given in parentheses.

<sup>d</sup> Best-fit parameters of the higher temperature component are given.

<sup>e</sup> Best-fit parameters of the lower temperature component are given.

## 7.3 Relations between Parameters

### 7.3.1 X-ray absorption versus NIR extinction

We examined the relation between  $A_V$  and  $N_H$ . The former reflects the amount of ISM in the solid-state, while the latter reflects that in any states. The  $A_V$  values were determined from the NIR color-magnitude diagram (Fig. 6.7) and the  $N_H$  values were from the X-ray spectral fittings (Tables 7.1, 7.2, and 7.3). We have 118 sources with  $A_V$  and  $N_H$  values, for which we fitted with a linear relation in Figure 7.21 to obtain

$$\left( \frac{N_H}{10^{21} \text{ cm}^{-2}} \right) = 1.60_{-0.15}^{+0.18} \times \left( \frac{A_V}{\text{mag}} \right). \quad (7.6)$$

The slope of  $1.60_{-0.15}^{+0.18}$  is smaller than that of the Galactic interstellar medium (1.79; Predehl & Schmitt 1995<sup>[154]</sup>) and is comparable to the values obtained in the  $\rho$  Ophiuchi dark cloud ( $1.59 \pm 0.40$ ; Imanishi et al. 2001<sup>[91]</sup>).

### 7.3.2 X-ray counts versus X-ray flux

The relation between X-ray counts and the flux ( $F_X$ ) in the 0.5–8.0 keV range was examined using bright (S) samples. The linear relation of

$$\log \left( \frac{F_X}{\text{ergs s}^{-1} \text{ cm}^{-2}} \right) = \log(\text{counts}) - 16.1 \quad (7.7)$$

(Figure 7.22) was used to estimate the detection limit of the *Chandra* observation (Sect. 5.1) and the expected number of background sources (Sect. 8.1).

### 7.3.3 X-ray counts versus X-ray luminosity

To estimate the  $L_X$  values of faint (S) sources, we examined the relation between the X-ray counts and luminosity ( $L_X$ ) in the 0.5–8.0 keV range of bright (S) sources (Fig. 7.23). The linear relation was derived to be

$$\log \left( \frac{L_X}{\text{ergs s}^{-1}} \right) = \log(\text{counts}) + 27.6. \quad (7.8)$$

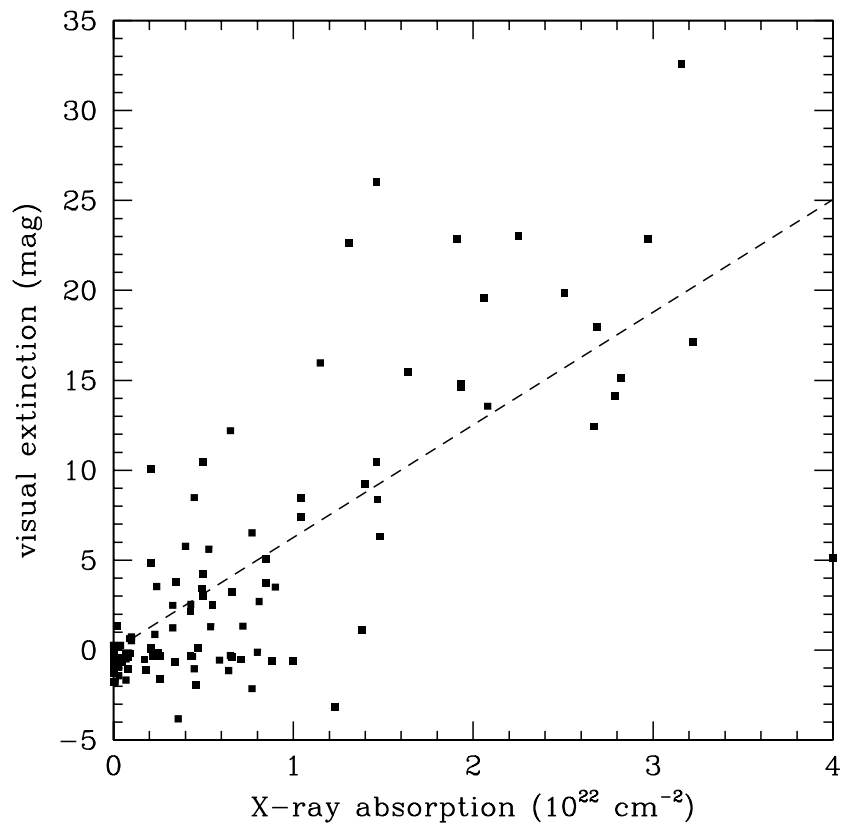


**Figure 7.21:** Relation between X-ray absorption ( $N_{\text{H}}$ ) and visual extinction ( $A_V$ ) for NIR-IDed *Chandra* sources. The  $N_{\text{H}}$  values are derived from fitting the X-ray spectra, while  $A_V$  values are from the color-magnitude diagram (Fig. 6.7). The best-fit linear relation is shown with the dashed line.

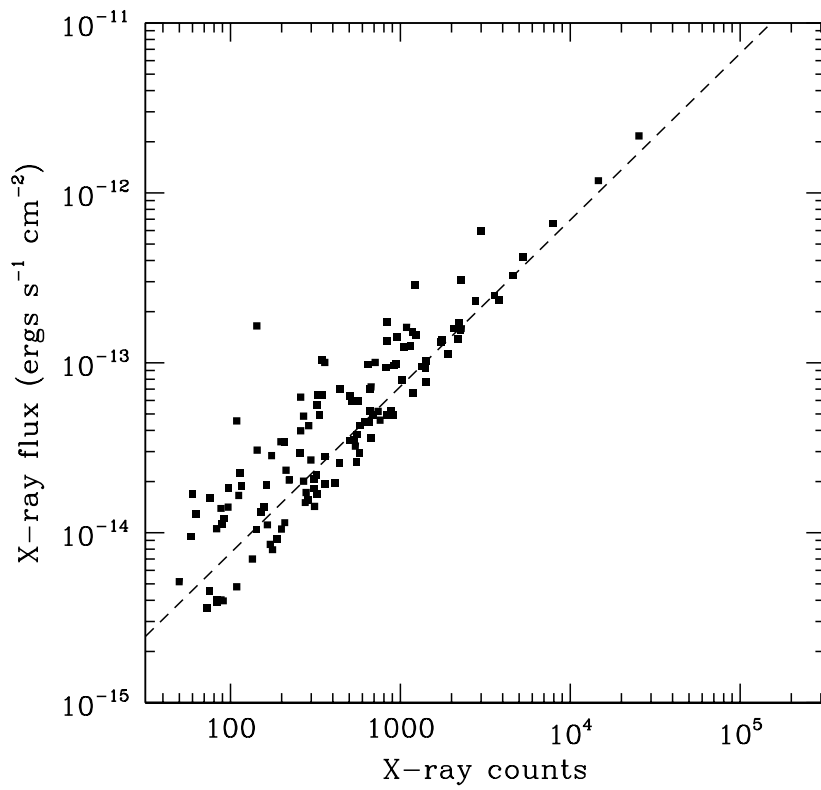


**Figure 7.22:** Relation between X-ray counts and X-ray flux ( $F_X$ ) for NIR-IDed bright (S) sources. The best-fit linear relation is shown with the dashed line.



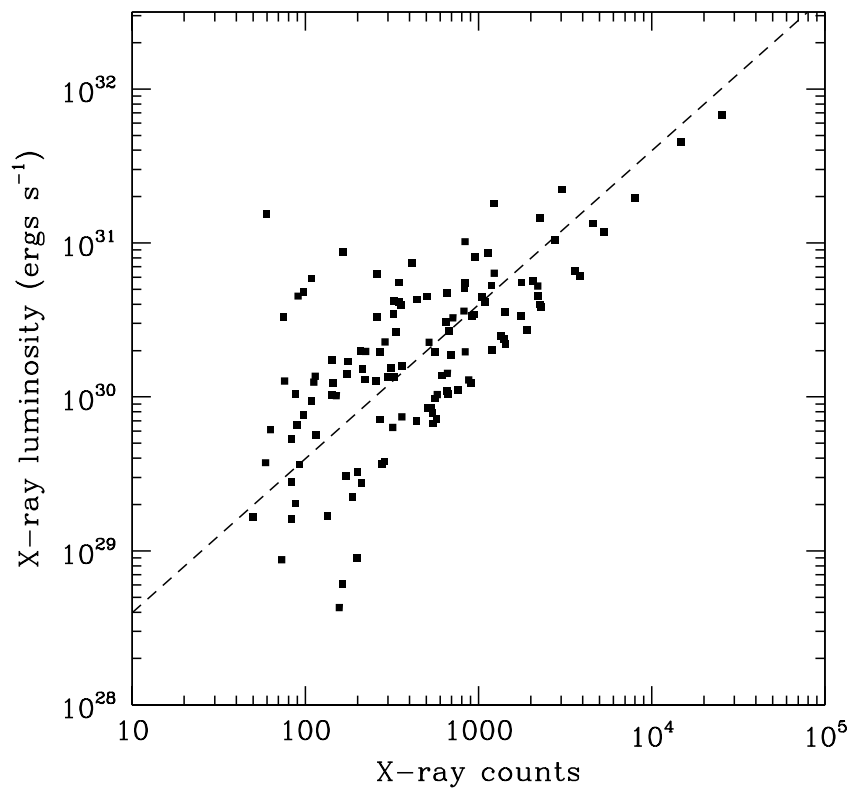


**Figure 7.23:** Relation between X-ray counts and X-ray luminosity ( $L_X$ ) for NIR-IDed bright (S) sources. The best-fit linear relation is shown with the dashed line.



# Chapter 8

## NIR-unIDed X-ray Sources

### Contents

---

<b>8.1</b>	<b>The Nature of NIR-unIDed X-ray Sources . . . . .</b>	<b>168</b>
8.1.1	Background AGNs . . . . .	168
8.1.2	Sources with YSO-like Features . . . . .	175
<b>8.2</b>	<b>H<sub>2</sub> Imaging Observations on OMC-3 . . . . .</b>	<b>177</b>
8.2.1	Observation . . . . .	177
8.2.2	Analysis & Results . . . . .	178
<b>8.3</b>	<b>NIR Observations on MMS 2 and MMS 3 . . . . .</b>	<b>178</b>
8.3.1	Observation . . . . .	178
8.3.2	Analysis & Results . . . . .	181
8.3.3	Discussion . . . . .	187
<b>8.4</b>	<b>Centimeter Observations on MMS 2 and MMS 3 . . . . .</b>	<b>188</b>
8.4.1	Observation . . . . .	188
8.4.2	Analysis & Results . . . . .	189
8.4.3	Discussion . . . . .	190

---

In this chapter, we discuss the nature of NIR-unIDed *Chandra* sources. In Sect. 8.1, we conclude that most of the NIR-unIDed sources are background AGNs based on the spectral analysis of some bright sources, their HR, and spatial distribution. There remain a dozen of exceptions, however, that have YSO-like features among NIR-unIDed sources. Some have a softer HR than AGNs and an association with cloud cores. These X-ray emissions are compared with the H<sub>2</sub> image of OMC-3 that we obtained with QUIRC on UH88 (Sect. 8.2). We found that some NIR-unIDed sources are located at 1.3 mm cloud cores and are associated with H<sub>2</sub> outflows. As a test case, we studied the X-ray emissions at MMS 2 and MMS 3 with follow-up observations in the NIR (Sect. 8.3) and the centimeter (Sect. 8.4) band respectively using Subaru and VLA. The nature of NIR and centimeter sources is discussed in each section, which gives vital clues to discuss the origin of these X-ray emissions in Chap. 9.

## 8.1 The Nature of NIR-unIDed X-ray Sources

### 8.1.1 Background AGNs

We have 107 *Chandra* ACIS-I sources that were identified with neither 2MASS nor QUIRC sources. Most of these sources are too faint to conduct temporal and spectral analyses unlike NIR-IDed sources, which makes it difficult to discuss their nature on a source basis. However, on the following arguments, we consider that most, if not all, of these NIR-unIDed sources are background AGNs.

First, we fitted the spectra of NIR-unIDed bright (S) sources with a power-law model;

$$M(E) \propto E^{-\Gamma}, \quad (8.1)$$

convolved with the ISM absorption. NIR-unIDed bright (S) sources were defined in Figure 8.1 with the same criteria for NIR-IDed bright (S) sources (Fig. 7.7). Fifteen (14%) sources were found to be bright (S), while 92 (86%) were faint (S).

All of the bright (S) sources were well fitted with a power-law model, with the upper probability of  $\alpha > 0.05$ . Photons in the 1.0–8.0 keV range were used. Using the best-fit parameters, we derived  $N_{\text{H}}$ , the photon index ( $\Gamma$ ), and  $F_{\text{X}}$  in Table 8.1. The spectra and the best-fit models are shown in Figures 8.2 and 8.3.

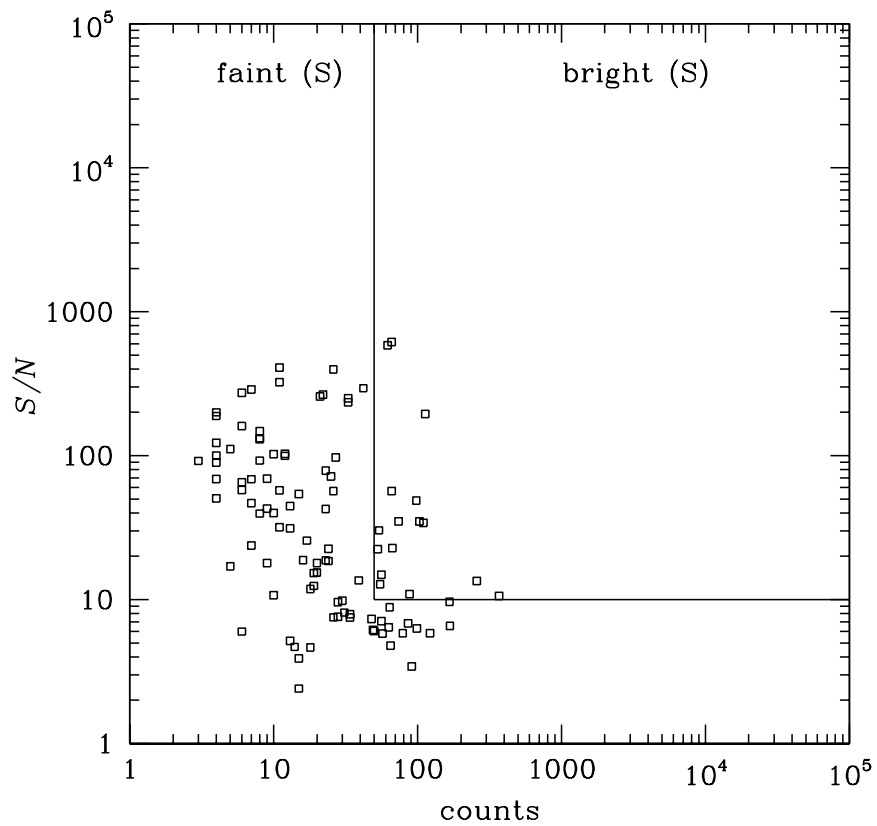


**Figure 8.1:** X-ray counts (0.5–8.0 keV) and  $S/N$  (2.0–8.0 keV) of NIR-unIDed ACIS-I sources. Sources with more counts than 50 and higher  $S/N$  than 10 (15 sources) are bright (S) sources, for which the spectral analysis was conducted.

The AGNs generally show the power-law index of  $\Gamma \sim 1.7$  in the X-ray band regardless of their types and luminosities (Charles & Seward 1995<sup>[33]</sup>). Most spectra are consistent with that of a typical AGN. Moreover, when fitted with a thin-thermal plasma model, many spectra had the unphysical best-fit values of  $k_{\text{B}}T > 15$  keV. These indicate that the X-ray emissions from these bright (S) sources are from mostly AGNs, not from YSOs.

**Table 8.1:** Power-law fittings of NIR-unIDed *Chandra* sources

ID <sup>a</sup>	counts <sup>b</sup>	$S/N$ <sup>c</sup>	$N_{\text{H}}$ <sup>d</sup> ( $10^{22} \text{ cm}^{-2}$ )	$\Gamma$ <sup>d</sup>	$F_{\text{X}}$ <sup>b</sup> ( $\text{ergs s}^{-1} \text{ cm}^{-2}$ )
I3 <sup>†</sup>	368	10.6	1.43 (0.74–2.00)	0.51 (0.17–0.98)	9.74e–14
I11 <sup>†</sup>	110	34.1	1.40 (0.05–3.48)	1.10 (0.14–2.11)	2.90e–14
I19 <sup>†</sup>	103	35.0	1.21 (0.00–3.20)	1.58 (0.52–2.94)	1.87e–14
I22 <sup>†</sup>	55	12.8	0.91 (0.00–5.27)	1.09 (–0.16–4.01)	1.13e–14
I23 <sup>†</sup>	98	48.7	1.74 (0.00–4.63)	1.35 (0.04–2.78)	2.18e–14
I50	54	30.3	2.27 (0.00–7.29)	2.11 (0.07–6.18)	9.25e–15
I98	62	586.2	2.08 (.....–.....)	2.01 (.....–.....)	1.46e–14
I186	66	615.8	1.34 (0.00–45.8)	0.99 (–0.54–10.0)	2.64e–14
I266	53	22.4	2.91 (.....–.....)	0.92 (.....–.....)	1.98e–14
I275	66	56.7	16.2 (.....–.....)	1.30 (.....–.....)	2.92e–14
I301	113	194.8	3.68 (1.32–6.57)	2.40 (1.65–3.60)	2.41e–14
I325 <sup>†</sup>	74	35.0	1.16 (0.00–5.61)	0.87 (–0.33–3.22)	1.97e–14
I330	67	22.8	7.15 (2.98–13.1)	4.36 (2.30–7.84)	1.03e–14
I336 <sup>†</sup>	88	10.9	0.84 (0.00–2.85)	0.98 (–0.11–1.65)	1.59e–14
I345 <sup>†</sup>	258	13.5	0.47 (0.00–1.10)	0.66 (0.09–0.88)	5.96e–14

<sup>a</sup> Sources that are rejected to have a thin-thermal plasma spectrum are marked with <sup>†</sup>.

<sup>b</sup> Values in the 0.5–8.0 keV range.

<sup>c</sup> Values in the 2.0–8.0 keV range.

<sup>d</sup> The lower and upper limit ( $1 \sigma$ ) are given in parentheses. Three sources (I98, I266, and I275) have too few spectral bins to derive the uncertainty of their best-fit parameters.

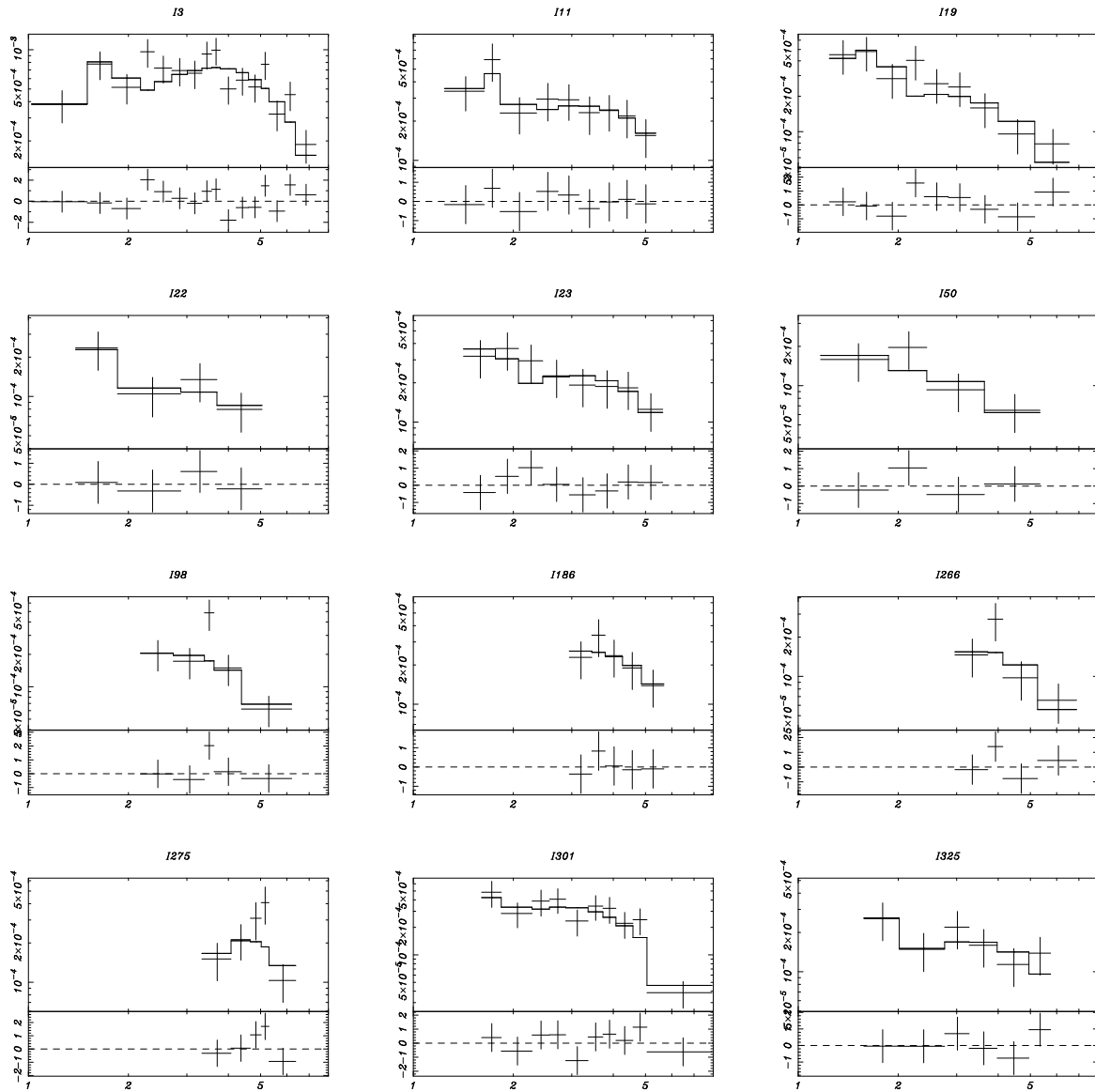


**Figure 8.2:** Spectra and the best-fit power-law models of NIR-unIDed bright (S) *Chandra* sources (I3–I325). In the upper panels, the data (*pluses*) and the best-fit model (*solid steps*) are plotted over the energy (keV; *horizontal axis*) versus normalized spectral intensity (count rate  $\text{keV}^{-1}$ ; *vertical axis*) plane. The response functions of the optics and the detector are convolved into the model. In the lower panels, the residuals between the background-subtracted data and the best-fit model are plotted over the energy (keV; *horizontal axis*) versus  $\chi^{(i)} = (E_{\text{data}}^{(i)} - E_{\text{model} \otimes \text{ARF} \otimes \text{RMF}}^{(i)}) / \Delta E_{\text{data}}^{(i)}$  (*vertical axis*) plane.

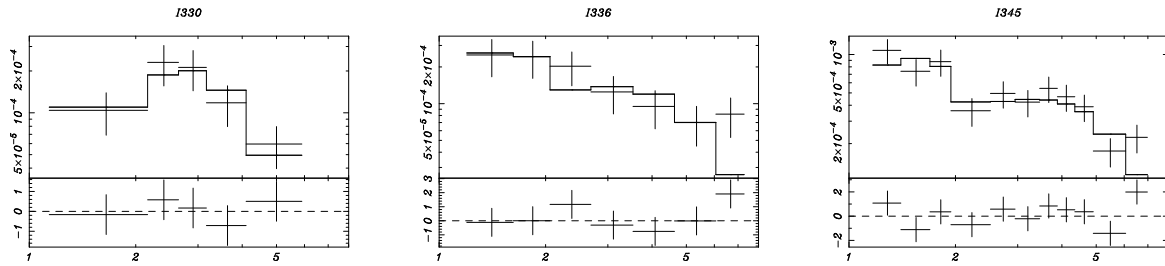


**Figure 8.3:** Spectra and the best-fit power-law models of NIR-unIDed bright (S) *Chandra* sources (I330–I345).

The second argument is the HR of NIR-unIDed sources. Figure 8.4 shows the histogram of the HR for NIR-IDed (*solid*) and NIR-unIDed (*dashed*) *Chandra* sources. These two histograms are in clear contrast with each other, where NIR-IDed source histogram peaks at  $-0.8 < \text{HR} < -0.6$  and NIR-unIDed source histogram at  $0.4 < \text{HR} < 0.6$ . With completely different profiles, it is natural to consider that NIR-IDed and NIR-unIDed sources have different origins for their X-ray emissions.

The spectra of bright (S) sources show the  $N_{\text{H}}$  values of  $\sim 1\text{--}3 \times 10^{22} \text{ cm}^{-2}$  (Table 8.1). When absorbed with this column density, a power-law spectrum of  $\Gamma = 1.7$  has the HR of 0.40–0.81. This corresponds to the peak of the NIR-unIDed histogram. On the other hand, a thin-thermal plasma spectrum with  $k_{\text{B}}T = 0.8 \text{ keV}$  and  $N_{\text{H}} = 6.6 \times 10^{21} \text{ cm}^{-2}$  (representative values for the lower-temperature component; see Sect. 9.2) has  $\text{HR} = -0.77$ , and that with  $k_{\text{B}}T = 3.0 \text{ keV}$  and  $N_{\text{H}} = 6.6 \times 10^{21} \text{ cm}^{-2}$  (representative values for the higher-temperature component) has  $\text{HR} = 0.02$ . These account for the NIR-IDed histogram. All these infer that the histogram of the NIR-unIDed sources is mainly composed of AGNs, while that of NIR-IDed sources is of YSOs.

To confirm this further, we combined the spectra of the NIR-unIDed sources in the same HR bin in Figure 8.4 from  $\text{HR} = 0.0\text{--}0.2$  to  $0.8\text{--}1.0$ , and fitted them with a power-law model. The spectra and the best-fit models are shown in Figure 8.5, while the best-fit values are in Table 8.2. The indices of the power-law are consistent with  $\Gamma = 1.7$  with increasing absorption from softer to harder HRs.

Third, the number of NIR-unIDed X-ray sources is roughly in the same order of the expected number of background AGNs. Giacconi et al. (2001)<sup>[68]</sup> derived the  $\log N - \log S$



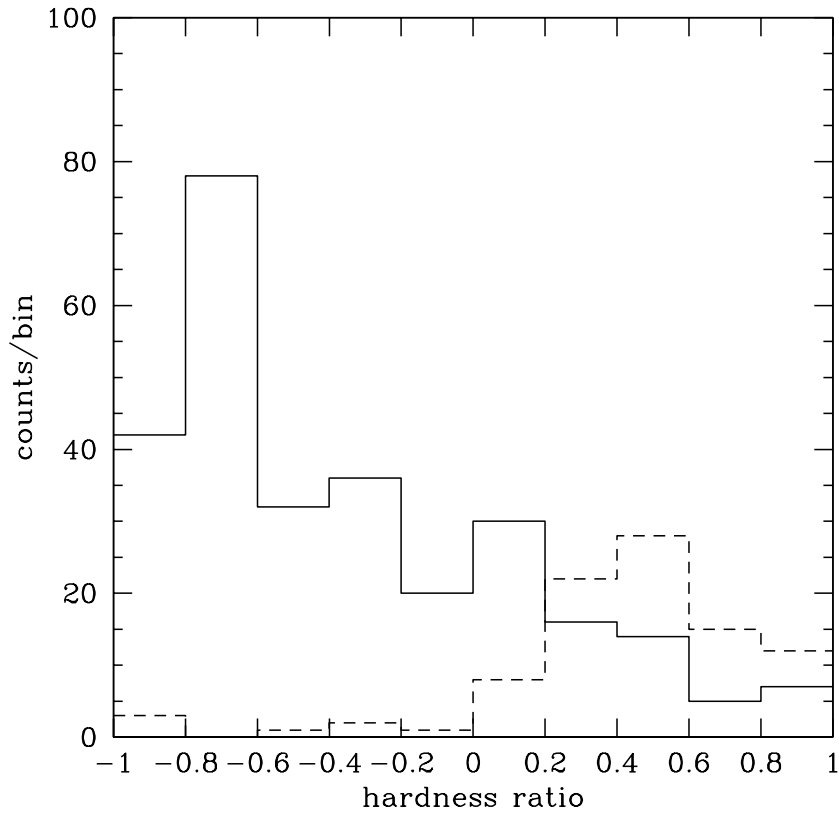


**Figure 8.4:** Histogram of *Chandra* hardness ratio separately for NIR-IDed (*solid*) and NIR-unIDed (*dashed*) sources.

**Table 8.2:** Power-law fittings of combined spectra of NIR-unIDed *Chandra* sources

<i>HR</i> range	$N_{\text{H}}^{\text{a}}$ ( $10^{22} \text{ cm}^{-2}$ )	$\Gamma^{\text{a}}$
0.0–0.2	0.34 (0.14–0.75)	1.20 (0.81–1.81)
0.2–0.4	1.19 (0.80–1.72)	1.27 (1.00–1.72)
0.4–0.6	2.16 (1.55–3.08)	1.49 (1.12–1.81)
0.6–0.8	3.54 (2.07–5.33)	1.58 (1.11–2.55)
0.8–1.0	5.17 (0.00–6.57)	1.70 (0.15–2.45)

<sup>a</sup> The lower and upper limit ( $1 \sigma$ ) are given in parentheses.

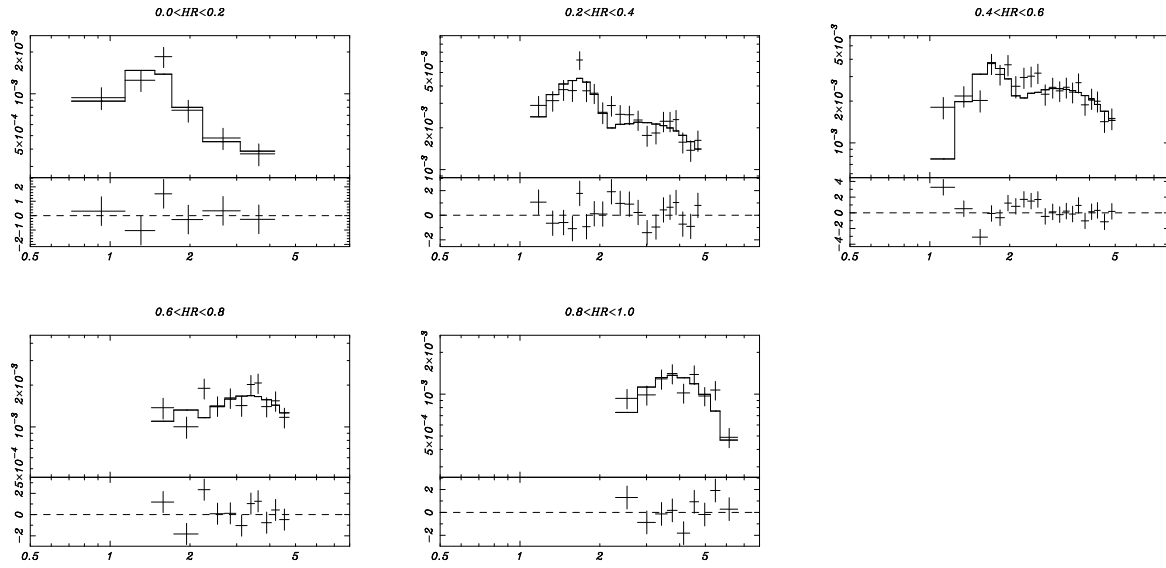


**Figure 8.5:** Spectra and the best-fit power-law models of the combined spectra of NIR-unIDed *Chandra* sources in the same *HR* bin from 0.0–0.2 to 0.2–1.0. In the upper panels, the data (*pluses*) and the best-fit model (*solid steps*) are plotted over the energy (keV; *horizontal axis*) versus normalized spectral intensity (count rate  $\text{keV}^{-1}$ ; *vertical axis*) plane. The response functions of the optics and the detector are convolved into the model. In the lower panels, the residuals between the background-subtracted data and the best-fit model are plotted over the energy (keV; *horizontal axis*) versus  $\chi^{(i)} = (E_{data}^{(i)} - E_{model \otimes ARF \otimes RMF}^{(i)}) / \Delta E_{data}^{(i)}$  (*vertical axis*) plane.

relation of extragalactic X-ray sources as

$$N(> S) = 1200 \times \left( \frac{S}{2 \times 10^{-15} \text{ ergs s}^{-1} \text{ cm}^{-2}} \right)^{-1.0}, \quad (8.2)$$

where  $N(> S)$  is the number of X-ray sources per square degree brighter than  $S$  ergs s<sup>-1</sup> cm<sup>-2</sup> in the hard X-ray band (2.0–7.0 keV). In Sect. 5.1, we discussed the completeness limit of our *Chandra* observation to be  $F_X \sim 10^{-14.5}$  ergs s<sup>-1</sup> cm<sup>-2</sup> in 0.5–8.0 keV. Assuming a power-law spectrum of  $\Gamma = 1.7$  and  $N_H = 1\text{--}3 \times 10^{22}$  cm<sup>-2</sup>, the expected number of the extragalactic sources is 74–81.

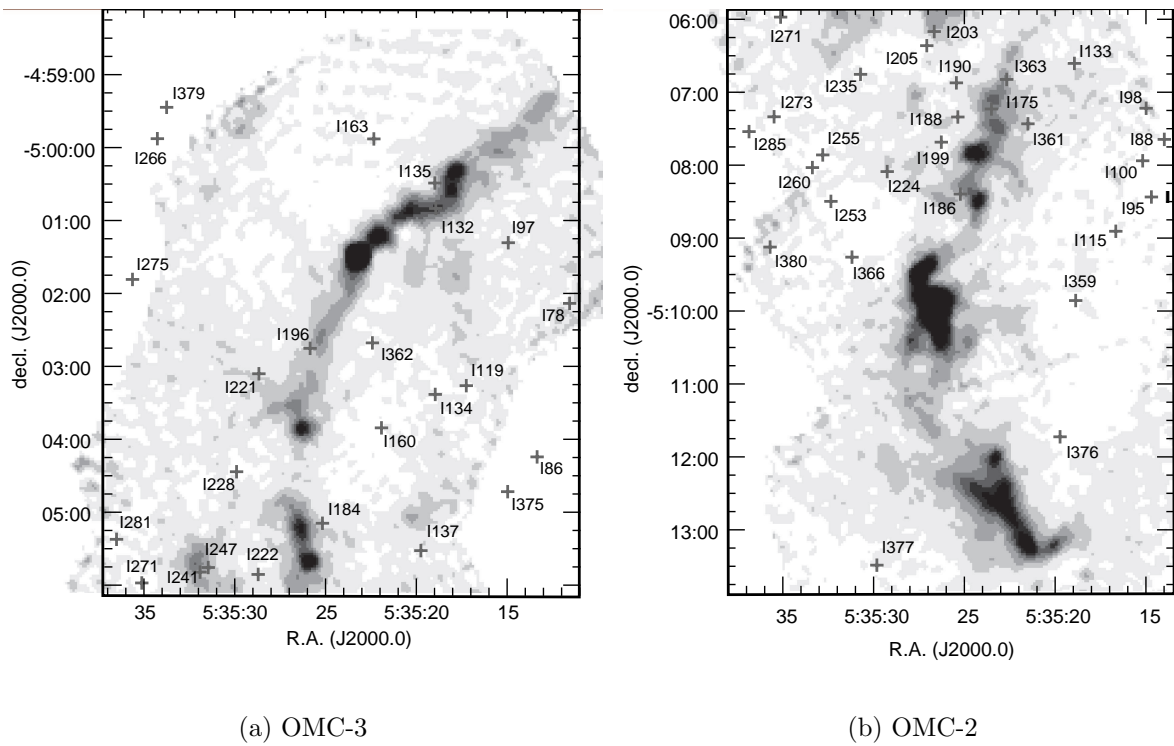
Finally, the spatial distribution of NIR-unIDed sources (Fig. 6.8 d) is not correlated with the 1.3 mm intensity map, but shows a rather uniform distribution. This is in contrast with protostar and cTTS X-ray sources.

### 8.1.2 Sources with YSO-like Features

There are, however, some exceptions for the NIR-unIDed X-ray sources to be of the extragalactic origin. Some sources show YSO-like features.

Figure 8.4 shows that there are some soft X-ray sources with  $HR < 0$  among NIR-unIDed sources. The overall extinction of our study field is derived to be  $A_K \sim 0.5\text{--}1$  mag (Fig. 6.4), which can be converted to  $N_H = 0.5\text{--}1 \times 10^{22}$  cm<sup>-2</sup> using the equation (7.6). With this absorption, the power-law spectrum of  $\Gamma = 1.7$  has the HR of 0.12–0.40. Even with no absorption, the spectrum has the HR of –0.45. Most of the NIR-unIDed X-ray sources with  $HR < 0$  are unlikely to be AGNs.

Some sources appear to be spatially associated with the 1.3 mm cloud ridge (Fig. 8.6). If all the NIR-unIDed sources were distributed uniformly in the ACIS-I FOV, the number density would be  $\sim 0.37$  arcmin<sup>2</sup>. The expected number of sources within the integral shape of the 1.3 mm intensity ( $\sim 9.7$  arcmin<sup>2</sup>) is thus calculated to be  $\sim 3.5$ . More than twice numbers of NIR-unIDed sources (I132, I135, I175, I186, I196, I203, I241, I247, and I363) are actually within the integral shape, indicating that some of them have physical associations with the cloud cores.



(a) OMC-3

(b) OMC-2

**Figure 8.6:** Positions of NIR-unIDed *Chandra* sources (*pluses*) with their name over the the 1.3 mm intensity in gray scale (Chini et al. 1997<sup>[35]</sup>). (a) OMC-3 and (b) OMC-2.

## 8.2 $H_2$ Imaging Observations on OMC-3

### 8.2.1 Observation

In order to identify the nature of the NIR-unIDed X-ray sources with YSO-like features, we further conducted  $H_2$  mapping observations of OMC-3 with QUIRC (Fig. 8.7). A global map of molecular outflows in star-forming regions is quite useful to see the position and distribution of protostars. QUIRC provides a  $3.2' \times 3.2'$  FOV with the pixel scale of  $0.189'' \text{ pixel}^{-1}$ . With dithering observations, we took images of three  $4.2' \times 4.2'$  regions in two narrow-bands ( $H_2$  at  $2.12 \mu\text{m}$  and  $K$ -continuum at  $2.26 \mu\text{m}$ ). Each FOV was exposed for 60 s on March 13, 2001. The seeing was  $\sim 1.0''$ .

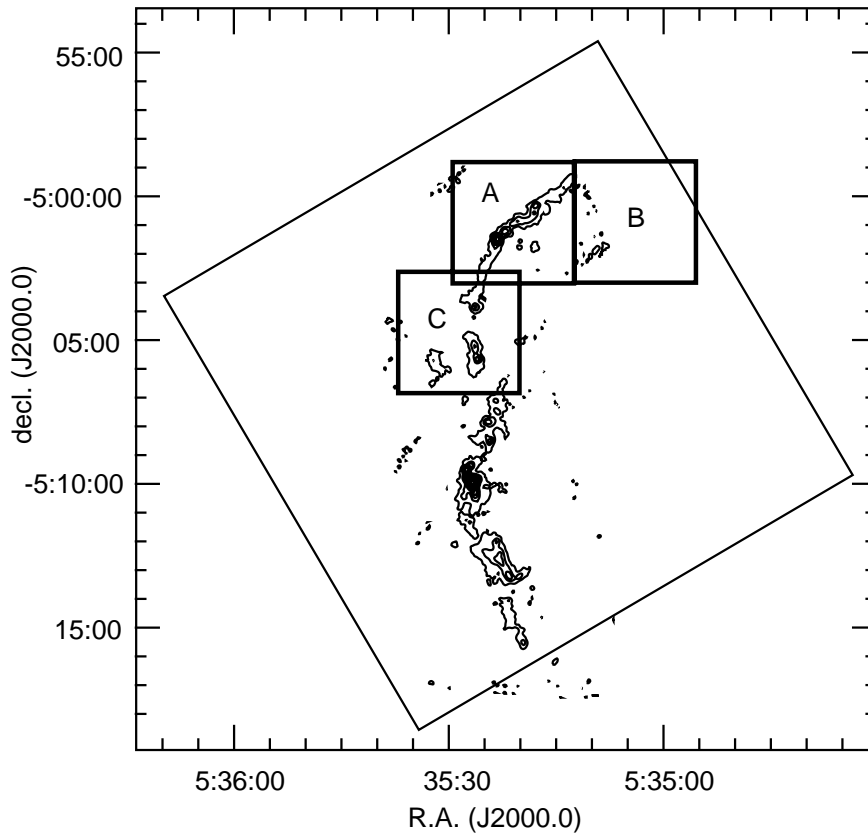


**Figure 8.7:** FOVs of the  $H_2$  and  $K$ -continuum observations using QUIRC. They are respectively named region A, B and C. The *Chandra* ACIS-I FOV is also shown with the large oblique square. The contours are the 1.3 mm intensity (Chini et al. 1997<sup>[35]</sup>).

## 8.2.2 Analysis & Results

The images were reduced following the standard procedures using IRAF; dark subtraction, flat fielding, sky subtraction, bad pixel removal for each frame, and correction for dithering to construct the final images.

The H<sub>2</sub> and *K-continuum* images in three regions were binned with the neighboring 2×2 pixels and smoothed with a Gaussian function to attain better signal-to-noise ratio. The obtained H<sub>2</sub> maps are shown in Figure 8.8. Some *Chandra* sources (e.g.; I241 and I247) were found to be associated both with 1.3 mm intensity and H<sub>2</sub> features.

## 8.3 NIR Observations on MMS 2 and MMS 3

### 8.3.1 Observation

As a test case to study the X-ray emission associated with the 1.3 mm cloud core and H<sub>2</sub> outflow, we focus on the X-ray sources at MMS 2 and MMS 3. Figure 8.9 gives a close-up view of MMS 2–MMS 3 region in the hard (3.0–6.0 keV) and soft (0.5–3.0 keV) X-ray band. These two images were binned with 0.1'' pixel<sup>-1</sup> and smoothed with a Gaussian function of 6 bins to attain the sub-pixel resolution, utilizing the dithering observation of *Chandra*. We see that I128 is separated into four components; three (I128a, I128b and I128c) are in the hard and one (I128d) is in the soft band image. Based on the spatial coincidence with 1.3 mm cores and their hard X-ray spectra, Tsuboi et al. (2001)<sup>[188]</sup> proposed that I128a at MMS 2 and I132 and MMS 3 are the first candidates of the X-ray-emitting class 0 objects.

Previous observations in the radio and NIR band revealed that there is a molecular outflow (Aso et al. 2000<sup>[11]</sup>; Yu et al. 1997<sup>[199]</sup>), an optical jet (Reipurth et al. 1997<sup>[161]</sup>) and a radio jet (Reipurth et al. 1999<sup>[162]</sup>) originating from MMS 2, which strongly indicates that a protostar or protostars are embedded in this core. However, the spatial resolutions of these NIR and radio observations (including our QUIRC observations) are not high enough to match the *Chandra* resolution, which makes impossible to discuss the correlation of the X-ray emissions with the outflow and jet sources. Clearly, follow-up observations with much higher spatial resolution, comparable to that of *Chandra* are needed.

Using IRCS at the Cassegrain focus of the Subaru telescope, we took three broad-band

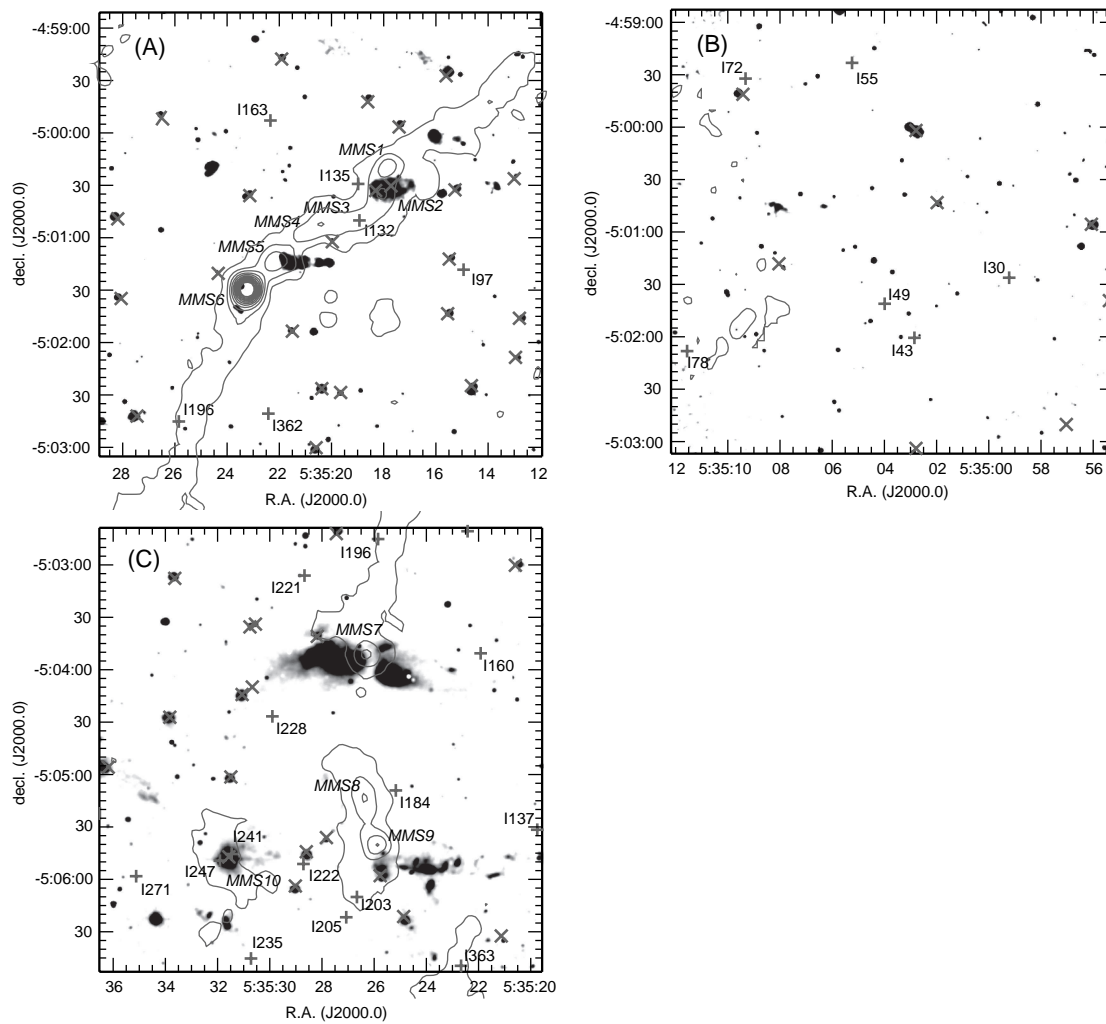


**Figure 8.8:** QUIRC H<sub>2</sub>-band images of three regions in OMC-3. The gray scale gives the H<sub>2</sub> intensity with *K-continuum* not subtracted, while the contours give the 1.3 mm intensity (Chini et al. 1997<sup>[35]</sup>). The crosses and pluses show the position of NIR-IDed and NIR-unIDed *Chandra* sources. The names of NIR-unIDed X-ray sources are given in Roman, while those of 1.3 mm cores are in italic.

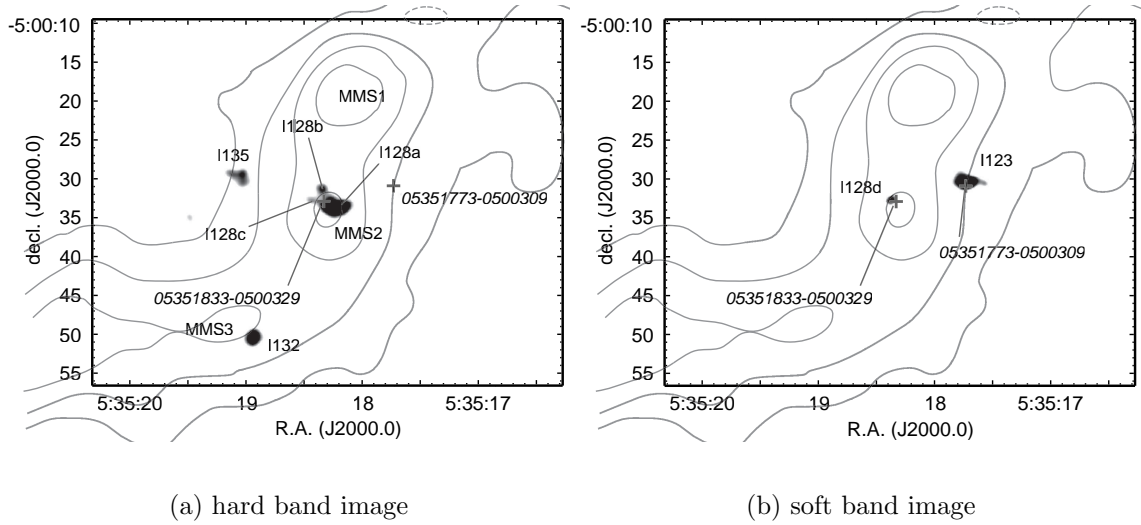


**Figure 8.9:** Close-up images on I128 in MMS 2 for the (a) hard (3.0–6.0 keV) and (b) soft (0.5–3.0 keV) X-ray band. I128 can be separated into four components; I128a, I128b, and I128c in the hard, and I128d in the soft band image. The positions of QUIRC sources are given with pluses with the prefix in their names (“TKK J”) omitted. The contours give the 1.3 mm intensity (Chini et al. 1997<sup>[35]</sup>).

(*J*, *H*, and *K*-band) and two narrow-band ( $H_2$  and *K-continuum*) images on November 30 and December 4, 2000. The seeing was  $\sim 0.5''$  on both nights. The *J*-, *K*-,  $H_2$ -, and *K-continuum*-band images were exposed for 600 s, while the *H*-band images were for 300 s.

IRCS provides a FOV of  $60'' \times 60''$  with a pixel scale of  $0.058'' \text{ pixel}^{-1}$ . With dithering of five FOVs (Fig. 8.10), we covered a  $90'' \times 90''$  field encompassing both MMS 2 and MMS 3 in the central  $30'' \times 30''$  region. Dithering compensates for the pixel-to-pixel variation in quantum efficiency of the detector and enables to construct the sky image by the median-sky technique without taking a sky frame. In a dithering observation of five FOVs, we have five ADU values at each pixel of the detector. By leaving the median values among the five, we can obtain the median-sky image.

As we had no detection in the *J* band from the two NIR sources at MMS 2, we obtained an additional *L'*-band image of MMS 2 with NSFCam at the Cassegrain focus of IRTF on December 23, 2000 with the integration time of 216 s. The seeing was  $\sim 1.0''$ . NSFCam provides a  $38'' \times 38''$  FOV with the pixel scale of  $0.148'' \text{ pixel}^{-1}$ . With dithering, we covered a  $64'' \times 64''$  field.



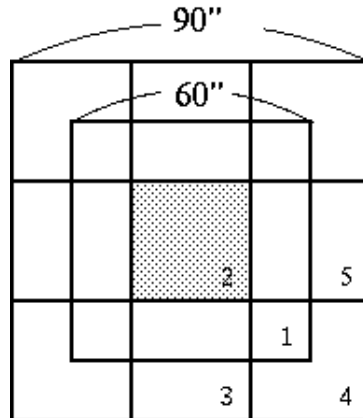


**Figure 8.10:** Configuration of IRCS dithering observations. Five frames (frame numbers are given at the bottom right of each frame) with  $60'' \times 60''$  were combined to construct a  $90'' \times 90''$  image. The hatched region at the center was covered by all frames. The same configuration with a different dithering amplitude was employed for QUIRC  $H_2$  and NSFCam observations.

### 8.3.2 Analysis & Results

#### Source Extraction and Photometry of Broad-band Images

The images were reduced following the standard procedures using IRAF; dark subtraction, flat fielding, sky subtraction, bad pixel removal for each frame, and correction for dithering to construct a final image (Figs. 8.11 and 8.12).

SExtractor (Bertin & Arnouts 1996<sup>[21]</sup>) was used for source extraction and photometry. Nine sources (IRS 1–IRS 9) were extracted from the  $K$ -band image (Table 8.3). For each  $K$ -band detected source, we performed a  $1.0''$ -aperture photometry in the  $J$ ,  $H$ , and  $K$  band. We transformed their magnitudes into the CIT color system in the following way. Seven sources have the counterpart in the Point Source Catalog of the 2MASS Second Incremental Data Release. Referring to their  $J$ -,  $H$ -, and  $K_s$ -band magnitudes, we derived a linear relation between IRCS and 2MASS magnitudes in each band. We first converted the IRCS magnitudes into 2MASS magnitudes using these relations and then into the CIT color system using the formulae given in Carpenter (2001)<sup>[27]</sup>.

For the  $L'$ -band image with NSFCam, we performed a  $2.0''$ -aperture photometry of IRS 3, IRS 4, and IRS 5. We first calculated the magnitudes with the photometric zero-

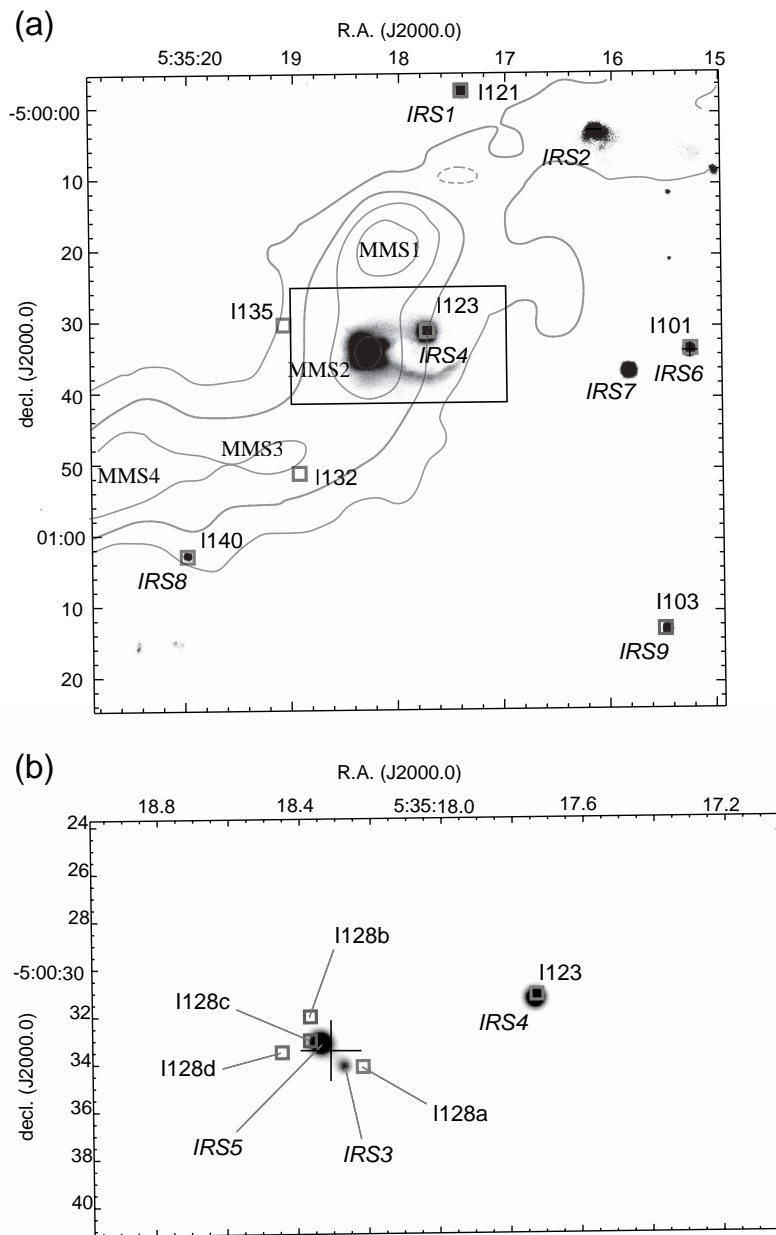


**Figure 8.11:** (a) IRCS *K*-band image with the logarithmic gray scale to stress diffuse features. (b) Close-up view of the MMS 2 region (shown in a rectangle in *a*) in the linear scale to show the accurate positions of point sources. The *K*-band sources (IRS 1–IRS 9) are labeled in *Italic*, while the positions of the X-ray sources are with squares with their names in *Roman*. The contours in (a) are the 1.3 mm intensity. Four 1.3 mm cores (MMS 1–MMS 4) are identified in this region (Chini et al. 1997<sup>[35]</sup>). The plus in (b) shows the position of the 3.6 cm source (Reipurth, Rodríguez, & Chini 1999<sup>[162]</sup>).

point of 20.3 mag<sup>1</sup>, then converted them into the CIT  $L$ -band color using<sup>2</sup>

$$(K - L)_{\text{CIT}} = 0.820 \times (K - L')_{\text{IRTF}}, \quad (8.3)$$

where we assumed  $K_{\text{CIT}} = K_{\text{IRTF}}$  as the first order approximation.

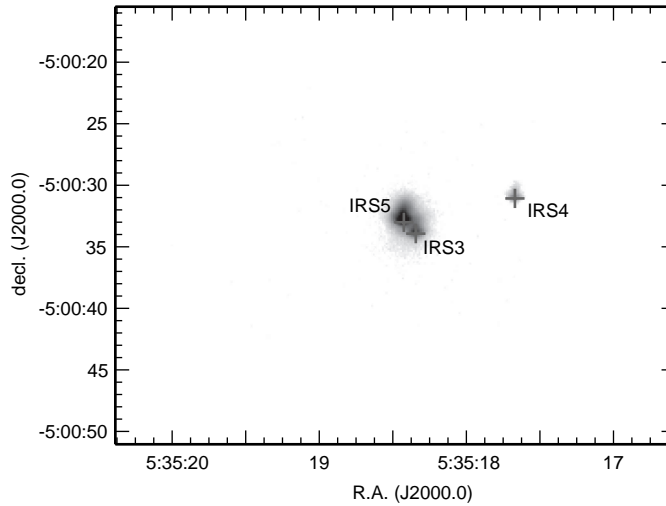


**Figure 8.12:** NSFCam  $L'$ -band image of MMS 2. The positions of the  $K$ -band sources (IRS 3–IRS 5) are shown with pluses.

### Correlation with X-ray Sources

The X-ray counterpart was searched for each NIR source using Table A.1. From the visual inspection of the NIR and X-ray images, we identified the X-ray sources I121, I123, I101, I140, and I103 to be the counterpart of IRS 1, IRS 4, IRS 6, IRS 8, and IRS 9, respectively.

Two NIR sources (IRS 3 and IRS 5) and four X-ray sources (I128a, I128b, I128c, and I128d in Fig. 8.9. These respectively correspond to the source 8, 8a, 8b, and 8c in Tsuboi et al. 2001<sup>[188]</sup>) are crowded at MMS 2. In order to find the X-ray counterpart of the NIR sources, we adjusted the X-ray image by a shift and a rotation so that each X-ray source (I101, I103, I121, I123, and I140) comes closest to its NIR counterpart. After this procedure, the positional offset between the NIR sources and their X-ray counterparts is  $\sim 0.25''$  ( $1 \sigma$ ).

<sup>1</sup>See <http://irtf.ifa.hawaii.edu/Facility/nsfcam/hist/backgrounds.html>.

<sup>2</sup>See <http://irtf.ifa.hawaii.edu/Facility/nsfcam/hist/color.html>.

Then, I128d is found to be the closest source to IRS 5 with the separation of  $0.46''$ , hence is the X-ray counterpart of IRS 5. On the other hand, IRS 3 is separated by  $0.81''$  from the closest X-ray source; I128a. Assuming that the separation between a NIR and X-ray counterpart pair follows a Gaussian distribution of  $\sigma = 0.25''$ , the separation between IRS 3 and I128a is more than  $3\sigma$ . We therefore conclude that I128a is not the X-ray emission from IRS 3. In fact, no separation larger than  $0.81''$  is found in any other NIR and X-ray counterpart pairs. I132 at MMS 3, as well as I128a at MMS 2, has no NIR counterpart.

We chose several source-free regions near the positions of I128a and I132 for a  $1.0''$ -aperture photometry in order to estimate the background level. We found the  $K$ -band upper limit of I128a and I132 to be  $\sim 19.6$  mag at the  $3\sigma$  level.

Table 8.3: IRCS &amp; NSF Cam sources

ID	R.A. <sup>a</sup> (J2000.0)	decl. <sup>a</sup> (J2000.0)	$J^b$ (mag)	$H^b$ (mag)	$K^b$ (mag)	$L^b$ (mag)	2MASS <sup>c</sup> identification	X-ray <sup>d</sup> identification
IRS 1	05:35:17.415	-04:59:57.24	17.8	14.7	13.0	.....	0535174-045957	I121 (6)
IRS 2	05:35:16.168	-05:00:02.58	17.0	14.1	12.3	.....	0535161-050002	.....
IRS 3 <sup>e</sup>	05:35:18.275	-05:00:33.93	>19.6	18.0	13.2	9.17	0535183-050033	.....
IRS 4	05:35:17.736	-05:00:31.07	15.4	13.2	11.7	10.5	0535177-050031	I123 (7)
IRS 5 <sup>e</sup>	05:35:18.340	-05:00:33.01	>19.6	15.8	11.4	7.86	0535183-050033	I128d (8c)
IRS 6	05:35:15.265	-05:00:33.47	13.3	12.7	12.5	.....	0535152-050033	I101 (2)
IRS 7	05:35:15.837	-05:00:36.34	12.3	11.8	11.7	.....	0535158-050036	.....
IRS 8	05:35:19.980	-05:01:02.64	>19.6	>18.8	14.4	.....	0535199-050102	I140 (12)
IRS 9	05:35:15.463	-05:01:12.59	14.2	13.6	13.4	.....	0535154-050112	I103 (3)

<sup>a</sup> The positions are determined from the IRCS  $K$ -band image in the equinox J2000.0.

<sup>b</sup> All magnitudes are in the CIT color system.

<sup>c</sup> 2MASS source names with "2MASS J" omitted for the prefix. IRS 3 and IRS 5 are not resolved in the 2MASS data.

<sup>d</sup> Given in parentheses are the nomenclatures in Tsuboi et al. (2001)<sup>[188]</sup>.

<sup>e</sup> Associated with MMS 2.

### Narrow-band Images

The vibrational-rotational transition of  $v = 1 - 0$  S(1) works as an effective coolant of the excited hydrogen molecules. Therefore, this emission line serves as a powerful tool to search for jets from a protostar and the position of its powering source (Bally et al. 1993<sup>[15]</sup>; Hodapp & Ladd 1995<sup>[88]</sup>). In the continuum-subtracted H<sub>2</sub>-band image, we identified a bubble-like feature originating from MMS 2. A close-up view of this bubble-like emission is shown in Figure 8.13, where we see the origin of this feature spatially coincides with I128a. No similar feature was found for I132 at MMS 3.

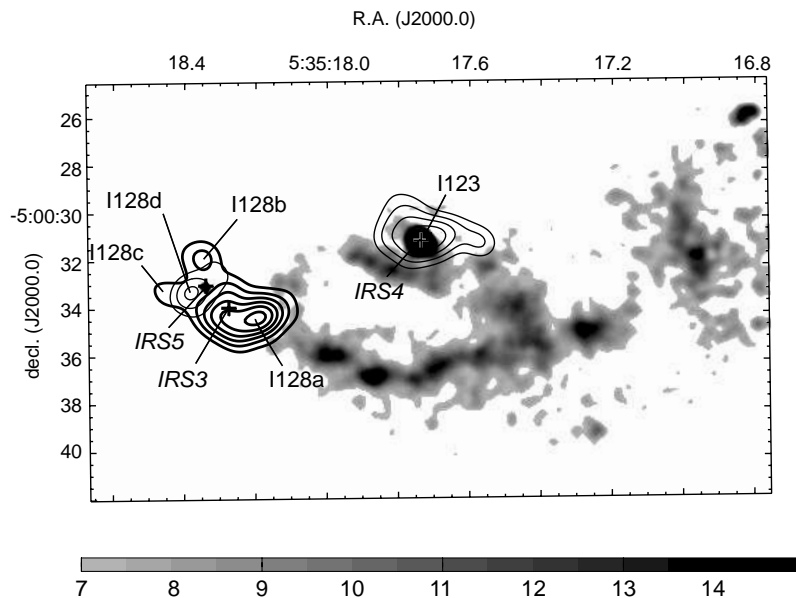


**Figure 8.13:** Continuum-subtracted H<sub>2</sub> intensity (gray scale). The hard (3.0–6.0 keV) and soft (0.5–3.0 keV) X-ray intensity are shown with thick and thin contours. The *K*-continuum image is multiplied by a factor and subtracted from the H<sub>2</sub> image, so that the emissions from IRS 3 and IRS 5 cancel out. Without *K*-continuum subtraction, however, we confirmed the same bubble-like feature in the H<sub>2</sub> image. The scale bar at the bottom is in the unit of intensity pixel<sup>-1</sup>, where the background level (*white*) is  $\sim 2.5$ . The positions of the *K*-band sources are shown with pluses. The X-ray and NIR sources are labeled in Roman and Italic, respectively.

### 8.3.3 Discussion

#### The Nature of NIR Sources

For the classification of IRCS sources, we used the color-color diagram (Lada & Adams 1992<sup>[114]</sup>). The  $(J-H)/(H-K)$  diagram is given in Figure 8.14 (a). Since IRS 3 and IRS 5 have no detection in the  $J$  band, we also give the  $(H-K)/(K-L)$  diagram in Figure 8.14 (b).

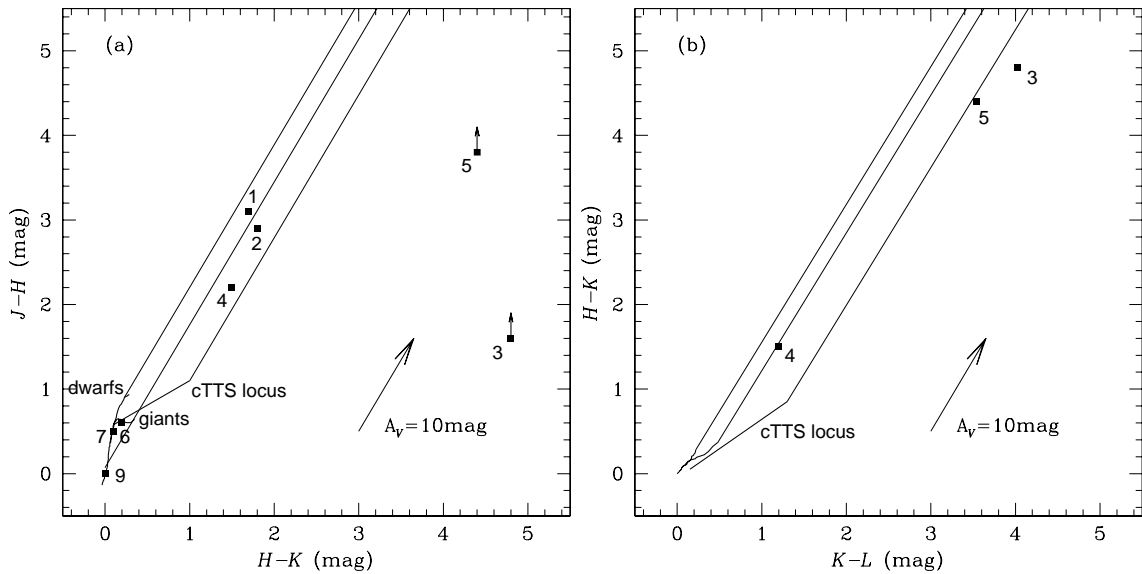


**Figure 8.14:** (a)  $(J-H)/(H-K)$  color-color diagram and (b)  $(H-K)/(K-L)$  color-color diagram. IRS 1–IRS 9 are plotted in the CIT color system with the label of their names (“IRS” is omitted). The uncertainty is less than roughly  $\pm 0.1$  mag for each color. The intrinsic colors of dwarfs and giants are given with thick solid curves (Tokunaga 2000<sup>[185]</sup>), and the cTTS locus is with the thick solid line (Meyer et al. 1997<sup>[130]</sup>). Their extinction vectors are given with the thin solid lines. We assumed the slope of the reddening lines to be  $E(J-H)_{\text{reddening}}/E(H-K)_{\text{reddening}} = 1.69$  and  $E(H-K)_{\text{reddening}}/E(K-L)_{\text{reddening}} = 1.63$  (Meyer et al. 1997<sup>[130]</sup>). The  $A_V$  of each source is estimated from  $E(H-K)_{\text{reddening}} = 0.065 \times A_V$  or  $E(K-L)_{\text{reddening}} = 0.04 \times A_V$  (Meyer et al. 1997<sup>[130]</sup>).

IRS 3 and IRS 5 are at the center of a millimeter core (MMS 2) and are located  $\sim 1.34''$  ( $\sim 600$  AU at the distance of 450 pc) apart from each other (Fig. 8.11). Together with their large extinction of more than  $A_V > 50$  mag and large NIR excess seen in Figure 8.14 (b), they are class I protostars probably comprising a binary system.

IRS 1, IRS 2 and IRS 4 are at the reddening region of the cTTS locus with a moderate extinction of  $A_V \sim 30$  mag (Fig. 8.14 a). They are located at the edge of 1.3 mm cores

(Fig. 8.11), thus are most likely to be cTTSs.

IRS 6, IRS 7, and IRS 9 are located away from the cloud cores (Fig. 8.11) and have less extinction (Fig. 8.14 a). Among them, IRS 6 and IRS 9 are considered to be wTTSs due to the association with X-ray emissions. IRS 7, which has no X-ray counterpart, may be a back- or foreground source.

It is hard to infer the nature of IRS 8 from NIR observation alone because it has only the  $K$ -band detection. However, its X-ray counterpart (I140) shows a thermal emission of  $k_{\text{B}}T = 3.12$  keV,  $L_{\text{X}} = 6.32 \times 10^{30}$  ergs  $\text{s}^{-1}$ , and  $N_{\text{H}} = 6.22 \times 10^{22} \text{cm}^{-2}$  (Table 7.1). These are typical values for class I sources (Table 9.5), hence this source is most likely to be a class I protostar.

## 8.4 Centimeter Observations on MMS 2 and MMS 3

### 8.4.1 Observation

We further took a centimeter image on the MMS 2 region. The purpose of this observation is to determine the position of the protostellar core with an accuracy of  $0.1''$  and to compare it with the X-ray image. Protostars are often accompanied by free-free emissions within 100 AU ( $0.2''$  at MMS 2), which is detectable mostly as point-like by the centimeter continuum imaging observations (Anglada et al. 1992<sup>[7]</sup>; Rodríguez, Anglada, & Raga 1995<sup>[164]</sup>). When observed with long-baseline interferometer observations, centimeter imaging is the most accurate method to determine the position of protostars, providing a vital clue to discuss the mechanism of the X-ray emissions from the youngest phase of protostars.

We conducted our centimeter observation with VLA on February 11, 2002. We used the A configuration to achieve the highest possible spatial resolution. A 3.6 cm map was obtained with the integration time of  $\sim 3.5$  hours, the band width of 50 MHz, and the phase center at R.A. =  $05^{\text{h}}35^{\text{m}}18.3^{\text{s}}$  and decl. =  $-05^{\circ}00'33''$ . The map is sensitive to the structure smaller than  $\sim 2''$  with the angular resolution of  $\sim 0.2''$ . 3C 48 (3.25 Jy) and 0541–056 (0.98 Jy) were used as the flux and phase calibrator, respectively.



### 8.4.2 Analysis & Results

Data reduction, calibration and analysis were performed using AIPS<sup>3</sup>. The natural weighted map is shown in Figure 8.15. We detected two sources (VLA 1a and VLA 1b) above the  $3\sigma$  level, for which we derived the position and the flux density (Table 8.4). VLA 1a is slightly extended, so we also determined the length of the major (minor) axis and position angle to be  $0.40''$  ( $0.09''$ ) and  $32.2$  degree, respectively. These two sources were not resolved in the prior D configuration observation and were named altogether as VLA 1 (Reipurth et al. 1999<sup>[162]</sup>).

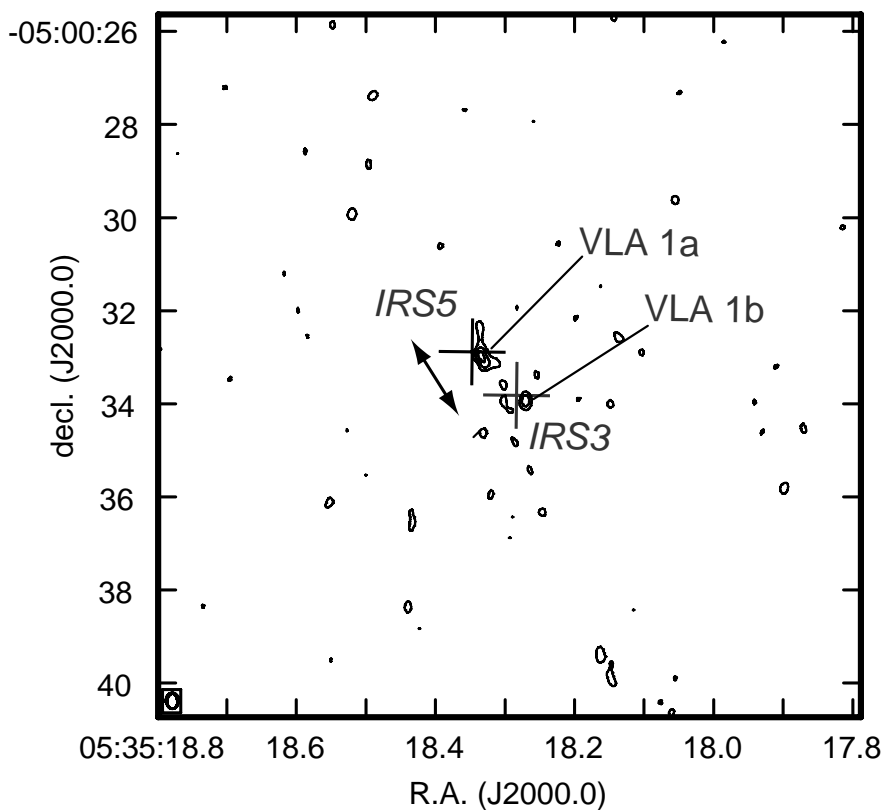


**Figure 8.15:** The 3.6 cm image of MMS 2 and MMS 3 with VLA. *Contours:* the 3.6 cm intensity. The contour levels are  $3-9\sigma$  with the step of  $3\sigma$ , where the background noise is  $\sim 7.7 \mu\text{Jy beam}^{-1}$ . The synthesized beam size is at the bottom left. *Pluses:* the positions of NIR sources. *Arrow:* the position angle of VLA 1a.

<sup>3</sup>See <http://www.cv.nrao.edu/aips/>.

**Table 8.4:** VLA sources

ID	R.A. (J2000.0)	decl. (J2000.0)	flux <sup>a</sup> ( $\mu$ Jy)	major axis ( $''$ )	minor axis ( $''$ )	IRCS counterpart
VLA 1a	05:35:18.335	-05:00:32.97	128	0.40	0.09	IRS 5
VLA 1b	05:35:18.271	-05:00:33.93	54	.....	.....	IRS 3

<sup>a</sup> The flux density is corrected for the primary beam response.

### 8.4.3 Discussion

#### The Nature of Centimeter Sources

For the following reasons, we conclude that both VLA 1a and VLA 1b are free-free emissions from H<sub>II</sub> regions ionized by the UV radiation from the shock front produced by the collision of a protostellar jet upon a dense ISM obstacle (Curiel et al. 1987<sup>[42]</sup>).

First, these centimeter sources are considered to be the counterpart of class I protostars (IRS 3 and IRS 5) from their proximity. The embedded protostars are frequently associated with centimeter emissions, and detailed studies indicate that most of them, if not all, are of free-free emission origin (Anglada 1996<sup>[8]</sup>).

Second, IRS 3 and IRS 5 have the NIR magnitudes and colors of  $J_0 > 11.3$  mag and  $J-H > 1.6$  mag, and  $J_0 > 11.3$  mag and  $J-H > 3.8$  mag, respectively (Table 8.3). This indicates that both sources have a mass less than  $2 M_\odot$ , which rules out the possibility that the centimeter emissions are from H<sub>II</sub> regions generated by stellar UV photons.

Third, the flux density multiplied by the square of the distance ( $S_\nu D^2$ ) and the momentum rate in the outflow ( $dP/dt$ ) of VLA 1a and VLA 1b fit well with a known empirical relation (Anglada et al. 1992<sup>[7]</sup>) and theoretical understandings (Curiel et al. 1987<sup>[42]</sup>) between these two parameters. Figure 8.16 shows the relation between  $S_\nu D^2$  and  $dP/dt$  of 16 embedded objects, where we added VLA 1a/b with  $S_\nu D^2 = 0.182 \times 0.45^2$  mJy kpc<sup>2</sup> (Table 8.4) and  $dP/dt = 3 \times 10^{-5} M_\odot \text{ yr}^{-1} \text{ km s}^{-1}$  (Table 3.2; Aso et al. 2000<sup>[11]</sup>). The limited spatial resolution of the HCO<sup>+</sup> and CO observations could not determine which of the three 1.3 mm clumps (MMS 2–MMS 4) is responsible for the molecular outflow. However, VLA 1a and VLA 1b in MMS 2 are the only 3.6 cm sources that are associated with MMS 2–MMS 4 (Reipurth et al. 1999<sup>[162]</sup>). We can therefore safely assume that the  $dP/dt$

value determined by the molecular outflow represents the sum of the momentum rate from VLA 1a and VLA 1b. Similarly, we summed the flux density of VLA 1a and VLA 1b for the  $S_\nu D^2$  value.

Fourth, in case of VLA 1a, the emission is elongated (the arrow in Fig. 8.15) along the direction of global outflow seen in the  $\text{H}_2 v = 1 - 0 \text{ S}(1)$  band (Fig. 8.13), which is characteristic for the free-free centimeter emissions of shock induced plasma (Anglada 1996<sup>[8]</sup>).

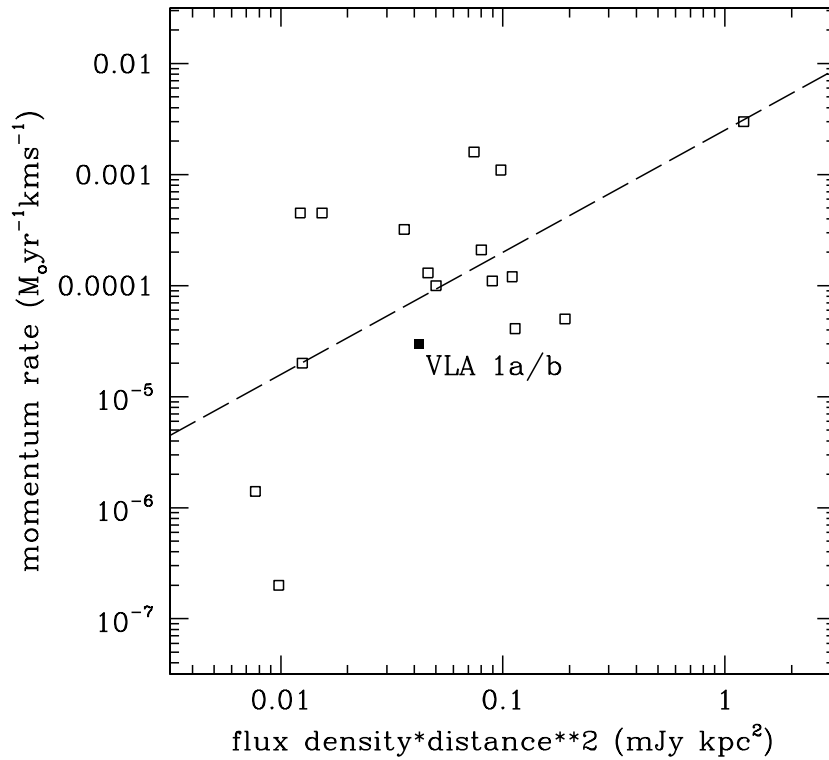


**Figure 8.16:** Relation between the flux density multiplied by the square of the distance ( $S_\nu D^2$ ) and the outflow momentum rate ( $dP/dt$ ). Open squares are from Anglada et al. (1992)<sup>[7]</sup>, who derived an empirical relation among these sources (*dashed line*). The filled square (VLA 1a/b) is roughly consistent with this relation.



# Chapter 9

## Discussion

### Contents

---

<b>9.1</b>	<b>X-ray Emissions from NIR-IDed Sources: (1) Mass . . . . .</b>	<b>194</b>
9.1.1	X-ray Properties among Mass Ranges . . . . .	194
9.1.2	High Mass Sources . . . . .	194
9.1.3	Intermediate Mass to Very Low Mass Sources . . . . .	196
<b>9.2</b>	<b>X-ray Emissions from NIR-IDed Sources: (2) Plasma Temperature</b>	<b>201</b>
9.2.1	Two-temperature Plasma Emissions . . . . .	201
9.2.2	Origins of Two-temperature Plasma . . . . .	203
9.2.3	X-ray Properties among Evolutional Classes . . . . .	206
<b>9.3</b>	<b>X-ray Emissions from NIR-unIDed Sources . . . . .</b>	<b>208</b>
9.3.1	Jet-induced Plasma Emissions . . . . .	208
9.3.2	Magnetic Activities of Deeply Embedded YSOs . . . . .	213

---

In this chapter, we discuss the X-ray emission mechanisms of X-ray sources based on their multi-wavelength features described in the previous chapters. The first two sections are for NIR-IDed X-ray sources. In Sect. 9.1, we compare the X-ray properties in different mass ranges (Sect. 9.1) and discuss that the IM, LM, and VLM sources have the same X-ray emission mechanisms in contrast to HM sources. In Sect. 9.2, we describe that their X-ray emissions consist of two components of different temperatures and propose that the hard component originates from flares while the soft component is from stellar coronae. In Sect. 9.3, we deal with NIR-unIDed X-ray sources, and interpret their X-ray emission in the context of jet-induced plasma and the magnetic activities of deeply embedded NIR invisible YSOs.

## 9.1 X-ray Emissions from NIR-IDed Sources: (1) Mass

### 9.1.1 X-ray Properties among Mass Ranges

Based on the mass estimates of NIR-IDed X-ray sources using the  $J/(J-H)$  color-magnitude diagram, we separated them into four mass ranges (HM, IM, LM, and VLM) in Sect. 6.2. The NIR sources in the ACIS-I FOV are separated in the same manner in order to calculate the X-ray detection rate of each mass range. Readers should note that NIR sources classified as LM and VLM are contaminated by back- or foreground sources (Sect. 6.1), which gives the lower limit of the X-ray detection rate of these groups. The number of NIR and X-ray sources and the detection rate are summarized in Table 9.1 along with the results of the X-ray temporal and spectral analyses. The averaged X-ray properties are in Table 9.2.

### 9.1.2 High Mass Sources

We have one HM source in our sample. The source;  $\nu$  Ori has the spectral type of B1 V (Kukarkin et al. 1971<sup>[111]</sup>), the mass of  $10^{1.05}M_{\odot}$  and the bolometric luminosity of  $10^{4.06}L_{\odot}$  (Greenstein 1998<sup>[71]</sup>). The X-ray counterpart (I242) shows a stable light curve with a soft spectrum. This source is faint (T) and faint (S), so no temporal and spectral analyses were performed (Sects. 7.1 and 7.2). In order to compare with sources in other mass ranges, we examined the temporal variation of I242 and found that the constant flux model was not rejected with  $\alpha > 0.05$  (Fig. 9.1). We also fitted the spectrum in the range of 0.5–2.0 keV

**Table 9.1:** Number of sources among mass ranges

	HM	IM	LM	VLM	sum
NIR sources .....	1	26	210	462	699
X-ray sources .....	1	21	139	107	268
	(100%)	(81%)	(66%)	(23%)	(38%)
NIR sources with NIR excess ..	0	12	45	74	131
X-ray sources with NIR excess	0	11	31	11	53
	(N/A)	(92%)	(69%)	(15%)	(40%)
bright (T) .....	1	16	78	18	113
variable .....	0	12	42	7	66
	(0%)	(75%)	(54%)	(39%)	(58%)
bright (S) .....	0	18	94	22	134
one-temperature .....	0	10	57	13	80
	(N/A)	(56%)	(61%)	(59%)	(60%)
two-temperature .....	0	8	27	6	41
	(N/A)	(44%)	(29%)	(27%)	(31%)

**Table 9.2:** Comparison of X-ray properties among mass ranges

	HM <sup>a</sup>	IM	LM	VLM
$\langle \log N_{\text{H}} (\text{cm}^{-2}) \rangle$ .....	21.5	21.9±0.4	21.6±0.7	21.7±0.6
$\langle kT^{(1)} (\text{keV}) \rangle$ .....	0.64	3.85±1.6	2.30±2.0	2.04±2.3
$\langle \log L_X^{(1)} (\text{ergs s}^{-1}) \rangle$ ...	30.3	30.5±0.4	30.1±0.5	29.8±0.4
$\langle kT_{\text{high}}^{(2)} (\text{keV}) \rangle$ .....	N/A	4.00±2.1	2.75±1.2	2.41±1.1
$\langle \log L_X^{(2)}{}_{\text{high}} (\text{ergs s}^{-1}) \rangle$	N/A	30.6±0.7	30.3±0.4	29.7±0.2
$\langle kT_{\text{low}}^{(2)} (\text{keV}) \rangle$ .....	N/A	0.89±0.2	0.77±0.3	0.44±0.3
$\langle \log L_X^{(2)}{}_{\text{low}} (\text{ergs s}^{-1}) \rangle$	N/A	30.5±0.5	30.1±0.5	29.9±0.7

<sup>a</sup> The result of the spectral fitting of I242 is shown.

to avoid background contamination in the hard X-ray band to have an acceptable fit with a thin-thermal plasma mode. The best-fit parameters are given in Table 9.3, while the spectrum and the best-fit model are in Figure 9.1.

The X-ray emissions from earlier-type main sequence stars than B2 are explained by the stellar wind model (Lucy & White 1980<sup>[118]</sup>; Lucy 1982<sup>[119]</sup>), in which the strong stellar wind propagating through the ambient matter at the speed of  $\sim 1000 \text{ km s}^{-1}$  ionizes the gas with shocks.

The past X-ray observations on this class of stars revealed that they show non-variable light curves, softer spectra than  $k_B T \sim 1 \text{ keV}$ , and  $L_X/L_{\text{bol}} = 10^{-7.1}-10^{-7.6}$  (Berghöfer et al. 1997<sup>[20]</sup>; Feigelson et al. 2002<sup>[54]</sup>). The X-ray features of I242 follow very well with that of the typical early-type stars with  $k_B T = 0.64$ ,  $L_X/L_{\text{bol}} = 10^{-7.3}$ , and an non-variable light curve. We conclude that I242 is a high-mass main sequence source and the X-ray emission from it is of stellar wind origin.

**Table 9.3:** One-temperature plasma fittings of the high mass source

ID	counts <sup>a</sup>	$S/N^b$	$N_H^c$ ( $10^{22} \text{ cm}^{-2}$ )	$k_B T^c$ (keV)	$L_X^a$ (ergs $\text{s}^{-1}$ )
I242	660	8.54	0.34 (0.25–0.39)	0.64 (0.58–0.69)	2.14e+30

<sup>a</sup> Values in the 0.5–8.0 keV range.

<sup>b</sup> Values in the 2.0–8.0 keV range.

<sup>c</sup> The lower and upper limit ( $1 \sigma$ ) are given in parentheses.

### 9.1.3 Intermediate Mass to Very Low Mass Sources

Previous X-ray observations mainly focused on the X-ray emissions from LM YSOs, revealing that they are of thin-thermal plasma origin generated and maintained by magnetic activities on the stellar surface. They show hard and strong X-ray emissions of  $k_B T = 0.5-2.0 \text{ keV}$  and  $L_X/L_{\text{bol}} = 10^{-2}-10^{-5}$  with occasional flare-like variability (Feigelson & Montmerle 1999<sup>[53]</sup>). Less is known for higher mass YSOs because they have lower population and evolve more quickly, making these samples fewer and more distant. The X-ray emissions from VLM sources are also behind our understandings on LM YSOs because they are fainter. Using our VLM, LM, and IM samples, we discuss that YSOs in these mass ranges have the same X-ray emission mechanism.



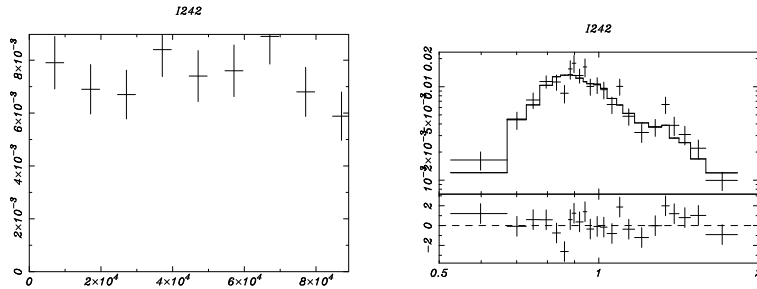


**Figure 9.1:** (*left*) Light curve of the high mass source (I242) over the count rate ( $\text{s}^{-1}$ ; *vertical axis*) versus the time from the start of the observation ( $\text{s}$ ; *horizontal axis*) plane. (*right*) Spectra and the best-fit models of one-temperature thin-thermal plasma fittings of the high mass source (I242). The metallicity of all elements is fixed to be 0.3 solar. In the upper panel, the data (*pluses*) and the best-fit model (*solid steps*) are plotted over the energy ( $\text{keV}$ ; *horizontal axis*) versus normalized spectral intensity (count rate  $\text{keV}^{-1}$ ; *vertical axis*) plane. The response functions of the optics and the detector are convolved into the model. In the lower panel, the residuals between the background-subtracted data and the best-fit model are plotted over the energy ( $\text{keV}$ ; *horizontal axis*) versus  $\chi^2(i) = (E_{\text{data}}^{(i)} - E_{\text{model} \otimes \text{ARF} \otimes \text{RMF}}^{(i)}) / \Delta E_{\text{data}}^{(i)}$  (*vertical axis*) plane.

First, we rule out the possibility that the X-ray emissions from IM YSOs are from their LM companion, which is the most favored scenario for the X-ray emissions from IM main sequence stars (Berghöfer & Schmitt 1994<sup>[20]</sup>). This is because IM main sequence stars have no mechanism to generate high temperature plasma. We compared the X-ray detection rate of our IM samples with the binary rate of the Orion and found that the former ( $\sim 80\%$ ) is much higher than the latter ( $\sim 15\%$ ). The binary rate is presented by Padgett et al (1997)<sup>[146]</sup>, who derived the value based on the *Hubble Space Telescope* observations on three Orion stellar clusters (NGC 2024, NGC 2068, and NGC 2071). They examined 99 sources down to  $I < 19$  mag and found that 15 of them have a binary companion in the separation range of  $0.3'' < \theta < 2.3''$  ( $\sim 100$ – $1000$  AU). As this rate gives the upper limit of IM sources to have a LM binary, all of the X-ray emissions from our IM sources can not be attributable to their companion sources.

We can confine our IM samples to those robustly in the pre-main-sequence stage by picking up sources with the NIR excess (the remainders are the mixture of main and pre-main sequence sources). All but one IM sources with NIR excess are found to have X-ray detections, indicating that virtually all IM YSOs emit X-rays.

We have three lines of evidence to conclude that the same X-ray emission mechanism functions for VLM, LM, and IM YSOs. First, all VLM–IM sources in our sample show

similar X-ray features when averaged over the group (Table 9.2). About  $\sim 60\%$  of them show one-temperature plasma spectra of 2–3 keV and  $\sim 30\%$  show two-temperature plasma with the combination of  $\sim 1.0$  keV and 2–3 keV. This is in contrast to the HM source (I242), which only shows low-temperature ( $\sim 0.5$  keV) plasma spectrum.

Second, the ratio of the X-ray and bolometric luminosity ( $L_X/L_{\text{bol}}$ ) of most of these sources is in the range of  $10^{-2}$ – $10^{-5}$  (Fig. 9.2). The value is consistent with the previous observational results on LM YSOs (Feigelson & Montmerle 1999<sup>[53]</sup>) and higher than that of the typical HM main sequence stars with stellar wind origin ( $\sim 10^{-7}$ ). In fact, the only HM (and some IM) source has  $L_X/L_{\text{bol}} \sim 10^{-7}$ . The trend of lower  $L_X/L_{\text{bol}}$  values toward higher mass sources (Fig. 9.2) is due to the observational bias. We are dealing with the X-ray-selected samples, which causes lower mass (smaller bolometric luminosity) sources not to be detected even with the same  $L_X/L_{\text{bol}}$  value. The bias is illustrated with the dashed curve representing the typical X-ray detection limit of  $10^{29}$  ergs  $\text{s}^{-1}$  (Sect. 5.1).

Third, the  $L_X$  values of VLM–IM sources increase toward the higher mass sources (Fig. 9.3). An empirical relation between these two parameters was presented by Preibisch, & Zinnecker (2002)<sup>[156]</sup> for VLM–LM YSOs in a low-mass star forming region (IC 348). We see that the relation can be extrapolated to apply for IM and VLM sources.

All these arguments infer that VLM–IM sources (including young brown dwarfs) are emitting X-rays with the same mechanism and the level of activity can be scaled with their mass.

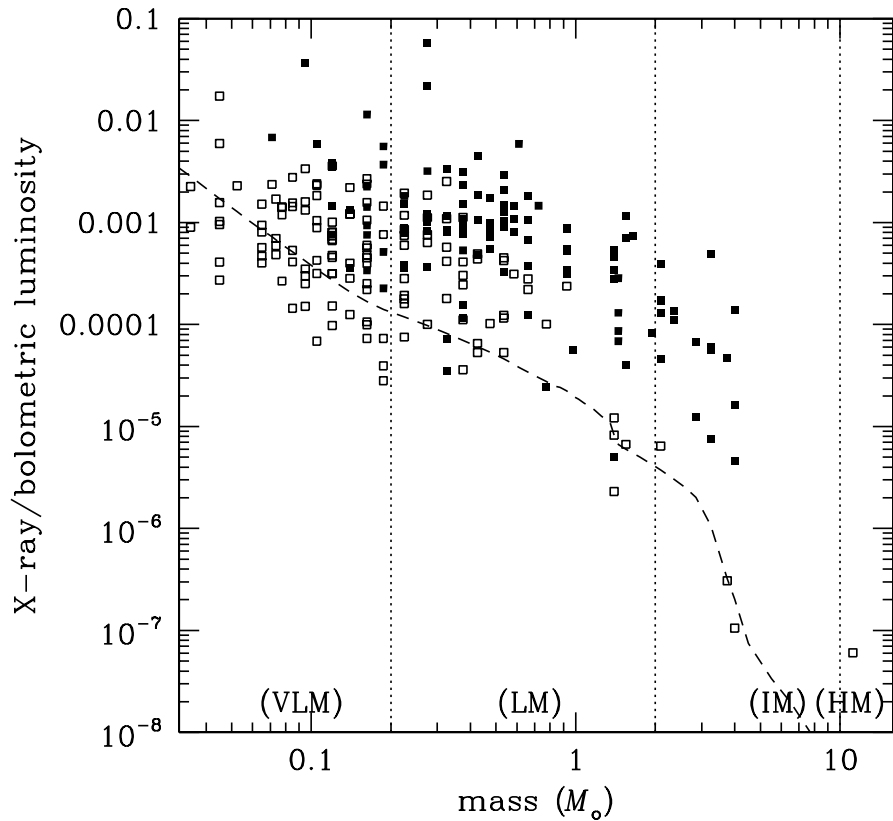


**Figure 9.2:** Relation between the mass ( $M$ ) and the ratio of the X-ray (0.5–8.0 keV) and bolometric luminosity ( $L_X/L_{\text{bol}}$ ) of NIR-IDed X-ray sources. Filled squares are with the X-ray luminosity derived from the spectral fittings, while open squares are with the  $L_X$  values estimated from their X-ray counts using the equation (7.8). The dashed curve shows the typical detection limit of  $L_X = 10^{29}$  ergs  $\text{s}^{-1}$ .

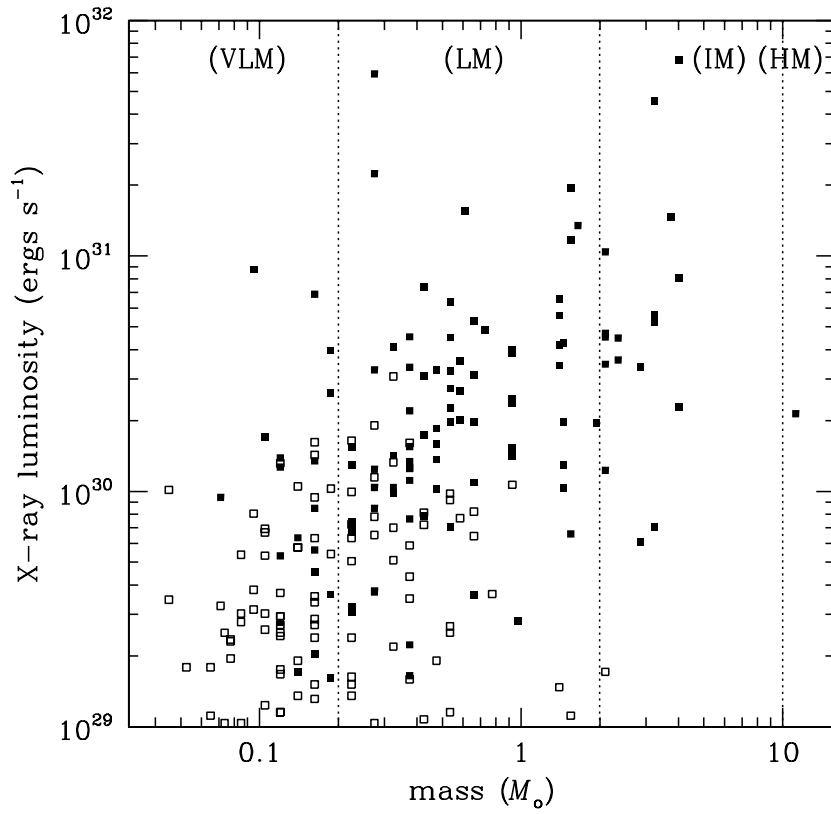


**Figure 9.3:** Relation between the mass ( $M$ ) and the X-ray luminosity ( $L_X$ ) of NIR-IDed X-ray sources in the 0.5–8.0 keV. Filled squares are with the luminosity derived from the spectral fittings, while open squares are with the  $L_X$  values estimated from their X-ray counts using the equation (7.8).

## 9.2 X-ray Emissions from NIR-IDed Sources: (2) Plasma Temperature

### 9.2.1 Two-temperature Plasma Emissions

The previous discussion that the same X-ray emission mechanism works for VLM–IM sources justifies us to deal with them collectively. We consider, for the following reasons, that these sources have the combination of two X-ray emission mechanisms of different temperature.

Figure 9.4 (a) shows the histogram of the plasma temperatures of VLM–IM sources, where we count the sources with two-temperature plasma twice at each temperature. We can see two peaks at  $k_{\text{B}}T \sim 1$  keV and 2–3 keV. According to the standard magnetic reconnection model of solar flares, the plasma temperature at a flare ( $T_f$ ) is described as a function of the pre-flare density ( $n_0$ ), the loop length ( $L$ ), and the magnetic field strength ( $B$ ); e.g.,

$$T_f = 2 \times 10^7 \left( \frac{B}{0.003 \text{ T}} \right)^{\frac{6}{7}} \left( \frac{n_0}{10^{-15} \text{ m}^{-3}} \right)^{-\frac{1}{7}} \left( \frac{L}{10^7 \text{ m}} \right)^{\frac{2}{7}} \text{ [K]} \quad (9.1)$$

(Yokoyama & Shibata 1998<sup>[197]</sup>). Taking into account that these parameters can change continuously, this histogram should appear with one peak with broad tails. It is more natural to understand, therefore, that these sources have two different X-ray emission mechanisms, each of which high and low temperature plasma are attributable to.

This is reinforced by examining sources with two-temperature plasma. Figure 9.4 (c) shows the histogram of plasma temperatures separately for the lower (*solid*) and higher (*dashed*) temperature component. The peak of the lower temperature component is at  $k_{\text{B}}T \sim 1$  keV, while that of the higher temperature component is at  $k_{\text{B}}T = 2\text{--}3$  keV. These two components coexist at flare and quiescent phases, because for the reason that the time-sliced spectra of some brightest sources require a two-temperature plasma model in both phases (Sect. 7.2). It is not the case, therefore, that these X-ray emissions are attributable to only one component that shows a higher temperature at flare phases and a lower temperature at quiescent phases.

It is also unlikely that the sources with two-temperature plasma are binaries. First, we confirmed both in the X-ray and the  $K$ -band images that only four (I42, I211, I256, and I314) among the 41 two-temperature sources can be contaminated with their close companion. Second, among the 30 bright (S) sources with more counts than 1000 (sources

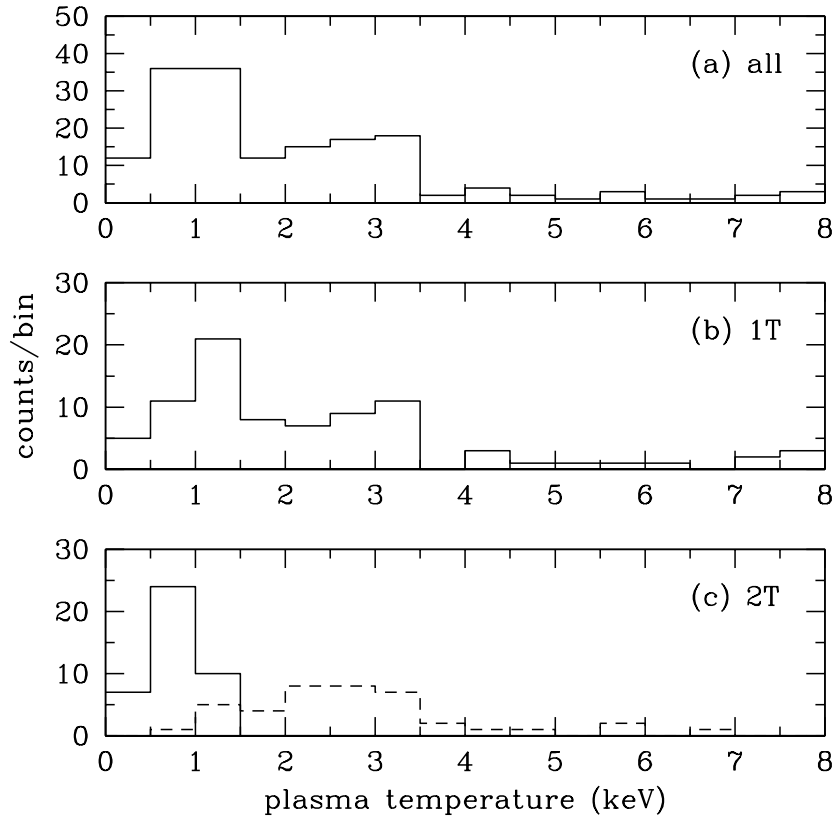


**Figure 9.4:** Histograms of plasma temperatures of bright (S) NIR-IDed X-ray sources; (a) total, (b) one-temperature plasma, and (c) two-temperature plasma sources. In (c), the histograms of the lower and higher temperature are given with solid and dashed, respectively.

with the spectrum of sufficient statistics to examine the two-temperature nature), 23 sources require two-temperature plasma models (Fig. 7.7). The rate of 77% is much higher than the binary rate ( $\sim 15\%$ ) of this region (Padgett, Strom, & Ghez 1997<sup>[146]</sup>). Finally, we have no reason to expect that the temperature of each binary component is always the combination of  $k_{\text{B}}T \sim 1$  keV and 2–3 keV.

One-temperature sources are considered to be with no or negligible contribution by either component. The two peak profile of their temperature histogram (Fig. 9.4 b) is consistent with this idea.

The two components show different temporal behavior. In Table 7.5, we see that the  $EM$  values of the high temperature component increase during flare phases, while those of the low temperature component stay constant or slightly decrease. This indicates that the flare-like variability is caused by the high temperature component. This is further strengthened by the fact that almost all the one-temperature plasma sources with flare-like variations (Figs. 7.2–7.6) have the plasma temperature of 2–3 keV or higher; e.g., I67 (2.7 keV), I131 (3.2 keV), I138 (7.5 keV), I165 (4.8 keV), I218 (3.1 keV), I264 (5.5 keV), and I280 (2.7 keV). In contrast, the light curves of the low temperature component show moderate variability of no flare-like episodes. Typical examples are the light curves of I54 (0.8 keV) and I282 (1.0 keV).

### 9.2.2 Origins of Two-temperature Plasma

A similar bimodal structure in the plasma temperature distribution is seen in the sun. Peres et al. (2000)<sup>[150]</sup> integrated all the X-ray emissions from the sun using the Soft X-ray Telescope (SXT) on *Yohkoh* and convolved the spectrum with the response function of *ASCA*/SIS in order to facilitate direct comparison with the X-ray emissions from other stars. The synthesized solar spectrum is well fitted with one- or two-temperature plasma model at the solar minimum and maximum. At the solar maximum, the plasma temperatures are  $k_{\text{B}}T \sim 0.2$  keV and  $\sim 0.5$  keV. From the geometrically well-defined data on solar X-ray emissions, the higher and lower temperature components are found to originate from the solar coronae and flares. We interpret the two-temperature plasma of YSOs in the same analog; i.e., the higher temperature (2–3 keV) component is from flares and the lower temperature component is from the coronae.

Two pieces of evidence support our idea. First, similar bimodal temperature structures

are also seen in other stars, with increasing plasma temperature toward younger samples (Figs. 2.7 and 9.5). Figure 9.6 shows the evolution of the representative plasma temperatures separately for the higher (*filled squares*) and lower (and middle) temperature component (*open squares*). Three G-type main sequence sources (EK Dra, HN Peg, and  $\kappa^1$  Cet; Güdel, Guinan, & Skinner 1997<sup>[74]</sup>) and one G-type pre-main-sequence source (SU Aur; Skinner & Walter 1998<sup>[173]</sup>) are plotted. As the stellar rotation becomes slower as increasing ages, main sequence sources evolve magnetically inactive and the plasma temperature decreases (Güdel et al. 1997<sup>[74]</sup>). Our sample sources are at the age of  $\sim 1$  Myr (or younger), which settles both of their typical high and low temperatures on this temperature-age relations.

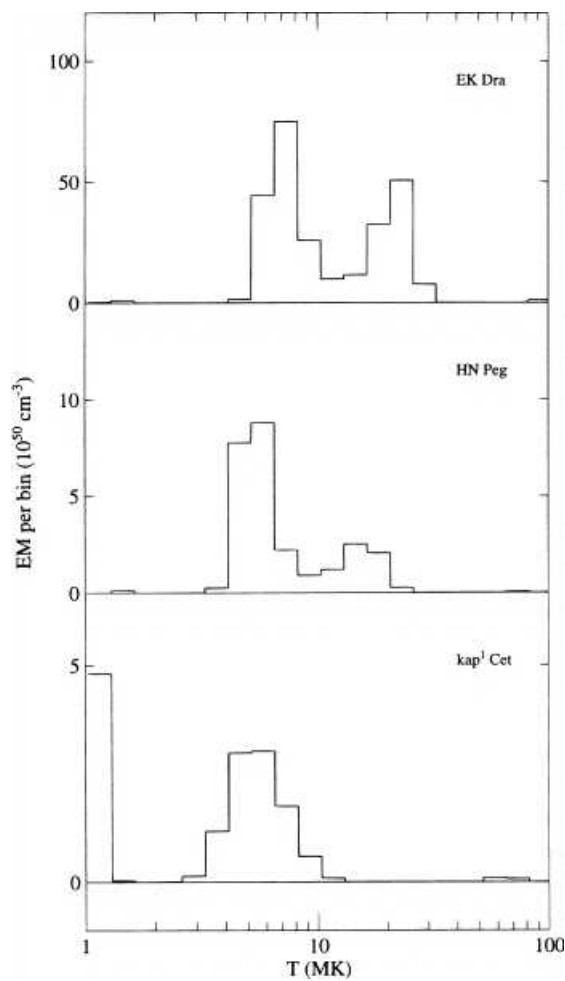


**Figure 9.5:** Differential emission measure distributions of coronally active main sequence stars (Güdel et al. 1997<sup>[74]</sup>); EK Dra (*top*), HN Peg (*middle*), and  $\kappa^1$  Cet (*bottom*).



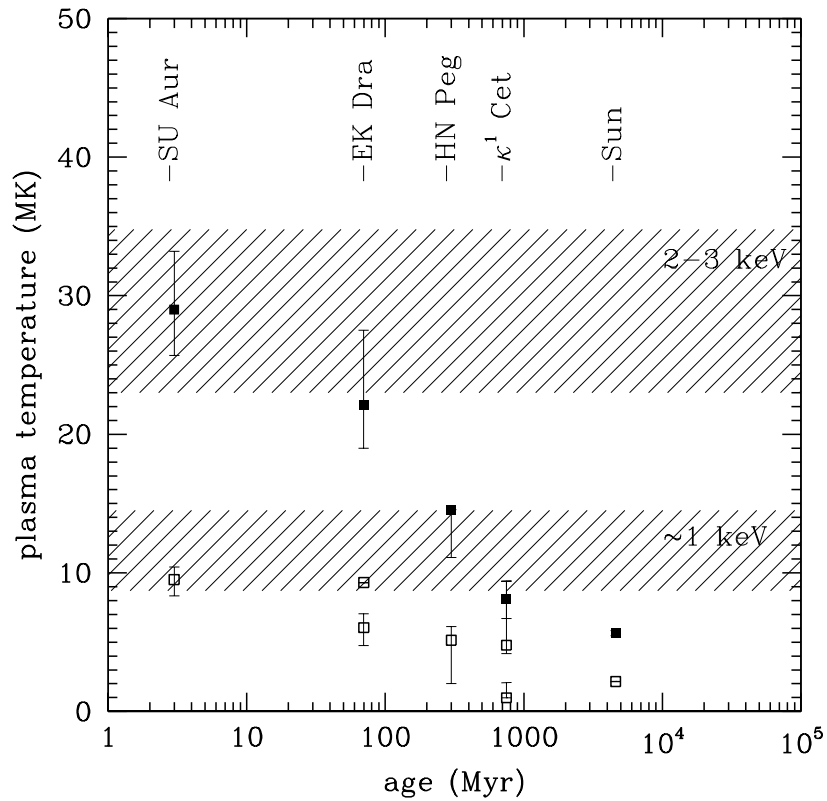


**Figure 9.6:** Evolution of the plasma temperatures of the soft (and middle) component (*open squares*) and the hard component (*filled squares*) of some main and pre-main-sequence stars (sun; Peres et al. 2000<sup>[150]</sup>, EK Dra, HN Peg, and κ<sup>1</sup> Cet; Güdel, Guinan, & Skinner 1997<sup>[74]</sup>, and SU Aur; Skinner & Walter 1998<sup>[173]</sup>).

Second, the time-sliced spectroscopy on our bright X-ray sources (Sect. 7.2) indicates that flaring activities are attributable to the high temperature component. This is the same with the solar plasma and main sequence stars (Güdel et al. 1997<sup>[74]</sup>; Güdel et al. 2002<sup>[75]</sup>).

The high-temperature plasma component seen in the spectra at quiescent phases may be the integration of small and temporally-unresolved flares. Güdel et al. (1997)<sup>[74]</sup> and Güdel et al. (2002)<sup>[75]</sup> further discussed, based on this interpretation, that the the  $EM$  ratio of both components can be a function of flare frequency. Future long-exposure observations on YSOs as well as main sequence stars will give an insight on this issue.

### 9.2.3 X-ray Properties among Evolutional Classes

Based on the evolutional class estimates of NIR-IDed X-ray sources using the  $(J-H)/(H-K)$  color-color diagram as well as the  $UV$  excess and  $H_\alpha$  emission data, we separated them into class I (protostars), class II (cTTSs), and class III (wTTSs) objects (Sect. 6.2). The statistics of each class are summarized in Table 9.4 with the results of X-ray temporal and spectral analyses, while the averaged X-ray properties are in Table 9.5.

**Table 9.4:** Number of sources among classes

	class I	class II	class III	others <sup>a</sup>	sum
X-ray sources...	13	59	170	36	278
bright (T).....	4	31	71	14	120
variable.....	3	18	38	7	66
	(75%)	(58%)	(54%)	(50%)	(55%)
bright (S).....	7	37	81	17	142
one-temperature	6	25	43	13	87
	(86%)	(68%)	(53%)	(76%)	(61%)
two-temperature	0	10	29	2	41
	(0%)	(27%)	(36%)	(12%)	(29%)

<sup>a</sup> NIR-IDed but not classified either into class I, II, or III based on their NIR colors.

Despite that we do not have class I objects of two-temperature plasma, we can regard that the  $\langle kT^{(1)} \rangle$  value represents  $\langle kT_{high}^{(2)} \rangle$  in this class. This is because class I objects, even if they have two-temperature emissions, appear only with higher temperature

**Table 9.5:** Comparison of X-ray properties among classes

	class I	class II	class III
$\langle \log N_{\text{H}} \text{ (cm}^{-2}\text{)} \rangle \dots\dots$	22.6 ( $\pm 0.3$ )	21.8 ( $\pm 0.7$ )	21.5 ( $\pm 0.6$ )
$\langle kT^{(1)} \text{ (keV)} \rangle \dots\dots\dots$	3.71 ( $\pm 1.9$ )	2.82 ( $\pm 1.9$ )	2.00 ( $\pm 1.7$ )
$\langle kT^{(1)} \text{ (keV)} \rangle_{\text{w}}^{\text{a}} \dots\dots\dots$	3.30 ( $\pm 1.1$ )	1.85 ( $\pm 1.0$ )	1.32 ( $\pm 0.4$ )
$\langle \log L_{\text{X}}^{(1)} \text{ (ergs s}^{-1}\text{)} \rangle \dots$	30.6 ( $\pm 0.5$ )	30.3 ( $\pm 0.4$ )	30.0 ( $\pm 0.5$ )
$\langle kT_{\text{high}}^{(2)} \text{ (keV)} \rangle \dots\dots\dots$	N/A	3.60 ( $\pm 2.1$ )	2.64 ( $\pm 1.2$ )
$\langle kT_{\text{high}}^{(2)} \text{ (keV)} \rangle_{\text{w}}^{\text{a}} \dots\dots\dots$	N/A	2.33 ( $\pm 0.5$ )	2.30 ( $\pm 0.8$ )
$\langle \log L_{\text{X high}}^{(2)} \text{ (ergs s}^{-1}\text{)} \rangle$	N/A	30.4 ( $\pm 0.3$ )	30.2 ( $\pm 0.6$ )
$\langle kT_{\text{low}}^{(2)} \text{ (keV)} \rangle \dots\dots\dots$	N/A	0.83 ( $\pm 0.1$ )	0.71 ( $\pm 0.3$ )
$\langle kT_{\text{low}}^{(2)} \text{ (keV)} \rangle_{\text{w}}^{\text{a}} \dots\dots\dots$	N/A	0.85 ( $\pm 0.1$ )	0.88 ( $\pm 0.2$ )
$\langle \log L_{\text{X low}}^{(2)} \text{ (ergs s}^{-1}\text{)} \rangle$	N/A	30.2 ( $\pm 0.3$ )	30.1 ( $\pm 0.6$ )

<sup>a</sup> Weighted means, which were calculated by weighting the values with the inverse square of their uncertainty.

plasma due to the heavier extinction at the soft X-ray band. A notable fact is that the  $\langle kT_{\text{high}}^{(2)} \rangle$  decreases along the evolution. A similar trend is seen in  $\langle kT^{(1)} \rangle$  and  $\langle kT_{\text{low}}^{(2)} \rangle$ , although we have to pay attention to the fact that X-ray detections from younger and more obscured sources are biased for the harder emissions. This trend of decreasing higher plasma temperature can be understood by extrapolating the relation in Figure 9.6 toward younger ages than 1 Myr.

### 9.3 X-ray Emissions from NIR-unIDed Sources

Ten NIR-unIDed X-ray sources (I128a, I132, I135, I175, I186, I196, I203, I241, I247, and I363) in the 1.3 mm integral-shaped ridge appear to be separated into two groups. The first group consists of four sources (I128a, I175, I241, and I247), which are associated with jet and outflow systems. The remaining sources comprise the second group, which has no such features. We try to interpret the X-ray emissions from these two groups in the context of jet-induced plasma and magnetic activities of deeply embedded NIR invisible YSOs.

#### 9.3.1 Jet-induced Plasma Emissions

Sources in the first group share many characteristics in common (Table 9.6). They are (1) located at the 1.3 mm cloud cores, and (2) are associated with  $\text{H}_2$  outflows seen in the QUIRC  $\text{H}_2$ -band image (Fig. 9.7), (3) CO and  $\text{HCO}^+$  outflows (Aso et al. 2000<sup>[11]</sup>), and (4) the centimeter emissions (Reipurth et al. 1999<sup>[162]</sup>). VLA 7 is extended in the direction of molecular outflows, indicating that this is a free-free emission from the  $\text{H}_{\text{II}}$  region ionized by protostar jets. We resolved VLA 1 into two sources (VLA 1a and VLA 1b) and discussed that these sources have free-free emissions in origin as well (Sect. 8.4).

Their close-up view in the QUIRC  $K$ -band image (Fig. 9.7) reveals more of their common features. (5) The 1.3 mm cores that contain these X-ray sources also possess a NIR source that is classified either into class I protostars or cTTSs. For TKK J05351833–0500329 at MMS 2, we resolved it into two NIR sources (IRS 3 and IRS 5) with our Subaru and IRTF observations, and classified them into class I protostars using their  $J$ -,  $H$ -,  $K$ -, and  $L$ -band colors (Sect. 8.3). TKK J05352333–0507096 at FIR 1c has the color  $(J-H)_{\text{CIT}} = 2.83$  and  $(H-K)_{\text{CIT}} = 2.19$ , showing its class I nature (Fig. 6.2). 2MASSI J0535315–050547 at MMS 10, although it shows no NIR excess in the  $(J-H)/(H-K)$  diagram (Fig. 6.2), have a large extinction with  $(J-H)_{\text{CIT}} = 2.00$  and  $(H-K)_{\text{CIT}} = 1.42$ . Considering its large extinction and the insensitivity of the  $K$  band to the NIR excess emissions, this source can also be a class I protostar. (6) These NIR sources show apparent reflection features in the  $K$ -band image. Finally, (7) the X-ray sources are close to but significantly offset from these NIR protostars in the direction of jet and outflow system.

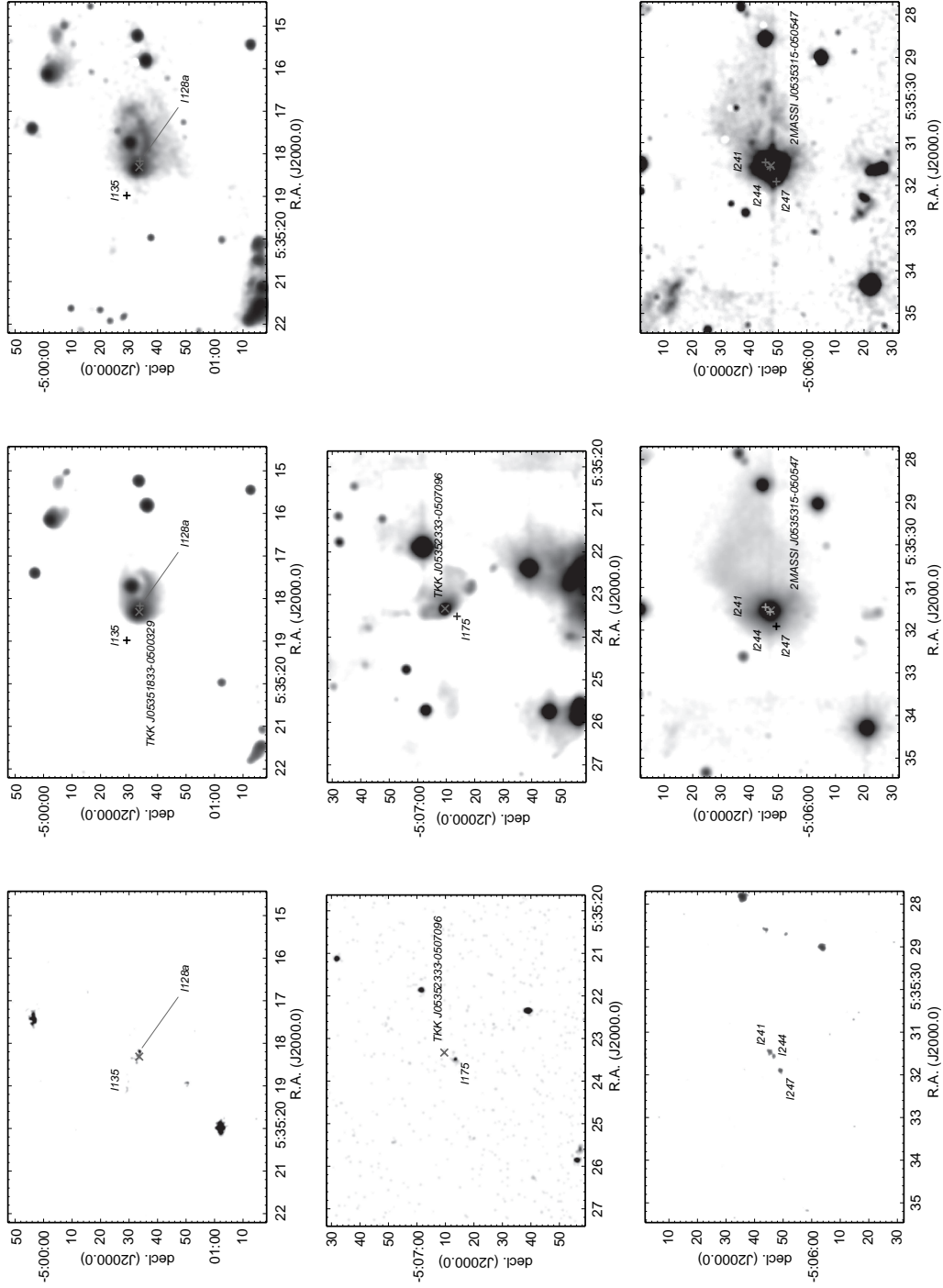


**Figure 9.7:** X-ray and NIR images of I128a at MMS 2 (*top*), I175 at FIR 1c (*middle*), and I241 and I247 at MMS 10 (*bottom*). The panels in the left column are the X-ray images in the hard band, while those in the middle column are the *K*-band images. The H<sub>2</sub> intensity images are in the right column. I175 was out of the FOV of our H<sub>2</sub> observations. The positions of X-ray and NIR sources are marked with pluses and crosses, respectively.

**Table 9.6:** NIR-unIDed X-ray sources associated with jet and outflow systems

ID	X-ray <sup>a</sup>	1.3 mm	— jet/outflow associations —				class I protostar <sup>f</sup>	
	counts	core <sup>b</sup>	H <sub>2</sub> <sup>c</sup>	CO <sup>d</sup>	H <sup>13</sup> CO <sup>+d</sup>	3.6 cm <sup>e</sup>		
I128a	66	MMS 2	yes	yes	yes	VLA 1	TKK J05351833–0500329	
I175	33	FIR 1c	N/A	yes	yes	VLA 7	TKK J05352333–0507096	
I241	22	MMS 10	yes	yes	yes	.....	2MASSI J0535315–050547	
I247	33	MMS 10	yes	yes	yes	.....	2MASSI J0535315–050547	

<sup>a</sup> Values in the 0.5–8.0 keV range.

<sup>b</sup> Chini et al. (1997)<sup>[35]</sup>.

<sup>c</sup> The H<sub>2</sub> emissions found in QUIRC images (Fig. 8.8). I175 was out of the FOV of our observation.

<sup>d</sup> Aso et al. (2000)<sup>[11]</sup>.

<sup>e</sup> Reipurth et al. (1999)<sup>[162]</sup>. VLA 7 has an extended structure. VLA 1 was resolved into VLA 1a and VLA 1b in our higher resolution VLA observation (Sect. 8.4), in which we found VLA 1a is also extended in the direction of the molecular outflow as well as VLA 7.

<sup>f</sup> The class I protostars located in the same 1.3 mm cloud. TKK J05351833–0500329 was resolved into two class I protostars (IRS 3 and IRS 5) in our higher resolution Subaru observation (Sect. 8.3). I244 is the X-ray counterpart of 2MASSI J0535315–050547.

We pick up I128a as a test case. We revealed the vicinity of this source with our follow-up studies with high resolution NIR and centimeter imaging observations as follows (Figs. 8.13 and 9.8). Two NIR sources of class I protostar nature (IRS 3 and IRS 5) are located at the center of 1.3 mm cloud core (MMS 2). These two protostars accompany centimeter emissions (VLA 1a and VLA 1b) that originate from the the H<sub>II</sub> region ionized by the protostellar jets from the two NIR sources. A global outflow is seen in the H<sub>2</sub> band, the direction of which aligns with the extended structure of VLA 1a (Sect. 8.3 and 8.4). A hard X-ray source (I128a) is located at the origin of this outflow and has a significant offset from these two protostars. The X-ray characteristics that we obtained on I128 can be applied to I128a, because I128a occupies most (~70%) of the X-ray photons of this complex (Fig. 8.9). It has a thin-thermal plasma spectrum of  $k_{\text{B}}T = 3.05$  keV and  $EM = 2.1 \times 10^{53}$  cm<sup>-3</sup> with the absorption of  $N_{\text{H}} = 1.27 \times 10^{23}$  cm<sup>-2</sup> (Sect. 7.2).

We propose an interpretation to explain these hard X-ray emissions together with the centimeter emissions based on the shock-induced plasma scenario. Figure 9.9 shows the schematic view, where the jet from a protostar collides into a dense obstacle and produces the shock front. The hard X-ray is emitted from the post shock (PS) region, while the centimeter emission is from the recombination zone (RZ) behind the shock. The RZ is maintained by the continuous ionization by UV photons from the PS region.

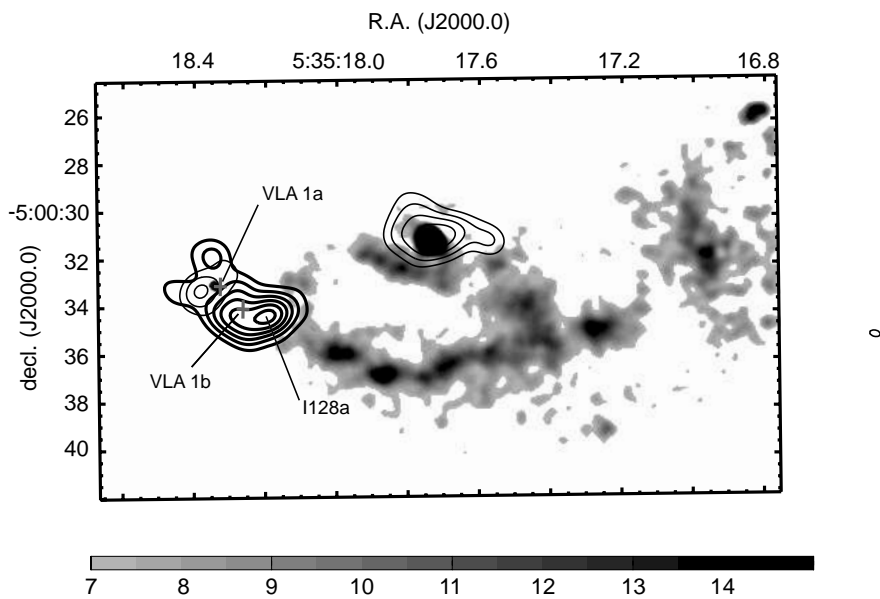


**Figure 9.8:** Multi-wavelength view on MMS 2. The H<sub>2</sub> intensity is in gray scale, the hard and soft X-rays are with the thin and the thick contours, and the position of centimeter sources (VLA 1a and VLA 1b) are marked with pluses. I128a, the hard X-ray peak, is significantly offset from two centimeter emissions in the direction of global H<sub>2</sub> outflow. See also Figure 8.13 for the positions of NIR sources.

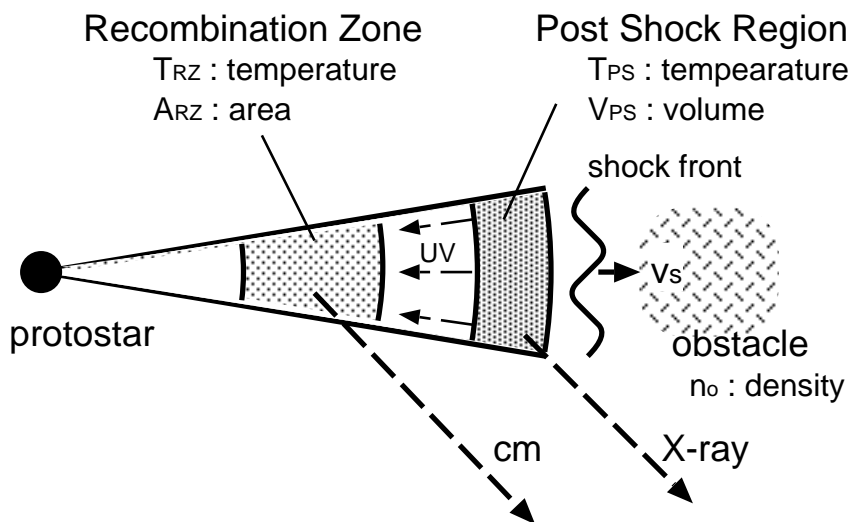


**Figure 9.9:** Schematic view of the X-ray and centimeter emissions of protostellar jet origin.

In PS, the temperature ( $T_{\text{PS}}$ ) and the density ( $n_{\text{PS}}$ ) are expressed as (Raga et al. 2002<sup>[158]</sup>)

$$T_{\text{PS}} = 1.5 \times 10^5 \left( \frac{v_s}{100 \text{ km s}^{-1}} \right)^2 \text{ [K]}, \quad (9.2)$$

$$n_{\text{PS}} = 4n_0 \text{ [cm}^{-3}\text{]}, \quad (9.3)$$

where  $v_s$  and  $n_0$  are the velocity and density of the shock produced by the collision of the jet upon the obstacle. Assuming that light elements are fully ionized in PS, the emission measure ( $EM$ ) is given with the electron density ( $n_{\text{PS}}$ ) and the volume ( $V_{\text{PS}}$ ) as

$$EM = n_{\text{PS}}^2 V_{\text{PS}} \text{ [cm}^{-3}\text{]}. \quad (9.4)$$

By substituting the observed values ( $T_{\text{PS}} = 35 \text{ MK}$  and  $EM = 2.1 \times 10^{53} \text{ cm}^{-3}$ ), we obtained  $v_s = 1.5 \times 10^3 \text{ km s}^{-1}$  and  $n_0 = 5.3 \times 10^2 \text{ cm}^{-3}$ . Here, we assumed that PS is a cube with the length of  $0.5''$  (=the scale of an ACIS-I pixel).

The values of  $v_s$  and  $n_0$  are consistent with what can be independently derived from the centimeter observations. In RZ, the centimeter intensity ( $S_\nu$ ) is given by

$$S_\nu = \frac{A_{\text{RZ}}}{D^2} 2k_B T_{\text{RZ}} \left( \frac{\nu}{c} \right)^2 \tau_\nu \quad (9.5)$$

at the optically-thin limit and with the Rayleigh-Jeans approximation. Here,  $D$  is the distance to the source, and  $T_{\text{RZ}}$  and  $A_{\text{RZ}}$  are the temperature and the surface area of RZ. Curiel et al. (1989)<sup>[43]</sup> showed that the optical depth ( $\tau_\nu$ ) is expressed in terms of the shock parameters by

$$\tau_\nu = 1.55 \times 10^{-7} \left( \frac{n_0}{1 \text{ cm}^{-3}} \right) \left( \frac{v_s}{100 \text{ km s}^{-1}} \right)^{1.68} \left( \frac{T_{\text{RZ}}}{10^4 \text{ K}} \right)^{-0.55} \left( \frac{\nu}{5 \text{ GHz}} \right)^{-2.1}. \quad (9.6)$$

By substituting the observed values of VLA 1a ( $\nu = 8.3 \text{ GHz}$ ,  $S_\nu = 0.128 \text{ mJy}$ , and  $D = 450 \text{ pc}$ ) as a typical value, we obtained

$$\left( \frac{n_0}{1 \text{ cm}^{-3}} \right) \left( \frac{v_s}{100 \text{ km s}^{-1}} \right)^{1.68} = 1.7 \times 10^5. \quad (9.7)$$

Here, we assumed that  $T_{\text{RZ}} = 10^4 \text{ K}$  and  $A_{\text{RZ}}$  is an ellipse of the observed major and minor axis lengths of VLA 1a.

From the X-ray observation, we can independently derive that

$$\left( \frac{n_0}{1 \text{ cm}^{-3}} \right) \left( \frac{v_s}{100 \text{ km s}^{-1}} \right)^{1.68} = 5.2 \times 10^4. \quad (9.8)$$



This is in good agreement with the value obtained with the centimeter data in a factor of a few, supporting the protostellar jet scenario for the origin of the X-ray and centimeter emissions.

Other three X-ray emissions with the same multi-wavelength features can be understood with the same scheme. The positions of X-ray and NIR sources are similar to the case of I128a, where X-ray emissions are  $1''$ – $6''$  offset from the protostar in the direction of jet and outflow. More interestingly, I241 and I247 are positioned at the opposite side of the central NIR source (Fig. 9.7). We may be seeing a jet and counter-jet pair of this system. The combined spectrum of I241 and I247 (Fig. 9.10 a; Table 9.7) supports this idea, which are well fitted by a thin-thermal plasma model with similar best-fit values ( $k_{\text{B}}T = 2.8$  keV,  $EM = 9.2 \times 10^{22}$ , and  $N_{\text{H}} = 5.8 \times 10^{22}$  cm $^{-2}$ ) with I128a. Likewise, I135 at MMS 2 may be the counter-jet of I128a (Fig. 9.7).

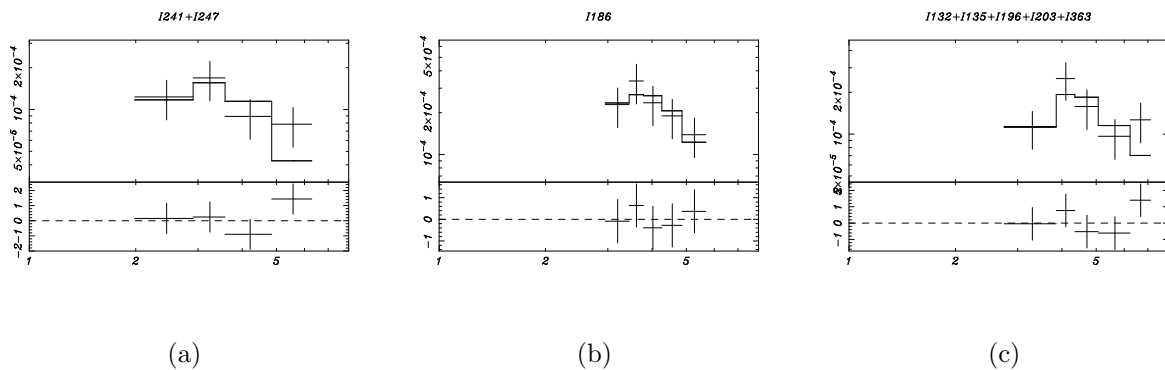


**Figure 9.10:** Spectra and the best-fit models of one-temperature thin-thermal plasma fittings of (a) I241+I247, (b) I186, and (c) I132+I135+I196+I203+I363. The metallicity of all elements is fixed to be 0.3 solar. In the upper panels, the data (*pluses*) and the best-fit model (*solid steps*) are plotted over the energy (keV; *horizontal axis*) versus normalized spectral intensity (count rate keV $^{-1}$ ; *vertical axis*) plane. The response functions of the optics and the detector are convolved into the model. In the lower panels, the residuals between the background-subtracted data and the best-fit model are plotted over the energy (keV; *horizontal axis*) versus  $\chi^{(i)} = (E_{\text{data}}^{(i)} - E_{\text{model} \otimes \text{ARF} \otimes \text{RMF}}^{(i)}) / \Delta E_{\text{data}}^{(i)}$  (*vertical axis*) plane.

### 9.3.2 Magnetic Activities of Deeply Embedded YSOs

Other X-ray sources (I132, I135, I186, I196, I203, and I363) that are associated with 1.3 mm emissions but not with jet and outflow systems can be deeply embedded YSOs such as class 0

**Table 9.7:** One-temperature plasma fittings of NIR-unIDed *Chandra* sources

ID	counts <sup>a</sup>	$N_{\text{H}}^{\text{b}}$ ( $10^{22} \text{ cm}^{-2}$ )	$k_{\text{B}}T^{\text{b}}$ (keV)	$L_{\text{X}}^{\text{a}}$ (ergs $\text{s}^{-1}$ )
I241+I247	55	5.83 (0.0–6.0)	2.80 (1.9–...)	1.00e+30
I186	66	14.2 (0.0–41)	1.91 (0.5–...)	2.07e+30
I132+I135+I196+I203+I363	66	20.2 (8.0–42)	3.71 (1.0–...)	3.47e+30

<sup>a</sup> Values in the 0.5–8.0 keV range. For combined fittings, the sum of all sources are shown for the count and luminosity.

<sup>b</sup> The lower and upper limit ( $1 \sigma$ ) are given in parentheses. Some have too few spectral bins to derive the uncertainty of their best-fit parameters.

objects for the following reasons.

First, it has no NIR counterpart brighter than the QUIRC limiting magnitude of  $K \sim 16.5$  mag. I132 at MMS 3, which was observed with the Subaru deep imaging observation, has much tighter upper limit of  $K \sim 19.6$  mag. Low-mass class I protostars are generally detected at 10–14 mag and class II at 8–12 mag in the  $K$  band at the distance of 450 pc (for example, see Fig. 24. in Aspin, Sandell, & Russel 1994<sup>[12]</sup>), hence are easily detected with our  $K$ -band sensitivity. In fact, all class I and class II sources with X-ray emissions (Table A.1) have the  $K$ -band magnitude of 6.5–15.1 mag and 9.3–15.3 mag, respectively. These six X-ray sources are fainter than typical class I protostars by more than 10–100 times in the  $K$  band, which indicates that these sources are either much more obscured than typical class I protostars, or are intrinsically faint in NIR because of their much lower mass than low-mass sources.

Our results of the X-ray spectral analysis on these sources favor the high obscuration interpretation. The spectrum of the brightest source (I186) and the combined spectrum of the rest of faint others (I132, I135, I196, I203, and I363) are well fitted with a thin-thermal plasma model (Fig. 9.10) with the best-fit value of  $L_{\text{X}} = 0.5\text{--}2.0 \times 10^{30} \text{ ergs s}^{-1}$  (Table 9.7). Here, we assumed that the  $L_{\text{X}}$  values are the same for I132, I135, I196, I203, and I363, because they have the same order of X-ray counts (Table A.1). If these sources follow the relation between the mass and  $L_{\text{X}}$  (Fig. 9.3), this X-ray luminosity corresponds to the source of 0.1–0.5  $M_{\odot}$ . If these X-ray sources are in this mass range with moderate extinction, they should be easily detected at the detection limit of our deep NIR observations. This rules out the possibility of these sources just to have a very low mass.

Second, they have much larger  $N_{\text{H}}$  values of  $1\text{--}2 \times 10^{23} \text{ cm}^{-2}$  than typical class I sources (Table 9.5). This is converted to  $A_V \approx 100$  mag using the equation (7.6).

Third, some of the sources spatially coincide with the  $350 \mu\text{m}$  cores (Lis et al. 1998<sup>[117]</sup>), which provides the position of protostellar cores with a better spatial resolution than 1.3 mm mapping observations by Chini et al. (1997)<sup>[35]</sup>. I132 and I186 are located within the positional uncertainty of  $\sim 5''$  respectively from CSO 7 and CSO 19, and I363 is within  $9''$  from CSO 15. I132 is also associated with MMS 3, a class 0 candidate source, detected by 1.3 mm mapping observations (Chini et al. 1997<sup>[35]</sup>).

These sources, if they are class 0 sources, would have magnetic activities in the same way as class I protostars. The best-fit values of their  $k_{\text{B}}T$  (2–3 keV) and  $L_{\text{X}}$  ( $0.5\text{--}2.0 \times 10^{30} \text{ ergs s}^{-1}$ ) is in the typical range of that of class I sources, which supports this idea. We may see the higher temperature component of these sources.

We note that no X-ray emissions from bona-fide class 0 sources were found in other star forming regions (e.g., NGC 2068) that were observed by *Chandra* with better sensitivity (E. D. Feigelson 2002, private communication). However, our X-ray observations are as deep as, or deeper than any other wavelength observations with unprecedented spatial resolution in this field. Just as an infrared source with no optical counterpart found by Becklin & Neugebauer (1967)<sup>[19]</sup> turned out to be a new class of YSOs in the Orion nebula, our X-ray sources can be of this kind. Further studies are mandatory to identify the nature of these sources, such as millimeter–sub-millimeter interferometer observations to detect circumstellar clumps of these prospective YSOs.



# Chapter 10

## Conclusions

Using OMC-2 and OMC-3 as our study field and taking a multi-wavelength observational approach, we discussed the origins and mechanisms of  $\sim 400$  X-ray sources to understand the wide variety of X-ray-emitting phenomena seen in star-forming regions.

1. We conducted deep X-ray and NIR observations respectively using ACIS on *Chandra* and QUIRC on the University of Hawaii 88 inch (2.2 m) telescope. The X-ray observation is complete down to  $F_X \sim 10^{-14.5}$  ergs s $^{-1}$  cm $^{-2}$  with the faintest detected source of  $F_X \sim 10^{-15.5}$  ergs s $^{-1}$  cm $^{-2}$  in the 0.5–8.0 keV energy range. The NIR image has the 90% completeness limit of  $J \sim 17.5$ ,  $H \sim 16.5$ , and  $K \sim 16.0$  mag, matching well with the *Chandra* limit (Sects. 5.1 and 5.2).
2. We extracted 385 X-ray sources in the  $17 \times 17$  arcmin $^2$  ACIS-I FOV and 1448 NIR sources in the 512 arcmin $^2$  QUIRC FOV. Combining the 2MASS catalog with our QUIRC source list and correlating them with our *Chandra* data, we identified the NIR counterpart for 278 ( $\sim 72\%$ ) X-ray sources (Sects. 5.1 and 5.2). Most of NIR-IDed X-ray sources are YSOs that belong to OMC-2 and OMC-3, considering their  $K$ -band flux and luminosity function (Sect. 6.2).
3. The NIR-IDed X-ray sources were examined for their  $J$ -,  $H$ -, and  $K$ -band colors to estimate their mass, bolometric luminosity, and evolutionary class (Sect. 6.2). Their X-ray temporal and spectral features were also analyzed to derive their flux variability, plasma temperature, emission measure, and X-ray luminosity (Sects. 7.1 and 7.2).
4. The averaged X-ray properties among different mass ranges were compared. We found

that IM ( $2.0 M_{\odot} \leq M < 10.0 M_{\odot}$ ), LM ( $0.2 M_{\odot} \leq M < 2.0 M_{\odot}$ ), and VLM ( $M < 0.2 M_{\odot}$ ) YSOs have the same X-ray emission mechanisms based on their  $L_{\text{bol}}/L_X$  values,  $L_X$ -mass relation, and averaged X-ray features. This is in contrast with the HM ( $M \geq 10.0 M_{\odot}$ ) sources that emit X-rays of the stellar wind origin (Sect. 9.1).

5. We revealed that the X-ray emission from IM, LM, and VLM sources consists of two components of different temperatures with  $k_B T \sim 1.0$  keV and 2.0–3.0 keV. Based on the time-sliced X-ray spectroscopy as well as comparison with the sun and other sources in the literature, we proposed that the soft component is from coronal and the hard component is from flare activities (Sect. 9.2).
6. Most of the NIR-unIDed X-ray sources are AGNs based on their X-ray spectra, HR distribution, and the number counts. However, the spatial distribution of these sources has an excess along the ridge of 1.3 mm cloud cores, indicating that  $\sim 10$  of them are related to star formation (Sect. 8.1).
7. We conducted follow-up observations to identify the nature of the NIR-unIDed X-ray sources associated with the 1.3 mm ridge using QUIRC on the University of Hawaii 88 inch (2.2 m) telescope in the  $\text{H}_2 v = 1 - 0$  S(1) band (Sect. 8.2), IRCS on the Subaru telescope and NSFCam on IRTF in the  $J$ ,  $H$ ,  $K$ ,  $L'$ , and  $\text{H}_2 v = 1 - 0$  S(1) bands (Sect. 8.3) in addition to the centimeter interferometer imaging observation using VLA (Sect. 8.4).
8. Four NIR-unIDed X-ray sources along the 1.3 mm ridge have many multi-wavelength features in common; association with the 1.3 mm cores,  $\text{H}_2$ , CO,  $\text{HCO}^+$  outflows, and centimeter emissions from radio jets. These X-ray sources are very close to but significantly offset from the class I NIR sources in the direction of the jet and outflow system. We proposed a picture of the jet-induced plasma to account for these X-ray emissions (Sect. 9.3).
9. We have six NIR-unIDed X-ray sources that are located along the 1.3 mm ridge but not with the jet and outflow associations. These sources can be deeply embedded X-ray-emitting YSOs such as class 0 objects, based on their X-ray luminosity, temperature, NIR flux upper limit, and association of some with 350  $\mu\text{m}$  and 1.3 mm cores (Sect. 9.3).

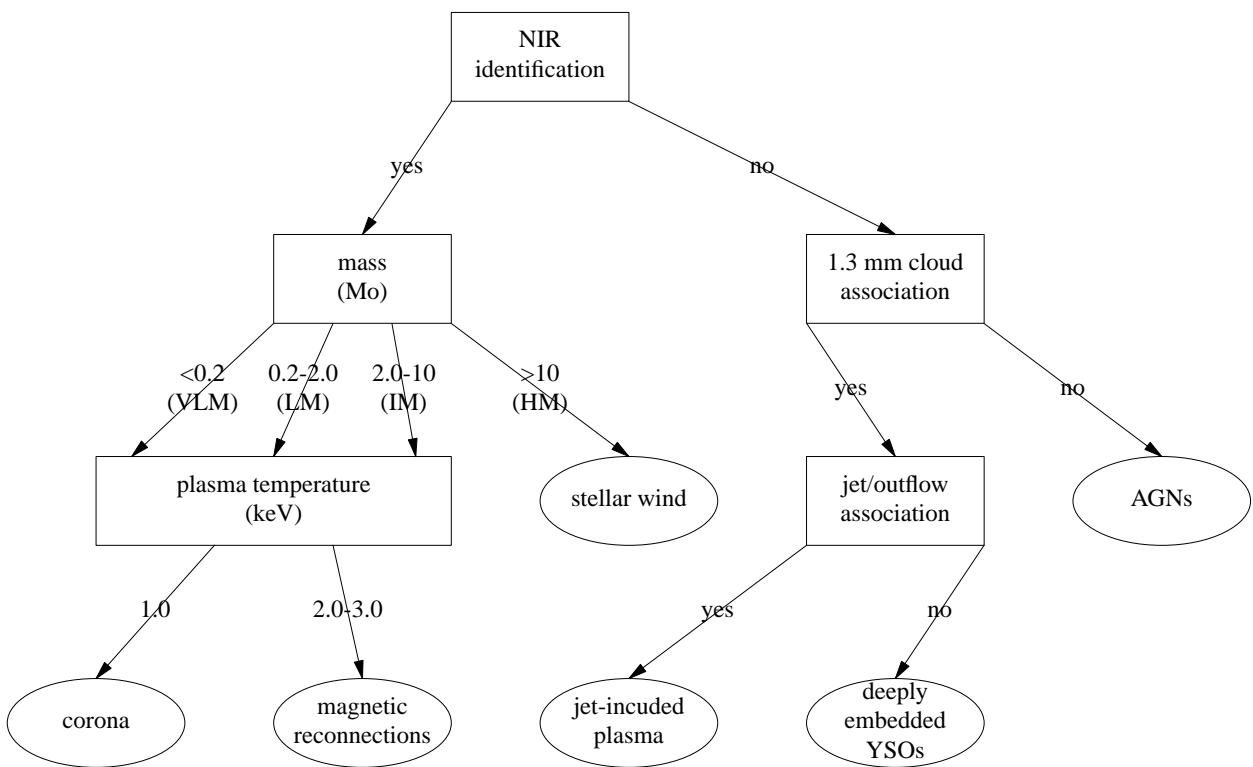


Figure 10.1: Summary





# Bibliography

- [1] Adams, F. C., Lada, C. J., & Shu, F. H. 1987, *Astrophysical Journal*, 312, 788
- [2] Ali, B., & DePoy, D. L. 1995, *Astronomical Journal*, 109, 709
- [3] Anders, E., & Ebihara, M. 1982, *Geochimica et Cosmochimica Acta*, 46, 2363
- [4] Anders, E., & Grevesse, N. 1989, *Geochimica et Cosmochimica Acta*, 53, 197
- [5] André, P., Ward-Thompson, D., & Barsony, M. 1993, *Astrophysical Journal*, 406, 122
- [6] André, P. 1996, in ASP Conf. Ser. 93, Radio Emission from the Stars and the Sun, ed. A. R. Taylor, & J. M. Paredes (San Francisco: ASP), 273
- [7] Anglada, G., Rodríguez, L. F., Cantó, J., Estalella, R., & Torrelles, J. M. 1992, *Astrophysical Journal*, 395, 494
- [8] Anglada, G. 1996, in ASP Conf. Ser. 93, Radio Emission from the Stars and the Sun, ed. A. R. Taylor, & J. M. Paredes (San Francisco: ASP), 3
- [9] Aschwanden, M. J., Tarbell, T. D., Nightingale, R. W., Schrijver, C. J., Title, A., Kankelborg, C. C., Martens, P., & Warren, H. P. 2000, *Astrophysical Journal*, 535, 1047
- [10] Aschwanden, M. J., & Charbonneau, P. 2000, *Astrophysical Journal*, 566, L59
- [11] Aso, Y., Tatematsu, K., Sekimoto, Y., Nakano, T., Umemoto, T., Koyama, K., & Yamamoto, S. 2000, *Astrophysical Journal Supplement*, 131, 465
- [12] Aspin, C., Sandell, G., & Russell, A. P. G. 1994, *Astronomy & Astrophysics Supplement*, 106, 165

- [13] Bachiller, R. 1996, *Annual Review of Astronomy & Astrophysics*, 34, 111
- [14] Bally, J., Langer, W. D., Stark, A. A., & Wilson, R. W. 1987, *Astrophysical Journal*, 312, L45
- [15] Bally, J., Devine, D., Herald, M., & Rauscher, B. J. 1993, *Astrophysical Journal*, 418, L75
- [16] Baraffe, I., Chabrie, G., Allard, F., & Hauschildt, P. H. 1998, *Astronomy & Astrophysics*, 337, 403
- [17] Barsony, M. 1994, in ASP Conf. Ser. 65, Clouds, Cores, and Low Mass Stars, ed. D. P. Clemens, & R. Barvainis (San Francisco: ASP), 197
- [18] Becker, R. H., & White, R. L. 1985, *Astrophysical Journal*, 297, 649
- [19] Becklin, E. E., & Neugebauer, G. 1967, *Astrophysical Journal*, 147, 799
- [20] Berghöfer, T. W., Schmitt, J. H. M. M., Danner, R., & Cassinelli, J. P. 1997, *Astronomy & Astrophysics*, 322, 167
- [21] Bertin, E., & Arnouts, S. 1996, *Astronomy & Astrophysics Supplement*, 117, 393
- [22] Beuther, H., Kerp, J., Preibisch, T., Stanke, T., & Schilke, P. 2002, *Astronomy & Astrophysics*, 395, 169
- [23] Bieging, J. H., & Cohen, M. 1989, *Astronomical Journal*, 98, 1686
- [24] Bontemps, S., et al. 2001, *Astronomy & Astrophysics*, 372, 173
- [25] Bouvier, J., Bertout, C., Benz, W., & Mayor, M. 1986, *Astronomy & Astrophysics*, 165, 110
- [26] Carpenter, J. M. 2000, *Astronomical Journal*, 120, 3139
- [27] Carpenter, J. M. 2001a, *Astronomical Journal*, 121, 2851
- [28] Carpenter, J. M., Hillenbrand, L. A., & Skrutskie, M. F. 2001b, *Astronomical Journal*, 121, 3160
- [29] Casanova, S., Montmerle, T., Feigelson, E. D., & André, P. 1995, *Astrophysical Journal*, 439, 752

- [30] Castets, A., & Langer, W. D. 1995, *Astronomy & Astrophysics*, 294, 835
- [31] Cesaroni, R., & Wilson, T. L. 1994, *Astronomy & Astrophysics*, 281, 209
- [32] *Chandra* IPI team 2001, The *Chandra* Proposers' Observatory Guide, ver. 4.0, MSFC, NASA
- [33] Charles, P. A., & Seward, F. D. 1995, Exploring the X-ray Universe (Cambridge: Cambridge University Press)
- [34] Chen, H., & Tokunaga, A. T. 1994, *Astrophysical Journal Supplement*, 90, 149
- [35] Chini, R., Reipurth, B., Ward-Thompson, D., Bally, J., Nyman, L-Å, Sievers, A., & Billawala, Y. 1997, *Astrophysical Journal*, 474, L135
- [36] Clark, B. G. 1999, in ASP Conf. Ser. 180, Synthesis Imaging in Radio Astronomy II, ed. G. B. Taylor, C. L. Carilli, & R. A. Perley (San Francisco: ASP), 1
- [37] Cohen, M., Bieging, J. H., & Schwartz, P. R. 1982, *Astrophysical Journal*, 253, 707
- [38] Cohen, M. 1993, *Astronomical Journal*, 105, 1860
- [39] Cohen, M. 1994, *Astronomical Journal*, 107, 582
- [40] Cohen, M., Sasseen, T. P., & Bowyer, S. 1994, *Astrophysical Journal*, 427, 848
- [41] Cohen, M. 1995, *Astrophysical Journal*, 444, 874
- [42] Curiel, S., Cantó, J., & Rodríguez, L. F. 1987, *Revista Mexicana de Astronomía y Astrofísica*, 14, 595
- [43] Curiel, S., Rodríguez, L. F., Bohigas, J., Roth, M., & Cantó, J. 1989, *Astrophysical Letters and Communications*, 27, 299
- [44] Dame, T. M., Hartmann, D., & Thaddeus, P. 2001, *Astrophysical Journal*, 547, 792
- [45] Dutrey, A., Duvert, G., Castets, A., Langer, W. D., Bally, J., & Wilson, R. W. 1993, *Astronomy & Astrophysics*, 270, 468
- [46] Edwards, S., Ray, T., & Mundt, R. 1993, in Protostars and Planets III, ed. E. H. Levy, & J. I. Lunine (Tucson: the University of Arizona Press), 567

- [47] Eislöffel, J., Mundt, R., Ray, T. P., & Rodríguez, L. F. 2000, in *Protostars and Planets IV*, ed. V. Mannings, A. P. Boss, & S. S. Russell (Tucson: the University of Arizona Press), 815
- [48] Favata, F., Micela, G., & Reale, F. 2001, *Astronomy & Astrophysics*, 375, 485
- [49] Favata, F., Fridlund, C. V. M., Micela, G., Sciortino, S., & Kaas, A. A. 2002, *Astronomy & Astrophysics*, 386, 204
- [50] Feigelson, E. D., & DeCampi, W. M. 1981, *Astrophysical Journal*, 243, L89
- [51] Feigelson, E. D., & Montmerle, T. 1985, *Astrophysical Journal*, 289, L19
- [52] Feigelson, E. D., Carkner, L., & Wilking, B. A. 1998, *Astrophysical Journal*, 494, 215
- [53] Feigelson, E. D., & Montmerle, T. 1999, *Annual Review of Astronomy & Astrophysics*, 37, 363
- [54] Feigelson, E. D., Garmire, G. P., & Pravdo, S. H. 2002a, *Astrophysical Journal*, 572, 335
- [55] Feigelson, E. D., Broos, P., Gaffney, J. A., III, Garmire, G. P., Hillenbrand, L. A., Pravdo, S. H., Townsley, L., & Tsuboi, Y. 2002b, *Astrophysical Journal*, 574, 258
- [56] Feigelson, E. D., Gaffney, J. A., III, Garmire, G. P., Hillenbrand, L. A., & Townsley, L. 2003, *Astrophysical Journal*, 584, 911
- [57] Fleming, T. A., Giampapa, M., & Schmitt, J. H. M. M. 2000, *Astrophysical Journal*, 533, 372
- [58] Folkard, C. 2003, *Guinness World Records 2003* (New York: Mint Publishers)
- [59] Fukui, Y., Iwata, T., Mizuno, A., Bally, J., & Lane, A. P. 1993, in *Protostars and Planets III*, ed. E. H. Levy, & J. I. Lunine (Tucson: the University of Arizona Press), 603
- [60] Gagné, M., & Caillault, J. -P. 1994, *Astrophysical Journal*, 437, 361
- [61] Gagné, M., Caillault, J. -P., & Stauffer, J. R. 1995, *Astrophysical Journal*, 445, 280
- [62] Garmire, G. P., Feigelson, E. D., Broos, P., Hillenbrand, L. A., Pravdo, S. H., Townsley, L., & Tsuboi, Y. 2000, *Astronomical Journal*, 120, 1426

- [63] Gatley, I., Becklin, E. E., Matthers, K., Neugebauer, G., Penston, M. V., & Scoville, N. 1974, *Astrophysical Journal*, 191, L121
- [64] Geier, S., Wendker, H. J., & Wisotzki, L. 1995, *Astronomy & Astrophysics*, 299, 39
- [65] Genzel, R., & Downes, D. 1979, *Astronomy & Astrophysics*, 72, 234
- [66] Genzel, R., & Stutzki, J. 1989, *Annual Review of Astronomy & Astrophysics*, 27, 41
- [67] Getman, K. V., Feigelson, E. D., Townsley, L., Bally, J., Lada, C. J., & Reipurth, B. 2002, *Astrophysical Journal*, 575, 354
- [68] Giacconi, R., et al. 2001, *Astrophysical Journal*, 551, 624
- [69] Giovanardi, C., Lizano, S., Natta, A., Evans, N. J., II, & Heiles, C. 1992, *Astrophysical Journal*, 397, 214
- [70] Glassgold, A. E., Feigelson, E. D., & Montmerle, T. 1999, in *Protostars and Planets IV*, ed. V. Mannings, A. P. Boss, & S. S. Russell (Tucson: the University of Arizona Press), 429
- [71] Greenstein, J. L. 1998, in *McGraw-Hill Encyclopedia of Astronomy*, ed. S. P. Parker (4th ed. of Japanese translation; Tokyo: Maruzen), 168
- [72] Grosso, N., Montmerle, T., Feigelson, E. D., André, P., Casanova, S., & Gregorio-Hetem, J. 1997, *Nature*, 387, 56
- [73] Grosso, N. 2001, *Astronomy & Astrophysics*, 370, L22
- [74] Güdel, M., Guinan, E. F., & Skinner, S. L. 1997, *Astrophysical Journal*, 483, 947
- [75] Güdel, M., Audard, M., Smith, K. W., Behar, E., Beasley, A. J., & Mewe, R. 2002, *Astrophysical Journal*, 577, 371
- [76] Haisch, K. E., Jr., Lada, E. A., Piña, R. K., Telesco, C. M., & Lada, C. J. 2001, *Astronomical Journal*, 121, 1512
- [77] Hamaguchi, K. 2000, PhD thesis, Kyoto University
- [78] Haro, G. 1952, *Astrophysical Journal*, 115, 572

- [79] Hartigan, P., Kenyon, S. J., Hartmann, L., Strom, S. E., Edwards, S., Welty, A. D., & Stauffer, J. 1991, *Astrophysical Journal*, 382, 617
- [80] Hartmann, L. 1982, *Astrophysical Journal Supplement*, 48, 109
- [81] Hayashi, C. 1966, *Annual Review of Astronomy & Astrophysics*, 4, 171
- [82] Herbig, G. H. 1951, *Astrophysical Journal*, 113, 697
- [83] Herbig, G. H., & Bell, K. R. 1988, Third Catalog of Emission-Line Stars of the Orion Population (Mt. Hamilton: Lick Observatory)
- [84] Herrmann, F., Madden, S. C., Nikola, T., Poglitsch, A., Timmermann, R., Geis, N., Townes, C. H., & Stacey, G. J. 1997, *Astrophysical Journal*, 481, 343
- [85] Hillenbrand, L. A. 1997, *Astronomical Journal*, 113, 1733
- [86] Hillenbrand, L. A., & Carpenter, J. M. 2000, *Astrophysical Journal*, 540, 236
- [87] Hodapp, K. -W., & Deane, J. 1993, *Astrophysical Journal Supplement*, 88, 119
- [88] Hodapp, K. -W., & Ladd, E. F. 1995, *Astrophysical Journal*, 453, 715
- [89] Hodapp, K. -W., Hora, J. L., & Metzger, M. R. 1997, Observer's Guide for QUIRC, University of Hawaii
- [90] Hofner, P., Delgado, H., Whitney, B., Churchwell, D., & Linz, H. 2002, *Astrophysical Journal*, 579, L95
- [91] Imanishi, K., Koyama, K., & Tsuboi, Y. 2001a, *Astrophysical Journal*, 557, 747
- [92] Imanishi, K., Tsujimoto, M., & Koyama, K. 2001b, *Astrophysical Journal*, 563, 361
- [93] Imanishi, K., Tsujimoto, M., & Koyama, K. 2002, *Astrophysical Journal*, 572, 300
- [94] Ikeda, M., et al. 1999, *Astrophysical Journal*, 527, L59
- [95] Johns-Krull, C. M., Valenti, J. A., & Koresko, C. 1999, *Astrophysical Journal*, 516, 900
- [96] Johnson, J. J., Gehrz, R. D., Jones, T. J., Hackwell, J. A., & Grasdalen, G. L. 1990, *Astronomical Journal*, 100, 518

- [97] Johnstone, R. M., & Penston, M. V. 1986, *Monthly Notices of the Royal Astronomical Society*, 219, 927
- [98] Johnstone, R. M., & Penston, M. V. 1987, *Monthly Notices of the Royal Astronomical Society*, 227, 797
- [99] Johnstone, D., & Bally, J. 1999, *Astrophysical Journal*, 510, L49
- [100] Jones, B. F., & Walker, M. F. 1988, *Astronomical Journal*, 95, 1755
- [101] Jones, T. J., Mergen, J., Odewahn, S., Gehrz, R. D., Gatley, I., Merrill, K. M., Probst, R., & Woodward, C. E. 1994, *Astronomical Journal*, 107, 2120
- [102] Kaastra, J. S. 1992, An X-Ray Spectral Code for Optically Thin Plasmas (Internal SRON-Leiden Report, updated version 2.0)
- [103] Kamata, Y., Koyama, K., Tsuboi, Y., & Yamauchi, S. 1997, *Publication of Astronomical Society of Japan*, 49, 461
- [104] Kastner, J. H., Huenenmoerder, D. P., Schulz, N. S., Canizares, C. R., & Weintraub, D. A. 2002, *Astrophysical Journal*, 567, 434
- [105] Kobayashi, N., et al. 2000, Proc. of SPIE, 4008, 1056
- [106] Kohno, M., Koyama, K., & Hamaguchi, K. 2002, *Astrophysical Journal*, 567, 423
- [107] Koyama, K., Hamaguchi, K., Ueno, S., & Kobayashi, N. 1996, *Publication of Astronomical Society of Japan*, 48, L87
- [108] Krishnamurthi, A., Reynolds, C. S., Linsky, J. L., Martin, E., & Gagné, M. 2001, *Astronomical Journal*, 121, 337
- [109] Ku, W. H. M., & Chanan, G. A. 1979, *Astrophysical Journal*, 234, L59
- [110] Kuhl, L. V. 1964, *Astrophysical Journal*, 140, 1409
- [111] Kukarkin, B. V., Kholopov, P. N., Pskovsky, Y. P., Efremov, Y. N., Kukarkina, N. P., Kurochkin, N. E., & Medvedeva, G. I. 1971, General Catalogue of Variable Stars, 3rd ed.
- [112] Lada, C. J., & Wilking, B. A. 1984, *Astrophysical Journal*, 287, 610

- [113] Lada, C. J. 1991, in *The Physics of Star Formation and Early Stellar Evolution*, ed. C. J. Lada, & N. D. Kylafis (Dordrecht: Kluwer Academic Publishers), 329
- [114] Lada, C. J., & Adams, F. C. 1992, *Astrophysical Journal*, 393, 278
- [115] Leggett, S., & Denault, T. 1996, NSFCAM 256×256 InSb Infrared Array Camera User's Guide, ver. 3, NASA Infrared Telescope Facility
- [116] Liedahl, D. A., Osterheld, A. L., & Goldstein, W. H. 1995, *Astrophysical Journal*, 438, L115
- [117] Lis, D. C., Serabyn, E., Dowell, C. D., Benford, D. J., Phillips, T. G., Hunter, T. R., & Wang, N. 1998, *Astrophysical Journal*, 509, 299
- [118] Lucy, L. B., & White, R. 1980, *Astrophysical Journal*, 241, 300
- [119] Lucy, L. B. 1982, *Astrophysical Journal*, 255, 286
- [120] Maddalena, R. J., Morris, M., Moscowitz, J., & Thaddeus, P. 1986, *Astrophysical Journal*, 303, 375
- [121] Markevitch, M. 2001, <http://exc.harvard.edu/contrib/maxim/bg/index.htm>
- [122] Martí, J., Rodríguez, L. F., & Reipurth, B. 1998, *Astrophysical Journal*, 502, 337
- [123] Mathis, J. S. 2000, in *Allen's Astrophysical Quantities*, ed. A. N. Cox (4th ed.; New York: Springer-Verlag), 523
- [124] Matthews, B. C., & Wilson, C. D. 2000, *Astrophysical Journal*, 531, 868
- [125] Matthews, B. C., Wilson, C. D., & Fiege, J. D. 2001, *Astrophysical Journal*, 562, 400
- [126] McNamara, B., Hack, W. J., Olson, R. W., & Mathieu, R. D. 1989, *Astronomical Journal*, 97, 1427
- [127] Mewe, R., Gronenschild, E. H. B. M., & van den Oord, G. H. J. 1985, *Astronomy & Astrophysics Supplement*, 62, 197
- [128] Mewe, R., Lemen, J. R., & van den Oord, G. H. J. 1986, *Astronomy & Astrophysics Supplement*, 65, 511
- [129] Mezger, P. G., Zylka, R., & Wink, J. E. 1990, *Astronomy & Astrophysics*, 228, 95



- [130] Meyer, M. R., Calvet, N., & Hillenbrand, L. A. 1997, *Astronomical Journal*, 114, 288
- [131] Miller, E., & Scalo, J. M. 1979, *Astrophysical Journal Supplement*, 41, 513
- [132] Moffat, A. F. J., et al. 2002, *Astrophysical Journal*, 573, 191
- [133] Montmerle, T., Koch-Miramond, L., Falgarone, E., & Grindlay, J. E. 1983, *Astrophysical Journal*, 269, 182
- [134] Montmerle, T., Grosso, N., Tsuboi, Y., & Koyama, K. 2000, *Astrophysical Journal*, 532, 1097
- [135] Morris, M., & Knapp, G. R. 1976, *Astrophysical Journal*, 204, 415
- [136] Morrison, R., & McCammon, D. 1983, *Astrophysical Journal*, 270, 119
- [137] Muench, A. A., Lada, E. A., & Lada, C. J. 2000, *Astrophysical Journal*, 533, 358
- [138] Mundt, R., & Fried, J. W. 1983, *Astrophysical Journal*, 274, 83
- [139] Mundt, R., Buehrke, T., Fried, J. W., Neckel, T., Sarcander, M., & Stocke, J. 1984, *Astronomy & Astrophysics*, 140, 17
- [140] Napier, P. J. 1999, in ASP Conf. Ser. 180, Synthesis Imaging in Radio Astronomy II, ed. G. B. Taylor, C. L. Carilli, & R. A. Perley (San Francisco: ASP), 37
- [141] Neuhäuser, R., & Preibisch, T. 1997, *Astronomy & Astrophysics*, 322, L37
- [142] Neuhäuser, R., & Comerón, F. 1998, *Nature*, 282, 83
- [143] Neuhäuser, R., et al. 1999, *Astronomy & Astrophysics*, 343, 883
- [144] Olofsson, G., et al. 1999, *Astronomy & Astrophysics*, 350, 883
- [145] Ozawa, H., Nagase, F., Ueda, Y., Dotani, T., & Ishida, M. 1999, *Astrophysical Journal*, 523, L81
- [146] Padgett, D. L., Strom, S. E., & Ghez, A. 1997, *Astrophysical Journal*, 477, 705
- [147] Pallavicini, R., Peres, G., Serio, S., Vaiana, G. S., Golub, L., & Rosner, R. 1981, *Astrophysical Journal*, 247, 692
- [148] Parenago, P. P. 1954, *Trudy Gosud. Astron. Sternberga*, 25, 1

- [149] Pendleton, Y., Werner, M. W., Capps, R., & Lester, D. 1986, *Astrophysical Journal*, 311, 360
- [150] Peres, G., Orlando, S., Reale, F., Rosner, R., & Hudson, H. 2000, *Astrophysical Journal*, 528, 537
- [151] Perley, R. A., & Taylor, G. B. 2002, The VLA Calibrator Manual, National Radio Astronomy Observatory
- [152] Persi, P., et al. 2000, *Astronomy & Astrophysics*, 357, 219
- [153] Pravdo, S. H., Feigelson, E. D., Garmire, G. P., Maeda, Y., Tsuboi, Y., & Bally, J. 2001, *Nature*, 413, 708
- [154] Predehl, P., & Schmitt, J. H. M. M. 1995, *Astronomy & Astrophysics*, 293, 889
- [155] Preibisch, T., & Zinnecker, H. 2001, *Astronomical Journal*, 122, 866
- [156] Preibisch, T., & Zinnecker, H. 2002a, *Astronomical Journal*, 123, 1613
- [157] Preibisch, T., Balega, Y. Y., Schertl, D., & Weigelt, G. 2002b, *Astronomy & Astrophysics*, 392, 945
- [158] Raga, A. C., Noriega-Crespo, A., & Velázquez, P. F. 2002, *Astrophysical Journal*, 576, L149
- [159] Rauw, G., Nazé, Y., Gosset, E., Stevens, I. R., Blomme, R., Corcoran, M. F., Pittard, J. M., & Runacres, M. C. 2002, *Astronomy & Astrophysics*, 395, 499
- [160] Rebull, L. M., Hillenbrand, L. A., Strom, S. E., Duncan, D. K., Patten, B. M., Pavlovsky, C. M., Makidon, R., & Adams, M. T. 2000, *Astronomical Journal*, 119, 3026
- [161] Reipurth, B., Bally, J., & Devine, D. 1997, *Astronomical Journal*, 114, 2708
- [162] Reipurth, B., Rodríguez, L. F., & Chini, R. 1999, *Astronomical Journal*, 118, 983
- [163] Richer, J. S., Shepherd, D. S., Cabrit, S., & Churchwell, E. 2000, in *Protostars and Planets IV*, ed. V. Mannings, A. P. Boss, & S. S. Russell (Tucson: the University of Arizona Press), 867
- [164] Rodríguez, L. F., Anglada, G., & Raga, A. 1995, *Astrophysical Journal*, 454, L149

- [165] Rohlfs, K., & Wilson, T. L. 1999, *Tools of Radio Astronomy* (3rd ed.; Berlin: Springer-Verlag)
- [166] Rommey, J. D. 1999, in ASP Conf. Ser. 180, *Synthesis Imaging in Radio Astronomy II*, ed. G. B. Taylor, C. L. Carilli, & R. A. Perley (San Francisco: ASP), 57
- [167] Rutledge, R. E., Barsi, G., Martin, E. L., & Bildsten, L. 2000, *Astrophysical Journal*, 538, L141
- [168] Ryter, Ch. E. 1996, *Astronomy & Space Science*, 236, 285
- [169] Schulz, N. S., Canizares, C., Huenemoerder, D., Kastner, J. H., Tayler, S. C., & Bergstorm, E. J. 2001, *Astrophysical Journal*, 549, 441
- [170] Shimizu, T. 1995, *Publication of Astronomical Society of Japan*, 47, 251
- [171] Siess, L., Dufour, E., & Forestini, M. 2000, *Astronomy & Astrophysics*, 358, 593
- [172] Skinner, S. L., Güdel, M., Koyama, K., & Yamauchi, S. 1998, *Astrophysical Journal*, 486, 886
- [173] Skinner, S. L., & Walter, F. M. 1998, *Astrophysical Journal*, 509, 761
- [174] Snell, R. L., Loren, R. B., & Plambeck, R. L. 1980, *Astrophysical Journal*, 239, L17
- [175] Strom, K. M., Strom, S. E., & Merrill, K. M. 1993, *Astrophysical Journal*, 412, 233
- [176] Strom, K. M., & Strom, S. E. 1994, *Astrophysical Journal*, 424, 237
- [177] Strom, K. M., Kepner, J., & Strom, S. E. 1995, *Astrophysical Journal*, 438, 813
- [178] Takagi, S., Murakami, H., & Koyama, K. 2002, *Astrophysical Journal*, 573, 275
- [179] Tatematsu, K., et al. 1993, *Astrophysical Journal*, 404, 643
- [180] Thompson, A. R. 1999, in ASP Conf. Ser. 180, *Synthesis Imaging in Radio Astronomy II*, ed. G. B. Taylor, C. L. Carilli, & R. A. Perley (San Francisco: ASP), 11
- [181] Thronson, H. A., Jr., Harper, D. A., Keene, J., Loewenstein, R. F., Moseley, H., & Telesco, C. M. 1978, *Astronomical Journal*, 83, 492
- [182] Thronson, H. A., Jr., Thompson, R. I. 1982, *Astrophysical Journal*, 254, 543

- [183] Tian, K. P., van Leeuwen, F., Zhao, J. L., & Su, C. G. 1996, *Astronomy & Astrophysics Supplement*, 118, 503
- [184] Tokunaga, A. T., et al. 1998, *Proc. of SPIE*, 3354, 512
- [185] Tokunaga, A. T. 2000, in *Allen's Astrophysical Quantities*, ed. A. N. Cox (4th ed.; New York: Springer-Verlag), 143
- [186] Tokunaga, A. T., Simons, D. A., & Vacca, W. D. 2002, *Publication of Astronomical Society of Pacific*, 114, 180
- [187] Tsuboi, Y., Imanishi, K., Koyama, K., Grosso, N., & Montmerle, T. 2000, *Astrophysical Journal*, 532, 1089
- [188] Tsuboi, Y., Koyama, K., Hamaguchi, K., Tatematsu, K., Sekimoto, Y., Bally, J., & Reipurth, B. 2001, *Astrophysical Journal*, 554, 734
- [189] Tsujimoto, M., Koyama, K., Tsuboi, Y., Goto, M., & Kobayashi, N. 2002a, *Astrophysical Journal*, 566, 974
- [190] Tsujimoto, M., Koyama, K., Tsuboi, Y., Chartas, G., Goto, M., Terada, H., Kobayashi, N., & Tokunaga, A. T. 2002b, *Astrophysical Journal*, 573, 270
- [191] Tsujimoto, M., Koyama, K., Imanishi, K., Kobayashi, N., Saito, M., Tsuboi, Y., & Chandler, C. 2002c, *Proc. of the IAU 8th Asian-Pacific regional meeting*, vol. 2, 223
- [192] Tsujimoto, M., Koyama, K., Kobayashi, N., Goto, M., Tsuboi, Y., & Tokunaga, A. T. 2003, *Astronomical Journal*, 125, 1537
- [193] van Altena, W. F., Lee, J. T., Lee, J. -F., Lu, P. K., & Uppgren, A. R. 1988, *Astronomical Journal*, 95, 1744
- [194] Williams, J. P., Plambeck, R. L., & Heyer, M. H. 2003, *Astrophysical Journal*, in press
- [195] Wolk, J. S., Bourke, T. L., Smith, R. K., Spitzbart, B., & Alves, J. 2002, *Astrophysical Journal*, 580, L161
- [196] Yamauchi, S., Koyama, K., Sakano, M., & Okada, K. 1996, *Publication of Astronomical Society of Japan*, 48, 719
- [197] Yokoyama, T., & Shibata, K. 1998, *Astrophysical Journal*, 494, L113

- [198] Yusef-Zadeh, F., Law, C., Wardle, M., Wang, D. Q., Fruscinone, A., Lang, C. C., Cotera, A. 2002, *Astrophysical Journal*, 570, 665
- [199] Yu, L. C., Bally, J., & Devine, D. 1997, *Astrophysical Journal*, 485, L45
- [200] Yu, K. C., Billawala, Y. S., Smith, M. D., Bally, J., Butner, H. M. 2000, *Astronomical Journal*, 120, 1974
- [201] Zhekov, S. A., Palla, F., Myasnikov, A. V. 1994, *Monthly Notices of the Royal Astronomical Society*, 271, 667
- [202] Zinnecker, H., & Preibisch, T. 1994, *Astronomy & Astrophysics*, 292, 152



# Appendix A

## *Chandra* Sources and NIR Counterpart

Table A.1: *Chandra* source list

ID <sup>a</sup>	R.A. <sup>b</sup> (hh:mm:ss.ss)	decl. <sup>b</sup> (dd:mm:ss.ss)	Photon Counts	HR <sup>c</sup>	NIR counterpart <sup>d</sup>	$J^e$ (mag)	$J - H^e$ (mag)	$H - K^e$ (mag)	class <sup>f</sup>	mass <sup>gh</sup> ( $M_{\odot}$ )
I1	05:34:38.60	-05:08:42.8	255	0.31	TKK J05343791-0508480	16.22	0.94	0.25	others	0.040-0.050
I2	05:34:40.86	-05:06:58.2	63	-0.02	TKK J05344064-0506586	15.50	2.33	1.28	III	0.500-0.570
I3	05:34:43.10	-05:09:18.0	368	0.62						
I4	05:34:44.89	-05:06:49.1	403	-0.54	2MASS J0534449-050649	11.88	0.72	0.38	III	0.350-0.400
I5	05:34:45.19	-05:10:45.1	176	-0.25	2MASS J0534451-051047	12.17	0.75	0.52	others	0.300-0.350
I6	05:34:48.29	-05:07:13.1	535	-0.66	2MASS J0534482-050713	12.99	0.66	0.22	III	0.150-0.175
I7	05:34:48.37	-05:05:01.1	549	-0.77	2MASS J0534484-050501	12.48	0.68	0.19	III	0.200-0.250
I8	05:34:49.18	-05:04:38.2	127	-0.97	2MASS J0534492-050438	12.55	0.69	0.23	III	0.200-0.250
I9	05:34:50.33	-05:06:38.1	70	-0.29	TKK J05345056-0506383	13.96	0.51	0.25	III	0.080-0.090
I10	05:34:50.43	-05:11:11.2	773	-0.75	2MASS J0534505-051110	11.96	0.66	0.17	III	0.300-0.350
I11	05:34:50.59	-05:06:49.8	110	0.40						
I12	05:34:50.64	-05:04:07.6	361	-0.70	2MASS J0534506-050407	12.65	0.72	0.29	III	0.200-0.250
I13	05:34:53.03	-05:03:26.9	1747	-0.73	2MASS J0534530-050327	11.95	0.75	0.45	II	0.350-0.400
I14	05:34:53.42	-05:10:28.2	579	-0.70	2MASS J0534534-051027	12.22	0.63	0.23	III	0.250-0.300
I15	05:34:53.45	-05:01:30.2	49	0.10	2MASS J0534536-050129	14.34	0.62	0.21	III	0.075-0.080
I16	05:34:53.71	-05:05:48.9	145	-0.75	2MASS J0534537-050548	13.33	0.64	0.25	III	0.130-0.150
I17	05:34:55.38	-05:01:39.3	534	-0.83	2MASS J0534554-050139	12.51	0.73	0.15	III	0.250-0.300
I18	05:34:55.66	-05:08:44.3	39	0.38						
I19	05:34:55.76	-05:07:42.5	103	0.24						
I20	05:34:56.07	-05:00:55.6	359	-0.69	2MASS J0534561-050055	12.80	0.64	0.21	III	0.150-0.175
I21	05:34:56.13	-05:06:01.5	276	-0.82	2MASS J0534561-050601	12.56	0.61	0.24	III	0.175-0.200
I22	05:34:56.64	-05:06:26.1	55	0.20						
I23	05:34:56.67	-05:04:37.9	98	0.47						
I24	05:34:56.71	-05:10:43.6	48	-0.33	2MASS J0534567-051043	13.46	0.73	0.30	III	0.130-0.150
I25	05:34:56.82	-05:11:33.5	2286	-0.82	2MASS J0534568-051132	10.89	0.71	0.47	others	0.900-0.950
I26	05:34:57.35	-05:06:04.0	19	0.58						
I27	05:34:58.19	-05:09:27.9	558	-0.71	2MASS J0534581-050927	12.29	0.76	0.28	III	0.300-0.350
I28	05:34:58.21	-05:11:54.6	258	-0.64	2MASS J0534581-051153	12.65	0.60	0.22	III	0.175-0.200
I29	05:34:58.52	-05:12:27.0	135	0.04	2MASS J0534586-051226	14.03	0.55	0.24	III	0.080-0.090
I30	05:34:59.22	-05:01:26.2	28	0.43						
I31	05:34:59.32	-05:05:30.0	740	-0.75	2MASS J0534593-050530	12.41	0.77	0.31	III	0.250-0.300
I32	05:34:59.47	-05:08:25.6	30	0.27						
I33	05:35:00.40	-05:09:44.8	213	0.13	2MASS J0535003-050944	13.81	0.57	0.31	III	0.090-0.100
I34	05:35:00.87	-05:09:39.4	135	-0.72	2MASS J0535008-050938	13.01	0.56	0.32	III	0.130-0.150
I35	05:35:01.37	-05:11:06.1	60	0.33	2MASS J0535014-051104	13.86	0.96	0.57	II	0.150-0.175
I36	05:35:01.43	-05:09:32.8	670	-0.85	2MASS J0535014-050932	12.13	0.67	0.18	III	0.300-0.350

(cont.)



ID <sup>a</sup>	R.A. <sup>b</sup>	decl. <sup>b</sup>	Counts	HR <sup>c</sup>	NIR counterpart <sup>d</sup>	J <sup>e</sup>	J - H <sup>e</sup>	H - K <sup>e</sup>	class <sup>f</sup>	mass <sup>g/h</sup>
I37	05:35:01.98	-05:00:43.2	63	-0.46	2MASS J0535019-050043	14.51	0.63	0.22	III	0.072-0.075
I38	05:35:02.16	-05:04:38.5	83	-0.76	2MASS J0535021-050438	13.88	0.76	0.37	III	0.110-0.130
I39	05:35:02.52	-05:04:10.0	11	0.82						
I40	05:35:02.56	-05:04:58.5	9	1.00						
I41	05:35:02.79	-05:03:03.9	20	-0.40	2MASS J0535028-050303	15.83	0.58	0.00	others	0.030-0.040
I42	05:35:02.79	-05:00:01.9	1023	-0.57	2MASS J0535027-050002	12.29	1.17	0.45	III	0.620-0.700
I43	05:35:02.85	-05:02:00.6	20	0.50						
I44	05:35:03.12	-05:09:17.3	90	-0.76	2MASS J0535031-050917	13.15	0.72	0.34	III	0.150-0.175
I45	05:35:03.30	-05:04:48.1	26	0.69						
I46	05:35:03.33	-05:13:07.2	159	0.17	TKK J05350365-0513104	15.07	1.69	0.74	III	0.200-0.250
I47	05:35:03.41	-05:05:40.4	1771	-0.62	2MASS J0535034-050540	9.17	0.22	0.03	III	1.400-1.400
I48	05:35:03.81	-05:05:19.1	17	0.53						
I49	05:35:03.99	-05:01:41.1	20	0.70						
I50	05:35:04.23	-05:08:42.5	54	0.26						
I51	05:35:04.30	-05:08:12.9	25402	-0.55	2MASS J0535042-050812	8.18	0.66	0.15	III	>4.000
I52	05:35:04.45	-05:07:36.5	14	-0.43	TKK J05350440-0507356	14.75	1.10	0.54	III	0.110-0.130
I53	05:35:04.55	-04:58:29.9	109	-0.21	2MASS J0535046-045829	12.83	1.05	0.74	II	0.350-0.400
I54	05:35:04.64	-05:09:56.1	437	-0.78	2MASS J0535046-050955	11.38	0.65	0.26	III	0.500-0.570
I55	05:35:05.24	-04:59:23.2	26	0.54						
I56	05:35:05.65	-04:58:53.6	334	-0.83	2MASS J0535056-045853	11.94	0.65	0.24	III	0.300-0.350
I57	05:35:05.66	-05:04:53.4	7	0.43						
I58	05:35:05.76	-05:11:34.5	92	-0.28	2MASS J0535057-051135	12.91	1.39	0.66	III	0.620-0.700
I59	05:35:05.95	-05:08:37.5	18	-0.67	2MASS J0535058-050838	15.17	1.08	0.50	III	0.090-0.100
I60	05:35:06.09	-05:12:17.0	43	-0.30	2MASS J0535061-051216	8.13	0.00	0.00	III	2.000-2.200
I61	05:35:06.36	-05:09:00.0	10	0.20						
I62	05:35:06.49	-04:58:40.4	58	-0.45	2MASS J0535063-045841	14.21	0.56	0.30	III	0.075-0.080
I63	05:35:06.58	-05:07:16.0	15	0.60						
I64	05:35:06.61	-05:04:51.2	42	0.43						
I65	05:35:06.71	-05:11:45.4	257	-0.19	2MASS J0535067-051145	13.85	1.44	0.62	III	0.350-0.400
I66	05:35:06.83	-05:10:39.1	200	-0.76	2MASS J0535068-051038	12.59	0.67	0.24	III	0.200-0.250
I67	05:35:07.54	-05:11:14.7	1232	-0.21	2MASS J0535075-051114	12.38	1.07	0.58	III	0.500-0.570
I68	05:35:08.04	-05:01:18.2	14	0.14	TKK J05350779-0501193	16.19	0.93	0.43	III	0.040-0.050
I69	05:35:08.75	-05:04:40.5	26	-0.85	2MASS J0535087-050440	12.37	0.74	0.36	III	0.250-0.300
I70	05:35:08.96	-05:10:25.6	12	-0.67	2MASS J0535089-051025	14.56	0.61	0.10	III	0.060-0.070
I71	05:35:09.15	-05:06:47.1	1192	-0.83	2MASS J0535091-050647	11.24	0.67	0.21	III	0.570-0.600
I72	05:35:09.32	-04:59:32.2	56	0.39						
I73	05:35:09.42	-04:59:41.2	72	-0.56	2MASS J0535094-045941	12.89	0.68	0.35	III	0.150-0.175
I74	05:35:09.85	-04:58:49.1	442	0.24	TKK J05350988-0458495	16.22	3.04	1.64	III	1.400-1.500
I75	05:35:10.14	-05:13:40.6	86	0.00						

(cont.)

ID <sup>a</sup>	R.A. <sup>b</sup>	decl. <sup>b</sup>	Counts	HR <sup>c</sup>	NIR counterpart <sup>d</sup>	J <sup>e</sup>	J - H <sup>e</sup>	H - K <sup>e</sup>	class <sup>f</sup>	mass <sup>g/h</sup>
I76	05:35:10.32	-05:11:11.1	13	0.54		>20.55	>6.77	>3.28	others	.....
I77	05:35:10.51	-04:58:45.5	835	0.52	TKK J05351053-0458460					
I78	05:35:11.56	-05:02:08.2	16	0.75						
I79	05:35:11.81	-05:14:00.0	237	-0.09	TKK J05351134-0514016	13.76	0.97	0.39	III	0.150-0.175
I80	05:35:12.72	-05:12:00.8	59	-0.46	2MASS J0535127-051200	14.11	0.52	0.25	III	0.075-0.080
I81	05:35:12.80	-05:01:46.1	79	-0.95	2MASS J0535128-050146	13.93	0.59	0.28	III	0.090-0.100
I82	05:35:12.92	-04:55:55.7	325	0.48	TKK J05351310-0455523	12.82	1.88	1.64	I	2.000-2.200
I83	05:35:12.95	-05:02:08.5	109	-0.83	2MASS J0535129-050208	14.38	0.56	0.33	III	0.070-0.072
I84	05:35:13.00	-05:00:26.2	29	0.38	TKK J05351303-0500261	>20.68	>3.77	2.45	II	
I85	05:35:13.34	-05:09:19.9	1088	-0.74	2MASS J0535133-050919	12.14	0.68	0.19	III	0.300-0.350
I86	05:35:13.35	-05:04:14.5	7	0.71						
I87	05:35:13.88	-04:58:03.2	207	0.11	2MASS J0535138-045803	15.63	2.36	1.16	III	0.500-0.570
I88	05:35:13.99	-05:07:38.8	21	0.81						
I89	05:35:14.28	-05:14:26.3	268	0.01	2MASS J0535142-051427	15.19	2.40	1.50	II	0.900-0.950
I90	05:35:14.29	-05:13:40.3	116	0.00	2MASS J0535143-051340	16.30	1.94	1.26	II	0.150-0.175
I91	05:35:14.63	-05:06:25.3	34	-0.65	2MASS J0535146-050625	14.39	1.16	0.65	II	0.130-0.150
I92	05:35:14.64	-05:02:24.7	312	-0.82	TKK J05351464-0502250	12.77	1.02	0.46	III	0.350-0.400
I93	05:35:14.66	-05:03:12.4	574	-0.85	2MASS J0535146-050312	12.45	0.68	0.18	III	0.200-0.250
I94	05:35:14.67	-05:08:52.3	33	-0.76	2MASS J0535146-050852	12.83	0.57	0.28	III	0.150-0.175
I95	05:35:14.70	-05:08:26.2	4	1.00						
I96	05:35:14.87	-05:06:48.8	333	0.16	TKK J05351486-0506489	16.75	2.23	1.09	III	0.175-0.200
I97	05:35:14.94	-05:01:18.3	24	0.58						
I98	05:35:14.99	-05:07:13.2	62	0.71						
I99	05:35:15.08	-05:06:53.6	112	0.21	2MASS J0535150-050653	15.89	2.29	1.20	III	0.350-0.400
I100	05:35:15.18	-05:07:56.4	4	0.50						
I101	05:35:15.27	-05:00:32.6	29	-0.86	2MASS J0535152-050033	13.42	0.63	0.26	III	0.110-0.130
I102	05:35:15.36	-05:13:40.2	68	-0.53	TKK J05351533-0513382	13.47	0.86	0.12	others	0.150-0.175
I103	05:35:15.49	-05:01:12.2	26	-0.31	2MASS J0535154-050112	14.34	0.68	0.34	III	0.080-0.090
I104	05:35:15.55	-05:01:43.5	34	-0.53	2MASS J0535155-050143	13.66	1.09	0.53	III	0.200-0.250
I105	05:35:15.59	-05:09:32.2	21	-0.33	2MASS J0535156-050931	13.93	0.59	0.28	III	0.090-0.100
I106	05:35:15.61	-04:59:27.3	151	-0.30	2MASS J0535156-045927	14.63	1.90	1.09	II	0.450-0.500
I107	05:35:15.64	-04:57:12.7	159	-0.47	2MASS J0535156-045713	13.30	0.77	0.32	III	0.150-0.175
I108	05:35:15.76	-05:12:27.4	72	0.06	TKK J05351580-0512264	18.18	2.99	1.26	others	0.250-0.300
I109	05:35:15.80	-05:03:26.0	177	-0.92	2MASS J0535158-050326	13.69	0.58	0.34	III	0.100-0.110
I110	05:35:15.93	-05:14:59.5	3013	0.20	TKK J05351596-0514591	11.57	0.44	>0.39	others	0.250-0.300
I111	05:35:16.14	-05:09:19.3	88	-0.91	2MASS J0535161-050919	12.91	0.62	0.23	II	0.150-0.175
I112	05:35:16.35	-05:04:36.3	17	-0.76	2MASS J0535163-050436	14.57	0.56	0.33	III	0.060-0.070
I113	05:35:16.40	-04:58:01.9	264	-0.79	2MASS J0535164-045802	13.22	0.60	0.16	III	0.130-0.150
I114	05:35:16.49	-05:03:30.2	294	-0.80	2MASS J0535164-050330	12.23	0.66	0.20	III	0.250-0.300

(cont.)

ID <sup>a</sup>	R.A. <sup>b</sup>	decl. <sup>b</sup>	Counts	HR <sup>c</sup>	NIR counterpart <sup>d</sup>	J <sup>e</sup>	J - H <sup>e</sup>	H - K <sup>e</sup>	class <sup>f</sup>	mass <sup>g/h</sup>
I115	05:35:16.66	-05:08:54.4	4	0.50						
I116	05:35:16.80	-05:07:27.4	45	-0.91	2MASS J0535167-050727	14.92	0.49	0.34	others	0.050-0.055
I117	05:35:16.86	-05:07:47.8	16	-0.62	2MASS J0535168-050747	13.81	0.99	0.54	III	0.150-0.175
I118	05:35:17.12	-05:12:39.1	74	-0.54	TKK J05351715-0512394	13.51	0.62	0.08	III	0.110-0.130
I119	05:35:17.25	-05:03:15.9	10	0.80						
I120	05:35:17.36	-05:12:29.3	65	-0.66	TKK J05351738-0512296	13.70	0.62	0.12	III	0.100-0.110
I121	05:35:17.41	-04:59:56.6	259	0.20	TKK J05351742-0459570	17.26	2.67	1.68	II	0.250-0.300
I122	05:35:17.46	-05:09:49.2	44	-1.00	2MASS J0535174-050949	13.31	0.58	0.30	II	0.110-0.130
I123	05:35:17.72	-05:00:30.3	29	-0.17	2MASS J0535177-050031	15.29	2.22	1.37	II	0.500-0.570
I124	05:35:17.92	-05:15:33.2	830	-0.14	TKK J05351792-0515329	11.47	>0.73	.....	.....	.....
I125	05:35:18.24	-05:13:07.1	561	-0.40	TKK J05351824-0513069	11.31	>0.99	.....	.....	.....
I126	05:35:18.24	-05:03:54.1	92	-1.00	2MASS J0535182-050354	9.29	0.04	0.01	III	0.750-0.800
I127	05:35:18.26	-05:08:05.1	7	-0.14	TKK J05351830-0508048	16.86	2.31	1.28	III	0.175-0.200
I128	05:35:18.31	-05:00:33.0	60	0.93	TKK J05351833-0500329	17.67	3.25	>3.73	I	0.600-0.620
I129	05:35:18.45	-05:08:30.9	15	-0.73	2MASS J0535184-050830	13.75	0.59	0.23	III	0.090-0.100
I130	05:35:18.61	-04:59:42.2	165	-0.71	2MASS J0535186-045942	13.78	0.58	0.20	III	0.090-0.100
I131	05:35:18.84	-05:14:46.3	661	-0.48	TKK J05351886-0514456	12.45	0.81	0.34	III	0.300-0.350
I132	05:35:18.93	-05:00:50.1	23	0.65						
I133	05:35:18.94	-05:06:36.3	26	0.85						
I134	05:35:18.96	-05:03:23.1	7	1.00						
I135	05:35:18.98	-05:00:29.2	24	0.83						
I136	05:35:19.65	-05:02:28.6	11	-0.82	2MASS J0535196-050228	14.47	0.65	0.31	III	0.075-0.080
I137	05:35:19.75	-05:05:31.6	6	0.67						
I138	05:35:19.75	-05:15:34.9	359	0.67	TKK J05351982-0515354	17.41	2.55	2.51	I	0.175-0.200
I139	05:35:19.86	-05:15:08.4	309	0.25	2MASS J0535198-051508	12.93	1.61	1.03	II	
I140	05:35:19.97	-05:01:02.3	259	0.83	TKK J05351998-0501024	>20.72	>2.61	3.95	I	
I141	05:35:19.98	-05:14:03.8	202	0.03	TKK J05351980-0514054	13.51	0.43	0.38	others	0.090-0.100
I142	05:35:19.99	-05:12:51.1	97	0.86	2MASS J0535200-051250	14.49	2.06	1.31	II	0.700-0.750
I143	05:35:19.65	-05:13:27.0	143	0.08	TKK J05351966-0513265	13.47	1.95	1.25	II	1.400-1.500
I144	05:35:20.14	-05:13:15.5	953	0.05	2MASS J0535201-051315	9.74	1.92	1.31	II	>4.000
I145	05:35:20.37	-05:02:26.4	73	-0.86	2MASS J0535203-050226	12.24	0.77	0.20	III	0.300-0.350
I146	05:35:20.59	-05:03:00.2	7	0.43	TKK J05352062-0503007	18.13	3.73	2.44	II	1.400-1.400
I147	05:35:20.74	-05:15:49.5	2276	-0.12	2MASS J0535207-051549	9.84	1.18	0.56	III	3.500-4.000
I148	05:35:20.76	-04:58:33.8	673	-0.37	2MASS J0535207-045834	12.33	1.12	0.46	III	0.570-0.600
I149	05:35:21.13	-05:06:32.4	109	0.63	TKK J05352115-0506324	>20.95	>2.52	3.14	I	
I150	05:35:21.26	-05:09:16.4	2202	-0.81	2MASS J0535212-050916	8.36	0.55	0.49	II	3.000-3.500
I151	05:35:21.31	-05:12:13.1	14667	-0.63	2MASS J0535213-051212	8.71	0.60	0.18	III	3.000-3.500
I152	05:35:21.39	-05:09:42.4	29	-0.79	2MASS J0535213-050942	13.71	0.69	0.49	others	0.110-0.130
I153	05:35:21.44	-05:09:03.8	142	-0.62	TKK J05352147-0509037	12.23	0.92	>0.37	III	0.400-0.450

(cont.)

ID <sup>a</sup>	R.A. <sup>b</sup>	decl. <sup>b</sup>	Counts	HR <sup>c</sup>	NIR counterpart <sup>d</sup>	J <sup>e</sup>	J - H <sup>e</sup>	H - K <sup>e</sup>	class <sup>f</sup>	mass <sup>g/h</sup>
I154	05:35:21.50	-05:01:53.5	97	0.13	TKK J05352152-0501539	18.24	3.23	1.92	II	0.350-0.400
I155	05:35:21.56	-05:09:39.2	76	0.84	2MASS J0535215-050938	13.98	0.84	0.71	others	0.110-0.130
I156	05:35:21.57	-05:09:49.9	260	-0.64	2MASS J0535215-050949	12.88	0.78	0.53	others	0.200-0.250
I157	05:35:21.86	-04:56:48.7	93	0.08	TKK J05352169-0456487	13.64	0.70	0.11	III	0.110-0.130
I158	05:35:21.87	-05:07:01.9	838	-0.71	2MASS J0535218-050701	10.93	0.95	0.56	II	1.400-1.500
I159	05:35:21.91	-04:59:17.7	15	-0.20	TKK J05352188-0459197	15.26	1.42	0.80	II	0.130-0.150
I160	05:35:21.92	-05:03:50.6	8	0.25						
I161	05:35:21.94	-05:14:28.3	345	-0.69	2MASS J0535219-051427	11.75	0.75	0.23	III	0.450-0.500
I162	05:35:22.11	-05:15:05.9	479	-0.32	TKK J05352191-0515012	12.75	0.90	0.32	III	0.250-0.300
I163	05:35:22.34	-04:59:52.9	23	0.65						
I164	05:35:22.35	-05:07:39.2	507	0.02	2MASS J0535223-050739	14.76	2.62	1.65	II	2.000-2.200
I165	05:35:22.40	-05:08:05.2	833	0.21	2MASS J0535224-050805	10.88	1.40	0.87	II	3.000-3.500
I166	05:35:22.45	-05:09:11.3	415	-0.92	2MASS J0535224-050911	11.35	0.58	0.12	III	0.400-0.450
I167	05:35:22.55	-05:08:00.8	921	-0.34	2MASS J0535225-050800	11.19	1.41	0.53	III	2.700-3.000
I168	05:35:22.67	-05:14:12.0	206	-0.69	2MASS J0535226-051411	11.69	0.90	0.52	II	0.620-0.700
I169	05:35:23.13	-05:00:35.9	13	-0.08	TKK J05352308-0500364	16.30	2.45	1.38	III	0.350-0.400
I170	05:35:23.20	-05:13:43.9	164	0.04	2MASS J0535231-051343	13.02	1.76	0.74	III	1.400-1.400
I171	05:35:23.22	-05:08:44.0	13	-0.38	TKK J05352322-0508436	>20.72	>5.77	1.77	others	
I172	05:35:23.33	-04:57:20.5	182	-0.63	TKK J05352330-0457207	12.88	0.83	0.10	others	0.200-0.250
I173	05:35:23.33	-05:08:21.8	59	0.19	TKK J05352335-0508216	16.60	2.40	1.78	I	0.250-0.300
I174	05:35:23.44	-05:10:52.1	1909	-0.82	2MASS J0535234-051051	11.31	0.63	0.25	III	0.500-0.570
I175	05:35:23.51	-05:07:13.8	33	0.76						
I176	05:35:23.53	-05:15:24.1	96	-0.25	TKK J05352348-0515234	14.03	0.66	0.41	III	0.090-0.100
I177	05:35:24.34	-05:01:20.4	277	0.58	TKK J05352434-0501205	>20.80	>1.51	4.69	I	
I178	05:35:24.58	-05:11:29.7	83	-0.25	2MASS J0535246-051129	12.11	1.23	0.67	III	0.950-1.000
I179	05:35:24.61	-05:11:58.9	363	-0.81	2MASS J0535246-051158	11.71	0.77	0.51	others	0.450-0.500
I180	05:35:24.66	-05:09:27.6	9	0.56	TKK J05352469-0509264	16.86	1.81	1.49	I	0.090-0.100
I181	05:35:24.87	-05:06:21.3	144	0.68	2MASS J0535248-050621	15.63	2.99	1.85	II	2.000-2.200
I182	05:35:25.03	-05:09:09.6	26	-0.85	2MASS J0535250-050909	14.54	0.63	0.32	III	0.072-0.075
I183	05:35:25.07	-05:10:23.5	22	0.82	2MASS J0535251-051023	14.86	1.96	1.87	I	0.400-0.450
I184	05:35:25.17	-05:05:09.1	12	0.00						
I185	05:35:25.17	-05:15:38.8	162	-0.06	TKK J05352524-0515357	11.67	0.89	0.68	others	0.620-0.700
I186	05:35:25.22	-05:08:23.8	66	0.94						
I187	05:35:25.24	-05:09:27.6	544	-0.86	2MASS J0535252-050927	11.77	0.69	0.23	III	0.400-0.450
I188	05:35:25.36	-05:07:20.4	4	0.50						
I189	05:35:25.40	-05:10:48.3	762	-0.83	2MASS J0535254-051048	11.60	0.60	0.13	III	0.350-0.400
I190	05:35:25.44	-05:06:52.3	6	1.00						
I191	05:35:25.53	-04:57:22.8	145	0.10	TKK J05352567-0457183	13.32	0.73	0.16	III	0.130-0.150
I192	05:35:25.64	-05:07:57.4	324	-0.64	2MASS J0535256-050757	11.77	0.66	0.89	others	0.350-0.400

(cont.)

ID <sup>a</sup>	R.A. <sup>b</sup>	decl. <sup>b</sup>	Counts	HR <sup>c</sup>	NIR counterpart <sup>d</sup>	J <sup>e</sup>	J - H <sup>e</sup>	H - K <sup>e</sup>	class <sup>f</sup>	mass <sup>g/h</sup>
I193	05:35:25.72	-05:07:03.4	5	-1.00	2MASS J0535257-050703	13.72	0.65	0.28	III	0.100-0.110
I194	05:35:25.73	-05:09:49.7	1411	-0.68	2MASS J0535257-050949	11.09	0.61	0.34	III	0.570-0.600
I195	05:35:25.77	-05:05:57.9	9	0.11	TKK J05352576-0505579	16.21	1.75	1.80	I	0.110-0.130
I196	05:35:25.85	-05:02:45.2	5	1.00						
I197	05:35:25.86	-05:07:56.5	878	-0.79	TKK J05352587-0507564	11.12	0.17	0.86	others	0.200-0.250
I198	05:35:26.05	-05:08:37.9	83	-0.76	TKK J05352606-0508377	12.51	0.59	1.91	others	0.175-0.200
I199	05:35:26.27	-05:07:41.1	8	1.00						
I200	05:35:26.29	-05:08:40.1	3840	-0.84	2MASS J0535262-050840	10.10	0.50	0.22	II	
I201	05:35:26.34	-05:16:12.0	231	-0.06	2MASS J0535264-051612	13.28	1.46	0.76	III	0.500-0.570
I202	05:35:26.47	-04:59:52.0	88	0.20	TKK J05352646-0459519	16.52	2.34	1.26	III	0.250-0.300
I203	05:35:26.66	-05:06:10.1	11	1.00						
I204	05:35:26.85	-05:11:07.9	289	0.13	2MASS J0535268-051107	8.85	1.04	0.77	II	>4.000
I205	05:35:27.07	-05:06:21.7	12	0.67						
I206	05:35:27.15	-05:15:45.3	196	-0.08	2MASS J0535270-051544	12.75	0.89	0.51	II	0.250-0.300
I207	05:35:27.41	-05:09:04.0	18	-0.89	2MASS J0535274-050903	14.84	0.77	0.45	III	0.072-0.075
I208	05:35:27.45	-05:02:42.1	270	0.16	TKK J05352744-0502424	16.60	3.32	2.22	II	1.900-2.000
I209	05:35:27.63	-05:09:36.8	24	0.42	2MASS J0535276-050937	12.90	2.44	1.50	II	3.500-4.000
I210	05:35:27.73	-05:13:55.6	55	0.60	2MASS J0535275-051356	13.62	1.28	0.66	III	0.300-0.350
I211	05:35:27.78	-05:17:03.0	711	-0.46	TKK J05352793-0516573	11.58	0.73	0.27	III	0.500-0.570
I212	05:35:27.83	-05:05:36.1	345	0.57	TKK J05352786-0505363	>20.62	>4.33	2.79	II	
I213	05:35:28.06	-05:01:34.8	326	0.42	TKK J05352806-0501351	18.99	4.09	2.69	II	1.400-1.400
I214	05:35:28.14	-05:10:13.5	37	-0.41	2MASS J0535281-051013	11.16	1.00	0.66	II	1.400-1.400
I215	05:35:28.18	-05:03:40.9	41	0.41	TKK J05352819-0503413	20.03	3.61	4.62	I	0.200-0.250
I216	05:35:28.19	-05:00:49.2	172	-0.79	2MASS J0535281-050049	12.49	0.65	0.22	III	0.200-0.250
I217	05:35:28.21	-05:11:37.2	50	-0.28	2MASS J0535281-051137	12.76	1.06	0.52	III	0.350-0.400
I218	05:35:28.27	-04:58:38.0	1228	0.61	TKK J05352826-0458384	>20.58	>6.47	2.65	others	
I219	05:35:28.50	-05:07:46.8	89	0.03	TKK J05352852-0507469	15.99	2.99	1.88	II	1.500-1.600
I220	05:35:28.60	-05:05:44.2	28	0.29	2MASS J0535285-050544	14.92	2.58	1.50	II	1.500-1.600
I221	05:35:28.67	-05:03:06.1	8	0.50						
I222	05:35:28.71	-05:05:51.2	11	0.82						
I223	05:35:29.02	-05:06:03.8	1424	-0.82	2MASS J0535290-050604	11.64	0.58	0.17	III	0.350-0.400
I224	05:35:29.25	-05:08:05.3	6	0.67						
I225	05:35:29.45	-05:16:33.5	1189	-0.53	2MASS J0535294-051633	11.59	0.86	0.26	III	0.620-0.700
I226	05:35:29.81	-05:16:07.6	476	-0.63	2MASS J0535298-051606	12.06	0.78	0.31	III	0.350-0.400
I227	05:35:29.89	-05:12:10.6	136	-0.78	2MASS J0535299-051210	12.68	0.65	0.20	III	0.175-0.200
I228	05:35:29.90	-05:04:26.7	8	1.00						
I229	05:35:30.00	-05:12:27.7	157	-0.61	2MASS J0535299-051227	12.08	0.70	0.49	others	0.300-0.350
I230	05:35:30.11	-05:09:09.5	23	-0.74	2MASS J0535301-050909	13.77	0.60	0.27	III	0.100-0.110
I231	05:35:30.13	-05:14:19.0	148	-0.27	2MASS J0535301-051418	13.16	1.18	0.61	III	0.350-0.400

(cont.)

ID <sup>a</sup>	R.A. <sup>b</sup>	decl. <sup>b</sup>	Counts	HR <sup>c</sup>	NIR counterpart <sup>d</sup>	J <sup>e</sup>	J - H <sup>e</sup>	H - K <sup>e</sup>	class <sup>f</sup>	mass <sup>g,h</sup>
I232	05:35:30.32	-05:13:52.0	213	-0.10	2MASS J0535302-051352	13.19	1.61	0.85	III	0.90-0.950
I233	05:35:30.55	-05:03:33.9	13	-0.08	TKK J05353054-0503345	15.31	1.67	0.87	III	0.175-0.200
I234	05:35:30.64	-04:59:35.6	222	-0.34	2MASS J0535306-045936	14.31	2.29	1.52	II	1.400-1.500
I235	05:35:30.72	-05:06:45.3	6	0.33						
I236	05:35:30.86	-04:58:12.4	67	0.25	TKK J05353080-0458136	17.60	3.13	1.65	III	0.500-0.570
I237	05:35:31.06	-05:04:14.2	91	-0.93	2MASS J0535310-050415	11.13	0.57	0.12	II	0.500-0.570
I238	05:35:31.22	-05:12:28.3	311	-0.80	2MASS J0535312-051228	13.03	0.66	0.23	III	0.150-0.175
I239	05:35:31.27	-05:12:01.8	82	-0.41	2MASS J0535313-051201	14.57	0.62	0.30	III	0.070-0.072
I240	05:35:31.31	-05:15:33.3	2773	-0.64	2MASS J0535312-051533	10.05	0.78	0.32	III	2.000-2.200
I241	05:35:31.46	-05:05:45.5	22	0.91						
I242	05:35:31.48	-05:16:03.2	660	-0.78	2MASS J0535313-051602	5.86	0.23	0.05	III	>4.000
I243	05:35:31.49	-05:05:01.4	187	-0.80	2MASS J0535315-050501	11.96	0.69	0.48	others	0.350-0.400
I244	05:35:31.57	-05:05:47.1	13	0.85	2MASS J0535315-050547	11.72	2.00	1.42	II	>4.000
I245	05:35:31.58	-05:16:56.4	181	-0.28	2MASS J0535316-051658	12.95	1.17	0.50	III	0.400-0.450
I246	05:35:31.61	-05:00:14.0	63	0.49	2MASS J0535316-050014	14.25	2.63	1.64	II	2.700-3.000
I247	05:35:31.91	-05:05:49.3	33	0.39						
I248	05:35:31.96	-05:09:27.9	2062	-0.65	2MASS J0535319-050927	9.34	0.81	0.41	II	3.000-3.500
I249	05:35:32.02	-05:08:05.2	7	-0.14	2MASS J0535320-050805	15.16	1.05	0.62	II	0.080-0.090
I250	05:35:32.24	-05:11:58.3	38	-0.53	2MASS J0535321-051157	12.61	0.75	0.48	III	0.200-0.250
I251	05:35:32.31	-05:11:44.0	175	0.29	2MASS J0535323-051143	14.58	2.18	1.14	III	0.900-0.950
I252	05:35:32.35	-05:14:26.3	150	-0.45	2MASS J0535324-051424	12.62	0.98	0.36	III	0.350-0.400
I253	05:35:32.35	-05:08:29.8	25	0.76						
I254	05:35:32.51	-05:02:09.9	14	-0.71	2MASS J0535325-050209	14.71	0.60	0.19	III	0.060-0.070
I255	05:35:32.80	-05:07:51.6	23	0.65						
I256	05:35:32.86	-05:16:04.6	1143	-0.39	2MASS J0535329-051605	11.59	1.09	0.30	others	
I257	05:35:32.97	-05:12:05.9	25	0.12	2MASS J0535329-051204	13.77	2.04	1.15	III	1.400-1.400
I258	05:35:33.00	-05:17:32.3	406	-0.63	2MASS J0535331-051733	12.81	0.62	0.27	III	0.150-0.175
I259	05:35:33.16	-05:14:11.1	974	-0.14	2MASS J0535331-051410	12.36	0.78	0.40	III	0.300-0.350
I260	05:35:33.37	-05:08:02.0	11	0.82						
I261	05:35:33.52	-05:15:19.3	646	-0.11	TKK J05353359-0515232	13.08	1.24	0.38	others	0.400-0.450
I262	05:35:33.61	-05:00:41.7	128	-0.83	2MASS J0535336-050042	11.93	0.65	0.20	III	0.300-0.350
I263	05:35:33.64	-05:03:07.7	223	-0.35	2MASS J0535336-050308	13.06	1.45	0.69	III	0.620-0.700
I264	05:35:33.83	-05:04:27.2	346	0.88	2MASS J0535338-050427	13.75	1.93	1.26	II	
I265	05:35:33.86	-05:09:05.6	20	-0.80	2MASS J0535338-050905	13.99	0.59	0.26	III	0.080-0.090
I266	05:35:34.26	-04:59:52.7	53	0.89						
I267	05:35:34.48	-05:13:07.3	76	-0.61	2MASS J0535345-051307	14.14	0.58	0.16	III	0.080-0.090
I268	05:35:34.52	-05:00:51.8	27	0.48	2MASS J0535345-050052	15.79	2.31	2.17	I	0.400-0.450
I269	05:35:34.68	-05:15:53.3	330	-0.67	2MASS J0535346-051552	13.33	0.56	0.55	others	0.110-0.130
I270	05:35:35.11	-05:14:47.2	99	0.33						

(cont.)

ID <sup>a</sup>	R.A. <sup>b</sup>	decl. <sup>b</sup>	Counts	HR <sup>c</sup>	NIR counterpart <sup>d</sup>	J <sup>e</sup>	J - H <sup>e</sup>	H - K <sup>e</sup>	class <sup>f</sup>	mass <sup>g/h</sup>
I271	05:35:35.12	-05:05:58.2	13	1.00						
I272	05:35:35.36	-05:11:11.8	506	-0.72	2MASS J0535353-0511111	12.66	0.58	0.22	III	0.150-0.175
I273	05:35:35.48	-05:07:20.2	27	0.93						
I274	05:35:35.55	-05:06:58.5	210	-0.90	2MASS J0535355-050658	13.35	0.63	0.21	III	0.110-0.130
I275	05:35:35.63	-05:01:48.5	66	0.91						
I276	05:35:35.64	-05:10:50.0	22	-0.55	2MASS J0535356-051050	14.24	0.52	0.35	III	0.072-0.075
I277	05:35:35.71	-05:15:43.3	204	-0.26	2MASS J0535356-051543	11.63	0.68	0.28	III	0.400-0.450
I278	05:35:36.02	-05:12:25.1	270	-0.61	2MASS J0535360-051225	11.09	1.55	1.04	II	3.000-3.500
I279	05:35:36.19	-05:04:55.8	114	0.60	2MASS J0535362-050455	13.17	1.35	0.72	III	0.450-0.500
I280	05:35:36.40	-05:01:15.2	943	-0.46	2MASS J0535364-050115	10.89	0.84	0.47	II	1.400-1.400
I281	05:35:36.51	-05:05:22.3	9	0.33						
I282	05:35:36.56	-05:04:39.1	909	-0.92	2MASS J0535365-050439	12.24	0.65	0.19	III	0.250-0.300
I283	05:35:36.69	-05:04:14.0	2221	-0.67	2MASS J0535366-050414	11.96	0.75	0.32	III	0.350-0.400
I284	05:35:36.77	-05:09:59.1	11	-0.45	2MASS J0535367-051000	13.30	0.80	0.56	others	0.150-0.175
I285	05:35:36.86	-05:07:32.4	10	0.60						
I286	05:35:36.95	-05:05:25.8	24	-0.33	2MASS J0535369-050526	14.59	0.51	0.43	others	0.060-0.070
I287	05:35:37.17	-05:10:29.6	312	-0.88	2MASS J0535371-051029	12.53	0.68	0.27	III	0.200-0.250
I288	05:35:37.57	-05:04:47.5	16	0.12	TKK J05353759-0504471	17.46	2.62	1.59	II	0.200-0.250
I289	05:35:37.70	-05:06:31.8	298	-0.64	2MASS J0535376-050631	12.95	0.67	0.28	III	0.150-0.175
I290	05:35:38.04	-05:15:08.3	122	0.48						
I291	05:35:38.07	-05:03:17.1	13	0.38						
I292	05:35:38.30	-05:14:19.1	246	-0.42	2MASS J0535382-051418	11.56	0.75	0.22	III	0.500-0.570
I293	05:35:38.52	-04:59:40.2	518	-0.31	TKK J05353853-0459410	12.00	0.92	>0.62	II	0.500-0.570
I294	05:35:38.57	-05:08:03.4	75	0.12	2MASS J0535385-050803	15.96	2.53	1.36	III	0.500-0.570
I295	05:35:38.65	-05:09:56.9	320	-0.72	2MASS J0535386-050956	13.06	0.58	0.30	III	0.130-0.150
I296	05:35:38.75	-05:04:55.3	40	-0.55	2MASS J0535387-050455	14.96	1.94	1.03	III	0.350-0.400
I297	05:35:38.88	-05:12:42.2	1047	-0.26	2MASS J0535388-051241	10.81	1.11	0.66	II	2.200-2.500
I298	05:35:39.03	-05:07:04.1	279	-0.84	2MASS J0535390-050704	12.60	0.56	0.29	III	0.150-0.175
I299	05:35:39.08	-05:08:56.4	198	-0.80	2MASS J0535390-050856	10.86	0.66	0.16	III	0.750-0.800
I300	05:35:39.17	-05:05:40.0	7	0.14						
I301	05:35:39.39	-05:05:07.7	113	0.59						
I302	05:35:39.72	-04:59:18.4	65	0.35						
I303	05:35:39.97	-05:06:36.5	75	-0.68	2MASS J0535399-050636	12.67	1.13	0.61	III	0.450-0.500
I304	05:35:40.19	-05:04:27.3	9	0.33						
I305	05:35:40.47	-05:04:18.7	19	0.58						
I306	05:35:40.59	-05:12:19.8	85	-0.13	2MASS J0535406-051219	12.96	0.69	0.27	III	0.150-0.175
I307	05:35:40.66	-05:11:10.0	76	0.11	2MASS J0535407-051111	13.77	0.65	0.29	III	0.100-0.110
I308	05:35:40.80	-05:09:01.1	825	-0.61	2MASS J0535407-050901	10.33	0.90	0.30	II	2.200-2.500
I309	05:35:41.04	-05:06:24.9	119	-0.76	2MASS J0535410-050625	12.66	0.62	0.30	III	0.175-0.200

(cont.)

ID <sup>a</sup>	R.A. <sup>b</sup>	decl. <sup>b</sup>	Counts	HR <sup>c</sup>	NIR counterpart <sup>d</sup>	J <sup>e</sup>	J - H <sup>e</sup>	H - K <sup>e</sup>	class <sup>f</sup>	mass <sup>g/h</sup>
I310	05:35:41.38	-05:03:52.6	38	-0.58	2MASS J0535413-050352	14.21	1.17	0.49	III	0.150-0.175
I311	05:35:41.72	-05:03:28.3	61	-0.74	2MASS J0535417-050329	13.45	0.61	0.20	III	0.110-0.130
I312	05:35:41.81	-05:05:19.1	15	-0.33	2MASS J0535417-050519	15.52	1.70	0.83	III	0.150-0.175
I313	05:35:42.04	-05:10:12.0	660	-0.32	2MASS J0535420-051011	11.47	1.33	0.62	III	2.000-2.200
I314	05:35:42.04	-05:13:00.0	617	-0.73	2MASS J0535420-051259	13.45	0.56	0.29	III	0.110-0.130
I315	05:35:42.40	-05:11:02.5	56	0.32						
I316	05:35:42.64	-04:59:55.4	79	0.34						
I317	05:35:42.78	-05:11:55.1	658	-0.79	2MASS J0535427-051154	11.18	0.70	0.16	III	0.620-0.700
I318	05:35:42.98	-05:03:05.3	42	-0.33	2MASS J0535430-050307	13.34	0.64	0.27	III	0.110-0.130
I319	05:35:43.27	-05:09:16.8	2262	-0.79	2MASS J0535432-050917	10.76	0.68	0.17	II	0.900-0.950
I320	05:35:43.54	-05:05:40.2	48	-0.08	2MASS J0535435-050541	11.96	0.87	0.69	others	0.450-0.500
I321	05:35:43.82	-05:09:59.8	174	-0.67	2MASS J0535438-050958	13.69	0.60	0.27	III	0.100-0.110
I322	05:35:44.52	-05:07:31.4	288	-0.87	2MASS J0535445-050731	12.25	0.70	0.20	II	0.250-0.300
I323	05:35:44.54	-05:00:04.9	45	0.24	TKK J05354461-0459576	14.91	0.65	0.22	III	0.060-0.070
I324	05:35:44.88	-05:07:16.7	5273	-0.70	2MASS J0535448-050716	10.07	0.63	0.25	II	1.500-1.600
I325	05:35:45.70	-05:06:44.7	74	0.51						
I326	05:35:46.10	-05:10:52.4	695	-0.76	2MASS J0535461-051051	11.83	0.78	0.41	III	0.450-0.500
I327	05:35:47.25	-05:02:50.1	64	0.41						
I328	05:35:47.77	-05:10:31.2	3604	-0.81	2MASS J0535477-051030	10.18	0.54	0.21	II	1.400-1.400
I329	05:35:48.26	-05:11:15.5	60	0.07	TKK J05354826-0511103	12.77	0.82	0.26	III	0.200-0.250
I330	05:35:48.39	-05:05:20.6	67	0.55						
I331	05:35:48.40	-05:01:27.9	193	-0.60	2MASS J0535483-050128	11.84	0.93	0.68	II	0.570-0.600
I332	05:35:48.88	-05:00:31.6	88	-0.45	TKK J05354884-0500285	12.63	0.96	0.29	II	0.350-0.400
I333	05:35:49.00	-05:05:42.2	31	0.10						
I334	05:35:49.04	-05:01:40.6	288	-0.49	2MASS J0535489-050139	12.59	0.77	0.35	II	0.250-0.300
I335	05:35:49.21	-05:02:23.2	49	0.55						
I336	05:35:49.96	-05:04:24.4	88	0.39						
I337	05:35:50.07	-05:10:22.2	63	-0.33	TKK J05355012-0510294	13.21	0.58	0.24	III	0.110-0.130
I338	05:35:50.51	-05:02:24.7	63	0.27						
I339	05:35:51.12	-05:07:08.7	1348	-0.78	2MASS J0535510-050708	11.00	0.74	0.37	III	0.900-0.950
I340	05:35:51.46	-05:02:03.7	167	0.46						
I341	05:35:51.61	-05:05:58.7	48	0.25						
I342	05:35:51.66	-05:08:09.0	7972	-0.73	2MASS J0535516-050809	10.04	0.62	0.14	III	1.500-1.600
I343	05:35:52.66	-05:05:05.2	4600	-0.75	2MASS J0535526-050505	9.82	0.58	0.37	III	1.600-1.700
I344	05:35:53.71	-05:02:33.8	164	-0.07	2MASS J0535535-050234	13.12	1.04	0.35	III	0.250-0.300
I345	05:35:53.86	-05:06:54.3	258	0.34						
I346	05:35:54.05	-05:04:14.5	1398	-0.81	2MASS J0535540-050414	11.29	0.87	0.49	II	0.900-0.950
I347	05:35:54.22	-05:05:43.2	74	-0.03	2MASS J0535542-050545	13.55	0.65	0.20	III	0.110-0.130
I348	05:35:54.67	-05:06:28.6	168	-0.56	2MASS J0535546-050627	13.48	0.55	0.30	III	0.100-0.110

(cont.)



ID <sup>a</sup>	R.A. <sup>b</sup>	decl. <sup>b</sup>	Counts	HR <sup>c</sup>	NIR counterpart <sup>d</sup>	J <sup>e</sup>	J - H <sup>e</sup>	H - K <sup>e</sup>	class <sup>f</sup>	mass <sup>g/h</sup>
I349	05:35:55.86	-05:04:42.5	87	0.24	TKK J05355574-0504377	16.88	1.26	1.44	I	0.040-0.050
I350	05:35:57.79	-05:05:02.8	169	0.14						
I351	05:36:00.05	-05:04:32.2	134	-0.27	2MASS J0535599-050430	13.54	0.57	0.41	others	0.100-0.110
I352	05:36:00.36	-05:05:50.5	68	0.06	TKK J05360045-0505540	13.38	0.55	0.19	III	0.110-0.130
I353	05:36:00.55	-05:05:03.5	413	-0.27	TKK J05360033-0505000	12.22	0.57	0.19	III	0.200-0.250
I354	05:36:04.60	-05:04:00.5	250	0.10	TKK J05360415-0504088	12.75	0.74	0.31	III	0.200-0.250
I355	05:34:54.47	-05:04:12.5	18	0.67						
I356	05:34:57.03	-05:02:50.2	6	1.00	TKK J05345731-0502508	18.31	1.82	0.77	others	0.040-0.050
I357	05:35:08.43	-05:12:24.5	34	0.47						
I358	05:35:13.13	-05:07:51.5	4	1.00						
I359	05:35:18.87	-05:09:51.4	5	1.00						
I360	05:35:21.33	-05:12:46.3	15	0.47	TKK J05352138-0512444	15.88	0.70	0.53	others	0.040-0.050
I361	05:35:21.50	-05:07:26.0	4	1.00						
I362	05:35:22.42	-05:02:40.7	4	1.00						
I363	05:35:22.67	-05:06:49.5	3	1.00						
I364	05:35:29.78	-04:59:53.9	27	0.63	TKK J05352956-0459567	17.93	0.77	1.08	others	<0.002
I365	05:35:30.67	-05:04:09.9	4	1.00	TKK J05353065-0504111	18.18	1.76	1.39	II	0.040-0.050
I366	05:35:31.19	-05:09:15.7	8	1.00						
I367	05:35:33.14	-05:15:08.7	268	0.26	TKK J05353244-0515067	13.53	1.30	0.75	II	0.300-0.350
I368	05:35:47.84	-05:08:21.5	28	0.57						
I369	05:35:50.91	-05:01:04.9	91	0.45						
I370	05:34:44.08	-05:05:58.3	57	0.30						
I371	05:34:52.91	-05:08:03.2	18	0.00						
I372	05:35:00.97	-05:05:39.6	8	-0.75	2MASS J0535009-050540	15.81	0.41	0.35	others	0.030-0.040
I373	05:35:07.89	-05:09:03.5	3	-1.00						
I374	05:35:10.79	-05:10:43.5	3	-1.00						
I375	05:35:14.97	-05:04:43.1	3	-1.00						
I376	05:35:19.73	-05:11:43.5	34	0.00						
I377	05:35:29.82	-05:13:29.1	49	0.18						
I378	05:35:30.76	-05:03:35.5	5	-1.00	TKK J05353072-0503355	15.25	1.66	0.81	III	0.175-0.200
I379	05:35:33.75	-04:59:26.9	15	-0.07						
I380	05:35:35.70	-05:09:07.4	6	-0.33						
I381	05:35:38.44	-05:10:08.7	28	-0.50	2MASS J0535384-051009	14.85	0.61	0.31	III	0.060-0.070
I382	05:35:42.37	-05:02:50.3	15	-0.60						
I383	05:35:44.67	-05:00:38.6	31	-0.55	2MASS J0535447-050039	14.04	0.75	0.35	III	0.100-0.110
I384	05:35:46.94	-05:06:58.9	14	-0.29						
I385	05:35:54.84	-05:05:25.8	23	-0.30	TKK J05355468-0505213	16.87	1.10	0.67	II	0.040-0.050
S1	05:35:54.73	-04:58:07.1	2987	-0.87	2MASS J0535546-045808	10.40	0.48	0.17	III	0.750-0.800
S2	05:35:56.14	-04:56:55.9	1681	-0.75	2MASS J0535560-045655	11.74	0.62	0.19	III	0.350-0.400

(cont.)

ID <sup>a</sup>	R.A. <sup>b</sup>	decl. <sup>b</sup>	Counts	HR <sup>c</sup>	NIR counterpart <sup>d</sup>	$J^e$	$J - H^e$	$H - K^e$	class <sup>f</sup>	mass <sup>g/h</sup>
S3	05:35:56.28	-04:55:04.1	510	0.13						
S4	05:35:58.84	-04:55:35.2	799	0.03	2MASS J0535588-045537	>15.42	>0.36	0.81	II	
S5	05:35:59.31	-04:58:44.3	743	-0.64	2MASS J0535592-045846	12.55	0.70	0.16	III	0.200-0.250
S6	05:36:02.99	-04:57:34.4	304	-0.30						
S7	05:36:04.24	-04:57:42.5	285	-0.25						
S8	05:36:05.75	-04:51:08.5	832	-0.39						
S9	05:36:11.84	-05:00:30.4	567	-0.47	2MASS J0536118-050032	12.23	0.69	0.17	III	0.250-0.300
S10	05:36:12.81	-04:55:13.7	462	-0.29						
S11	05:36:28.11	-04:57:07.5	185	0.43						
S12	05:36:14.94	-04:57:05.9	72	0.47						
S13	05:36:20.26	-04:54:22.2	164	0.34						

<sup>a</sup> I1-I354 and S1-S11 are detected in the total band (0.5–8.0 keV) image of ACIS-I and ACIS-S2. I355-I369 and S12-S13 are detected only in the hard band (2.0–8.0 keV) image of ACIS-I and ACIS-S2. I370-I385 are detected only in the soft band (0.5–2.0 keV) image of ACIS-I. No new source was detected in the soft band image of ACIS-S2.

<sup>b</sup> The equinox in J2000.0.

<sup>c</sup> Defined as  $(H - S)/(H + S)$  where  $H$  and  $S$  are the X-ray photon counts in the hard (2.0–8.0 keV) and soft (0.5–2.0 keV) band, respectively.

<sup>d</sup> The QUIRC and 2MASS counterpart has the prefix “TKK J” and “2MASS J”, respectively. The nomenclatures follow the IAU convention.

<sup>e</sup> NIR colors in the CIT color system.

<sup>f</sup> The evolutionary classes of NIR-IDed *Chandra* sources estimated from the NIR excess,  $UV$  excess, and  $H_\alpha$  emission data (see Sect. 6.2).

<sup>g</sup> The mass of NIR-IDed *Chandra* sources estimated from the  $J/(J-H)$  color-magnitude diagram (see Sect. 6.2).

<sup>h</sup> Four sources have two estimates of their mass on Figure 6.7; i.e., 1.050–1.000  $M_\odot$  or 1.300–1.400  $M_\odot$  for I139 and I264, and 1.100–1.150  $M_\odot$  or 1.400–1.400  $M_\odot$  for I200 and I256.

## Appendix B

# QUIRC Sources and 2MASS Counterpart

Table B.1: QUIRC source list

ID	R.A. <sup>a</sup>	decl. <sup>a</sup>	$J^{bcd}$ (mag)	$H^{bcd}$ (mag)	$K^{cd}$ (mag)	2MASS counterpart	ID	R.A. <sup>a</sup>	decl. <sup>a</sup>	$J^{bcd}$ (mag)	$H^{bcd}$ (mag)	$K^{cd}$ (mag)	2MASS counterpart
1	34:28.94	-5:08:38.7	15.52	14.13	13.74	0534289-050838	37	34:36.72	-5:09:37.3	17.71	16.98	16.44	
2	34:29.36	-5:11:14.4	17.45	16.75	16.51		38	34:36.76	-5:01:55.3	20.87	19.90	17.27	
3	34:29.48	-5:05:24.7	17.64	16.82	16.44		39	34:36.83	-5:06:09.9	15.74	14.96	14.73	0534368-050609
4	34:29.60	-5:04:29.0	14.05	13.47	13.15	0534295-050428	40	34:36.84	-5:05:19.8	17.75	16.71	15.68	
5	34:29.86	-5:04:05.6	12.83	12.16	11.95	0534298-050405	41	34:36.92	-5:05:11.9	16.92	16.46	16.09	
6	34:30.15	-5:11:56.7	15.70	14.35	13.99	0534301-051156	42	34:36.93	-5:08:14.5	17.01	16.77	16.65	
7	34:30.27	-5:11:48.2	11.53	10.64†	9.95†	0534302-051148	43	34:37.03	-5:12:39.1	16.80	15.41	14.98	
8	34:30.61	-5:11:05.0	13.90	13.30	13.08	0534305-051104	44	34:37.63	-5:04:49.3	16.82	15.79	14.94	
9	34:30.97	-5:03:56.9	16.94	16.14	15.80		45	34:37.80	-5:14:29.4	15.17	14.08	13.72	0534377-051429
10	34:31.07	-5:06:17.1	17.42	16.64	16.23		46	34:37.91	-5:08:48.0	16.25	15.28	15.00	0534379-050847
11	34:31.47	-5:08:54.1	16.45	15.84	15.56		47	34:37.91	-5:13:32.3	14.46	13.93	13.63	0534378-051332
12	34:31.52	-5:12:30.0	9.49†	8.40†	7.95†	0534315-051230	48	34:38.00	-5:14:06.4	16.77	16.17	15.59	
13	34:31.58	-5:11:50.3	17.78	16.59	16.21		49	34:38.08	-5:13:09.7	16.75	15.73	15.36	
14	34:31.85	-5:04:09.3	13.31	12.66	12.50	0534318-050408	50	34:38.13	-5:03:05.5	16.26	15.26	14.55	0534381-050305
15	34:32.03	-5:10:23.2	15.21	14.63	14.51	0534320-051023	51	34:38.13	-5:04:57.9	12.30	11.70	11.40	0534381-050458
16	34:32.05	-5:11:24.8	13.01	12.19	11.83	0534320-051124	52	34:38.16	-5:05:17.2	14.35	13.84	13.33	0534381-050517
17	34:32.36	-5:12:59.6	18.64	15.67	15.12		53	34:38.34	-5:01:26.0	15.26	14.24	13.90	0534383-050125
18	34:32.55	-5:04:21.3	17.65	16.83	16.63		54	34:38.39	-5:02:06.5	19.60	19.02	16.59	
19	34:32.88	-5:10:15.5	16.25	15.33	15.06	0534328-051015	55	34:38.49	-5:10:42.2	16.42	15.49	15.09	0534384-051042
20	34:32.89	-5:09:30.9	20.34	>20.72	17.05		56	34:38.57	-5:04:19.5	15.73	14.78	14.54	0534385-050419
21	34:33.26	-5:07:26.8	14.51	14.22	13.85	0534332-050726	57	34:38.58	-5:00:44.9	16.12	15.30	15.06	0534385-050044
22	34:33.27	-5:11:44.1	17.50	16.44	16.00		58	34:38.74	-5:04:05.7	15.72	15.18	14.72	0534387-050405
23	34:34.06	-5:12:27.0	15.37	14.43	14.14	0534340-051227	59	34:38.86	-5:04:40.7	16.05	15.26	14.97	0534388-050440
24	34:34.16	-5:05:57.0	17.18	16.44	16.12		60	34:38.90	-5:02:36.6	13.65	12.91	12.69	0534388-050236
25	34:34.17	-5:05:17.1	13.30	12.71	12.40	0534341-050516	61	34:38.90	-5:14:28.5	14.45	13.34	13.02	0534388-051428
26	34:34.62	-5:04:49.7	14.02	13.25	13.03	0534346-050449	62	34:39.20	-5:04:52.9	16.44	15.01	14.03	
27	34:34.66	-5:05:08.4	16.22	15.37	15.18	0534346-050508	63	34:39.24	-5:01:48.9	13.81	13.24	12.83	
28	34:35.55	-5:08:45.0	17.42	16.49	16.19		64	34:39.29	-5:00:47.1	14.62	13.94	13.73	0534393-050046
29	34:35.55	-5:09:04.8	17.43	16.77	16.46		65	34:39.35	-5:11:35.1	18.24	16.94	16.23	
30	34:35.95	-5:09:03.2	16.10	15.27	14.94	0534359-050903	66	34:39.38	-5:01:46.7	12.86	12.26	11.89	0534393-050146
31	34:36.14	-5:05:08.0	16.34	15.48	15.46	0534361-050507	67	34:39.43	-5:03:43.7	18.09	16.93	16.05	
32	34:36.26	-5:00:48.2	19.98	18.96	16.79		68	34:39.75	-5:03:06.2	12.95	12.16	11.95	0534397-050306
33	34:36.35	-5:02:54.7	16.61	15.67	15.40		69	34:39.78	-5:00:34.0	16.19	15.03	14.39	
34	34:36.39	-5:11:40.6	14.82	14.19	14.12	0534363-051140	70	34:39.86	-5:02:13.2	16.73	15.51	15.12	
35	34:36.69	-5:05:03.4	16.05	15.23	15.05	0534366-050503	71	34:39.88	-5:07:59.7	16.48	16.06	15.84	0534398-050800
36	34:36.69	-5:08:17.5	18.13	17.49	16.55		72	34:39.97	-5:04:08.8	15.91	15.03	14.80	0534399-050408

(cont.)

(cont.)

ID	R.A. <sup>a</sup>	decl. <sup>a</sup>	$J^{bcd}$	$H^{bcd}$	$K^{cd}$	2MASS	ID	R.A. <sup>a</sup>	decl. <sup>a</sup>	$J^{bcd}$	$H^{bcd}$	$K^{cd}$	2MASS
73	34:39.98	-5:10:07.0	9.11 <sup>†</sup>	8.96 <sup>†</sup>	8.83 <sup>†</sup>	0534399-051007	112	34:45.14	-5:00:05.9	16.37	15.48	15.12	0534451-050005
74	34:40.41	-5:07:53.2	15.85	15.43	15.21	0534403-050753	113	34:45.19	-5:10:47.6	12.21	11.43	11.04	0534451-051047
75	34:40.64	-5:06:58.6	15.67	13.21	11.87	0534406-050658	114	34:45.33	-5:00:50.0	14.35	13.53	13.27	0534453-050049
76	34:40.66	-5:12:24.5	15.10	14.49	14.20	0534406-051224	115	34:45.45	-5:02:07.9	12.27	11.58	11.33	0534454-050207
77	34:40.73	-5:09:24.1	15.62	14.98	14.66	0534407-050924	116	34:45.53	-5:10:16.0	14.65	13.99	13.89	0534455-051016
78	34:41.32	-5:01:19.6	15.36	14.34	14.03	0534413-050119	117	34:45.95	-5:04:14.3	17.53	16.73	16.56	
79	34:41.53	-5:07:02.4	15.01	14.69	14.29	0534415-050702	118	34:46.02	-5:08:58.1	16.53	15.63	15.31	0534460-050858
80	34:41.55	-5:02:25.2	16.34	15.58	15.37	0534415-050225	119	34:46.08	-5:13:11.6	15.77	14.96	14.41	
81	34:41.84	-5:08:39.7	16.80	16.29	16.04		120	34:46.35	-5:01:22.8	>21.62	>20.67	16.70	
82	34:42.01	-5:06:41.9	16.84	16.15	15.81		121	34:46.60	-5:04:46.6	15.75	15.05	14.92	0534465-050446
83	34:42.03	-5:02:25.0	14.01	13.33	13.09	0534420-050224	122	34:46.63	-5:10:40.4	12.05	11.47	11.32	0534466-051040
84	34:42.05	-5:04:31.8	13.95	13.23	12.52	0534420-050431	123	34:46.79	-5:04:26.8	16.85	15.81	15.37	
85	34:42.28	-5:07:14.6	9.58 <sup>†</sup>	9.64 <sup>†</sup>	9.58 <sup>†</sup>	0534422-050714	124	34:46.82	-4:59:10.9	12.31	11.51	11.16	
86	34:42.39	-5:04:00.0	17.78	16.83	16.44		125	34:46.91	-5:06:46.3	17.30	16.38	16.23	
87	34:42.41	-5:12:38.2	13.22	12.40	12.13	0534424-051238	126	34:46.94	-4:59:13.1	12.13	11.38	11.03	0534469-045912
88	34:42.42	-5:12:18.8	10.00 <sup>†</sup>	9.18 <sup>†</sup>	8.86 <sup>†</sup>	0534424-051218	127	34:47.03	-5:08:12.4	17.18	16.51	16.19	
89	34:42.60	-5:03:16.2	15.96	15.19	15.00	0534425-050316	128	34:47.08	-5:00:22.3	16.68	15.78	15.51	0534470-050022
90	34:42.69	-4:58:55.9	17.29	16.42	15.67		129	34:47.09	-5:08:45.6	16.62	15.58	15.45	
91	34:43.09	-5:00:11.6	16.22	15.72	15.43	0534430-050011	130	34:47.68	-4:59:16.3	>21.51	19.94	16.71	
92	34:43.16	-5:13:33.8	17.65	16.72	16.31		131	34:47.68	-4:59:33.3	13.65	13.00	12.75	0534476-045933
93	34:43.18	-5:01:57.9	16.91	15.87	15.66		132	34:47.85	-5:00:18.7	16.89	15.83	15.38	
94	34:43.24	-5:07:28.3	16.44	15.86	15.77		133	34:47.96	-5:04:54.9	11.89	11.16	10.67 <sup>†</sup>	0534479-050455
95	34:43.48	-5:14:42.5	15.40	14.09	13.84	0534434-051442	134	34:48.25	-5:10:39.0	16.00	15.32	15.27	0534482-051038
96	34:43.50	-5:14:21.2	15.34	14.38	14.12	0534434-051421	135	34:48.26	-5:03:30.3	17.05	15.99	15.89	
97	34:43.52	-5:01:26.3	17.11	16.33	16.06		136	34:48.28	-5:09:00.8	15.25	14.22	13.93	0534482-050900
98	34:43.58	-5:06:24.5	16.37	15.81	15.53	0534435-050624	137	34:48.29	-5:07:13.5	12.83	12.16	12.02	0534482-050713
99	34:43.65	-5:07:13.1	16.32	15.65	15.27		138	34:48.42	-5:05:01.4	12.47	11.79	11.64	0534484-050501
100	34:43.88	-5:14:22.2	16.93	15.88	15.80		139	34:48.49	-5:01:52.3	17.57	15.92	15.67	
101	34:43.89	-5:12:55.8	14.21	13.16	12.89	0534438-051255	140	34:48.51	-5:07:11.0	13.30	12.70	12.51	0534485-050710
102	34:43.96	-4:59:33.4	13.48	12.80	12.58	0534439-045933	141	34:48.77	-5:02:46.8	17.02	16.06	15.57	
103	34:44.08	-5:06:26.5	16.72	16.19	15.55	0534440-050626	142	34:48.98	-5:06:56.9	17.71	16.47	15.94	
104	34:44.14	-4:59:10.1	17.36	16.20	15.70		143	34:49.17	-4:56:01.0	19.36	16.27	14.88	
105	34:44.18	-5:06:43.2	13.93	13.30	13.12	0534441-050643	144	34:49.18	-5:01:38.1	17.53	16.45	15.85	
106	34:44.48	-5:02:55.3	17.51	16.48	16.23		145	34:49.22	-5:04:38.1	12.48	11.77	11.58	0534492-050438
107	34:44.57	-5:02:13.5	21.20	18.76	16.66		146	34:49.35	-5:11:53.5	17.21	16.09	15.70	
108	34:44.90	-5:12:31.8	15.28	14.33	13.75	0534448-051231	147	34:49.37	-4:59:38.2	16.61	15.70	15.35	0534493-045937
109	34:44.98	-5:06:49.5	11.74	11.25	10.75 <sup>†</sup>	0534449-050649	148	34:49.49	-5:11:34.8	17.78	16.19	15.51	
110	34:45.07	-5:06:20.1	13.79	12.58	12.14	0534450-050620	149	34:49.58	-5:04:59.6	13.31	12.59	12.29	0534495-050459
111	34:45.12	-5:14:06.1	14.57	13.46	12.91	0534451-051406	150	34:49.59	-5:11:18.0	17.13	16.19	16.01	

(cont.)

(cont.)

ID	R.A. <sup>a</sup>	decl. <sup>a</sup>	$J^{bcd}$	$H^{bcd}$	$K^{cd}$	2MASS	ID	R.A. <sup>a</sup>	decl. <sup>a</sup>	$J^{bcd}$	$H^{bcd}$	$K^{cd}$	2MASS
151	34:49.69	-5:07:07.4	17.62	16.23	15.83		190	34:53.71	-4:59:13.8	17.92	16.74	16.23	
152	34:49.73	-5:00:03.0	15.27	14.71	14.55	0534497-050003	191	34:53.73	-5:05:48.8	13.25	12.61	12.39	0534537-050548
153	34:50.04	-5:00:37.4	17.73	16.54	16.05		192	34:53.80	-5:12:24.2	16.58	15.98	15.45	
154	34:50.04	-5:02:57.3	17.62	16.15	15.56		193	34:53.87	-4:56:22.4	12.43	11.42	10.99 <sup>†</sup>	0534538-045622
155	34:50.11	-4:58:18.6	17.16	16.21	15.95		194	34:53.89	-5:07:55.4	16.98	15.72	15.13	
156	34:50.15	-4:56:42.5	>21.50	>20.55	16.55		195	34:53.96	-4:56:15.7	17.30	16.14	15.52	
157	34:50.15	-5:16:06.3	18.08	16.58	15.66		196	34:54.16	-5:11:21.9	18.74	16.88	16.42	
158	34:50.27	-4:59:24.3	16.13	15.20	14.97	0534502-045924	197	34:54.58	-4:56:05.4	12.17	11.15	10.54 <sup>†</sup>	0534545-045605
159	34:50.32	-5:15:04.7	17.00	15.84	15.23		198	34:54.82	-5:10:12.6	16.77	16.42	15.40	
160	34:50.51	-5:11:10.5	11.80	11.21	11.09 <sup>†</sup>	0534505-051110	199	34:54.90	-5:02:43.6	17.07	16.02	15.16	
161	34:50.56	-5:06:38.3	13.97	13.46	13.18	0534505-050638	200	34:54.92	-5:01:28.4	18.00	16.94	16.22	
162	34:50.66	-5:04:07.8	12.66	11.88	11.60	0534506-050407	201	34:54.93	-5:02:21.2	12.13	11.52	11.25 <sup>†</sup>	0534549-050220
163	34:50.73	-4:58:37.0	12.25	11.21	10.81 <sup>†</sup>	0534507-045836	202	34:55.00	-4:55:37.6	>21.40	17.64	16.16	
164	34:51.15	-4:55:48.4	17.44	15.28	14.48		203	34:55.11	-5:17:45.5	>21.00	15.65	14.57	
165	34:51.15	-5:12:32.2	13.73	12.80	12.41	0534511-051232	204	34:55.23	-5:15:58.4	18.36	15.43	14.73	
166	34:51.31	-4:56:13.5	>21.24	19.75	15.07		205	34:55.32	-4:56:59.6	14.37	13.70	13.49	0534553-045659
167	34:51.41	-5:00:11.4	13.20	12.46	12.20	0534514-050011	206	34:55.35	-5:09:25.5	16.80	15.62	15.08	
168	34:51.43	-5:13:29.5	12.86	12.19	11.94	0534514-051329	207	34:55.38	-5:13:51.9	17.57	16.27	16.04	
169	34:51.43	-5:14:40.3	19.83	17.94	16.40		208	34:55.40	-5:16:00.9	17.33	14.97	14.29	
170	34:51.73	-5:08:18.8	16.44	15.34	15.01	0534517-050818	209	34:55.42	-5:01:39.5	12.51	11.71	11.55	0534554-050139
171	34:51.77	-4:55:55.4	15.88	13.67	12.68	0534517-045555	210	34:55.49	-5:11:15.1	17.97	16.48	15.95	
172	34:51.82	-4:58:28.9	>21.76	>20.81	17.72		211	34:55.49	-5:12:59.3	18.24	16.79	16.14	
173	34:52.08	-4:58:24.1	17.44	16.24	15.82		212	34:55.61	-5:12:34.9	19.06	16.89	16.45	
174	34:52.26	-5:12:03.2	13.10	12.36	12.17	0534522-051203	213	34:55.64	-5:06:30.3	18.14	16.82	15.94	
175	34:52.40	-5:14:19.6	15.96	14.96	14.67		214	34:55.67	-4:56:12.0	12.39	11.10	10.26 <sup>†</sup>	0534556-045611
176	34:52.61	-5:15:36.5	13.04	11.74	11.18	0534526-051536	215	34:55.81	-4:58:17.1	18.87	17.40	16.07	
177	34:52.69	-5:10:32.7	16.37	15.19	14.92	0534526-051032	216	34:55.86	-5:07:30.0	16.89	15.81	15.31	0534558-050730
178	34:52.76	-5:00:50.8	13.10	12.39	12.16	0534527-050050	217	34:55.87	-5:08:21.2	12.84	11.96	11.74	0534558-050821
179	34:52.93	-5:15:19.5	16.47	15.34	14.64		218	34:55.91	-5:15:47.8	17.79	16.53	16.54	
180	34:53.05	-5:03:27.0	12.01	11.40	10.73 <sup>†</sup>	0534530-050327	219	34:56.10	-5:00:55.2	12.73	11.94	11.74	0534561-050055
181	34:53.13	-4:56:49.4	>21.49	>20.54	16.66		220	34:56.13	-5:06:01.8	12.53	11.93	11.64	0534561-050601
182	34:53.43	-5:10:27.8	12.14	11.51	11.29	0534534-051027	221	34:56.17	-5:09:25.4	15.00	14.08	13.76	0534561-050925
183	34:53.44	-4:57:32.8	13.38	12.52	12.29	0534534-045732	222	34:56.18	-5:05:06.6	18.32	17.51	16.73	
184	34:53.53	-5:11:52.2	15.73	14.47	13.91		223	34:56.36	-5:08:04.8	17.90	16.21	15.85	
185	34:53.56	-5:02:55.1	18.17	16.64	16.21		224	34:56.38	-5:15:28.3	18.30	15.76	15.13	
186	34:53.56	-5:03:47.5	17.97	16.68	16.06		225	34:56.54	-5:01:07.2	14.35	13.54	13.10	0534565-050107
187	34:53.63	-5:01:29.0	14.32	13.71	13.38	0534536-050129	226	34:56.63	-5:11:12.4	13.56	12.53	12.04	0534566-051112
188	34:53.64	-5:02:02.6	14.91	13.84	13.55	0534536-050202	227	34:56.66	-5:11:03.3	17.17	15.50	15.00	
189	34:53.65	-5:04:47.3	17.23	15.87	15.15		228	34:56.67	-5:14:52.3	14.94	13.83	13.25	0534566-051452

(cont.)

(cont.)

ID	R.A. <sup>a</sup>	decl. <sup>a</sup>	$J^{bcd}$	$H^{bcd}$	$K^{cd}$	2MASS	ID	R.A. <sup>a</sup>	decl. <sup>a</sup>	$J^{bcd}$	$H^{bcd}$	$K^{cd}$	2MASS
229	34:56.72	-5:13:56.9	15.95	14.89	14.35		268	34:59.88	-4:55:27.1	17.03	13.89	12.46	0534598-045527
230	34:56.77	-5:09:58.5	14.10	12.99	12.58	0534567-050958	269	34:59.99	-5:10:41.0	17.01	15.79	15.18	
231	34:56.78	-5:10:43.8	13.46	12.57	12.31	0534567-051043	270	35:00.19	-5:00:09.4	17.99	16.78	16.57	
232	34:56.82	-5:11:33.0	10.92 <sup>†</sup>	10.19 <sup>†</sup>	9.69 <sup>†</sup>	0534568-051132	271	35:00.24	-5:15:58.9	14.06	12.81	12.19	0535002-051558
233	34:56.95	-4:54:36.0	18.24	15.22	13.64		272	35:00.25	-4:56:08.8	14.34	13.12	12.57	0535002-045608
234	34:57.07	-5:00:55.9	18.23	16.87	16.20		273	35:00.34	-5:00:59.6	19.74	17.68	16.81	
235	34:57.16	-5:01:35.5	17.63	16.47	16.15		274	35:00.40	-5:09:44.0	13.72	13.01	12.72	0535003-050944
236	34:57.18	-5:07:16.8	16.06	14.95	14.55	0534571-050716	275	35:00.41	-5:09:54.5	16.98	16.25	15.78	
237	34:57.20	-5:08:23.9	12.08	11.36	11.01	0534571-050823	276	35:00.44	-5:15:21.7	18.69	16.69	16.01	
238	34:57.31	-5:02:50.8	18.42	16.50	15.68		277	35:00.64	-4:58:53.5	15.90	15.10	14.75	0535006-045853
239	34:57.32	-5:04:00.2	18.59	16.98	16.58		278	35:00.67	-5:05:08.6	10.07 <sup>†</sup>	9.95 <sup>†</sup>	9.89 <sup>†</sup>	0535006-050508
240	34:57.38	-5:14:33.5	13.44	12.30	11.81	0534573-051433	279	35:00.73	-5:11:27.6	16.60	14.95	14.48	
241	34:57.46	-4:56:45.5	14.40	12.51	11.63	0534574-045645	280	35:00.86	-5:09:39.1	12.99	12.28	12.07	0535008-050938
242	34:57.61	-4:54:33.3	>21.31	17.55	16.12		281	35:00.87	-5:09:16.0	17.51	16.59	16.63	
243	34:57.63	-5:06:25.4	18.46	16.91	15.81		282	35:00.91	-5:05:40.1	15.84	15.25	14.94	0535009-050540
244	34:57.68	-5:12:29.7	14.35	12.89	12.34	0534576-051229	283	35:01.05	-5:05:33.5	15.50	14.90	14.55	0535010-050533
245	34:57.71	-4:57:20.0	17.98	14.82	12.83		284	35:01.30	-5:06:32.9	17.06	16.08	15.75	
246	34:57.89	-5:08:42.7	16.78	15.85	15.67	0534579-050842	285	35:01.32	-4:55:57.0	14.34	13.25	12.82	0535013-045557
247	34:58.03	-5:06:25.9	17.84	16.33	15.51		286	35:01.39	-4:56:32.6	16.47	15.62	15.11	0535013-045632
248	34:58.03	-5:16:01.9	14.60	13.09	12.29	0534580-051601	287	35:01.43	-5:09:32.7	12.17	11.48	11.24	0535014-050932
249	34:58.05	-5:17:37.5	12.61	11.48	11.08	0534580-051737	288	35:01.50	-5:11:04.1	13.77	12.69	12.18	0535014-051104
250	34:58.15	-5:07:12.4	16.88	15.66	15.18		289	35:01.63	-4:56:46.2	18.78	16.41	15.23	
251	34:58.19	-5:09:27.5	12.26	11.51	11.16	0534581-050927	290	35:01.93	-5:00:43.3	14.50	13.72	13.52	0535019-050043
252	34:58.19	-5:11:53.7	12.61	11.98	11.71	0534581-051153	291	35:02.10	-5:15:37.5	12.69	11.93	11.77	0535020-051537
253	34:58.21	-5:00:13.2	17.50	16.38	16.37		292	35:02.18	-5:04:38.4	13.77	12.99	12.65	0535021-050438
254	34:58.24	-4:54:04.3	17.28	14.71	13.71	0534582-045404	293	35:02.38	-5:15:47.9	9.32 <sup>†</sup>	8.32 <sup>†</sup>	7.91 <sup>†</sup>	0535023-051547
255	34:58.49	-5:07:48.2	15.88	14.84	14.39	0534584-050748	294	35:02.64	-4:54:17.3	16.84	14.89	13.89	0535026-045417
256	34:58.69	-5:12:21.6	16.74	16.10	15.76		295	35:02.64	-5:09:59.1	15.53	14.44	14.07	0535026-050959
257	34:58.69	-5:12:26.1	14.04	13.44	13.14	0534586-051226	296	35:02.66	-4:56:42.8	18.07	16.37	15.06	
258	34:58.83	-5:15:35.7	17.70	16.75	15.95		297	35:02.67	-4:58:18.3	19.53	18.16	16.27	
259	34:58.84	-5:17:01.1	15.45	14.57	13.53		298	35:02.73	-5:08:53.9	18.38	16.93	16.09	
260	34:58.93	-5:13:45.4	13.72	12.43	11.86	0534589-051345	299	35:02.75	-5:00:03.0	12.24	11.18	10.64 <sup>†</sup>	0535027-050002
261	34:58.93	-5:16:13.3	16.56	15.57	14.35		300	35:02.89	-5:03:03.7	15.82	15.06	14.76	0535028-050303
262	34:59.08	-4:57:34.0	18.61	16.82	16.43		301	35:02.90	-4:54:30.2	20.83	16.27	13.64	
263	34:59.21	-5:17:39.9	16.81	15.72	15.21		302	35:02.99	-4:57:04.0	14.05	13.33	13.16	0535029-045703
264	34:59.31	-5:05:30.0	12.37	11.63	11.24	0534593-050530	303	35:03.04	-4:59:59.9	12.57	11.85	11.66	0535030-045959
265	34:59.32	-5:06:06.9	16.43	15.37	14.94	0534593-050606	304	35:03.07	-5:13:54.4	13.32	11.84	11.07	0535030-051354
266	34:59.43	-4:57:37.1	18.58	16.59	15.83		305	35:03.12	-5:09:17.1	13.14	12.28	12.05	0535031-050917
267	34:59.67	-5:02:54.4	18.54	16.60	15.66		306	35:03.24	-5:17:53.1	12.89	12.44	11.51	0535032-051753

(cont.)

(cont.)

ID	R.A. <sup>a</sup>	decl. <sup>a</sup>	$J^{bcd}$	$H^{bcd}$	$K^{cd}$	2MASS	ID	R.A. <sup>a</sup>	decl. <sup>a</sup>	$J^{bcd}$	$H^{bcd}$	$K^{cd}$	2MASS
307	35:03.25	-5:17:26.2	15.11	13.82	12.80	0535033-051622	346	35:06.37	-5:03:02.5	16.23	14.80	14.28	0535063-050302
308	35:03.34	-5:16:22.7	14.02	12.38	11.56	0535033-045643	347	35:06.50	-5:17:22.2	14.39	12.66	11.67	0535067-051145
309	35:03.35	-4:56:43.0	12.36	11.59	11.34	0535033-050853	348	35:06.72	-5:11:45.3	13.91	12.43	11.75	0535068-051038
310	35:03.37	-5:08:53.8	13.41	12.09	11.66	0535034-050540	349	35:06.73	-5:16:46.4	16.89	15.31	14.13	
311	35:03.40	-5:05:40.3	9.14 <sup>†</sup>	8.95 <sup>†</sup>	8.90 <sup>†</sup>		350	35:06.83	-5:10:38.4	12.56	11.81	11.61	
312	35:03.40	-5:16:45.1	19.92	18.68	16.13		351	35:06.86	-5:11:50.0	15.84	14.91	14.23	
313	35:03.59	-5:16:00.4	14.38	13.40	12.87	0535035-051600	352	35:06.88	-5:11:33.0	17.78	15.82	14.77	
314	35:03.65	-5:13:10.4	15.17	13.39	12.60	0535036-051310	353	35:06.97	-4:57:04.2	18.48	15.25	13.59	
315	35:03.85	-5:07:49.0	16.96	15.83	15.52		354	35:07.02	-5:01:34.8	17.68	16.86	16.16	
316	35:04.08	-5:17:42.8	17.18	15.47	14.68		355	35:07.04	-4:54:56.7	12.80	11.95	11.84	0535070-045456
317	35:04.20	-5:15:21.4	13.70	12.64	12.35	0535042-051521	356	35:07.13	-4:55:50.7	14.66	13.18	12.61	0535071-045550
318	35:04.29	-5:13:13.9	17.78	17.15	15.34		357	35:07.16	-4:55:43.2	19.38	17.23	15.15	
319	35:04.30	-5:08:12.6	8.19 <sup>†</sup>	7.52 <sup>†</sup>	7.34 <sup>†</sup>	0535042-050812	358	35:07.40	-5:07:38.0	17.37	15.56	14.62	
320	35:04.38	-5:01:15.4	16.24	14.48	13.68	0535043-050115	359	35:07.54	-5:11:14.5	12.31	11.32	10.70 <sup>†</sup>	0535075-051114
321	35:04.38	-5:08:16.7	<10.05	<10.01	<9.56		360	35:07.75	-5:04:55.4	17.43	15.87	15.64	
322	35:04.40	-4:57:15.4	14.73	13.80	13.43	0535044-045715	361	35:07.79	-5:01:19.3	16.23	15.27	14.80	0535077-050119
323	35:04.40	-5:07:35.6	14.81	13.67	13.09		362	35:07.83	-5:02:43.7	17.37	15.91	15.64	
324	35:04.60	-4:56:45.4	>21.87	>20.93	16.99		363	35:07.85	-5:10:06.7	16.79	15.72	15.21	
325	35:04.62	-4:58:29.0	13.43	12.10	11.01 <sup>†</sup>	0535046-045829	364	35:07.88	-5:17:05.4	13.99	12.98	12.14	
326	35:04.63	-5:09:55.7	11.32	10.74 <sup>†</sup>	10.45 <sup>†</sup>	0535046-050955	365	35:08.23	-4:54:10.2	14.57	11.91	10.28 <sup>†</sup>	0535082-045410
327	35:04.64	-4:54:02.5	15.85	14.30	13.56	0535046-045402	366	35:08.37	-5:16:20.5	14.19	13.21	12.49	
328	35:04.70	-5:01:50.9	17.50	16.04	16.11		367	35:08.38	-5:16:25.0	>21.73	>20.78	17.45	
329	35:04.78	-5:17:41.9	11.49	10.11 <sup>†</sup>	9.34 <sup>†</sup>	0535047-051742	368	35:08.45	-5:07:13.5	14.37	13.13	12.71	0535084-050713
330	35:05.10	-4:53:51.4	18.10	16.05	14.91		369	35:08.48	-5:03:48.5	18.74	16.64	15.92	
331	35:05.20	-5:14:50.2	8.23 <sup>†</sup>	7.71 <sup>†</sup>	7.38 <sup>†</sup>	0535051-051450	370	35:08.60	-5:09:30.3	17.51	15.57	14.78	
332	35:05.21	-5:03:39.8	19.48	17.22	16.26		371	35:08.64	-5:16:47.6	14.83	13.64	12.52	
333	35:05.45	-4:57:05.5	20.56	16.77	14.57		372	35:08.67	-5:16:13.3	16.30	13.73	11.79	
334	35:05.48	-4:54:34.6	19.85	18.29	16.83		373	35:08.68	-4:59:33.2	19.66	17.98	16.78	
335	35:05.61	-5:11:50.5	12.90	11.46	10.86 <sup>†</sup>	0535056-051150	374	35:08.69	-4:54:41.2	17.32	15.82	14.83	
336	35:05.68	-4:58:53.9	11.99	11.30	11.04	0535056-045853	375	35:08.69	-5:17:30.6	>20.98	16.59	14.18	
337	35:05.68	-5:02:40.1	17.54	15.96	15.27		376	35:08.75	-5:04:40.8	12.81	11.61	11.44	0535087-050440
338	35:05.70	-4:58:33.4	15.95	13.51	12.46	0535056-045833	377	35:08.83	-5:17:05.9	15.54	13.94	12.59	
339	35:05.74	-5:11:35.0	12.94	11.46	10.83 <sup>†</sup>	0535057-051135	378	35:08.95	-5:05:52.5	9.05 <sup>†</sup>	7.91 <sup>†</sup>	7.41 <sup>†</sup>	0535089-050552
340	35:05.78	-4:55:36.2	19.76	17.02	15.38		379	35:08.96	-5:10:25.8	14.54	13.83	13.74	0535089-051025
341	35:05.88	-5:08:38.2	15.06	14.00	13.46	0535058-050838	380	35:09.09	-5:10:09.7	17.39	15.81	15.31	
342	35:06.06	-5:03:19.0	17.19	15.81	15.23		381	35:09.14	-5:16:44.2	16.43	14.36	12.63	
343	35:06.10	-5:14:24.9	13.28	12.14	11.50	0535061-051425	382	35:09.15	-5:06:47.1	11.24	10.57 <sup>†</sup>	10.33 <sup>†</sup>	0535091-050647
344	35:06.19	-5:12:15.8	8.09 <sup>†</sup>	8.22 <sup>†</sup>	8.21 <sup>†</sup>	0535061-051216	383	35:09.19	-5:16:51.7	14.62	13.31	12.14	
345	35:06.34	-4:58:41.6	14.08	13.46	13.27	0535063-045841	384	35:09.24	-5:10:22.6	18.20	16.59	16.13	

(cont.)

(cont.)



ID	R.A. <sup>a</sup>	decl. <sup>a</sup>	$J^{bcd}$	$H^{bcd}$	$K^{cd}$	2MASS	ID	R.A. <sup>a</sup>	decl. <sup>a</sup>	$J^{bcd}$	$H^{bcd}$	$K^{cd}$	2MASS
385	35:09.28	-5:16:55.7	13.82	12.76	11.96		424	35:11.87	-5:17:25.9	13.55	11.89	11.81 <sup>†</sup>	0535118-051725
386	35:09.38	-4:55:13.6	>21.53	>20.58	16.21		425	35:11.89	-5:00:00.9	>21.66	>20.71	16.69	
387	35:09.45	-5:16:53.3	14.19	13.14	12.15		426	35:12.05	-5:14:14.7	13.93	13.47	13.41	0535120-051414
388	35:09.46	-4:57:11.7	13.92	13.11	12.51	0535094-045711	427	35:12.13	-5:03:48.4	18.26	16.44	15.59	
389	35:09.49	-4:59:41.4	12.94	12.24	11.85	0535094-045941	428	35:12.17	-5:14:30.1	17.18	15.93	15.10	
390	35:09.54	-5:14:45.8	>21.13	15.94	14.78		429	35:12.30	-5:04:26.4	18.51	16.27	14.99	
391	35:09.82	-4:53:52.6	17.07	14.95	13.66		430	35:12.31	-5:17:50.0	15.74	13.99	12.49	
392	35:09.83	-4:56:19.4	19.33	17.22	15.26		431	35:12.51	-5:16:26.3	>21.04	15.79	13.45	
393	35:09.88	-4:58:49.5	16.45	13.22	11.51		432	35:12.52	-4:57:13.7	15.07	13.13	12.35	0535125-045713
394	35:09.96	-5:14:50.1	14.42	13.50	12.99	0535099-051450	433	35:12.55	-4:56:01.9	17.49	14.20	12.28	
395	35:10.01	-5:14:57.3	16.57	15.74	15.00		434	35:12.57	-5:16:33.2	13.87	11.40	9.90 <sup>†</sup>	0535125-051633
396	35:10.05	-5:16:22.9	17.50	15.35	14.58		435	35:12.69	-4:54:02.6	16.76	14.12	12.24	
397	35:10.09	-5:17:06.8	14.68	12.98	11.84		436	35:12.69	-4:56:00.7	17.45	14.20	12.24	
398	35:10.11	-5:16:16.9	17.08	15.06	14.06		437	35:12.69	-5:02:26.5	18.55	16.65	15.69	
399	35:10.28	-5:03:05.0	16.85	14.99	14.16		438	35:12.70	-5:12:00.7	14.17	13.53	13.20	0535127-051200
400	35:10.30	-5:17:19.9	21.61	16.60	14.72		439	35:12.70	-5:12:28.8	16.43	14.95	13.78	
401	35:10.38	-4:54:41.2	15.93	15.26	15.31	0535103-045441	440	35:12.72	-5:16:13.4	12.60	11.91	11.67	0535127-051613
402	35:10.53	-4:58:46.0	>21.08	13.84	<10.45		441	35:12.73	-5:15:43.2	14.67	14.05	13.33	
403	35:10.73	-5:08:16.8	16.11	14.32	13.14		442	35:12.74	-5:16:52.7	11.37	10.18 <sup>†</sup>	9.62 <sup>†</sup>	0535127-051652
404	35:10.79	-5:10:34.4	12.46	11.11	10.41 <sup>†</sup>	0535107-051034	443	35:12.81	-5:01:46.3	13.92	13.27	13.01	0535128-050146
405	35:10.83	-5:17:33.2	15.09	13.40	11.99		444	35:12.82	-5:15:23.9	11.65	10.72 <sup>†</sup>	10.39 <sup>†</sup>	0535128-051524
406	35:10.85	-4:55:42.6	17.33	15.75	14.36		445	35:12.87	-5:15:48.7	14.82	14.35	13.71	
407	35:10.97	-4:56:39.7	16.85	14.71	13.33	0535109-045639	446	35:12.95	-5:02:08.7	14.42	13.76	13.42	0535129-050208
408	35:11.00	-5:15:21.8	15.99	13.39	11.13		447	35:12.97	-5:07:47.5	>21.67	19.58	17.14	
409	35:11.11	-5:16:01.8	16.30	14.38	13.16		448	35:13.03	-5:00:26.1	>20.99	16.97	14.43	
410	35:11.12	-4:54:14.9	20.13	17.13	16.00		449	35:13.10	-4:55:52.3	12.98	11.00	9.29 <sup>†</sup>	0535131-045552
411	35:11.16	-4:55:28.0	18.16	15.46	14.00		450	35:13.11	-5:15:26.3	13.27	12.60	12.27	
412	35:11.18	-4:55:38.1	17.86	15.89	14.60		451	35:13.19	-5:17:30.6	15.22	12.86	<10.88	
413	35:11.23	-5:17:20.8	12.30	<10.55	<9.22		452	35:13.32	-5:09:19.5	12.06	11.35	11.19	0535133-050919
414	35:11.24	-5:17:42.3	16.28	14.89	13.96		453	35:13.41	-4:54:21.2	18.16	17.42	17.41	
415	35:11.34	-5:14:01.6	13.80	12.80	12.37	0535113-051401	454	35:13.47	-5:17:10.5	11.49	10.39 <sup>†</sup>	9.93 <sup>†</sup>	0535134-051710
416	35:11.41	-5:17:46.5	15.12	13.23	11.72		455	35:13.48	-5:05:51.3	19.09	17.51	16.51	
417	35:11.45	-5:05:16.2	16.20	14.94	14.28	0535114-050516	456	35:13.52	-5:17:31.4	13.14	11.45	11.16 <sup>†</sup>	0535135-051731
418	35:11.50	-5:17:57.3	15.42	12.56	<10.52		457	35:13.53	-5:17:17.6	13.24	12.09	11.61	0535135-051717
419	35:11.63	-5:16:57.6	9.56 <sup>†</sup>	8.94 <sup>†</sup>	8.70 <sup>†</sup>	0535116-051657	458	35:13.59	-5:17:45.9	17.34	14.23	11.40	
420	35:11.76	-5:16:52.0	14.16	13.20	12.99		459	35:13.64	-5:14:22.2	15.74	15.02	15.15	0535136-051421
421	35:11.79	-4:54:21.5	16.06	14.37	13.56	0535118-045421	460	35:13.86	-4:58:03.5	15.58	13.12	11.93	0535138-045803
422	35:11.81	-5:03:30.2	14.54	13.07	12.51	0535118-050330	461	35:13.92	-4:53:58.4	>22.11	>21.16	16.97	
423	35:11.87	-5:01:56.0	17.30	15.91	14.93		462	35:13.92	-5:18:53.2	13.57	12.89	11.55 <sup>†</sup>	0535139-051853

(cont.)

(cont.)



ID	R.A. <sup>a</sup>	decl. <sup>a</sup>	$J^{bcd}$	$H^{bcd}$	$K^{cd}$	2MASS	ID	R.A. <sup>a</sup>	decl. <sup>a</sup>	$J^{bcd}$	$H^{bcd}$	$K^{cd}$	2MASS
541	35:16.41	-4:58:02.0	13.25	12.54	12.35	0535164-045802	580	35:17.61	-5:18:32.6	15.01	12.13	<10.92	
542	35:16.42	-4:56:53.1	19.40	17.61	16.45		581	35:17.62	-5:16:41.1	16.84	16.39	16.31	
543	35:16.44	-4:58:07.0	13.41	12.59	12.34	0535164-045807	582	35:17.67	-5:16:55.2	17.10	16.17	15.64	
544	35:16.48	-5:06:00.6	15.32	14.60	12.86		583	35:17.71	-5:03:08.9	20.58	17.33	15.93	
545	35:16.49	-4:57:17.4	18.77	16.53	15.41		584	35:17.73	-5:00:30.9	15.07	12.86	11.55	0535177-050031
546	35:16.51	-5:03:30.4	12.42	11.72	11.35	0535164-050330	585	35:17.79	-5:16:15.7	11.94	<10.65	<9.97	
547	35:16.51	-5:17:47.3	14.55	12.73	11.65		586	35:17.82	-5:19:28.1	14.11	11.75	<10.82	
548	35:16.61	-5:16:20.6	15.72	14.19	13.36		587	35:17.83	-4:55:17.2	16.98	14.51	13.14	
549	35:16.63	-5:17:23.5	13.12	11.10	<9.77		588	35:17.91	-5:17:56.0	14.61	12.86	11.84	
550	35:16.74	-5:18:44.8	15.29	13.38	11.64		589	35:17.91	-5:18:35.2	13.54	<10.59	<9.54	
551	35:16.78	-5:17:16.9	13.43	12.47	11.91		590	35:17.92	-5:15:32.9	11.50	<10.76	<10.18	
552	35:16.79	-5:07:27.3	14.89	14.41	14.01	0535167-050727	591	35:17.98	-4:57:59.7	18.33	16.27	15.40	
553	35:16.80	-5:14:47.4	15.61	14.58	13.92		592	35:17.98	-5:16:45.1	13.07	11.70	11.04	
554	35:16.80	-5:16:53.3	13.60	12.79	12.42		593	35:17.99	-5:15:38.7	13.06	12.39	11.86	
555	35:16.80	-5:19:01.1	13.95	11.40	<10.03		594	35:18.01	-5:16:13.6	11.18	<10.00	<9.37	
556	35:16.86	-5:07:47.8	13.77	12.81	12.32	0535168-050747	595	35:18.11	-5:15:46.1	13.37	12.69	12.39	
557	35:16.89	-5:15:09.2	16.05	14.15	12.96		596	35:18.19	-5:17:53.9	15.01	13.54	13.04	
558	35:16.91	-5:17:03.0	13.40	11.73	<10.80		597	35:18.21	-5:03:54.5	9.26†	9.26†	9.21†	0535182-050354
559	35:16.94	-5:18:41.0	15.50	12.81	11.38		598	35:18.21	-5:16:33.9	12.76	11.97	11.70	
560	35:17.01	-5:17:32.1	14.92	13.67	13.34		599	35:18.21	-5:17:22.0	15.69	13.41	11.57	
561	35:17.02	-5:15:44.3	12.50	11.64	11.01		600	35:18.22	-5:15:06.1	17.15	16.69	16.08	
562	35:17.07	-5:17:29.0	15.03	13.79	13.87		601	35:18.24	-5:13:06.9	11.36	<10.34	<9.78	
563	35:17.12	-5:19:00.7	14.91	12.38	<10.87		602	35:18.24	-5:17:44.9	13.68	11.61	<10.12	
564	35:17.13	-5:18:13.7	>21.68	>20.73	14.59		603	35:18.30	-5:08:04.8	17.02	14.58	13.24	
565	35:17.14	-4:58:06.1	16.48	14.91	14.06	0535171-045806	604	35:18.33	-5:00:32.9	18.02	14.57	<10.72	
566	35:17.15	-4:57:47.1	15.14	14.47	14.17	0535171-045747	605	35:18.35	-5:13:16.7	14.53	13.30	12.67	
567	35:17.15	-5:12:39.4	13.51	12.89	12.78		606	35:18.37	-5:19:17.5	15.32	13.72	12.26	
568	35:17.15	-5:18:06.5	>21.67	18.80	13.47		607	35:18.38	-5:15:01.5	>21.86	>20.91	16.27	
569	35:17.38	-5:12:29.6	13.70	13.08	12.93		608	35:18.44	-5:07:14.5	>21.28	17.44	15.94	
570	35:17.42	-4:59:57.0	17.47	14.64	12.89		609	35:18.45	-5:06:45.9	19.93	18.01	15.45	
571	35:17.42	-5:05:00.9	>21.57	19.73	17.19		610	35:18.46	-5:16:37.7	<10.36	<9.89	<9.57	
572	35:17.43	-5:17:12.5	16.56	15.63	15.02		611	35:18.47	-5:08:30.7	13.79	13.13	12.97	0535184-050830
573	35:17.45	-5:16:57.0	14.42	13.61	13.12		612	35:18.52	-5:13:38.4	11.34	<10.40	<9.61	
574	35:17.50	-5:09:49.1	13.34	12.70	12.47	0535174-050949	613	35:18.55	-5:18:20.5	12.80	11.36	11.10	
575	35:17.50	-5:16:50.0	19.02	18.79	16.76		614	35:18.60	-4:55:11.0	17.52	15.58	14.09	
576	35:17.51	-5:18:22.5	16.02	12.73	<10.90		615	35:18.60	-4:59:42.3	13.86	13.22	12.96	0535186-045942
577	35:17.54	-5:17:40.1	<10.79	<9.46	<8.53		616	35:18.60	-5:16:35.1	<10.54	<9.97	<9.57	
578	35:17.56	-5:16:13.0	12.56	11.22	<10.60		617	35:18.62	-5:06:47.3	20.70	16.47	14.15	
579	35:17.57	-5:19:28.9	13.53	11.07	<10.16		618	35:18.62	-5:13:27.5	16.73	14.53	13.25	

(cont.)

(cont.)

ID	R.A. <sup>a</sup>	decl. <sup>a</sup>	$J^{bcd}$	$H^{bcd}$	$K^{cd}$	2MASS
619	35:18.64	-5:18:35.1	14.10	12.05	11.26	
620	35:18.69	-5:17:43.1	16.17	14.42	13.27	
621	35:18.71	-5:15:18.1	14.30	13.67	12.97	
622	35:18.75	-5:18:02.2	12.86	<10.95	<10.00	
623	35:18.82	-5:17:29.0	11.37	<9.68	<8.35	
624	35:18.83	-5:17:20.9	16.09	14.46	13.11	
625	35:18.86	-5:14:45.6	12.48	11.65	11.27	
626	35:18.90	-5:19:02.9	15.06	12.91	11.58	
627	35:18.92	-5:16:13.9	11.66	11.36	11.27	
628	35:18.95	-5:12:31.3	17.89	16.33	15.64	
629	35:18.97	-5:17:51.6	16.50	14.60	13.01	
630	35:19.10	-4:54:07.8	13.70	13.03	12.97	0535191-045407
631	35:19.20	-5:18:39.1	15.89	14.38	13.63	
632	35:19.25	-5:16:58.6	15.89	14.59	13.71	
633	35:19.25	-5:17:31.6	15.58	13.24	11.43	
634	35:19.28	-5:19:11.9	16.94	13.47	12.02	
635	35:19.31	-5:16:44.6	12.87	12.03	11.46	0535193-051644
636	35:19.32	-4:55:44.9	15.67	12.87	10.25†	0535193-045545
637	35:19.32	-5:16:10.0	14.48	13.97	13.66	
638	35:19.33	-5:19:03.7	15.49	13.24	12.12	
639	35:19.38	-5:17:19.2	14.59	13.53	12.51	
640	35:19.48	-5:16:08.2	13.93	13.26	12.77	
641	35:19.52	-5:08:58.1	19.28	18.18	15.59	
642	35:19.58	-5:17:03.1	13.55	11.31	10.06†	0535195-051703
643	35:19.66	-5:02:28.8	14.54	13.82	13.50	0535196-050228
644	35:19.66	-5:13:26.5	13.61	11.55	10.24†	0535196-051326
645	35:19.67	-5:03:34.5	18.72	16.57	15.30	
646	35:19.74	-5:19:30.1	>21.03	13.23	11.27	
647	35:19.75	-5:04:54.3	18.13	>20.17	13.94	
648	35:19.80	-4:57:06.7	>21.06	16.83	14.86	
649	35:19.80	-5:14:05.4	13.52	13.10	12.68	0535197-051405
650	35:19.82	-5:15:35.4	17.65	14.95	12.35	
651	35:19.84	-5:15:09.0	13.00	11.43	10.26†	0535198-051508
652	35:19.98	-5:01:02.4	>21.05	18.28	14.20	
653	35:20.00	-5:18:46.6	13.91	12.04	12.09	
654	35:20.03	-5:12:50.5	13.87	11.96	11.17	0535200-051250
655	35:20.12	-4:58:40.2	19.20	16.74	16.25	
656	35:20.20	-5:15:59.5	14.55	12.94	12.26	
657	35:20.24	-5:13:16.2	9.89†	7.86†	6.49†	0535201-051315
658	35:20.25	-5:12:11.2	14.74	14.04	14.12	
659	35:20.25	-5:13:59.6	12.24	10.75†	9.88†	0535202-051359
660	35:20.36	-5:02:26.4	12.39	11.57	11.28	0535203-050226
661	35:20.42	-5:17:14.6	11.99	11.21†	10.43†	0535204-051714
662	35:20.44	-5:01:15.1	18.43	17.32	15.98	
663	35:20.45	-5:06:38.0	>21.18	17.87	15.62	
664	35:20.62	-5:03:00.7	18.44	14.47	11.94	
665	35:20.67	-5:09:02.9	14.19	13.17	12.70	0535206-050902
666	35:20.68	-5:01:54.2	13.16	12.35	12.20	0535206-050154
667	35:20.74	-5:19:26.6	15.93	14.66	11.78	
668	35:20.76	-5:15:49.4	9.90†	8.68†	8.08†	0535207-051549
669	35:20.77	-4:58:34.0	12.39	11.34	10.72†	0535207-045834
670	35:20.78	-5:13:23.4	15.11	14.03	13.40	
671	35:20.82	-4:57:16.9	16.28	13.91	12.74	0535208-045717
672	35:20.83	-5:02:57.7	19.49	16.28	13.60	
673	35:20.86	-4:56:53.0	>21.30	18.48	15.16	
674	35:20.99	-5:16:37.7	12.02	11.36	11.19	0535210-051637
675	35:21.07	-5:01:16.6	16.87	16.34	14.12	
676	35:21.09	-5:19:16.3	>21.78	>20.83	15.56	
677	35:21.15	-5:06:32.4	>21.23	18.56	15.31	
678	35:21.17	-5:18:21.4	12.85	11.97	11.57	0535211-051821
679	35:21.22	-5:06:47.8	>21.15	>20.20	15.39	
680	35:21.28	-5:09:16.2	8.38†	7.84†	7.31†	0535212-050916
681	35:21.32	-4:58:35.0	15.41	14.13	13.62	
682	35:21.32	-5:12:12.8	8.71†	8.11†	7.90†	0535213-051212
683	35:21.38	-5:12:44.4	15.91	15.20	14.63	
684	35:21.41	-5:09:42.3	13.74	12.89	12.57	0535213-050942
685	35:21.45	-4:57:18.8	20.51	17.02	15.77	
686	35:21.47	-5:09:03.7	12.27	11.32	<10.91	
687	35:21.47	-5:17:11.0	>21.46	>20.51	14.56	
688	35:21.50	-5:01:15.9	15.48	14.82	12.37	
689	35:21.52	-5:01:53.9	18.49	15.06	13.06	
690	35:21.59	-5:09:38.9	13.75	12.85	12.56	0535215-050938
691	35:21.60	-5:09:49.7	13.01	12.03	11.75	0535215-050949
692	35:21.63	-5:15:17.2	17.42	14.81	13.55	
693	35:21.65	-5:17:19.4	13.26	11.82	10.78†	0535216-051718
694	35:21.67	-5:17:17.0	13.22	11.83	<10.83	
695	35:21.69	-4:56:48.7	13.65	12.94	12.80	
696	35:21.74	-5:17:40.2	>21.20	>20.25	14.16	

(cont.)

(cont.)

ID	R.A. <sup>a</sup>	decl. <sup>a</sup>	$J^{bcd}$	$H^{bcd}$	$K^{cd}$	2MASS	ID	R.A. <sup>a</sup>	decl. <sup>a</sup>	$J^{bcd}$	$H^{bcd}$	$K^{cd}$	2MASS
697	35:21.76	-5:06:32.8	>21.18	17.30	14.77		736	35:23.22	-5:08:43.6	>21.11	14.94	13.10	
698	35:21.76	-5:17:27.8	>21.32	>20.37	15.58		737	35:23.24	-5:00:38.2	16.56	13.90	12.44	
699	35:21.77	-5:09:45.3	19.37	17.65	16.23		738	35:23.27	-5:13:48.3	15.35	14.29	13.53	
700	35:21.85	-4:55:21.8	20.53	19.61	17.31		739	35:23.27	-5:15:43.4	15.68	14.41	13.39	
701	35:21.88	-4:54:07.6	11.91	11.31	<10.68		740	35:23.30	-4:56:11.9	16.82	14.30	12.95	
702	35:21.88	-4:59:19.7	15.35	13.86	13.01		741	35:23.30	-4:57:20.7	12.90	12.05	11.92	
703	35:21.88	-5:07:01.9	11.27	10.00 <sup>†</sup>	9.40 <sup>†</sup>	0535218-050701	742	35:23.30	-5:03:23.4	17.01	14.35	12.85	
704	35:21.90	-5:18:12.0	17.22	16.66	14.62		743	35:23.33	-5:07:09.6	17.79	14.78	12.51	
705	35:21.91	-5:15:01.2	12.78	11.85	11.49	0535219-051501	744	35:23.35	-5:08:21.6	16.80	14.26	12.41	
706	35:21.94	-4:57:09.1	18.35	15.70	14.35		745	35:23.40	-5:12:03.1	15.96	15.03	12.47	
707	35:21.94	-5:08:03.7	13.05	12.03	11.58	0535219-050803	746	35:23.41	-5:18:50.6	11.32	10.54 <sup>†</sup>	10.23 <sup>†</sup>	0535234-051850
708	35:21.94	-5:17:04.4	12.19	11.81	11.65	0535219-051704	747	35:23.42	-5:01:28.7	>21.42	>20.47	16.17	
709	35:21.95	-5:14:27.7	11.79	11.36	11.31	0535219-051427	748	35:23.47	-5:10:51.7	11.17	11.06	10.40 <sup>†</sup>	0535234-051051
710	35:22.08	-5:00:14.1	20.75	17.25	16.13		749	35:23.48	-5:15:23.4	14.05	13.38	12.93	
711	35:22.08	-5:12:22.6	17.36	16.69	15.15		750	35:23.54	-5:18:57.0	11.89	11.14	11.18 <sup>†</sup>	0535235-051857
712	35:22.13	-5:18:57.6	>21.67	>20.72	14.17		751	35:23.59	-5:19:11.9	14.82	13.71	12.60	
713	35:22.23	-4:53:57.3	16.59	15.50	15.44		752	35:23.60	-5:19:30.2	14.97	13.83	12.28	
714	35:22.25	-5:00:39.0	18.22	17.03	14.99		753	35:23.65	-5:01:40.3	>21.02	18.18	14.94	
715	35:22.26	-5:18:08.8	13.20	12.49	11.98	0535222-051808	754	35:23.77	-5:18:39.8	12.53	11.62	10.90 <sup>†</sup>	0535237-051839
716	35:22.37	-5:07:39.2	14.47	12.05	10.46 <sup>†</sup>		755	35:23.82	-4:59:24.9	18.49	16.70	15.75	
717	35:22.37	-5:08:17.9	14.67	13.72	13.52		756	35:23.89	-5:18:20.9	17.02	13.95	12.20	
718	35:22.39	-5:17:32.9	14.55	12.98	12.01		757	35:23.92	-5:04:11.6	16.88	15.33	14.48	
719	35:22.42	-5:08:05.2	10.97 <sup>†</sup>	9.51 <sup>†</sup>	8.59 <sup>†</sup>	0535224-050805	758	35:23.92	-5:06:01.7	>20.88	17.96	14.38	
720	35:22.46	-5:09:11.1	11.44	11.12	10.62 <sup>†</sup>	0535224-050911	759	35:23.96	-5:07:53.4	18.29	16.64	15.26	
721	35:22.57	-5:08:00.7	11.26 <sup>†</sup>	9.78 <sup>†</sup>	9.21 <sup>†</sup>	0535225-050800	760	35:23.99	-5:19:07.4	12.92	12.14	11.80	0535239-051907
722	35:22.58	-4:59:05.3	17.46	16.02	15.39		761	35:24.00	-5:18:38.6	12.59	11.86	11.20	
723	35:22.60	-5:13:28.4	14.33	13.64	13.37	0535226-051328	762	35:24.06	-4:56:30.4	15.69	15.06	14.82	
724	35:22.63	-5:14:11.3	11.69	11.19	10.24 <sup>†</sup>	0535226-051411	763	35:24.06	-5:19:23.3	14.72	13.35	11.96	
725	35:22.67	-5:15:08.6	13.38	12.63	12.35	0535226-051508	764	35:24.09	-5:09:06.7	14.50	13.90	13.51	0535240-050906
726	35:22.71	-5:16:14.0	13.21	12.19	11.82	0535226-051613	765	35:24.14	-5:18:54.3	17.72	15.13	13.41	
727	35:22.75	-5:18:38.1	>21.25	16.67	12.80		766	35:24.14	-5:19:27.6	15.23	13.55	12.01	
728	35:22.89	-4:59:09.4	14.61	13.69	13.12		767	35:24.34	-5:01:20.5	>21.10	19.52	14.68	
729	35:22.93	-5:13:40.0	14.10	12.52	11.66	0535229-051339	768	35:24.38	-5:14:57.9	16.57	14.66	13.58	0535243-051457
730	35:22.99	-5:15:21.8	16.43	16.44	13.73		769	35:24.49	-5:16:59.8	11.65	10.75 <sup>†</sup>	10.18 <sup>†</sup>	0535244-051659
731	35:23.01	-5:17:45.2	>21.07	14.04	11.63		770	35:24.55	-5:00:21.1	18.00	15.88	14.07	
732	35:23.03	-5:14:39.5	>21.75	20.73	16.14		771	35:24.61	-5:11:58.3	11.29	10.96 <sup>†</sup>	10.41 <sup>†</sup>	0535246-051158
733	35:23.07	-5:11:50.3	15.88	14.27	13.20		772	35:24.63	-5:11:29.5	12.20	11.30	10.18 <sup>†</sup>	0535246-051129
734	35:23.08	-5:00:36.4	16.48	13.89	12.45		773	35:24.63	-5:19:33.2	16.14	13.21	11.47	
735	35:23.13	-5:13:43.6	13.02	11.33	10.49 <sup>†</sup>	0535231-051343	774	35:24.64	-5:06:25.9	16.95	15.16	13.89	

(cont.)

(cont.)

ID	R.A. <sup>a</sup>	decl. <sup>a</sup>	$J^{bcd}$	$H^{bcd}$	$K^{cd}$	2MASS	ID	R.A. <sup>a</sup>	decl. <sup>a</sup>	$J^{bcd}$	$H^{bcd}$	$K^{cd}$	2MASS
775	35:24.66	-5:19:09.5	11.86	10.99 <sup>†</sup>	10.29 <sup>†</sup>	0535246-051909	814	35:26.46	-4:59:51.9	16.69	14.21	12.89	
776	35:24.69	-5:09:26.4	17.01	15.11	13.55		815	35:26.49	-5:17:56.6	12.20	<10.86	<10.21	
777	35:24.72	-5:16:41.1	13.85	11.68	<10.38		816	35:26.51	-5:19:18.7	>21.18	>20.23	12.61	
778	35:24.74	-5:06:56.2	>21.27	>20.32	14.23		817	35:26.58	-4:58:25.3	20.52	16.46	14.51	
779	35:24.79	-5:10:29.5	<10.34	<8.79	<7.16		818	35:26.58	-5:17:53.1	12.11	12.38 <sup>†</sup>	11.36 <sup>†</sup>	0535265-051753
780	35:24.88	-5:06:21.5	16.08	12.93	11.07	0535248-050621	819	35:26.58	-5:19:08.3	18.17	>19.94	13.97	
781	35:24.94	-5:12:55.9	16.92	16.23	13.87		820	35:26.59	-4:56:06.7	11.85	11.32	10.93 <sup>†</sup>	0535265-045606
782	35:25.03	-5:09:09.4	14.60	13.96	13.49	0535250-050909	821	35:26.62	-5:03:54.6	14.89	12.12	<9.96	
783	35:25.03	-5:19:25.2	15.21	13.95	12.76		822	35:26.63	-5:18:18.6	16.06	16.08	14.53	
784	35:25.15	-5:06:30.7	>21.86	18.45	16.58		823	35:26.64	-4:55:02.5	16.78	15.56	15.03	0535266-045502
785	35:25.24	-5:15:35.7	11.72	10.81 <sup>†</sup>	10.09 <sup>†</sup>	0535252-051535	824	35:26.73	-5:16:45.2	13.11	12.28	11.87	0535267-051645
786	35:25.25	-5:09:27.5	11.82	11.25	11.03	0535252-050927	825	35:26.75	-5:14:44.5	15.07	14.39	14.19	0535267-051444
787	35:25.34	-5:12:05.7	14.09	13.19	12.93	0535253-051205	826	35:26.75	-5:19:02.8	16.15	14.06	12.70	
788	35:25.38	-5:16:36.1	16.39	16.17	15.55		827	35:26.87	-5:09:24.6	15.18	13.21	11.17	0535268-050924
789	35:25.42	-5:10:48.0	11.62	11.30	11.15	0535254-051048	828	35:26.87	-5:17:13.1	16.50	15.52	14.37	
790	35:25.44	-4:54:04.1	13.72	13.01	12.89	0535254-045403	829	35:26.94	-5:04:07.0	15.90	14.22	13.11	
791	35:25.56	-4:55:27.0	14.90	12.98	12.33	0535255-045526	830	35:26.94	-5:18:06.9	13.84	12.63	11.88	
792	35:25.64	-5:07:57.1	11.82 <sup>†</sup>	11.15 <sup>†</sup>	10.22 <sup>†</sup>	0535256-050757	831	35:26.96	-5:11:07.7	8.92 <sup>†</sup>	7.84 <sup>†</sup>	7.03 <sup>†</sup>	0535268-051107
793	35:25.66	-5:09:41.9	18.17	15.94	13.91		832	35:26.96	-5:15:37.2	>21.73	17.64	16.10	
794	35:25.66	-5:18:04.2	13.96	12.94	12.31		833	35:26.97	-5:10:17.4	13.23	10.93 <sup>†</sup>	8.73 <sup>†</sup>	0535269-051017
795	35:25.67	-4:57:18.3	13.33	12.59	12.40	0535256-045718	834	35:27.00	-5:13:14.5	10.55 <sup>†</sup>	10.26 <sup>†</sup>	10.17 <sup>†</sup>	0535269-051314
796	35:25.68	-5:00:28.4	18.50	16.77	15.98		835	35:27.01	-5:09:54.4	14.83	13.41	12.55	0535269-050954
797	35:25.70	-5:07:03.0	13.74	13.14	12.95	0535257-050703	836	35:27.06	-5:15:44.8	12.83	11.91	11.25	0535270-051544
798	35:25.73	-5:07:46.2	14.74	12.36	11.22	0535257-050746	837	35:27.18	-4:58:34.5	18.91	16.61	15.59	
799	35:25.75	-5:09:49.3	11.39	10.48 <sup>†</sup>	10.11 <sup>†</sup>	0535257-050949	838	35:27.21	-4:55:18.6	14.05	12.74	12.29	0535272-045518
800	35:25.76	-5:05:57.9	16.37	14.53	12.66		839	35:27.27	-5:05:27.2	17.52	16.54	15.61	
801	35:25.87	-5:07:56.4	11.14	11.00 <sup>†</sup>	10.09 <sup>†</sup>	0535258-050756	840	35:27.44	-5:02:42.4	16.87	13.34	11.04	
802	35:26.02	-5:19:12.9	>22.41	>21.46	18.22		841	35:27.44	-5:09:04.0	15.09	14.35	13.80	0535274-050903
803	35:26.06	-5:08:37.7	12.61 <sup>†</sup>	12.02 <sup>†</sup>	10.03 <sup>†</sup>	0535260-050837	842	35:27.45	-5:17:12.1	11.21	<10.36	<9.78	
804	35:26.16	-5:08:33.4	14.55	13.78	13.39		843	35:27.47	-5:17:09.8	11.20	10.24 <sup>†</sup>	9.53 <sup>†</sup>	0535274-051709
805	35:26.29	-5:08:39.9	10.10 <sup>†</sup>	9.60 <sup>†</sup>	9.35 <sup>†</sup>	0535262-050840	844	35:27.49	-5:09:44.3	11.66	10.51 <sup>†</sup>	9.83 <sup>†</sup>	0535274-050944
806	35:26.31	-5:15:11.4	10.25 <sup>†</sup>	9.85 <sup>†</sup>	9.80 <sup>†</sup>	0535263-051511	845	35:27.49	-5:11:50.1	16.27	15.16	13.45	
807	35:26.34	-5:17:44.7	15.16	14.58	13.75		846	35:27.53	-5:13:56.4	13.71	12.46	11.60	0535275-051356
808	35:26.36	-5:10:50.4	14.76	14.04	13.74	0535263-051050	847	35:27.53	-5:16:55.9	14.09	12.79	12.26	
809	35:26.38	-5:18:57.6	16.24	14.02	12.77		848	35:27.55	-5:18:19.3	14.72	13.06	12.17	
810	35:26.41	-5:16:12.5	13.31	11.91	11.15	0535264-051612	849	35:27.56	-5:10:08.6	16.73	14.27	12.36	
811	35:26.41	-5:16:37.9	14.79	13.87	13.00		850	35:27.59	-5:05:31.2	19.96	19.55	14.99	
812	35:26.44	-5:00:56.9	14.85	14.12	13.88	0535264-050057	851	35:27.64	-4:54:38.9	19.09	17.33	16.73	
813	35:26.45	-5:15:05.4	16.74	15.63	15.14		852	35:27.64	-5:09:32.9	13.65	<10.76	<9.14	

(cont.)

(cont.)

ID	R.A. <sup>a</sup>	decl. <sup>a</sup>	$J^{bcd}$	$H^{bcd}$	$K^{cd}$	2MASS	ID	R.A. <sup>a</sup>	decl. <sup>a</sup>	$J^{bcd}$	$H^{bcd}$	$K^{cd}$	2MASS
853	35:27.65	-5:18:00.7	13.15	12.08	11.64		892	35:29.14	-5:00:18.2	19.47	16.58	15.32	
854	35:27.66	-5:09:37.3	13.25	10.51†	8.94†	0535276-050937	893	35:29.17	-5:18:18.3	14.67	13.71	13.09	
855	35:27.67	-5:09:49.9	12.74	11.74	<10.60		894	35:29.37	-5:02:14.8	17.10	15.44	14.63	
856	35:27.75	-5:18:04.7	11.98	10.55†	9.94†	0535277-051804	895	35:29.37	-5:11:46.9	>22.20	>21.25	17.51	
857	35:27.81	-5:07:54.8	14.20	13.28	12.75	0535277-050754	896	35:29.44	-4:55:45.6	19.09	17.69	16.73	
858	35:27.86	-5:05:36.3	>20.99	16.26	13.37		897	35:29.45	-5:16:33.4	11.52	10.73†	10.44†	0535294-051633
859	35:27.93	-5:16:57.3	11.60	10.86†	10.56†	0535279-051657	898	35:29.45	-5:17:55.4	14.22	13.20	12.26	
860	35:27.94	-4:53:52.1	17.69	16.71	17.04		899	35:29.46	-5:18:45.6	13.94	12.26	10.09†	0535294-051845
861	35:27.97	-5:18:59.8	13.90	11.53	<10.25		900	35:29.51	-5:00:00.5	>21.44	20.19	16.25	
862	35:28.01	-5:19:14.0	>21.03	15.78	14.36		901	35:29.54	-5:17:47.1	>22.05	17.75	18.06	
863	35:28.05	-5:05:38.4	>21.13	17.06	14.49		902	35:29.55	-5:18:40.0	14.99	13.46	12.71	
864	35:28.05	-5:17:20.3	12.45	11.69	11.43	0535280-051720	903	35:29.56	-4:59:56.7	18.00	17.21	16.07	
865	35:28.06	-5:01:35.1	19.33	14.97	12.18		904	35:29.79	-4:56:11.7	>21.50	>20.55	16.53	
866	35:28.14	-5:18:57.0	13.36	11.03	9.68†	0535281-051857	905	35:29.82	-5:16:06.3	11.98	11.26	10.94†	0535298-051606
867	35:28.15	-5:10:13.9	11.03	10.19†	9.48†	0535281-051013	906	35:29.90	-5:18:53.0	16.14	13.70	12.19	
868	35:28.17	-5:00:49.8	12.53	11.74	11.51	0535281-050049	907	35:29.91	-5:12:10.3	12.64	12.08	11.85	0535299-051210
869	35:28.17	-5:15:50.9	14.06	12.54	11.78		908	35:29.93	-4:57:08.2	14.25	12.35	11.60	0535299-045708
870	35:28.19	-5:03:41.3	20.45	16.61	11.84		909	35:29.93	-5:08:20.2	>20.63	15.57	13.12	
871	35:28.19	-5:11:37.6	12.96	11.87	11.55	0535281-051137	910	35:30.00	-5:12:27.4	12.06	11.43	10.86†	0535299-051227
872	35:28.19	-5:16:01.4	14.70	14.16	13.15		911	35:30.07	-5:19:06.4	17.64	16.37	15.14	
873	35:28.26	-4:58:38.4	>21.06	14.14	11.39		912	35:30.11	-5:09:09.5	13.75	13.24	13.20	0535301-050909
874	35:28.30	-4:55:42.1	17.33	15.79	14.98		913	35:30.15	-5:14:18.5	13.03	12.00	11.35	0535301-051418
875	35:28.36	-5:17:54.4	13.52	12.36	11.93	0535283-051754	914	35:30.22	-5:16:57.5	16.83	15.90	15.04	
876	35:28.36	-5:18:23.0	12.34	11.64	11.46	0535283-051823	915	35:30.23	-5:08:19.1	>20.74	15.79	13.52	
877	35:28.40	-4:58:07.2	14.65	13.88	13.67	0535283-045807	916	35:30.26	-5:09:32.3	17.07	16.03	14.21	
878	35:28.41	-5:07:44.1	16.22	13.07	11.11		917	35:30.28	-4:55:53.9	18.00	16.27	15.42	
879	35:28.43	-5:19:02.0	13.23	12.59	12.22	0535284-051902	918	35:30.29	-5:13:52.6	13.29	11.66	10.70†	0535302-051352
880	35:28.44	-4:53:57.0	17.46	16.42	15.95		919	35:30.36	-5:18:05.6	14.26	13.36	13.09	
881	35:28.46	-4:57:16.9	>21.66	18.34	16.67		920	35:30.46	-5:19:00.7	15.10	13.39	12.33	
882	35:28.52	-5:07:46.9	16.23	13.05	11.09		921	35:30.48	-5:19:33.9	13.94	12.03	<10.40	
883	35:28.60	-4:55:03.8	11.05	10.54†	10.38†	0535286-045503	922	35:30.53	-5:17:15.2	14.01	12.68	12.15	
884	35:28.60	-5:05:44.6	15.04	12.50	10.81†	0535285-050544	923	35:30.54	-5:03:34.5	15.42	13.67	12.75	0535305-050334
885	35:28.66	-5:02:44.8	15.49	13.83	12.99	0535286-050244	924	35:30.59	-4:57:21.5	14.77	14.01	13.74	0535305-045721
886	35:28.71	-5:19:25.7	18.58	15.86	15.62		925	35:30.61	-4:59:36.0	14.36	11.65	10.48†	0535306-045936
887	35:28.87	-4:57:39.3	18.00	14.98	13.11		926	35:30.63	-5:15:16.2	13.65	13.11	12.88	0535306-051516
888	35:28.88	-4:54:36.1	18.68	16.39	15.11		927	35:30.65	-5:04:11.1	18.32	16.47	15.02	
889	35:28.93	-4:54:20.6	14.93	13.91	13.34	0535289-045420	928	35:30.70	-5:18:07.0	12.38	11.40	10.98†	0535307-051807
890	35:28.94	-5:16:18.4	11.22	10.37†	9.63†	0535289-051618	929	35:30.72	-5:03:35.5	15.35	13.61	12.75	0535307-050335
891	35:29.04	-5:06:04.0	11.93	11.41	11.12	0535290-050604	930	35:30.73	-4:55:49.8	18.66	16.92	16.51	

(cont.)

(cont.)

ID	R.A. <sup>a</sup>	decl. <sup>a</sup>	$J^{bcd}$	$H^{bcd}$	$K^{cd}$	2MASS	ID	R.A. <sup>a</sup>	decl. <sup>a</sup>	$J^{bcd}$	$H^{bcd}$	$K^{cd}$	2MASS
931	35:30.80	-4:54:43.7	16.89	15.23	14.54		970	35:32.03	-5:08:34.9	17.13	15.86	15.32	
932	35:30.80	-4:58:13.6	17.83	14.50	12.78		971	35:32.04	-4:56:42.4	16.08	14.79	14.24	0535320-045642
933	35:30.89	-4:55:17.9	11.87	11.36	10.68†	0535308-045517	972	35:32.10	-5:00:23.7	15.57	13.91	13.06	0535321-050023
934	35:30.91	-5:18:17.8	11.54	10.80†	10.46†	0535309-051817	973	35:32.19	-5:11:57.8	12.63	11.92	11.54	0535321-051157
935	35:30.97	-5:04:44.1	18.65	16.77	15.46		974	35:32.20	-5:16:03.6	12.52	12.04	11.70	
936	35:31.03	-4:57:20.0	12.27	11.50	11.28	0535310-045720	975	35:32.31	-5:16:26.8	14.00	12.92	12.51	
937	35:31.04	-5:18:07.6	16.56	15.84	16.24		976	35:32.34	-5:11:43.3	14.92	12.67	11.57	0535323-051143
938	35:31.04	-5:18:44.9	13.26	12.37	11.87	0535310-051845	977	35:32.34	-5:18:07.7	11.53	10.67†	10.30†	0535323-051807
939	35:31.07	-5:04:15.0	11.51	11.01	10.41†		978	35:32.36	-4:58:29.9	17.18	14.54	13.10	
940	35:31.13	-5:15:13.9	15.79	15.33	15.62		979	35:32.38	-5:12:53.0	16.61	16.22	16.39	
941	35:31.14	-4:54:15.2	9.15†	9.20†	9.22†	0535311-045415	980	35:32.39	-5:12:10.8	19.48	18.40	17.13	
942	35:31.14	-5:13:43.8	16.40	14.14	13.03	0535311-051343	981	35:32.43	-5:14:24.6	12.68	11.66	11.43	0535324-051424
943	35:31.20	-4:57:27.1	14.92	13.00	12.03	0535312-045727	982	35:32.44	-5:15:06.7	13.61	12.25	11.45	0535324-051506
944	35:31.21	-5:12:27.9	12.94	12.33	12.16	0535312-051228	983	35:32.53	-5:01:57.2	15.39	13.60	12.65	0535325-050157
945	35:31.22	-5:19:31.8	14.28	13.21	12.63		984	35:32.54	-5:02:09.8	14.86	14.12	13.76	0535325-050209
946	35:31.26	-5:15:10.7	15.14	14.12	13.83		985	35:32.62	-5:05:37.9	15.74	14.84	14.32	0535326-050538
947	35:31.27	-5:18:55.7	10.80†	10.07†	9.58†	0535312-051855	986	35:32.64	-4:56:52.7	18.45	17.21	16.33	
948	35:31.29	-5:15:32.9	10.07†	9.28†	8.93†	0535312-051533	987	35:32.64	-5:15:51.2	13.49	12.42	11.99	0535326-051551
949	35:31.33	-5:12:01.5	14.53	13.95	13.61	0535313-051201	988	35:32.72	-5:12:00.7	15.52	14.12	12.80	
950	35:31.44	-5:16:03.4	5.84†	5.64†	5.56†	0535313-051602	989	35:32.81	-5:17:38.5	13.36	12.28	11.78	0535328-051738
951	35:31.48	-4:57:47.7	16.88	15.07	14.14	0535314-045747	990	35:32.84	-5:18:19.8	13.90	12.44	11.62	
952	35:31.51	-5:05:01.6	12.16	11.57	10.77†	0535315-050501	991	35:32.90	-5:16:30.2	15.67	17.92	13.98	
953	35:31.54	-5:05:47.2	11.83	9.77†	8.28†	0535315-050547	992	35:32.92	-5:16:05.3	11.31	10.50†	10.16†	0535329-051605
954	35:31.54	-5:14:44.7	>21.33	15.97	15.55		993	35:32.93	-5:02:46.8	17.58	15.60	14.51	
955	35:31.55	-5:16:36.8	12.59	11.58	10.85†	0535315-051636	994	35:32.95	-4:57:54.2	18.03	16.25	15.59	
956	35:31.58	-5:15:23.4	13.00	12.07	11.74	0535315-051523	995	35:32.96	-5:12:04.8	13.27	11.52	10.55†	0535329-051204
957	35:31.59	-4:54:37.4	14.88	13.40	12.74	0535316-045437	996	35:32.96	-5:16:40.1	14.52	13.98	13.07	
958	35:31.59	-5:06:25.0	17.22	16.52	14.95		997	35:33.02	-5:17:39.2	14.51	13.26	12.54	
959	35:31.61	-5:19:27.5	>21.29	14.48	13.09		998	35:33.10	-5:13:38.7	>20.85	>19.90	13.92	
960	35:31.62	-5:16:58.1	12.98	11.72	11.25	0535316-051658	999	35:33.12	-5:17:34.0	12.84	12.17	11.85	0535331-051733
961	35:31.64	-5:00:14.0	14.11	11.53	9.96†	0535316-050014	1000	35:33.17	-5:14:10.6	12.20	11.47	11.06	0535331-051410
962	35:31.64	-5:03:46.1	18.52	16.24	15.38		1001	35:33.21	-5:16:05.4	11.45	10.74†	9.82†	0535331-051605
963	35:31.75	-5:16:39.8	12.80	11.86	11.32	0535317-051639	1002	35:33.34	-5:11:45.6	17.54	16.58	15.32	
964	35:31.76	-5:14:52.2	11.38	10.03†	9.47†	0535317-051452	1003	35:33.43	-4:56:54.5	17.67	16.44	16.02	
965	35:31.97	-5:09:27.9	9.37†	8.54†	8.09†	0535319-050927	1004	35:33.44	-5:08:45.1	>21.31	20.12	15.20	
966	35:31.98	-5:15:59.5	11.64	11.03	<10.68		1005	35:33.45	-4:56:01.7	13.03	12.33	12.09	0535334-045601
967	35:32.00	-5:16:20.0	12.56	12.58	11.56	0535319-051620	1006	35:33.49	-5:05:00.9	19.23	15.91	14.19	
968	35:32.01	-4:55:35.7	13.94	13.24	13.02	0535320-045535	1007	35:33.58	-4:55:17.9	18.29	17.84	16.25	
969	35:32.02	-5:08:05.8	14.14	12.90	12.76	0535320-050805	1008	35:33.59	-5:15:23.2	13.13	11.84	11.42	0535335-051523

(cont.)

(cont.)



ID	R.A. <sup>a</sup>	decl. <sup>a</sup>	$J^{bcd}$	$H^{bcd}$	$K^{cd}$	2MASS	ID	R.A. <sup>a</sup>	decl. <sup>a</sup>	$J^{bcd}$	$H^{bcd}$	$K^{cd}$	2MASS
1009	35:33.63	-5:00:42.0	12.01	11.30	11.03	0535336-050042	1048	35:36.05	-5:13:17.1	15.97	14.77	13.81	
1010	35:33.65	-5:03:08.0	13.29	11.77	10.89†	0535336-050308	1049	35:36.21	-5:04:55.8	13.26	11.76	11.12	0535362-050455
1011	35:33.68	-4:57:20.9	18.10	16.72	16.10		1050	35:36.26	-5:14:30.2	15.10	14.49	13.77	
1012	35:33.80	-4:55:00.2	13.11	12.09	11.69	0535338-045500	1051	35:36.42	-5:01:15.5	10.93†	10.07†	9.56†	0535364-050115
1013	35:33.83	-5:04:27.5	13.82	11.82	10.53†	0535338-050427	1052	35:36.44	-5:09:11.5	16.63	15.89	15.41	
1014	35:33.84	-5:17:10.8	14.40	13.27	12.82	0535338-051710	1053	35:36.48	-5:15:32.3	>21.51	16.71	15.55	
1015	35:33.88	-5:09:06.2	13.96	13.40	13.22	0535338-050905	1054	35:36.57	-5:04:39.2	12.05	11.30	11.15	0535365-050439
1016	35:33.88	-5:15:54.4	14.27	12.96	12.32	0535338-051554	1055	35:36.57	-5:12:31.0	15.77	15.32	14.56	
1017	35:33.92	-5:03:33.5	12.54	11.97	11.74	0535339-050333	1056	35:36.58	-4:58:40.6	17.64	16.53	16.11	
1018	35:34.00	-4:53:57.6	13.48	12.08	11.61	0535340-045357	1057	35:36.67	-5:18:50.7	14.14	13.27	12.80	0535366-051850
1019	35:34.03	-4:54:11.0	12.73	12.04	11.88	0535340-045411	1058	35:36.68	-5:04:14.4	11.98	11.31	10.87†	0535366-050414
1020	35:34.08	-5:17:09.5	15.36	14.47	14.26		1059	35:36.69	-4:57:29.9	13.61	12.38	11.92	0535366-045730
1021	35:34.29	-5:06:21.2	9.31†	9.33†	9.31†	0535342-050621	1060	35:36.72	-4:56:44.7	18.74	16.79	15.43	
1022	35:34.42	-5:18:38.4	15.23	13.66	12.42		1061	35:36.74	-5:10:00.4	13.13	12.43	11.97	0535367-051000
1023	35:34.46	-5:03:30.7	17.73	16.63	16.21		1062	35:36.87	-4:58:05.0	13.73	12.21	11.64	0535368-045805
1024	35:34.50	-5:00:52.4	16.28	13.69	11.28	0535345-050052	1063	35:36.89	-5:18:21.6	>21.55	18.84	14.64	
1025	35:34.52	-5:13:07.7	14.32	13.74	13.58	0535345-051307	1064	35:36.95	-5:03:26.2	21.10	>20.73	16.43	
1026	35:34.58	-5:19:05.5	15.89	14.33	13.08		1065	35:36.95	-5:04:05.3	17.02	15.84	15.19	
1027	35:34.59	-4:57:52.8	18.56	16.93	15.64		1066	35:36.97	-5:05:26.2	14.58	14.06	13.70	0535369-050526
1028	35:34.62	-5:15:52.8	12.98	12.33	11.71	0535346-051552	1067	35:37.06	-5:18:58.6	20.98	18.74	16.60	
1029	35:34.80	-5:15:31.2	14.13	12.94	12.29	0535348-051531	1068	35:37.16	-5:10:29.5	12.47	11.81	11.64	0535371-051029
1030	35:34.98	-5:12:30.2	14.50	13.83	12.85		1069	35:37.18	-4:56:53.7	>21.64	>20.69	17.39	
1031	35:35.04	-5:11:09.2	14.16	13.40	12.91	0535350-051109	1070	35:37.33	-5:02:36.3	15.27	13.16	12.10	0535373-050236
1032	35:35.20	-5:00:14.7	18.10	15.92	15.55		1071	35:37.45	-4:58:26.8	11.69	10.01†	9.19†	0535374-045826
1033	35:35.28	-4:58:02.2	18.40	16.61	15.68		1072	35:37.59	-5:04:47.1	17.66	14.88	13.22	
1034	35:35.34	-5:05:24.9	17.22	15.08	13.89		1073	35:37.70	-5:06:31.9	12.96	12.25	12.10	0535376-050631
1035	35:35.35	-5:11:11.5	12.61	12.05	11.88	0535353-051111	1074	35:37.89	-5:03:46.2	17.42	15.77	15.20	0535378-050346
1036	35:35.40	-5:08:46.9	13.84	13.09	12.87	0535353-050846	1075	35:38.01	-4:57:13.5	18.79	16.98	16.46	
1037	35:35.45	-5:07:53.1	16.31	14.28	13.07	0535354-050753	1076	35:38.01	-5:03:29.8	17.46	16.05	15.64	
1038	35:35.55	-5:06:58.6	13.28	12.68	12.53	0535355-050658	1077	35:38.03	-5:19:26.7	17.55	16.59	15.96	
1039	35:35.60	-5:15:43.2	11.66	10.96†	10.64†	0535356-051543	1078	35:38.10	-5:18:11.1	11.53	9.78†	8.86†	0535381-051811
1040	35:35.68	-5:10:51.0	14.13	13.64	13.36	0535356-051050	1079	35:38.13	-4:55:41.0	14.26	13.11	12.65	
1041	35:35.77	-4:56:27.6	16.93	15.51	15.05		1080	35:38.19	-4:56:37.0	>21.54	>20.59	16.73	
1042	35:35.79	-5:12:20.5	9.79†	9.84†	9.76†	0535357-051220	1081	35:38.19	-5:03:33.7	15.76	14.92	14.51	0535382-050333
1043	35:35.93	-5:12:06.8	18.41	17.06	16.92		1082	35:38.22	-5:14:18.8	11.58	11.01	10.56†	0535382-051418
1044	35:35.97	-5:11:01.0	19.93	17.39	16.26		1083	35:38.32	-4:58:01.2	16.18	14.81	14.31	
1045	35:35.98	-5:02:12.6	18.14	16.66	16.04		1084	35:38.45	-5:10:08.9	14.82	14.36	14.13	0535384-051009
1046	35:36.01	-5:12:25.2	11.20†	9.57†	8.47†	0535360-051225	1085	35:38.51	-5:04:51.4	16.33	13.69	11.95	0535385-050451
1047	35:36.02	-4:57:41.6	14.47	13.73	13.47	0535360-045741	1086	35:38.53	-4:59:41.0	12.05	11.10	<10.44	

(cont.)

(cont.)

ID	R.A. <sup>a</sup>	decl. <sup>a</sup>	$J^{bcd}$	$H^{bcd}$	$K^{cd}$	2MASS	ID	R.A. <sup>a</sup>	decl. <sup>a</sup>	$J^{bcd}$	$H^{bcd}$	$K^{cd}$	2MASS
1087	35:38.57	-5:08:03.2	15.91	13.46	12.01	0535385-050803	1126	35:40.65	-5:19:33.0	15.35	15.56	14.81	
1088	35:38.58	-5:07:31.1	17.86	16.89	16.76		1127	35:40.68	-5:01:53.3	19.32	17.28	16.29	
1089	35:38.65	-5:09:56.6	12.98	12.47	12.22	0535386-050956	1128	35:40.68	-5:03:56.1	14.79	13.36	12.71	0535406-050356
1090	35:38.72	-5:16:58.9	13.44	12.21	11.53	0535387-051659	1129	35:40.77	-5:12:47.9	13.29	12.17	11.64	0535407-051247
1091	35:38.75	-5:04:55.4	14.95	12.91	11.94	0535387-050455	1130	35:40.78	-5:09:01.6	10.36 <sup>†</sup>	9.43 <sup>†</sup>	9.09 <sup>†</sup>	0535407-050901
1092	35:38.79	-5:11:19.9	17.78	16.48	15.82		1131	35:40.78	-5:11:11.9	13.67	13.09	12.74	0535407-051111
1093	35:38.82	-4:57:10.2	16.12	14.98	14.62		1132	35:40.80	-5:18:39.1	16.80	15.84	14.95	
1094	35:38.83	-5:12:15.3	15.40	14.86	14.84	0535388-051215	1133	35:40.86	-5:18:32.6	16.50	15.81	15.29	
1095	35:38.86	-5:12:41.8	10.87 <sup>†</sup>	9.72 <sup>†</sup>	9.02 <sup>†</sup>	0535388-051241	1134	35:40.96	-5:16:57.5	15.97	15.31	15.12	
1096	35:38.98	-5:19:14.6	>21.93	17.56	16.32		1135	35:41.05	-5:06:25.3	12.55	11.89	11.67	0535410-050625
1097	35:39.03	-5:07:04.2	12.52	11.97	11.79	0535390-050704	1136	35:41.10	-5:09:55.8	17.10	16.59	16.00	
1098	35:39.08	-5:08:56.3	10.87 <sup>†</sup>	10.20 <sup>†</sup>	10.00 <sup>†</sup>	0535390-050856	1137	35:41.29	-5:03:52.2	14.17	12.92	12.43	0535413-050352
1099	35:39.16	-5:12:20.2	13.72	12.74	12.27	0535391-051220	1138	35:41.35	-5:16:41.3	16.81	16.07	15.21	
1100	35:39.20	-5:16:35.5	14.12	12.31	11.36	0535392-051635	1139	35:41.38	-5:04:38.8	17.04	15.70	14.93	
1101	35:39.27	-5:13:50.9	18.14	17.41	15.06		1140	35:41.38	-5:12:58.9	11.31	10.61 <sup>†</sup>	10.38 <sup>†</sup>	0535413-051258
1102	35:39.29	-5:18:31.7	>21.45	>20.50	16.55		1141	35:41.42	-5:16:44.9	16.88	16.09	15.40	
1103	35:39.68	-5:12:08.2	>21.07	>20.12	15.03		1142	35:41.57	-5:16:05.5	15.10	14.21	14.06	0535415-051605
1104	35:39.73	-5:01:54.0	>21.09	15.62	14.18		1143	35:41.63	-4:56:53.9	12.64	11.87	11.85	0535416-045653
1105	35:39.84	-5:15:49.4	14.01	12.89	12.42	0535398-051549	1144	35:41.74	-5:03:29.0	13.41	12.66	12.55	0535417-050329
1106	35:39.92	-4:57:31.3	<10.95	<10.32	<9.93		1145	35:41.74	-5:05:19.8	15.37	13.77	12.82	0535417-050519
1107	35:39.93	-4:58:39.1	12.82	11.99	11.82		1146	35:41.77	-4:58:13.9	17.95	16.52	15.92	
1108	35:39.97	-5:06:36.7	12.48	11.47	10.91 <sup>†</sup>	0535399-050636	1147	35:41.85	-5:01:25.6	15.61	14.45	14.08	0535418-050125
1109	35:40.01	-5:02:36.9	14.12	13.45	13.16	0535400-050236	1148	35:41.99	-5:17:36.4	18.17	17.01	16.63	
1110	35:40.03	-4:57:28.9	11.06	<10.38	<9.97		1149	35:42.01	-5:10:11.5	11.46	10.16 <sup>†</sup>	9.50 <sup>†</sup>	0535420-051011
1111	35:40.04	-5:11:38.2	16.71	14.97	14.49		1150	35:42.04	-5:16:11.2	17.89	16.91	16.75	
1112	35:40.17	-5:09:56.0	18.34	15.51	14.88		1151	35:42.07	-5:12:59.4	13.37	12.81	12.51	0535420-051259
1113	35:40.17	-5:16:25.8	>20.88	14.62	14.13		1152	35:42.16	-5:19:09.3	17.89	16.96	15.86	
1114	35:40.19	-5:16:32.0	15.58	13.67	13.17	0535402-051631	1153	35:42.28	-5:15:59.3	16.86	15.44	14.91	
1115	35:40.20	-5:17:29.1	10.35 <sup>†</sup>	9.53 <sup>†</sup>	9.01 <sup>†</sup>	0535401-051729	1154	35:42.29	-5:15:08.0	13.55	12.08	11.60	0535422-051507
1116	35:40.25	-5:15:47.5	>20.89	14.35	14.04		1155	35:42.35	-5:11:57.4	15.19	14.73	14.54	
1117	35:40.29	-5:13:36.8	15.97	14.15	13.65		1156	35:42.50	-5:12:38.2	15.35	14.70	13.89	
1118	35:40.32	-5:03:05.5	16.79	15.31	14.78		1157	35:42.52	-4:59:40.1	12.58	11.83	11.79	0535425-045940
1119	35:40.34	-5:12:31.9	15.97	14.79	14.37	0535403-051232	1158	35:42.61	-5:01:03.4	15.77	14.38	13.89	0535426-050103
1120	35:40.38	-4:55:44.0	13.28	12.39	12.03		1159	35:42.69	-5:10:16.3	14.64	14.13	13.73	0535426-051016
1121	35:40.53	-4:59:12.8	15.76	15.08	14.84		1160	35:42.69	-5:10:49.1	19.76	17.17	16.24	
1122	35:40.56	-5:03:04.6	16.41	14.99	14.52	0535405-050304	1161	35:42.77	-5:11:54.7	11.20	10.47 <sup>†</sup>	10.28 <sup>†</sup>	0535427-051154
1123	35:40.62	-5:12:19.3	12.95	12.21	11.99	0535406-051219	1162	35:42.97	-4:57:43.5	13.62	12.85	12.44	0535429-045743
1124	35:40.63	-5:13:20.6	16.92	16.11	16.06		1163	35:42.97	-5:19:05.8	18.82	16.97	16.16	
1125	35:40.63	-5:19:02.6	>21.13	16.06	14.31		1164	35:43.06	-5:03:07.3	13.32	12.62	12.39	0535430-050307

(cont.)

(cont.)

ID	R.A. <sup>a</sup>	decl. <sup>a</sup>	$J^{bcd}$	$H^{bcd}$	$K^{cd}$	2MASS	ID	R.A. <sup>a</sup>	decl. <sup>a</sup>	$J^{bcd}$	$H^{bcd}$	$K^{cd}$	2MASS
1165	35:43.11	-5:13:46.8	10.19 <sup>†</sup>	9.89 <sup>†</sup>	9.78 <sup>†</sup>	0535431-051346	1204	35:45.62	-5:18:42.6	15.22	13.83	14.24	0535456-051842
1166	35:43.20	-4:58:23.3	13.76	13.03	12.78	0535431-045823	1205	35:45.63	-5:13:36.0	13.30	12.25	11.67	0535456-051336
1167	35:43.25	-5:09:17.0	10.78 <sup>†</sup>	10.08 <sup>†</sup>	9.88 <sup>†</sup>	0535432-050917	1206	35:45.70	-5:14:05.4	18.67	16.52	15.35	
1168	35:43.55	-5:05:41.3	11.96	11.48	10.38 <sup>†</sup>	0535435-050541	1207	35:45.71	-5:10:55.3	13.54	13.03	12.68	0535457-051055
1169	35:43.55	-5:08:49.4	15.95	14.90	14.26	0535435-050849	1208	35:45.97	-5:16:09.9	17.08	15.40	14.04	
1170	35:43.58	-5:09:33.9	16.28	15.26	14.92	0535435-050933	1209	35:46.02	-4:55:31.9	15.16	13.98	13.78	0535460-045532
1171	35:43.63	-5:01:52.8	>21.29	16.89	15.99		1210	35:46.07	-5:17:49.4	12.34	11.56	11.06	0535460-051749
1172	35:43.64	-4:56:54.0	20.18	>20.76	16.23		1211	35:46.10	-5:12:24.3	18.08	16.30	14.77	
1173	35:43.65	-5:17:28.7	15.20	14.08	13.64		1212	35:46.11	-4:56:41.0	17.39	16.15	15.69	
1174	35:43.66	-5:07:07.5	17.82	16.87	16.09		1213	35:46.13	-5:10:51.8	12.02	11.23	10.62 <sup>†</sup>	0535461-051051
1175	35:43.66	-5:17:25.5	14.27	13.20	12.79	0535436-051725	1214	35:46.14	-5:00:43.4	16.68	15.45	15.16	0535461-050043
1176	35:43.80	-5:14:39.1	14.37	13.47	13.16	0535437-051439	1215	35:46.20	-4:58:49.5	15.20	14.07	13.70	0535462-045849
1177	35:43.81	-5:09:58.7	13.61	13.07	12.71	0535438-050958	1216	35:46.24	-5:15:39.8	12.64	11.53	10.98 <sup>†</sup>	0535462-051539
1178	35:43.93	-5:14:04.8	18.45	17.19	16.53		1217	35:46.26	-5:16:25.4	>21.37	19.05	15.92	
1179	35:43.96	-5:03:42.9	14.86	13.63	13.09	0535439-050343	1218	35:46.31	-5:13:24.3	16.52	15.40	15.04	
1180	35:44.03	-4:56:18.5	15.56	14.54	13.90	0535440-045618	1219	35:46.48	-4:58:17.8	15.33	14.24	13.94	0535464-045817
1181	35:44.09	-5:08:37.5	14.63	13.19	11.86	0535440-050837	1220	35:46.49	-4:57:54.8	16.59	15.51	15.29	0535465-045755
1182	35:44.09	-5:12:56.5	17.36	16.33	16.22		1221	35:46.56	-5:03:41.3	16.37	15.17	14.65	0535465-050341
1183	35:44.35	-4:57:16.8	13.23	12.49	12.25	0535443-045716	1222	35:46.57	-5:05:33.4	18.25	16.39	15.24	
1184	35:44.50	-5:07:31.6	12.07	11.60	11.30	0535445-050731	1223	35:46.62	-5:15:55.5	20.34	15.90	15.59	
1185	35:44.53	-5:08:56.3	16.12	14.93	14.18	0535445-050856	1224	35:46.67	-5:17:29.0	16.52	14.43	14.33	
1186	35:44.59	-4:56:24.8	16.81	15.58	15.37	0535446-045625	1225	35:46.82	-5:16:46.8	12.77	11.88	11.55	0535468-051646
1187	35:44.61	-4:59:57.6	14.92	14.26	14.01	0535446-045957	1226	35:46.90	-5:10:43.3	14.12	13.22	12.89	0535469-051043
1188	35:44.70	-5:00:39.6	14.00	13.13	12.89	0535447-050039	1227	35:47.01	-5:16:14.1	15.22	14.52	13.88	
1189	35:44.71	-4:58:35.3	16.18	15.01	14.65	0535447-045835	1228	35:47.02	-5:06:13.2	16.22	15.31	14.96	0535470-050612
1190	35:44.79	-4:58:12.4	18.62	16.83	15.90		1229	35:47.09	-5:14:42.5	15.26	14.10	13.59	
1191	35:44.86	-5:07:16.8	10.09 <sup>†</sup>	9.45 <sup>†</sup>	9.17 <sup>†</sup>	0535448-050716	1230	35:47.17	-5:00:44.9	16.16	15.39	15.13	0535471-050044
1192	35:44.93	-4:57:01.4	16.12	15.40	14.80	0535449-045701	1231	35:47.20	-5:16:43.2	16.27	15.94	15.85	
1193	35:44.95	-5:15:20.1	14.43	13.39	13.10	0535449-051520	1232	35:47.25	-5:17:43.1	12.15	11.64	11.33	
1194	35:44.99	-4:56:02.8	13.57	12.63	12.39	0535450-045602	1233	35:47.39	-5:13:18.5	11.58	11.03 <sup>†</sup>	10.84 <sup>†</sup>	0535473-051318
1195	35:45.07	-5:13:55.4	16.70	15.34	15.36		1234	35:47.42	-5:10:28.5	11.17	10.88 <sup>†</sup>	10.47 <sup>†</sup>	0535474-051028
1196	35:45.12	-5:17:27.3	17.34	16.38	16.36		1235	35:47.47	-5:00:46.9	17.69	16.58	16.01	
1197	35:45.19	-5:00:47.6	17.01	15.85	15.53		1236	35:47.48	-5:14:30.4	17.51	16.25	15.35	
1198	35:45.24	-5:07:09.1	15.94	15.02	14.43	0535452-050709	1237	35:47.50	-5:16:57.8	10.42 <sup>†</sup>	10.06 <sup>†</sup>	9.93 <sup>†</sup>	0535475-051657
1199	35:45.32	-5:19:08.3	15.69	13.82	12.92	0535453-051908	1238	35:47.54	-5:07:10.0	16.16	14.95	14.57	0535475-050709
1200	35:45.38	-5:10:11.9	16.30	14.67	13.90	0535453-051012	1239	35:47.54	-5:12:18.1	12.88	12.23	12.21	0535475-051218
1201	35:45.48	-5:09:45.9	>21.90	>20.95	16.95		1240	35:47.79	-5:10:30.8	10.18 <sup>†</sup>	9.64 <sup>†</sup>	9.40 <sup>†</sup>	0535477-051030
1202	35:45.58	-5:18:02.9	13.07	13.80	13.04		1241	35:47.83	-4:58:54.6	17.95	16.38	15.91	
1203	35:45.61	-5:18:13.3	12.55	11.52	11.37	0535456-051813	1242	35:47.83	-5:13:17.7	13.29	12.08	11.70	0535478-051317

(cont.)

(cont.)

ID	R.A. <sup>a</sup>	decl. <sup>a</sup>	$J^{bcd}$	$H^{bcd}$	$K^{cd}$	2MASS	ID	R.A. <sup>a</sup>	decl. <sup>a</sup>	$J^{bcd}$	$H^{bcd}$	$K^{cd}$	2MASS
1243	35:48.01	-5:08:11.6	15.09	13.61	12.78	0535480-050811	1282	35:51.49	-5:17:22.6	18.49	17.31	16.57	
1244	35:48.11	-5:15:24.7	17.39	16.42	15.92		1283	35:51.55	-4:57:11.7	19.45	17.98	16.07	
1245	35:48.26	-5:11:10.3	12.79	11.95	11.66	0535482-051110	1284	35:51.56	-5:09:01.9	14.97	14.14	13.83	0535515-050901
1246	35:48.32	-4:57:42.7	15.50	14.25	13.83	0535483-045742	1285	35:51.56	-5:15:09.5	16.79	16.19	16.02	
1247	35:48.39	-5:01:28.7	12.24	11.39	10.21†	0535483-050128	1286	35:51.64	-5:08:09.0	10.05†	9.42†	9.24†	0535516-050809
1248	35:48.39	-5:08:52.6	17.59	16.40	16.05		1287	35:51.78	-5:17:39.2	13.44	12.68	12.33	0535517-051739
1249	35:48.50	-5:15:35.7	17.07	16.18	16.14		1288	35:51.82	-4:58:45.2	18.65	17.21	16.33	
1250	35:48.55	-5:15:21.1	15.18	14.39	14.15	0535485-051521	1289	35:51.84	-5:15:30.5	14.80	14.14	13.93	0535518-051530
1251	35:48.59	-5:17:42.6	14.56	13.49	13.09	0535485-051742	1290	35:51.93	-5:14:16.5	14.72	13.87	13.65	0535519-051416
1252	35:48.62	-5:11:53.2	16.72	15.78	15.56		1291	35:51.94	-5:11:56.6	17.41	16.52	16.25	
1253	35:48.76	-4:58:38.5	18.01	16.70	16.50		1292	35:51.96	-5:03:57.7	16.41	15.48	15.23	0535519-050357
1254	35:48.84	-5:00:28.5	12.66	11.67	11.35	0535488-050028	1293	35:52.26	-5:13:18.6	13.91	13.24	12.87	0535522-051318
1255	35:48.96	-5:09:53.0	16.15	15.11	14.60	0535489-050953	1294	35:52.29	-4:57:41.8	19.09	17.02	16.54	
1256	35:48.99	-5:01:39.3	12.61	11.81	11.53	0535489-050139	1295	35:52.33	-5:12:57.0	12.84	12.18	11.87	0535523-051256
1257	35:49.02	-5:15:52.7	15.95	15.15	14.97		1296	35:52.48	-4:57:04.2	16.64	15.07	14.52	0535524-045704
1258	35:49.03	-5:15:37.6	13.13	12.33	12.07	0535490-051537	1297	35:52.63	-5:05:05.3	9.84†	9.26†	8.85†	0535526-050505
1259	35:49.66	-5:00:34.7	17.47	16.16	15.67		1298	35:52.77	-5:12:59.0	11.73	11.07†	10.45†	0535527-051258
1260	35:49.66	-5:06:02.7	13.26	12.57	12.46	0535496-050602	1299	35:52.88	-4:59:29.0	17.84	16.52	15.81	
1261	35:49.80	-5:06:39.7	15.48	14.69	14.41	0535497-050639	1300	35:52.89	-4:58:34.4	16.04	15.09	14.68	0535528-045834
1262	35:49.81	-4:58:22.8	18.37	17.06	16.58		1301	35:52.95	-5:01:18.3	15.21	14.19	13.93	0535529-050118
1263	35:49.84	-5:15:12.8	15.44	14.65	14.24		1302	35:53.09	-5:10:17.9	17.42	16.02	15.65	
1264	35:50.03	-5:17:17.8	14.98	14.01	13.54	0535500-051718	1303	35:53.31	-4:57:26.2	18.56	17.09	16.09	
1265	35:50.06	-4:58:16.1	14.46	13.26	12.93	0535500-045816	1304	35:53.35	-5:01:16.0	16.83	15.78	15.36	
1266	35:50.08	-5:09:46.2	13.39	12.48	12.15	0535500-050946	1305	35:53.44	-5:09:39.2	17.62	16.07	15.47	
1267	35:50.12	-5:10:29.4	13.22	12.64	12.37	0535501-051029	1306	35:53.54	-5:02:34.7	13.02	11.99	11.62	0535535-050234
1268	35:50.12	-5:17:00.2	17.76	16.51	16.60		1307	35:53.64	-5:10:09.6	15.67	14.75	14.35	0535536-051009
1269	35:50.41	-5:17:29.9	17.44	16.38	15.82		1308	35:53.71	-5:02:00.7	15.88	15.00	14.64	0535537-050200
1270	35:50.56	-5:16:11.7	17.67	16.13	15.93		1309	35:53.99	-5:10:40.0	15.59	15.00	14.85	0535539-051039
1271	35:50.58	-5:09:20.9	14.29	13.18	12.55		1310	35:54.00	-5:00:30.7	17.72	16.51	16.37	
1272	35:50.66	-5:14:58.9	17.39	16.58	14.31		1311	35:54.03	-5:04:14.9	11.32†	10.43†	9.90†	0535540-050414
1273	35:50.76	-5:16:28.9	11.36	10.65†	10.21†	0535507-051629	1312	35:54.09	-5:13:29.8	16.79	16.30	16.01	
1274	35:50.77	-5:16:53.3	16.69	15.46	15.15		1313	35:54.19	-5:14:43.8	17.22	15.95	15.93	
1275	35:50.82	-5:09:29.9	8.49†	7.20†	6.67†	0535508-050930	1314	35:54.20	-5:05:45.4	13.43	12.79	12.61	0535542-050545
1276	35:50.84	-5:05:49.3	17.74	16.41	15.65		1315	35:54.21	-5:13:43.0	>21.91	18.38	17.27	
1277	35:51.02	-5:17:33.0	17.36	16.41	15.31		1316	35:54.32	-5:11:52.3	16.98	16.07	15.82	
1278	35:51.05	-5:15:08.7	11.81	11.30†	10.97†	0535510-051508	1317	35:54.68	-5:05:21.3	16.93	15.79	15.08	
1279	35:51.08	-5:07:08.7	11.01	10.28†	9.87†	0535510-050708	1318	35:54.69	-5:06:27.8	13.34	12.85	12.57	0535546-050627
1280	35:51.31	-5:11:59.9	15.92	14.98	14.80		1319	35:54.77	-5:10:55.6	13.21	12.61	12.47	0535547-051055
1281	35:51.45	-5:08:01.8	15.59	14.30	13.52		1320	35:54.80	-4:59:20.2	16.40	15.17	14.75	0535548-045920

(cont.)

(cont.)

ID	R.A. <sup>a</sup>	decl. <sup>a</sup>	$J^{bcd}$	$H^{bcd}$	$K^{cd}$	2MASS	ID	R.A. <sup>a</sup>	decl. <sup>a</sup>	$J^{bcd}$	$H^{bcd}$	$K^{cd}$	2MASS
1321	35:54.82	-5:00:48.9	16.87	16.00	15.89		1360	35:58.27	-5:00:48.1	17.23	16.09	15.93	
1322	35:54.95	-5:10:27.9	14.48	13.78	13.59	0535549-051027	1361	35:58.37	-5:06:27.4	16.95	16.19	15.75	
1323	35:54.97	-5:13:15.5	12.35	11.64	11.43	0535549-051315	1362	35:58.74	-4:59:32.2	16.07	14.85	14.47	0535587-045932
1324	35:55.03	-5:03:16.1	17.03	16.00	15.66		1363	35:58.75	-4:59:19.8	17.66	16.18	15.81	
1325	35:55.06	-5:02:37.3	13.87	12.72	12.33	0535550-050237	1364	35:58.81	-5:10:14.6	15.23	14.66	14.12	0535588-051014
1326	35:55.18	-5:14:42.6	17.25	15.87	15.60		1365	35:58.82	-5:00:26.1	15.03	14.38	14.07	0535588-050026
1327	35:55.35	-5:14:13.9	16.14	15.32	14.92		1366	35:59.00	-5:12:40.6	16.12	15.38	14.96	
1328	35:55.41	-5:09:50.2	16.39	15.60	15.19	0535554-050950	1367	35:59.22	-4:58:46.2	12.55	11.83	11.61	0535592-045846
1329	35:55.45	-5:13:55.3	13.15	12.52	12.29	0535554-051355	1368	35:59.22	-5:07:33.7	14.81	14.24	13.82	0535592-050733
1330	35:55.60	-5:10:00.4	17.22	16.58	16.52		1369	35:59.48	-5:10:21.4	16.22	15.19	15.27	0535595-051021
1331	35:55.65	-5:08:11.9	16.71	15.97	15.40		1370	35:59.61	-5:01:28.7	13.52	12.62	12.34	0535596-050128
1332	35:55.74	-5:04:37.7	16.99	15.68	14.18		1371	35:59.67	-5:01:38.6	16.59	15.31	15.03	0535596-050138
1333	35:55.94	-5:00:07.5	14.69	14.09	13.78	0535559-050007	1372	35:59.71	-5:06:43.5	15.10	14.28	14.26	0535597-050643
1334	35:56.00	-5:05:37.3	16.50	15.40	15.15	0535560-050537	1373	35:59.91	-5:00:37.7	17.34	15.98	15.49	
1335	35:56.02	-5:00:51.5	14.08	13.05	12.79	0535560-050051	1374	35:59.93	-5:04:31.0	13.41	12.82	12.52	0535599-050430
1336	35:56.02	-5:12:09.0	15.23	14.29	14.01	0535560-051209	1375	36:00.33	-5:05:00.0	12.23	11.66	11.44	0536003-050459
1337	35:56.04	-5:09:03.1	11.17	10.39†	10.12†	0535560-050903	1376	36:00.45	-5:05:54.0	13.38	12.83	12.61	0536004-050553
1338	35:56.49	-5:10:30.7	14.95	14.35	14.22	0535564-051030	1377	36:00.77	-4:59:14.7	15.46	14.53	14.24	0536007-045914
1339	35:56.55	-4:58:58.7	15.45	14.44	14.09	0535565-045858	1378	36:00.92	-5:08:48.7	15.88	15.17	15.04	0536009-050848
1340	35:56.61	-5:02:16.5	17.40	16.29	15.75		1379	36:01.07	-5:03:09.3	17.11	15.99	15.79	
1341	35:56.69	-4:59:02.5	17.56	16.43	16.07		1380	36:01.27	-5:01:59.2	16.18	15.23	14.93	0536012-050158
1342	35:56.81	-5:13:28.9	17.65	16.58	16.44		1381	36:01.28	-5:07:56.4	15.44	14.71	14.54	0536012-050756
1343	35:56.84	-4:59:14.6	14.68	14.11	13.77	0535568-045914	1382	36:01.31	-5:07:39.1	17.35	16.34	15.62	
1344	35:57.04	-5:01:40.7	17.66	16.52	15.94		1383	36:01.51	-5:00:21.0	16.58	15.18	14.86	0536015-050020
1345	35:57.14	-5:01:49.5	17.64	16.79	16.23		1384	36:01.55	-5:11:55.3	16.95	16.08	15.86	
1346	35:57.15	-5:02:31.9	16.93	15.94	15.72		1385	36:01.64	-5:10:40.4	15.41	14.83	14.69	0536016-051040
1347	35:57.24	-5:07:22.4	16.84	16.11	15.70		1386	36:01.74	-4:59:24.3	16.37	15.21	14.67	0536017-045924
1348	35:57.47	-5:05:32.2	17.36	16.29	16.05		1387	36:01.87	-5:08:35.1	16.09	15.18	14.88	0536018-050835
1349	35:57.47	-5:08:29.1	17.85	16.80	16.48		1388	36:02.17	-5:00:13.1	17.98	16.97	16.42	
1350	35:57.54	-5:08:44.2	17.44	16.60	16.34		1389	36:02.52	-5:04:42.1	16.79	16.05	15.89	
1351	35:57.61	-5:10:02.6	17.82	16.83	16.22		1390	36:02.63	-5:07:36.5	11.31	10.69†	10.49†	0536026-050736
1352	35:57.66	-5:10:29.6	16.73	16.19	15.97	0535576-051029	1391	36:02.70	-5:04:18.9	17.08	16.35	16.23	
1353	35:57.89	-5:12:18.0	15.97	15.33	15.05		1392	36:02.73	-5:04:44.7	17.67	16.57	16.25	
1354	35:58.07	-5:12:54.3	9.15†	8.30†	8.05†	0535580-051254	1393	36:02.81	-5:04:23.7	14.89	14.39	14.06	0536028-050423
1355	35:58.10	-5:11:42.7	15.49	14.54	13.85		1394	36:02.87	-5:09:00.1	17.25	16.43	16.27	
1356	35:58.17	-5:13:07.1	17.04	16.27	15.98		1395	36:02.91	-5:05:43.3	17.61	16.30	15.65	
1357	35:58.19	-5:11:22.9	17.81	16.58	16.00		1396	36:02.93	-5:07:53.2	17.16	16.13	15.45	
1358	35:58.20	-5:11:53.8	16.51	15.61	15.41		1397	36:03.03	-5:01:11.0	17.58	16.40	15.97	
1359	35:58.22	-5:09:32.1	15.16	14.45	14.22	0535582-050932	1398	36:03.04	-5:07:18.7	15.16	14.36	14.16	0536030-050718

(cont.)

(cont.)

ID	R.A. <sup>a</sup>	decl. <sup>a</sup>	$J^{bcd}$	$H^{bcd}$	$K^{cd}$	2MASS	ID	R.A. <sup>a</sup>	decl. <sup>a</sup>	$J^{bcd}$	$H^{bcd}$	$K^{cd}$	2MASS
1399	36:03.14	-4:58:58.9	15.71	14.73	14.49	0536031-045859	1424	36:06.30	-5:09:40.1	17.30	16.32	16.03	
1400	36:03.21	-5:07:09.6	17.39	16.55	16.44		1425	36:06.62	-5:06:07.4	>21.91	>20.96	17.47	
1401	36:03.25	-5:09:30.9	15.66	14.86	14.70	0536032-050931	1426	36:06.65	-5:03:06.9	17.24	16.24	16.06	
1402	36:03.29	-5:04:21.4	16.59	15.69	15.32	0536032-050421	1427	36:06.79	-5:06:15.5	12.98	12.25	12.04	0536067-050615
1403	36:03.39	-5:04:00.8	14.81	14.03	13.85	0536034-050401	1428	36:06.85	-5:08:50.8	16.68	15.93	15.93	0536068-050851
1404	36:03.53	-5:07:31.0	17.73	16.81	16.54		1429	36:07.07	-5:04:07.6	16.98	15.86	15.61	0536070-050407
1405	36:03.54	-5:04:45.2	16.74	15.73	15.51	0536035-050445	1430	36:07.61	-5:04:15.4	17.67	16.56	16.43	
1406	36:04.15	-5:04:08.8	12.77	12.02	11.67	0536041-050409	1431	36:07.71	-5:09:41.2	16.28	15.28	15.07	0536077-050941
1407	36:04.32	-5:07:15.6	10.90 <sup>†</sup>	10.57 <sup>†</sup>	10.51 <sup>†</sup>	0536043-050715	1432	36:07.96	-5:09:37.3	17.23	16.64	16.72	
1408	36:04.48	-5:07:00.9	16.04	15.36	15.16		1433	36:08.26	-5:04:01.8	14.68	14.04	13.97	0536082-050401
1409	36:04.51	-5:09:28.6	11.23	10.62 <sup>†</sup>	10.44 <sup>†</sup>	0536045-050929	1434	36:08.49	-5:06:14.7	17.02	16.07	15.90	
1410	36:04.70	-5:13:03.7	>21.66	>20.71	16.61		1435	36:08.54	-5:01:41.3	15.28	14.42	14.30	0536085-050141
1411	36:04.86	-4:58:45.1	15.67	14.73	14.39	0536048-045845	1436	36:08.68	-5:04:34.3	15.97	14.91	14.70	0536086-050434
1412	36:04.87	-4:59:32.6	17.29	16.02	15.72		1437	36:08.70	-5:02:32.2	18.70	18.08	16.34	
1413	36:04.97	-4:59:41.5	11.71	11.20	11.13		1438	36:08.80	-5:02:35.0	15.94	14.96	14.70	0536088-050235
1414	36:05.07	-5:10:57.9	>21.41	>20.46	16.14		1439	36:08.92	-5:02:26.3	17.84	16.69	16.44	
1415	36:05.09	-4:59:42.9	11.75	11.24	11.16	0536050-045943	1440	36:09.81	-5:00:49.9	13.48	12.63	12.53	0536098-050050
1416	36:05.09	-5:03:12.2	15.35	14.68	14.55	0536050-050312	1441	36:09.96	-5:05:35.3	14.23	13.63	13.39	0536099-050535
1417	36:05.11	-5:11:13.4	13.78	13.32	12.88	0536051-051113	1442	36:10.17	-5:07:02.7	15.51	14.55	14.36	0536101-050703
1418	36:05.43	-5:04:43.6	16.45	16.03	14.15		1443	36:10.57	-5:06:12.3	17.79	16.88	16.83	
1419	36:05.48	-5:07:58.6	15.62	15.09	14.69	0536054-050758	1444	36:10.76	-5:04:34.0	15.85	14.92	14.84	0536107-050434
1420	36:05.87	-5:02:18.2	14.63	13.97	13.77	0536058-050218	1445	36:10.81	-5:02:31.3	15.50	14.80	14.71	0536108-050231
1421	36:05.94	-5:00:41.0	14.92	14.00	13.77	0536059-050041	1446	36:11.00	-5:03:41.2	8.44 <sup>†</sup>	8.22 <sup>†</sup>	8.14 <sup>†</sup>	0536110-050341
1422	36:06.02	-5:08:15.0	15.81	15.30	15.19	0536060-050815	1447	36:11.79	-5:00:32.4	12.12	11.37	11.24	0536118-050032
1423	36:06.14	-5:07:55.6	>21.72	>20.77	17.05		1448	36:12.41	-5:00:53.8	15.97	14.73	14.55	0536124-050053

(cont.)

<sup>a</sup> The equinox in J2000.0 in the format of 05:mm:ss.ss for R.A. and dd:mm:ss.ss for decl. The hundredth and the tenth order in the arc seconds of R.A. and decl. are truncated.

<sup>b</sup> The upper limit of the flux (the lower limit of the magnitude) is given for sources with less than a  $3\sigma$  detection in the  $J$ ,  $H$ , or both bands.

<sup>c</sup> Saturated QUIRC magnitudes (brighter than 11 mag) are replaced with 2MASS magnitudes and labeled <sup>†</sup> if they have the 2MASS counterpart.

<sup>d</sup> Saturated QUIRC magnitudes (brighter than 11 mag) are labeled  $<$  if they have no 2MASS counterpart, recognizing the value as the lower limit of the flux (the upper limit of the magnitude).

# Acknowledgments

Without the support from my wonderful collaborators, this thesis could not have been completed. I am grateful to Katsuji Koyama who introduced me to the X-ray astronomy and to the X-ray studies of star formation. I also appreciate Kensuke Imanishi in Kyoto University and Yohko Tsuboi in Chuo University for their interesting discussions on X-ray emissions from young stars.

For the NIR part of this work, I am particularly indebted to Naoto Kobayashi in NAOJ, who instructed me in the infrared astronomy and oriented me to take a multi-wavelength approach. Miwa Goto and Hiroshi Terada in NAOJ, and Alan T. Tokunaga in the University of Hawaii also helped me to obtain and analyze the NIR data and to publish results.

The radio part is based on my collaboration with Masao Saito in NAOJ and Claire Chandler in NRAO, who gave me invaluable advice on the radio astronomy, interferometer observations, data reductions, and publications.

I am obliged to all the staff members of various observatories that I visited for this work; the Subaru telescope on September 8–30, 2000, November 27–December 27, 2000, and March 15–24, 2001, the University of Hawaii 88 inch (2.2 m) telescope on February 2–10, 2001 and March 10–14, 2001, and VLA on February 6–17, 2002. The observation using Subaru/IRCS was conducted during its engineering time. Miwa Goto took me the  $L'$ -band data at IRTF. Michael Connelley spent a part of his observation time for our QUIRC calibration data. The hospitality of all these people was the largest incentive for me to write the next observation proposal.

My gratitude is also for Rolf Chini and Markus Nielbock who kindly offered me their 1.3 mm map of OMC-2 and OMC-3 including unpublished parts of their data, for Martin Cohen who let me use his SKY model to estimate the galactic star count of our study field, for Luisa M. Rebull who sent me the  $UV$  excess data of Orion sources, and for Hiroaki Isobe

who gave me precious information on solar flares.

The members of my laboratory should be acknowledged as well for their continuous encouragements. In particular, Hironori Matsumoto, Aya Bamba, and Junko Kushida helped me to improve the manuscript through their critical proofreading and comments. Shigeo Yamauchi in Iwate University also read the proofs. I would also like to thank Toru Tanimori, Hideo Kodama, Shu-ichiro Inutsuka, and Hidetoshi Kubo for their constructive refereeing of this thesis.

Finally, I express my most sincere appreciation to my thesis advisor, Professor Katsuji Koyama, who mentored me throughout my graduate course. It is of my greatest honor that I could start my career with fruitful five years under his gracious and thoughtful guidance.

This work is based on data collected at Subaru Telescope, which is operated by the National Astronomical Observatory of Japan. The National Radio Astronomy Observatory is a facility of the National Science Foundation operated under cooperative agreement by Associated Universities, Inc. The *Chandra* data were obtained through the *Chandra* X-ray Observatory Science Center (CXC) operated for NASA by the Smithsonian Astrophysical Observatory. This publication makes use of data products from the Two Micron All Sky Survey, which is a joint project of the University of Massachusetts and the Infrared Processing and Analysis Center/California Institute of Technology, funded by the National Aeronautics and Space Administration and the National Science Foundation. This research has made use of the Astronomical Data Center (ADC) at NASA Goddard Space Flight Center, and the SIMBAD database operated at CDS, Strasbourg, France. This research has made use of NASA's Astrophysics Data System Bibliographic Services. IRAF is distributed by the National Optical Astronomy Observatory, which is operated by the Association of Universities for Research in Astronomy, Inc., under cooperative agreement with the National Science Foundation.

I acknowledge financial support by the Japan Society for the Promotion of Science and the Hayakawa Satio Foundation of the Astronomical Society of Japan.